

CRANFIELD UNIVERSITY

CLAUDIA MOIA

*In vitro* toxicological assessment of amorphous silica particles in relation to their characteristics and mode of action in human skin cells

SCHOOL OF ENERGY, ENVIRONMENT AND AGRIFOOD  
Environmental Technology

MPhil/PhD  
Academic Year: 2012 - 2015

Supervisor: Dr. Huijun Zhu  
September 2015



CRANFIELD UNIVERSITY

SCHOOL OF ENERGY, ENVIRONMENT AND AGRIFOOD  
Environmental Technology

MPhil/PhD

Academic Year 2012 - 2015

CLAUDIA MOIA

*In vitro* toxicological assessment of amorphous silica particles in relation to their characteristics and mode of action in human skin cells

Supervisor: Dr. Huijun Zhu  
September 2015

© Cranfield University 2015. All rights reserved. No part of this publication may be reproduced without the written permission of the copyright owner.

## ABSTRACT

**Background:** Silica is the common name for silicon dioxide ( $\text{SiO}_2$ ) materials and exists in both crystalline and amorphous forms. While crystalline silica is known for its severe health effects, amorphous silica has been considered safe and applied in many areas. However, some recent studies have showed evidence of their toxicity, raising concerns about its use as nanomaterial for biomedical applications. When nanomaterials enter the body, they are enveloped in biological fluids rich in biomolecules, which compete for binding to the nanomaterial. Such effect could alter their surface chemistry and therefore affect their bio-distribution and interaction with cells.

**Aim and objectives:** As part of the EU-funded NANODRUG network programme, the aim of this project was the *in vitro* toxicity assessment of commercially-sourced fumed and colloidal amorphous silica particles in relation to their physico-chemical properties and potential application as carriers for drug delivery. The objectives were 1) characterization of silica particles hydrodynamic ( $H_d$ ) size and dispersity in different cell culture media; 2) *in vitro* toxicological assessment of silica particles in human skin cells; 3) delineation of toxicity mechanisms in relation to their size; 4) assessment of the influence of Foetal Bovine Serum (FBS) on particle  $H_d$  size and toxicity; and 5) contributing to the overall objective of the NANODRUG programme - development of safe nanodrugs for skin application - through collaborations with different partners.

**Methods:** A group of amorphous silica including fumed silica 7 nm and 14 nm (SiNP7 and SiNP14), and colloidal silica nanoparticles of 20 nm and 70 nm (SiNP20 and SiNP70) and submicroparticles 200 nm and 500 nm (SMP200 and SMP500) were selected for the study. They were dispersed in different media (used for culture of different cells) and characterized for size, shape, dispersion and zeta potential using Dynamic Light Scattering (DLS), Zeta Potential (ZP), Scanning and Transmission Electron Microscopy (SEM and TEM). HaCaT keratinocytes were used to assess the toxicity potential of all the silica particles after 24 h treatment at 5-200  $\mu\text{g/ml}$ , while K17 keratinocytes, and BJ fibroblasts and Human Dermal Fibroblasts (HDF) were also used to assess cell type

specific effect. Toxicity assessment included morphology, cellular uptake, cell viability, cell membrane damage, apoptosis, wound healing, and gene expression.

**Results:** TEM and SEM imaging showed that fumed SiNPs formed irregular chain-like aggregates, while all colloidal silica displayed spherical shape apart from SiNP20, which also formed chain-like aggregates. DLS assays suggested that FBS and some other components of cell culture media could alter the hydrodynamic size and dispersity of the particles. Fumed SiNP7 and SiNP14 induced significant cytotoxicity in the absence of FBS, while the effect was diminished in the presence of FBS. Colloidal SiNP20 also induced significant toxicity in the absence of FBS, while the effect was attenuated in the presence of FBS. For colloidal SiNP70, the toxicity was only detected in the absence of FBS. These SiNPs toxicity were detected by assays including cell viability, cell membrane leakage and apoptosis, and appeared to be associated with cellular internalization. SMP200 and SMP500, on the other hand, appeared to sediment during incubation with cells. Although they were readily internalized by the cells their toxicity was only detected in the absence of FBS by apoptosis assay. Moreover, all the colloidal silica also showed a dose-dependent effect in promoting wound healing at 5-25 ug/ml, with SiNP70 being most significant. In K17 keratinocytes, cellular internalization occurred to all the silica tested, yet only SiNP20 induced a significant toxicity. In BJ fibroblasts and human dermal fibroblast cells, silica toxicity appeared not to be associated with their internalization.

**Conclusions:** This study clearly demonstrated that 1) fumed and colloidal SiNPs exhibited different dispersity in cell culture media; 2) silica particles exerted toxicity in a size-dependent manner in four human skin cell lines including two cell types; 3) SiNPs toxicity involved activation of apoptosis; 4) SiNPs dispersity, cellular uptake and toxicity were modulated by FBS; 5) silica promoted wound healing in size- and dose-dependent manner. This *in vitro* study suggests that 1) SiNP7, SiNP14, SiNP20 may not be suitable for biomedical applications due to their instability in biological media and toxicity

induction respectively; 2) the potential of silica toxicity could be different *in vivo* as components of FBS used *in vitro* are different from that of human serum; 3) there seems to be dose thresholds for colloidal silica to interfere with different cellular processes such as toxicity and wound healing. Although this project aimed to assess the toxicity silica particles for drug delivery, it has also provides new evidence supporting development of new regulations specific for nanomaterials.

Keywords:

Silica, bovine serum, *in vitro* cytotoxicity, wound healing

## **ACKNOWLEDGEMENTS**

I would like to thank Dr. Zhu for giving me the opportunity to do my PhD in Cranfield, and for the support and guidance, she has given me as my supervisor. I would like to thank Dr. Adeel Irfan for the mentoring he provided at the start of my journey at Cranfield University. I would also like to thank Prof. Marina Resmini and the NANODRUG network for providing emotional and professional support, as well as important opportunities for fruitful collaborations. Special thanks go to Kiran Kumar Chereddy, Dr. Sara Vicente, Michela Comune, Prof. Veronique Pr at, Xavier Vig e and Lino Ferreira for the amazing collaboration support. I would also like to thank my beloved parents, who have always loved and supported me despite the distance, and my friends Gianluca, Ravi, Carla, Sara and Raniero, who may be far away but always ready to help when in need.

# TABLE OF CONTENTS

ABSTRACT .....	i
ACKNOWLEDGEMENTS.....	iv
LIST OF EQUATIONS.....	xviii
LIST OF ABBREVIATIONS .....	xix
1 LITERATURE REVIEW .....	1
1.1 Introduction .....	1
1.2 Nanomaterials – An Overview .....	1
1.2.1 History of nanotechnology and nanomaterials .....	1
1.2.2 Nanomaterials’ characteristics and influence upon interaction with biological systems .....	3
1.2.3 Toxicity of nanomaterials.....	6
1.2.4 Current status of nanomaterials regulation.....	16
1.3 Silica Nanomaterials .....	21
1.3.1 Synthesis methods and characteristics .....	21
1.3.2 Relationship between characteristics and toxicity .....	24
1.4 Skin – A Major Target of Nanomaterials .....	29
1.4.1 Structure and function .....	29
1.4.2 The <i>stratum corneum</i> , its composition and barrier function.....	31
1.4.3 Basic principles of <i>in vitro</i> tissue culture.....	38
1.4.4 Interaction of culture medium and biological fluids with nanomaterials .....	40
1.5 Conclusions .....	45
2 AIMS AND OBJECTIVES.....	46
2.1 Aims.....	46
2.1.1 Research hypothesis.....	46
2.2 Objectives .....	46
2.2.1 Objective 1: Characterization of silica particles behaviour in cell culture medium.....	46
2.2.2 Objective 2: Toxicological assessment of silica particles <i>in vitro</i> in human skin cells.....	47
2.2.3 Objective 3: Delineation of toxicity mechanisms in relation to silica particle size .....	47
2.2.4 Objective 4: Assessment of the effect of serum on silica particle behaviour in cell culture medium and toxicity potential .....	48
2.2.5 Collaboration with partners to achieve the overall objectives of the NANODRUG consortium.....	48
2.3 Research Approach .....	49
3 MATERIALS AND METHODS.....	50
3.1 Materials .....	50
3.2 Characterization of Nanoparticles.....	53



3.2.1	Dynamic light scattering (DLS).....	53
3.2.2	Zeta potential .....	57
3.2.3	Electron microscopy (scanning electron microscopy and transmission electron microscopy).....	62
3.3	Cytotoxicity Assessment.....	65
3.3.1	Cell lines used for the assays.....	65
3.3.2	Cell culture .....	67
3.3.3	Cell viability and membrane damage assays .....	68
3.3.4	Phase contrast microscopy for cell imaging .....	73
3.3.5	Flow cytometry assays for cell uptake of particles and apoptosis assay.....	75
3.3.6	TEM imaging for cellular uptake.....	78
3.3.7	Confocal microscopy .....	79
3.3.8	Wound healing assay .....	82
3.3.9	Western blot.....	84
3.3.10	Molecular pathway analysis .....	87
3.3.11	Statistics.....	93
4	RESULTS.....	94
4.1	Fumed Amorphous Silica.....	94
4.1.1	Characteristics in suspension.....	94
4.1.2	<i>In vitro</i> cytotoxicity assessment and induction of apoptotic cell death .....	100
4.2	Colloidal Amorphous Silica .....	104
4.2.1	Characteristics in suspension.....	104
4.2.2	<i>In vitro</i> cytotoxicity assessment and wound healing induction on HaCaT cells.....	114
4.2.3	<i>In vitro</i> toxicity potential in other human skin cells.....	140
5	DISCUSSION .....	156
5.1	Silica particles dispersion properties in biological media depend on size, media composition and temperature.....	156
5.2	Silica particles uptake into HaCaT cells is endocytosis-related .....	162
5.3	Modulation of silica size dependent toxicity by FBS .....	165
5.4	Silica induction of apoptotic cell death is size- and dose-dependent ....	168
5.5	Silica particles enhance wound healing <i>in vitro</i> in the HaCaT model system .....	174
5.6	Cell-type related toxicological effects of colloidal silica .....	176
6	CONCLUSIONS.....	179
7	FUTURE PERSPECTIVES .....	182
	REFERENCES.....	184
	APPENDICES .....	209

## LIST OF FIGURES

<b>Figure 1.1</b> An overview of some of the different nanomaterials that are available today. This explains how challenging a complete classification of nanomaterials can be (modified from [9] Algar et al. (2011)).....	4
<b>Figure 1.2</b> An overview of the factors involved in nanotoxicology (modified from [7] Nel et al. 2006).....	7
<b>Figure 1.3</b> Schematics of endocytosis mechanisms. ....	9
<b>Figure 1.4</b> Impairment in ROS control can give rise to several pathologies (modified from [37] Murphy et al., 2009).....	12
<b>Figure 1.5</b> The molecular mechanism of apoptosis (modified from [39] Cullen et al. (2009)).....	13
<b>Figure 1.6</b> The intrinsic activation pathway (modified from [38] Alberts et al. (2002)).....	14
<b>Figure 1.7</b> Drawing showing the routes of exposure to nanomaterials (modified from [10] Chen et al. 2011).....	14
<b>Figure 1.8</b> The <i>stratum corneum</i> and its pathways for molecule diffusion (modified from [19] Schneider et al. 2009). ....	15
<b>Figure 1.9</b> Schematics of the reaction used to obtain fumed silica. ....	24
<b>Figure 1.10</b> Siloxane rings that constitute the architecture of amorphous silica (modified from [62] Zhang et al. 2012). ....	25
<b>Figure 1.11</b> Drawing of the skin tissue and main components of cells. At the bottom is the hypodermis, consisting of adipose cells; the next layer up is the dermis, consisting of fibroblasts; at the top is the epidermis consisting of viable and nonviable keratinocytes and melanocyte (from [70] Brohem et al. 2011). ....	30
<b>Figure 1.12</b> The structure of ceramides, fatty acids and cholesterol (modified from [78] Lee et al. 2006). ....	33
<b>Figure 1.13</b> Major SC lipid content by weight. Ceramides are the most abundant lipids, being approximately 40-50% of total, followed by cholesterol and fatty acids.....	34
<b>Figure 1.14</b> Steps in the formation of the <i>stratum corneum</i> . Starting from the <i>stratum basale</i> , keratinocytes undergo a stepwise differentiation process that ends with corneocyte desquamation on the <i>stratum corneum</i> . (Skin Image from <a href="http://php.med.unsw.edu.au/embryology/index.php?title=File:Adult_epidermis_histology_01.jpg">http://php.med.unsw.edu.au/embryology/index.php?title=File:Adult_epidermis_histology_01.jpg</a> ) .....	35

<b>Figure 1.15</b> The bricks and mortar model with the various functions of the SC (modified from [78] Lee et al. 2006). .....	36
<b>Figure 1.16</b> The principle behind protein corona formation (Modified from [88] Aggarwal et al., 2009). .....	41
<b>Figure 2.1</b> An overview of the research approach used in this study.....	49
<b>Figure 3.1</b> The DLS measuring system has six components: a laser (1), a cell (2), a detector (3), an attenuator (4) a correlator (5) and a computer (6) (modified from [98] Malvern Zetasizer User Guide).....	55
<b>Figure 3.2</b> The correlation function measures the similarity between signals over very short periods of time; the decay rate is directly related to particle size (modified from [98] Zetasizer User Guide).....	56
<b>Figure 3.3</b> Size distribution graph derived from the correlation function (modified from [98] Zetasizer User Guide). .....	56
<b>Figure 3.4</b> The basic principle of zeta potential (modified from [98] Zetasizer User Guide).....	58
<b>Figure 3.5</b> The cell system used to measure zeta potential is equipped with a positive and negative electrode, where potential is applied (modified from [98] Zetasizer User Guide). .....	59
<b>Figure 3.6</b> A schematic version of the ZP measurement system including a laser (1), a cell (2), a detector (3), a digital signal processor (4), a computer (5), an attenuator (6) and compensation optics (7) (modified from [98] Zetasizer User Guide). .....	61
<b>Figure 3.7</b> The basics of TEM (from <a href="http://www.nobelprize.org/educational/physics/microscopes/tem/">http://www.nobelprize.org/educational/physics/microscopes/tem/</a> ). .....	63
<b>Figure 3.8</b> The difference between SEM and TEM (from <a href="http://bsp.med.harvard.edu/node/221">http://bsp.med.harvard.edu/node/221</a> ). .....	64
<b>Figure 3.9</b> The general structure of the tetrazolium dyes and the formazan salts.....	69
<b>Figure 3.10</b> The structures of MTT (A) and WST-1 (B).....	69
<b>Figure 3.11</b> The mechanism behind MTT and WST-1 reduction by cells (modified from [109] Berridge et al., 2005).....	70
<b>Figure 3.12</b> The LDH enzyme catalyzes the interconversion between pyruvate (left) and lactate (right). .....	72
<b>Figure 3.13</b> The structure of a phase contrast microscope and its phase ring. The portion of light that passed the specimen without experiencing diffraction passes the phase ring (A), whereas the retention plate retards the phase of the non-diffracted light to allow interference with the light waves that experienced phase shift and diffraction by passing the sample	

(B) (from [113] <a href="http://www.leica-microsystems.com/science-lab/phase-contrast/">http://www.leica-microsystems.com/science-lab/phase-contrast/</a> ).	74
<b>Figure 3.14</b> The basic structure of a confocal microscope (modified from [122] <a href="http://www.olympusfluoview.com/theory/confocalintro.html">http://www.olympusfluoview.com/theory/confocalintro.html</a> ).	80
<b>Figure 3.15</b> The detection mechanisms in western blot (from <a href="http://www.leinco.com/general_wb">http://www.leinco.com/general_wb</a> ).	86
<b>Figure 3.16</b> The principle for Taqman™ RT-PCR (modified from <a href="http://www.nature.com/nrd/journal/v3/n9/fig_tab/nrd1496_F1.html">http://www.nature.com/nrd/journal/v3/n9/fig_tab/nrd1496_F1.html</a> ).	89
<b>Figure 3.17</b> SYBR Green and its intercalation inside dsDNA (modified from <a href="http://img.guidechem.com/pic/image/163795-75-3.png">http://img.guidechem.com/pic/image/163795-75-3.png</a> and <a href="http://eng.bioneer.com/products/geneexpression/qPCRArrayService-detection.aspx">http://eng.bioneer.com/products/geneexpression/qPCRArrayService-detection.aspx</a> ).	90
<b>Figure 3.18</b> The three steps involved in real-time PCR (modified from QIAGEN RT-PCR Handbook).	91
<b>Figure 4.1</b> DLS profiling of particle dispersion patterns in CM-10% and CM. a, f: culture media presenting background particles; b, c, d and e: dispersion patterns of SiNP7 and SiNP14 in CM-10%; g, h, i and l: dispersion patterns of SiNP7 and SiNP14 in CM.	99
<b>Figure 4.2</b> SEM Imaging of SiNP7. SEM imaging in water at 10 µg/ml was performed using Philips XL30 SFEG. Scale bar: 1 µm.	99
<b>Figure 4.3</b> Effect of fumed silica nanoparticles on cell viability in HaCaT cells assessed by MTT assay. HaCaT cells were treated with SiNP7 and SiNP14 in CM-10% and CM and cell viability was assessed at 24 h treatment. Results were expressed as percentage of negative control, indicating increase/decrease of cellular metabolism in particle-treated samples compared with cellular metabolism in particle-free control. Black line serves as reference for normal cellular activity. Each particle concentration was tested in triplicates and the results analysed by one-way ANOVA and Student's t-test. Statistically significant results (p<0.05) are marked with an asterisk (*) on top of the corresponding bar.	100
<b>Figure 4.4</b> Flow cytometry assay of cellular uptake of fumed silica nanoparticles. HaCaT cells were treated with the particles at 10-200 µg/ml in CM-10% and CM for 24 h. Results are expressed as number of cells vs. detected fluorescence. The red line separates the left part of the graph, which indicates non-fluorescent cells associated with particle-free cells, from the right part of the graph, which shows fluorescence positive cells associated with silica particles uptake.	101
<b>Figure 4.5</b> Apoptosis assay of fumed silica in CM-10%. HaCaT cells were treated with SiNP7 and SiNP14 at 5-25 µg/ml in CM-10% for 24 h. Following treatment, double staining with propidium iodide (PI) and Annexin V/FITC was performed and using BD Accuri C6 flow cytometer. For each sample 10.000 events were recorded, and the results expressed as PI	

fluorescence vs. Annexin V/FITC fluorescence. In each quadrant, quantification is reported as percentage of detected fluorescence..... 103

**Figure 4.6** Apoptosis assay of fumed silica in CM. HaCaT cells were treated with SiNP7 and SiNP14 at 5-25 µg/ml in CM for 24 h. Following treatment, double staining with propidium iodide (PI) and Annexin V/FITC was performed and using BD Accuri C6 flow cytometer. For each sample 10.000 events were recorded, and the results expressed as PI fluorescence vs. Annexin V/FITC fluorescence. In each quadrant, quantification is reported as percentage of detected fluorescence..... 104

**Figure 4.7** SEM imaging of colloidal silica particles. a: SiNP20; b: SiNP70; c: SMP200; d:SMP500. Particles were analysed in deionized water at 25 µg/ml using Philips XL30 SFEG. Scale bar: 1 µm. .... 113

**Figure 4.8** TEM imaging of colloidal silica particle in water. a: SiNP20; b: SiNP70; c: SMP200; d:SMP500. Particles were analysed in deionized water at 25 µg/ml using Philips CM20 TEM (Philips, Netherlands). Scale Bar: 100 nm..... 114

**Figure 4.9** MTT and LDH assays on HaCaT cells following 24 hours treatment with colloidal silica. a, b: cells treated with particles in CM-10%; c, d: cells treated with particles in CM-0.5%; e-f: cells treated with particles in CM. Results were expressed as percentage of negative control, black line serves as reference for normal activity. Each particle concentration was tested in triplicates and the results analysed by one-way ANOVA and Student's t-test. Statistically significant results ( $p < 0.05$ ) are marked with an asterisk (\*) on top of the corresponding bar. .... 116

**Figure 4.10** Phase contrast imaging of HaCaT cells after 24 h treatment with colloidal silica. a, f: Untreated cells; b, g: cells treated with SiNP20; c, h: cells treated with SiNP70; d, i: cells treated with SMP200; e, j: cells treated with SMP500. Arrows in images a, c, d indicate cellular proliferation in the corresponding sample..... 118

**Figure 4.11** Cellular uptake of colloidal silica measured by flow cytometry. HaCaT cells were treated with colloidal silica at 25-200 µg/ml for 24 h in CM-10% and CM. Results are expressed as number of cells vs. detected fluorescence. The red line separates the left part of the graph, which indicates non-fluorescent cells associated with particle-free cells, from the right part of the graph, which shows fluorescence positive cells associated with silica particles uptake..... 119

**Figure 4.12** Uptake of colloidal silica inside HaCaT cells measured by TEM imaging. HaCaT cells were treated with particles at 25 µg/ml for 24 h in CM-10%. a,b: untreated cells; c, d: cells treated with SiNP20; e, f: cells treated with SiNP70; g, h: cells treated with SMP200; i, j: SMP500. Scale bar: 1µm. Black/white arrows indicate the corresponding particle in each image, while N=nucleus. Images taken by Dr. David Dinsdale, MRC Toxicology Unit (Leicester, UK)..... 122

- Figure 4.13** *In vitro* wound healing assay for HaCaT cells treated with colloidal silica (microscopy imaging). Cells were treated 0, 24, 48 and 72 h with colloidal silica 5-200 µg/ml in CM-0.5%. Images show effect at 25 µg/ml. a, d: untreated cells; e, h: cells treated with SiNP20; i, l: cells treated with SiNP70; m, p: cells treated with SMP200; q, t: cells treated with SMP500. .... 123
- Figure 4.14** *In vitro* wound healing assay for HaCaT cells treated with colloidal silica. Cells were treated 24, 48 and 72 h with colloidal silica 5-200 µg/ml in CM-0.5%. Results are expressed as percentage of wound closure in particle-treated samples compared with particle-free culture. .... 124
- Figure 4.15** Annexin V/FITC – PI staining of HaCaT cells treated with colloidal silica to detect apoptotic cell death. Cells were treated with colloidal silica 10-50 µg/ml; only CM-10% measurement is showed for cells treated with SiNP20 (b-d), while CM measurements are shown for cells treated with SiNP70, SMP200 and SMP500 (f-n). Following treatment, double staining with propidium iodide (PI) and Annexin V/FITC was performed and using BD Accuri C6 flow cytometer. For each sample 10.000 events were recorded, and the results expressed as PI fluorescence vs. Annexin V/FITC fluorescence. In each quadrant, quantification is reported as percentage of detected fluorescence. .... 126
- Figure 4.16** Western blot analysis of caspase 3 in cells treated with colloidal silica in CM-10% for 24 h. Caspase 3 inactive preform is located in the 36 kDa row, while p17 product is located in the 16 kDa row. Image taken by Dr. Xiao Ming, MRC Toxicology Unit (Leicester, UK). .... 127
- Figure 4.17** Gene expression scatter plots following HaCaT 24 h treatment with SiNP20 10-50 µg/ml in CM-10%. Results are expressed as Log10 of normalized expression. a: SiNP20 10 µg/ml; b: SiNP20 25 µg/ml; c: SiNP20 50 µg/ml. Down-regulated are indicated in green, while red indicates up-regulated genes. Black central line indicates unchanged gene expression. The dotted lines indicate the selected fold regulation threshold (fold = ± 2). .... 131
- Figure 4.18** WST-1 analysis of cell viability in K17 keratinocytes treated with colloidal silica. Cells were treated with colloidal silica 10-200 µg/ml for 24 h. Results were expressed as percentage of negative control; black line serves as reference for normal activity. Each particle concentration was tested in triplicates and the results analyzed by one-way ANOVA and Student's t-test. Statistically significant results (p<0.05) are marked with an asterisk (\*) on top of the corresponding bar. .... 142
- Figure 4.19** Propidium Iodide measurement of K17 keratinocytes after treatment with colloidal silica. Cells were treated with colloidal silica at 10-200 µg/ml for 24 hours, plus Triton X-100 0.025% for 15 minutes at 37 °C as positive control. .... 143
- Figure 4.20** Caspase 3/7 assay on K17 keratinocytes treated with colloidal silica. Cells were treated with colloidal silica at 10 and 100 µg/ml for 24

hours, plus staurosporine 10  $\mu$ M as positive control, for 6 hours at 37°C. Results were expressed as fold increase of caspase 3/7; black line serves as reference for normal activity. Each particle concentration was tested in triplicates and the results analysed by one-way ANOVA and Student's t-test. Statistically significant results ( $p < 0.05$ ) are marked with an asterisk (\*) on top of the corresponding bar. .... 144

**Figure 4.21** Confocal microscopy imaging of K17 keratinocytes treated with colloidal silica. Cells were treated with FITC-particles (green) at 10  $\mu$ g/ml and co-stained with Hoechst 33342 for nuclei (blue) and actin (red)..... 145

**Figure 4.22** Z-Stacks of K17 keratinocytes treated with colloidal silica..... 146

**Figure 4.23** WST-1 analysis of HDF fibroblasts treated with colloidal silica. Cells were treated with colloidal silica at 10-200  $\mu$ g/ml for 24 h at 37 °C. Results were expressed as percentage of negative control; black line serves as reference for normal activity. Each particle concentration was tested in triplicates and the results analysed by one-way ANOVA and Student's t-test. Statistically significant results ( $p < 0.05$ ) are marked with an asterisk (\*) on top of the corresponding bar. .... 147

**Figure 4.24** Propidium Iodide measurement of HDF after treatment with colloidal silica. Cells were treated with colloidal silica 10-200  $\mu$ g/ml for 24 h, with Triton X-100 0.025% positive control. .... 148

**Figure 4.25** Caspase 3/7 assay on HDF treated with colloidal silica. Cells were treated with colloidal silica at 10-100  $\mu$ g/ml for 24 h at 3°C, with staurosporine 10  $\mu$ M as positive control. Results were expressed as fold increase of caspase 3/7; black line serves as reference for normal activity. Each particle concentration was tested in triplicates and the results analyzed by one-way ANOVA and Student's t-test. Statistically significant results ( $p < 0.05$ ) are marked with an asterisk (\*) on top of the corresponding bar..... 149

**Figure 4.26** Confocal microscopy imaging of HDF fibroblasts. Cells were treated with FITC-particles (green) at 10  $\mu$ g/ml for 24 h. Cells were co-stained with Hoechst 33342 for nuclei (blue) and actin (red). No specific localization could be detected, as particles appeared to be free in the cytoplasm..... 150

**Figure 4.27** Z-Stacks of HDF treated with colloidal silica. Laser scanning of cells previously treated with FITC-labelled silica particles and double stained with Hoechst 33342 for nuclei (blue) and actin (red) revealed that particles are mostly free inside the cytoplasm, making exact localization difficult; none reached the nuclei..... 151

**Figure 4.28** MTT and LDH assay of BJ fibroblasts after treatment with colloidal silica. Cells were treated with particles at 25-100  $\mu$ g/ml for 24 h in CM-10%, CM-0.5% and CM. a, b: treatment in CM-10%; c, d: treatment in CM-0.5%; e, f: treatment with CM. Results were expressed as percentage of negative control; black line serves as reference for normal activity. Each particle

concentration was tested in triplicates and the results analysed by one-way ANOVA and Student's t-test. Statistically significant results ( $p < 0.05$ ) are marked with an asterisk (\*) on top of the corresponding bar. .... 153

**Figure 4.29** Phase contrast imaging of BJ fibroblasts cells treated with SiNP20-70. Cells were treated with particles at 50  $\mu\text{g/ml}$  for 24 h in CM-10% and CM. Arrows in image a indicate cellular proliferation in the corresponding sample..... 155

**Figure A.1** MTT assay for NLCs particles. HaCaT cells were treated 24 h with NLCs 25-100  $\mu\text{g/ml}$ , then analysed for mitochondrial activity..... 211

**Figure A.2** Phase contrast imaging of HaCaT cells following treatment with NLCs. Cells were treated with NLC, NLC+, NLC- and NLC/Ludox at 50  $\mu\text{g/ml}$  for 24 hours at 37°C. .... 212

**Figure A.3** Cytotoxicity assessment in HaCaT cells. JR-P2-34 and JR-P2-35 at 10-200  $\mu\text{g/ml}$  were used to treat cells for 24 h at 37°C. .... 216



## LIST OF TABLES

<b>Table 1.1</b> Possible patho-physiological outcomes due to various nanomaterials (modified from [24] Arora et al. 2012).....	8
<b>Table 1.2</b> FDA-approved nanoformulations in the last 15 years (modified from [53] Tinkle et al (2014)). .....	20
<b>Table 1.3</b> The different types of silica nanoparticles that can be obtained by reaction in aqueous solution (modified from [56] Napierska et al (2010)).	22
<b>Table 1.4</b> Summary of relevant <i>in vitro</i> studies regarding silica particles.....	26
<b>Table 1.5</b> Summary of relevant <i>in vivo</i> studies regarding silica particles. ....	28
<b>Table 1.6</b> Lipid conversion in the <i>stratum corneum</i> . The table summarizes the precursor lipids present in the lamellar bodies, which undergo lysosomal degradation, thus freeing the precursors in the lipid phase of the SC. From there, they are enzymatically converted in ceramides, fatty acids and cholesterol (edited from [77] Del Rosso et al. 2011). .....	32
<b>Table 1.7</b> Main components and properties of FBS (modified from [91] Gstraunthaler et al., 2003).....	40
<b>Table 1.8</b> Major effect of NPs properties on corona formation (from [95] Aggarwal et al. 2009). .....	42
<b>Table 3.1</b> Nanomaterials used in this study. ....	50
<b>Table 3.2</b> Cell lines, media and supplements.....	51
<b>Table 3.3</b> Cell-based and molecular biology assay reagents.....	52
<b>Table 3.4</b> Excitation/Emission outputs of the fluorescent dyes and silica particles.....	81
<b>Table 4.1</b> Characteristics of fumed silica (see Appendices for full Sigma Aldrich specification sheets).....	94
<b>Table 4.2</b> DLS assay of particle-free CM-10% and CM. Particle-free media was measured in order to detected background molecule clusters after 0 and 24 h incubation at 4 °C (storage conditions). Results are expressed as Average size (Average (nm)), to indicate the size of measured clusters, and polydispersion index (PDI) to indicate stability of the clusters in solution. Average size was measured lower in CM due to the different amount of proteins and other serum components. Five measurements were performed for each sample using Malvern Zetasizer. ....	95
<b>Table 4.3</b> DLS assay of fumed silica in CM-10%. SiNP7 and SiNP14 were analysed at 25 and 100 µg/ml after 0 and 24 h incubation at 4 °C (storage conditions). Results are expressed as Average size (Ave. (nm)), to indicate the size of measured clusters, and polydispersion index (PDI) to indicate	

stability of the clusters in solution. Five measurements were performed for each sample using Malvern Zetasizer..... 96

**Table 4.4** DLS assay of fumed silica in CM. SiNP7 and SiNP14 were analysed at 25 and 100 µg/ml after 0 and 24 h incubation at 4 °C (storage conditions). Results are expressed as Average size (Ave. (nm)), to indicate the size of measured clusters, and polydispersion index (PDI) to indicate stability of the clusters in solution. Five measurements were performed for each sample using Malvern Zetasizer..... 96

**Table 4.5** Flow cytometry quantification of silica nanoparticles' cellular uptake. The results as shown in Figure 4.4 were qualitatively analyzed using BD CSampler software as described in the methods section. Each value of the table corresponds to the percentage of fluorescence detected by the flow cytometer and previously expressed as cell count vs. fluorescence. .... 102

**Table 4.6** DLS assay of cell culture media. Five different types of media were used for particle dispersion: CM-10% (DMEM/F-12 + 10% FBS), CM-0.5% (DMEM/F-12 + 0.5% FBS), CM (DMEM/F-12 + 0%FBS), EpiLife™ Medium, and Medium 106. Particle free media were analysed as background controls after 0 and 24 h incubation at 4 °C (storage conditions). Results are expressed as Average size (Average (nm)), to indicate the size of measured clusters, and polydispersion index (PDI) to indicate stability of the clusters in solution. Five measurements were performed for each sample using Malvern Zetasizer..... 105

**Table 4.7** Characteristics of colloidal silica (see Appendices for full Sigma Aldrich and Postnova Analytics specification sheets)..... 106

**Table 4.8** DLS assay of colloidal silica in CM-10%. SiNP20, SiNP70, SMP200 and SMP500 were analysed at 25, 50 and 100 µg/ml after 0 and 24 h incubation at 4 °C (storage conditions). Results are expressed as Average size (Ave. (nm)), to indicate the size of measured clusters, and polydispersion index (PDI) to indicate stability of the clusters in solution. Five measurements were performed for each sample using Malvern Zetasizer. .... 107

**Table 4.9** DLS assay of colloidal silica in CM-0.5%. Particles were analyzed at 25, 50 and 100 µg/ml after 0 and 24 h incubation at 4 °C (storage conditions). Results are expressed as Average size (Ave. (nm)), to indicate the size of measured clusters, and polydispersion index (PDI) to indicate stability of the clusters in solution. Five measurements were performed for each sample using Malvern Zetasizer..... 108

**Table 4.10** DLS assay of colloidal silica in CM. Particles were analyzed at 25, 50 and 100 µg/ml after 0 and 24 h incubation at 4 °C (storage conditions). Results are expressed as Average size (Ave. (nm)), to indicate the size of measured clusters, and polydispersion index (PDI) to indicate stability of the clusters in solution. Five measurements were performed for each sample using Malvern Zetasizer..... 109

<b>Table 4.11</b> DLS assay of colloidal silica in EpiLife™ Medium. Particles were analyzed at 50 µg/ml after 0 and 24 h incubation at 4 °C (storage conditions). Results are expressed as Average size (Ave. (nm)), to indicate the size of measured clusters, and polydispersion index (PDI) to indicate stability of the clusters in solution. Three measurements were performed for each sample using Malvern Zetasizer.....	110
<b>Table 4.12</b> DLS assay of colloidal silica in Medium 106. Particles were analyzed at 50 µg/ml after 0 and 24 h incubation at 4 °C (storage conditions). Results are expressed as Average size (Ave. (nm)), to indicate the size of measured clusters, and polydispersion index (PDI) to indicate stability of the clusters in solution. Three measurements were performed for each sample using Malvern Zetasizer.....	111
<b>Table 4.13</b> DLS assay of colloidal silica in CM-10% and CM after 24 h at 37°C. Results are expressed as Average size (Ave. (nm)), to indicate the size of measured clusters, and polydispersion index (PDI) to indicate stability of the clusters in solution. Five measurements were performed for each sample using Malvern Zetasizer.....	112
<b>Table 4.14</b> Zeta potential assay of colloidal silica in CM-10% and CM. Particles were examined at 100 µg/ml using Malvern Zetasizer. Three measurements were performed for each sample using Malvern Zetasizer. ....	112
<b>Table 4.15</b> Flow cytometry quantification of silica nanoparticles' cellular uptake. The results as shown in Figure 4.11 were qualitatively analyzed using BD CSampler software as described in the methods section. Each value of the table corresponds to the percentage of fluorescence detected by the flow cytometer and previously expressed as cell count vs. fluorescence. ....	120
<b>Table 4.16</b> Quality of the cDNA synthesis from total RNA extracted from HaCaT cells treated with SiNP20 of different concentrations. ....	129
<b>Table 4.17</b> Mean concentrations of cDNA synthesized from total RNA extracted from HaCaT cells treated with SiNP20 of different concentrations. For A), B), C) n° replicates = 3, for D) n° replicates = 2. SD indicates the standard deviation for each sample. ....	130
<b>Table 4.18</b> Effect of SiNP20 on the expression of mRNAs involved in apoptosis regulation. Full names of the corresponding genes were given with symbols included in brackets; values in red indicate genes up-regulated ≥ 2 folds; values in green indicates genes down regulated more than 2 fold; gene descriptions were obtained through UniProt and GENE bank at National Centre for Biotechnology Information (NCBI).....	132
<b>Table 5.1</b> The main upregulated genes in this study and their related pathways. ....	173

<b>Table A.1</b> DLS assay of CM as background control. ....	210
<b>Table A.2</b> DLS assay of NLC+ and NLC- in CM at 0 and 24 h after incubation at 4°C (storage conditions).....	211
<b>Table A.3</b> Composition of JR-P2-34. ....	214
<b>Table A.4</b> Composition of JR-P2-35. ....	215
<b>Table A.5</b> JR-P2-34 and JR-P2-35 specifications.....	215
<b>Table A.6</b> DLS assay of JR-P2-34 and JR-P2-35.....	216

## LIST OF EQUATIONS

<b>Equation 1.1</b> The two-step process (1) hydrolysis and (2) condensation to form colloidal silica. ....	23
<b>Equation 3.1</b> The Stokes-Einstein equation. ....	54
<b>Equation 3.2</b> The Henry equation. ....	60

## LIST OF ABBREVIATIONS

2D	Two-Dimensional
3D	Three-Dimensional
ADME	Absorption, Distribution, Metabolism and Excretion
AFM	Atomic Force Microscope
ALP	Alkaline Phosphatase
APO-TF	Apo-Transferrin
APTT	Activated Partial Thromboplastin Time
ATP	Adenosine Triphosphate
cAMP	Cyclic Adenosine Monophosphate
BBB	Blood Brain Barrier
BPE	Bovine Pituitary Extract
BSA	Bovine Serum Albumin
cDNA	Complementary DNA
CE	Cornified Envelope
CM	DMEM/F-12 Culture Medium + 0% FBS
CM-0.5%	DMEM/F-12 Culture Medium + 0.5% FBS
CM-10%	DMEM/F-12 Culture Medium + 10% FBS
DLS	Dynamic Light Scattering
DMEM/F-12	Dulbecco's Modified Eagle Medium and Ham's F-12 Nutrient Mixture
DNA	Deoxyribonucleic acid
DPPC	1,2-Dipalmitoyllecithin
EC	European Commission
ECHA	European Chemicals Agency
ECM	Extracellular Matrix
EDTA	Ethylene Diamine Tetra-acetic Acid
ELISA	Enzyme-Linked Immuno Sorbent Assay
EM	Electron Microscopy
ENMs	Engineered Nanomaterials
EU	European Union
FBS	Foetal Bovine Serum
FDA	Food and Drug Administration

FG	Fibrinogen
FITC	Fluorescein Isothiocyanate
FSC	Forward Scatter
GIT	Gastro-Intestinal Tract
G-CSF	Filgrastim
H <sub>d</sub>	Hydrodynamic
HKGS	Human Keratinocyte Growth Supplement
HRP	Horseradish Peroxidase
HSA	Human Serum Albumin
HSEM	Human Skin Equivalent Model
IgG	Immunoglobulin G
IHRP	Inter- $\alpha$ - Trypsin Inhibitor Family Heavy Chain-Related Protein
IUCLID	International Uniform Chemical Information Database
LBs	Lamellar Bodies
LC	Liquid Chromatography
LDH	Lactate Dehydrogenase
LSV	Laser Doppler Velocity
MEM	Minimum Essential Medium
MOMP	Mitochondrial Outer Membrane Permeabilization
MTT	3-(4,5-dimethylthiazol-2-yl) -2,5-diphenyltetrazolium bromide
MRC	Medical Research Council
mRNA	Messenger RNA
MS	Mass Spectrometry
MSNs	Mesoporous Silica
NADH	Nicotinamide Adenine Dinucleotide
NAD(P)H	Nicotinamide Adenine Dinucleotide Phosphate
NC	Negatively Charged
NCBI	National Centre for Biotechnology Information
NLCs	Nanostructured Lipid Carriers
NLC+	Positively charged Nanostructured Lipid Carrier
NLC-	Negatively charged Nanostructured Lipid Carrier
NLC	Neutrally charged Nanostructured Lipid Carrier
NLC/Ludox	Nanostructured Lipid Carrier conjugated with Ludox™ Silica

NMs	Nanomaterials
NNI	National Nanotechnology initiative
NOAEL	No Observed Adverse Effect Level
NPs	Nanoparticles
PBS	Phosphate Buffered Saline
PC	Protein Corona
PCR	Polymerase Chain Reaction
PDI	Polydispersity Index
PEG	Polyethylene Glycol
PEG-G- CSF	Pegfilgrastim
PEG-hGH	Pegvisomant
PFA	Paraformaldehyde
PI	Propidium Iodide
PLGA	poly(lactic-co-glycolic acid)
PLGH	poly(DL-lactide-co-glycolide) co-polymer
PMS	Phenazine Methosulfate
PS	Phosphatidylserine
PTP	Permeability Transition Pore
PVDF	Polyvinylidene Fluoride
qPCR	Quantitative Polymerase Chain Reaction
qRT-PCR	Quantitative Real-time Polymerase Chain Reaction
REACH	Registration, Evaluation, Authorization & Restriction of Chemicals
RES	Reticuloendothelial System
RME	Receptor-Mediated Endocytosis
RNA	Ribonucleic Acid
ROS	Reactive Oxygen Species
RPA	Ribonuclease Protection Assay
RT	Real-Time
RT-PCR	Reverse Transcription-Polymerase Chain Reaction
SAGE	Serial Analysis of Gene Expression
SC	Stratum Corneum
SD	Standard Deviation
SDS	Sodium Dodecyl Sulphate



SDS-PAGE	Sodium Dodecyl Sulphate - PolyAcrylamide Gel Electrophoresis
SE	Secondary Electron
SEM	Scanning Electron Microscopy
SLN	Solid Lipid Nanoparticles
SiNP7	Silica nanoparticle 7 nm
SiNP14	Silica nanoparticle 14 nm
SiNP20	Silica nanoparticle 20 nm
SiNP70	Silica nanoparticle 70 nm
SMPs	Submicroparticles
SMP200	Silica submicroparticle 200 nm
SMP500	Silica submicroparticle 500 nm
SNPs	Silica Nanoparticles
SPIONs	Superparamagnetic Iron Oxide Nanoparticles
SSC	Side Scatter
STM	Scanner Tunneling Microscope
TBS-T	Tris-Buffered Saline and Tween 20
TCA	Tricarboxylic Acid
TEM	Transmission Electron Microscopy
TEOS	Tetraethyl Orthosilicate
TNF	Tumor Necrosis Factor
US	United States
UV	Ultraviolet
VECs	Vascular Endothelial Cells
VEGF	Vascular Endothelial Growth Factor
WNC	Weakly Negatively Charged
WST-1	2-(4-Iodophenyl)-3-(4-nitrophenyl)-5-(2,4-disulfophenyl)-2H-tetrazolium, monosodium salt
Z-DEVD-R110	rhodamine 110, bis-N-CBZ- L-aspartyl-L-glutamyl-L-valyl-L-aspartic acid amide
ZP	Zeta Potential



# **1 LITERATURE REVIEW**

## **1.1 Introduction**

Nanotechnology is a new scientific research area, which has undergone intensive development over the last two decades, bringing new hopes in improving human life in many ways, including medicine, transport, clothing and food [1]. The purpose of this review is to go through the brief history of nanotechnology-enabled materials, nanomaterials, in regards to their definition, physico-chemical characteristics and potential toxicity. The status of current EU and USA regulation has been included to highlight the need for research. Such an overview will help delineate the aims and objectives of this project, which is part of NANODRUG, a European Commission-funded project with the aim of developing and characterizing a selected set of nanomaterials to study their suitability as drug delivery systems targeting inflammatory skin diseases. The review was based on literature that was searchable from Cranfield-provided Scopus library, National Centre for Biotechnology Information (NCBI) and Google Scholar.

## **1.2 Nanomaterials – An Overview**

### **1.2.1 History of nanotechnology and nanomaterials**

Nanotechnology can be defined as the manipulation of matter that has at least one dimension between 1-100 nm [1]. Even though the most significant increase in nanomaterials popularity occurred between the 1990s and 2000s, the first observations and size measurements of nanoparticles can be dated back to 1914, when Richard Adolf Zsigmondy developed the first system classification based on particle size in the nanometre range [1]. Even though the idea of nanotechnology was given for the first time in 1959 by Richard Feynman, the term was first used in 1974, in a publication by a Japanese student named Norio Taniguchi. He stated: “Nanotechnology mainly consists of the processing of, separation, consolidation, and deformation of materials by one atom or one molecule” [1, 2].

Nanotechnology did not start developing into a field of science until the 1980s, when MIT scientist Eric Drexler expanded Feynman's vision by publishing in 1981 an article entitled "Molecular engineering: An approach to the development of general capabilities for molecular manipulation" in the journal "Proceedings of the National Academy of Sciences" [3]. The article discussed the possibility of molecular manufacturing as a process for the fabrication of objects with specific atomic specifications. This concept was further developed into a book entitled "Engines of Creation: The Coming Era of Nanotechnology" [4]; right after this publication, Drexler founded the Foresight Institute, whose stated goal was to "ensure the beneficial implementation of nanotechnology." As a direct result, a lot of publicity was generated on both Drexler's work and the Foresight Institute, prompting scientists from all over the world to begin studies in the field of nanotechnology [1].

The development of nanotechnology was further driven by the development of tools such as the scanning tunnelling microscope (STM) in 1981, which allowed the clear identification of individual atoms for the first time. The STM invention was followed by the Atomic Force Microscope (AFM) in 1986. AFM proved to be quite an important development in materials analysis, as it allowed the imaging of non-conducting materials (e.g. organic molecules) for the first time; it consequently could be used to study biological macromolecules and living organisms. With the development of such microscopic technologies, nanotechnology could develop and evolve to include research in several fields, including chemistry, materials science, medicine, toxicology, ecotoxicology, and industrial hygiene [5].

There was a significant boost in the popularity of nanotechnology in the 1990s and 2000s, with the development of several nanomaterials as well as their incorporation in a wide variety of consumer products. In 2001, the National Nanotechnology Initiative (NNI), a US federal funding initiative for nanotechnology begun under President Clinton, gave the first definition of nanoscale technology as "anything with a size between 1 and 100 nm with novel properties". This broad definition was adopted in a range of application

areas including cutting-edge semiconductor research, several developing areas of chemistry, nanomedicine, and advances in nanomaterials [1].

In the early 2000s, concerns about the potential human and environmental health effects of nanomaterials were also being considered by many scientists, regulators, and non-governmental agencies, as particles and materials in the nanosize range might pose toxicological hazards due to their enhanced reactivity and potential for systemic availability and environmental occurrence. Consequently, the term “nanotoxicology” was first used in 2004 in an editorial by Donaldson et al [6]. Since then, there has been a significant increase in the amount of *in vitro* and *in vivo* nanotoxicological research, as well as toxicokinetics and toxicodynamics of nanomaterials evaluation.

### **1.2.2 Nanomaterials’ characteristics and influence upon interaction with biological systems**

Engineered Nanomaterials (ENMs) can be defined as intentionally developed nanomaterials that have at least one dimension of 1-100 nm [7]. They can be composed of a variety of materials including noble metals (Au, Ag, Pt, Pd), semiconductors (CdSe, CdS, ZnS, TiO<sub>2</sub>, PbS, InP, SiO<sub>2</sub>), magnetic compounds (Fe<sub>3</sub>O<sub>4</sub>, CoFe<sub>2</sub>O<sub>4</sub>, FePt, CoPt) and their combinations. Their composition is not limited to these materials, but also includes non-metallic compounds such as silica and carbon, as well as polymers and biologically originated materials (phospholipids, lipids, lactic acid and chitosan) [8, 9]. Nanomaterials (NMs) can be produced in different formats, such as single particles, aggregates, powders, colloids, suspensions, nanolayers, carbon fullerenes, and their derivatives [10]. A great number of NMs are available nowadays, thus making a clear classification quite challenging (**Figure 1.1**); moreover, most nanomaterials do not consist of only one substance, but typically are hybrid materials, involving surface coatings and other modifications. Even NMs formed out of only one material will turn effectively into a hybrid NMs upon contact with any biological system, as an organic coating of biomolecules will envelope them.

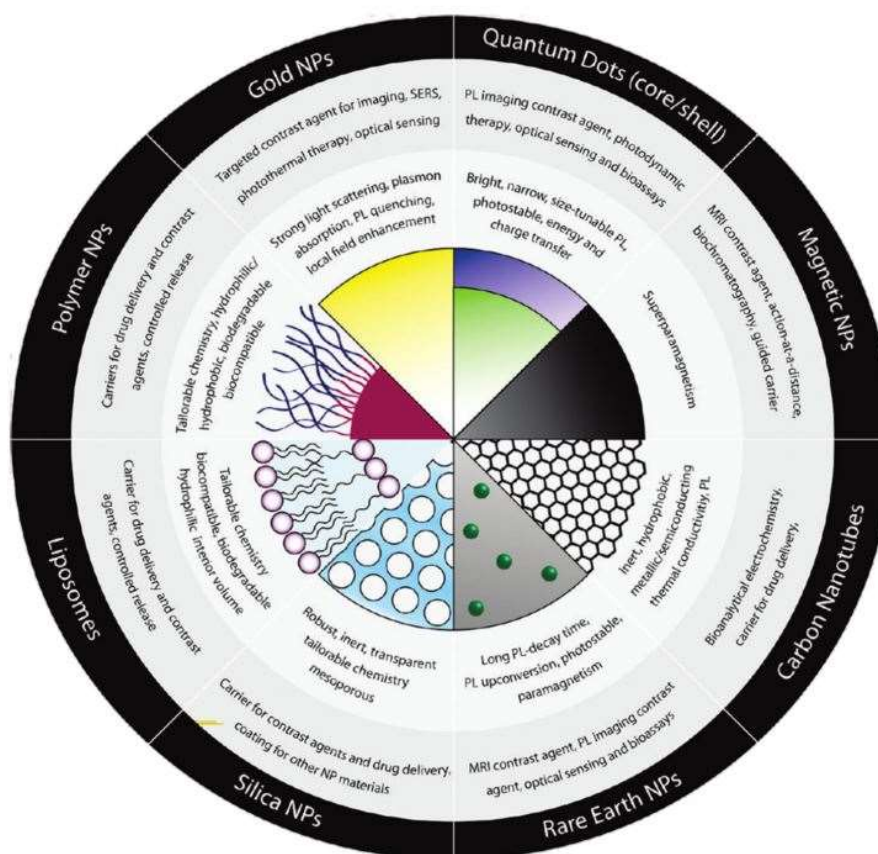


**Figure 1.1** An overview of some of the different nanomaterials that are available today. This explains how challenging a complete classification of nanomaterials can be (modified from [9] Algar et al. (2011)).

Nanomaterials have attracted considerable interest over the years because of their unique physico-chemical properties, which greatly differ from their corresponding bulk materials. Their main characteristic is size, which falls in the transitional zone between individual atoms or molecules and the corresponding bulk materials; as a consequence, the electronic, magnetic, optic, catalytic, biomedical and thermodynamic properties are affected as well [11]. The reasons for this phenomenon lie in the increased surface/volume ratio, which can be defined as the amount of surface area per unit volume of an object or collection of objects. Surface/volume ratio is an important factor both in chemistry, where it influences the reactivity of solid materials, and in biology, where it affects the physiology and behaviour of cells and organisms [12].

Physico-chemical properties, including size, surface area, surface charge, shape, chemical composition, solubility, agglomeration state and surface coating, influence not only the nanomaterial itself, but also any biological system it might come in contact with depending on the function for which it's designed [13]. Particle size and surface area are interconnected, as a decrease in particle size leads to an exponential increase in surface area. This increase consequently makes the nanomaterial surface more reactive on itself and to its contiguous environment. Size and surface area both play a major role in the interaction of nanomaterials with biological systems. Particle size and surface area have a direct influence on how a biological system responds to, distributes, and eliminates nanomaterials [13, 14]. It has also been established that various biological mechanisms including endocytosis, cellular uptake, and efficiency of particle processing in the endocytic pathway are dependent on size. Size also dictates nanomaterials' pharmacological behaviours, as it has been observed that NMs smaller than 50 nm administered by intravenous injection readily transverse and impart potentially toxic manifestations in various tissues; on the other hand, those bigger than 50 nm are readily taken up by the reticuloendothelial system (RES) therefore refraining their path to other tissues [15]. Surface charge is important as well, as it is a major determinant of colloidal behaviour and therefore particle stability in solution [16]. It plays an important role also in the interaction of nanoparticles with biological systems, as it can influence the uptake rate depending on the type of charge [17]. Nanomaterials come in different shapes, including rings, tubes, spheres, and planes. The shape of nanomaterials directly influences the membrane wrapping processes *in vivo* during endocytosis or phagocytosis. It has been observed that endocytosis of spherical nanoparticles is easier and faster when compared to rod shaped nanoparticles; non-spherical nanomaterials tend to go through capillaries, thus causing different biological effects [18]. Surface coatings may also be an important factor on the properties of nanomaterials, as it can change their magnetic, electric, and optical properties and chemical reactivity [13] and alter their pharmacokinetics, distribution, accumulation, and toxicity. Because of these characteristics, nanomaterials behave differently when interacting with

biological barriers, especially with proteins, causing modification in both themselves and the interacting species. This is very important when NMs are designed for nanomedicine applications, as they must satisfy certain criteria. For *in vitro* applications such as fluorescent staining of proteins and Transmission Electron Microscopy (TEM) imaging, they must outperform the conventional agents while having minimal cytotoxicity. For *in vivo* applications, NMs must avoid non-specific interactions with plasma proteins (opsonisation) and be able to either evade or allow uptake by the reticulo-endothelial system (RES), depending on the application, to reach their intended target efficiently; they must also maintain colloidal stability under physiological conditions. Nanomaterials (NMs) carrying a payload, such as drug molecules or DNA for gene therapy, must avoid premature release yet specifically deliver the load to the desired site [19].

### **1.2.3 Toxicity of nanomaterials**

In the last few years, nanotechnology has provided enormous benefits in areas such as materials science, communication, electronics, medicine, energy, and environmental sciences. But as manipulation and application of engineered nanomaterials is involved, nanotechnology has also become the subject of debate regarding its toxicological and environmental impact, considering that nanomaterials are not only used for various commercial applications, but also in the biomedical field, where their applications involve deliberate ingestion or injection into the body [20, 21, 22]. Nanomaterials for imaging and drug delivery are often intentionally coated with biomolecules such as DNA, proteins, and monoclonal antibodies to target specific cells [23]. Because of the growing interest in exploring nanomaterials' uses for imaging, systemic delivery of drugs, target specific killing of cancerous cells, understanding the relationship between the physico-chemical properties of nanomaterials and their absorption, distribution, metabolism and elimination (ADME) characteristics is critical to achieve the desired biological effect . Given these concerns, nanotoxicology was proposed as a new branch of toxicology to address the gaps in knowledge



and to specifically address the adverse health effects likely to be caused by nanomaterials [24]. Nanotoxicology encompasses the physicochemical determinants, routes of exposure, bio distribution, molecular determinants, genotoxicity, and regulatory aspects, as summarized in **Figure 1.2**; it is also involved in proposing reliable, robust, and data-assured test protocols for nanomaterials in human and environmental risk assessment.

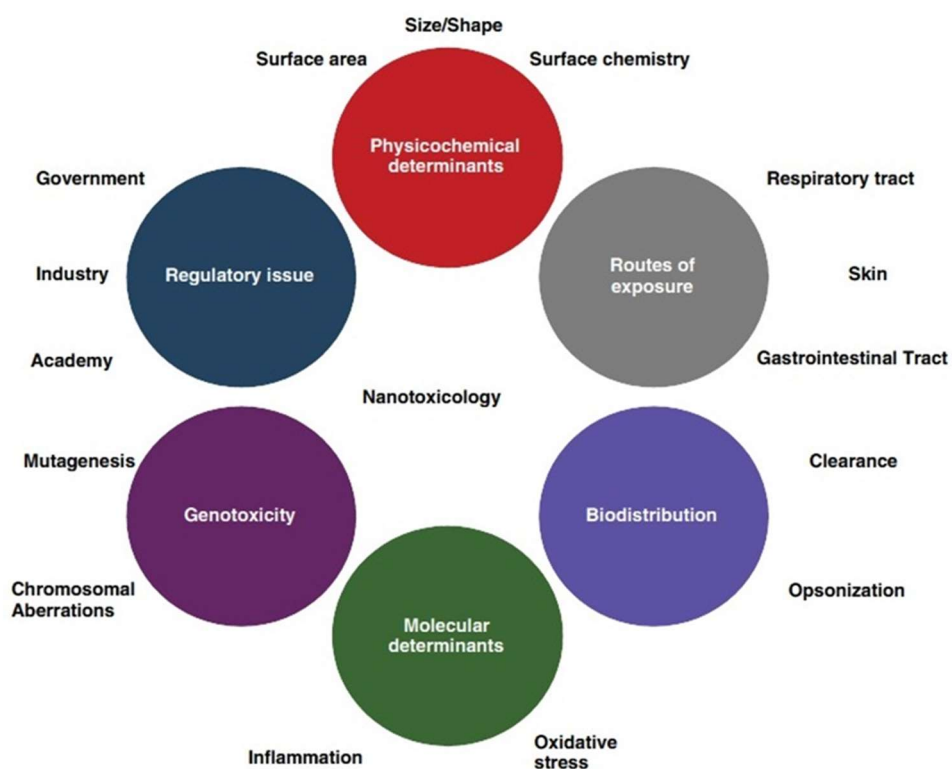


**Figure 1.2** An overview of the factors involved in nanotoxicology (modified from [7] Nel et al. 2006).

The physico-chemical determinants play an important role in toxicity. Among them, size and surface area play the most pivotal role, as the size of nanoparticles/aggregates is an essential parameter in determining nanoparticle toxicity due to a more effective macrophage clearance for larger particles compared to smaller ones, leading to reduced toxicity when nanoparticles aggregate at sizes larger than 100–200 nm [25, 26]. Size and surface area also

play an important role in the potential dose-dependent increase in oxidation and DNA damage, as nanomaterials with smaller size and higher surface area could cause much higher damage than larger materials [27, 28]. Among the other determinants, NMs chemistry also plays an important part in toxicity, as it can influence cellular uptake, subcellular localization, and ability to catalyse the production of reactive oxygen species. Moreover, surfactants used in nanoparticle synthesis can drastically change the physico-chemical properties of nanoparticles, such as magnetic, electric, and optical properties, and chemical reactivity, affecting their cytotoxicity.

The macromolecules most frequently affected by nanomaterial toxicity are those genes or proteins with significant roles in oxidative stress, DNA damage, inflammation or injury to the immune system. **Table 1.1** summarises some of the potential pathological effects that nanomaterials can have after contact with human cells.

**Table 1.1** Possible patho-physiological outcomes due to various nanomaterials (modified from [24] Arora et al. 2012).

Experimental NMs Effects	Pathophysiological Outcomes
<b>ROS generation and Oxidative Stress</b>	Protein, DNA, Membrane Damage
<b>Mitochondrial Perturbation</b>	Cytotoxicity, Inflammation, Energy Failure, Apoptosis
<b>Uptake by Reticulo-Endothelial System</b>	Asymptomatic sequestration and storage in the liver, spleen and lymph nodes, possible organ enlargement and dysfunction
<b>Nuclear Uptake and DNA Damage</b>	Nucleoprotein Clumping, Mutagenesis, Carcinogenesis
<b>Generation of neo-antigens, perturbation of phagocytic function</b>	Autoimmunity, Chronic Inflammation
<b>Altered Cell Cycle Regulation</b>	Proliferation, Cell Cycle Arrest, Senescence

Because nanomaterial size is comparable to that of cellular components, they can efficiently enter living cells by exploiting the cellular endocytosis machinery [29]. Endocytosis is a mechanism to overcome the barrier function of the cell membrane; it can be defined as the uptake of particulate matter (proteins, nutrients) inside cells via enclosure by the cell membrane. It is also exploited for the clearance of cell debris and foreign cells from the body. Several forms of endocytosis can be distinguished based on the substance to be internalized (**Figure 1.3**) [30, 31].

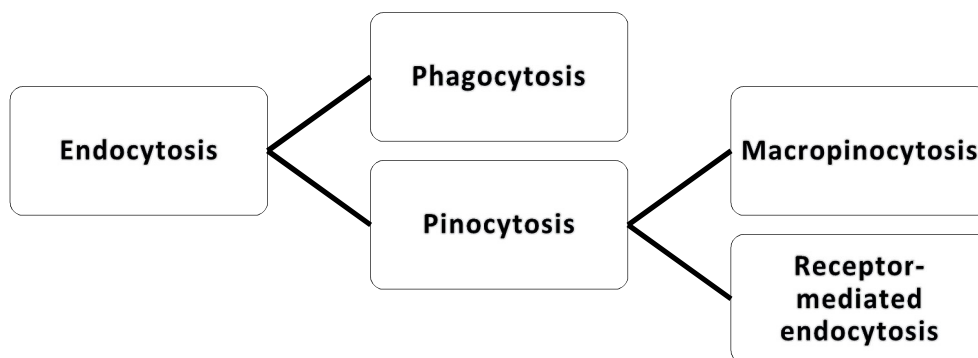


**Figure 1.3** Schematics of endocytosis mechanisms.

Opsonin-bound particulates and small solute volumes are internalized by phagocytosis. In animals, phagocytosis is part of the immune defense and is typically restricted to cells specialized in the uptake and degradation of foreign cells as well as cell debris and apoptotic cells belonging to the organism itself [30]. Particles in large amounts of solute, on the other hand, are taken up by a process termed pinocytosis. Pinocytosis can be further divided into macropinocytosis and receptor-mediated endocytosis (RME) [30, 32, 33]. Macropinocytosis is a non-specific mechanism in which fluid contents are taken up in the same concentration as in the surrounding medium. It is a constitutive process occurring continuously in highly ruffled regions of the cell membrane; ruffles trap the surrounding medium when their tips bend back toward the cell

surface. Materials adsorbed onto the cell membrane can be taken up as well, in what is called adsorptive macropinocytosis. Caveolae- and clathrin-mediated endocytosis are receptor-mediated endocytosis which allow different types of ligand (toxins, cholesterol-carrying proteins, vitamins, and iron transport proteins, as well as hormones and growth factors) to enter cells by binding to specific receptors localized on the cell membrane [30]. Particle uptake by endocytosis is a complex interplay of energy release by several factors, including particle size, number of bound receptors, number of vesicles that can be formed from the membrane, receptor diffusion toward the attached particle, and time to complete this process. For large NPs, only one particle can be taken up per vesicle, and attachment occurs to numerous receptors at a time, resulting in a major change in free energy. Large particles will also require more time to complete wrapping. For small particles, several NPs can be taken up in a single vesicle, but energy release is weaker because only single attachment sites exist. Because a local decrease in the free energy is required to induce membrane wrapping, a minimum size for a single particle at a given ligand density must exist; otherwise endocytosis is energetically impossible. Uptake is only initiated after a certain number of receptors have been triggered. If the change in free energy is too small, membrane wrapping will not be induced [30, 34, 35, 36].

When exposed to molecular determinants such as light or transition metals, nanomaterials may also promote the formation of pro-oxidants, which, in turn, destabilizes the delicate balance between the biological system's ability to produce and detoxify the reactive oxygen species (ROS). ROS include free radicals such as singlet oxygen ( $^1\text{O}_2$ ), the superoxide anion ( $\text{O}_2^\bullet$ ), hydroxyl radicals ( $\bullet\text{OH}$ ) and the non-radical hydrogen peroxide ( $\text{H}_2\text{O}_2$ ); they are constantly generated in cells' mitochondria during normal metabolism, and they are involved in enzymatic reactions, mitochondrial electron transport, signal transduction, activation of nuclear transcription factors and gene expression. When cells are exposed to any chemical or physical damage, it results in the production of ROS. However, cells are also endowed with an extensive antioxidant defence system to combat them, either directly by interception or

indirectly through reversal of oxidative damage. Oxidative stress induced by nanomaterials is reported to enhance inflammation through up-regulation of redox-sensitive transcription factors. As shown in **Figure 1.4**, ROS production by mitochondria can lead to oxidative damage to mitochondrial proteins, membranes and DNA, impairing the ability of mitochondria to synthesize ATP and to carry out their wide range of metabolic functions. It also increases the tendency of mitochondria to release inter-membrane space proteins such as cytochrome c to the cytosol by mitochondrial outer membrane permeabilization (MOMP) and thereby activate the cells apoptotic machinery. In addition, mitochondrial ROS production leads to induction of the mitochondrial permeability transition pore (PTP), which renders the inner membrane permeable to small molecules in situations such as ischemia/reperfusion injury. Consequently, it is unsurprising that mitochondrial oxidative damage contributes to a wide range of pathologies. In addition, mitochondrial ROS may act as a mouldable redox signal, reversibly affecting the activity of a range of functions in the mitochondria, cytosol and nucleus [24, 37].

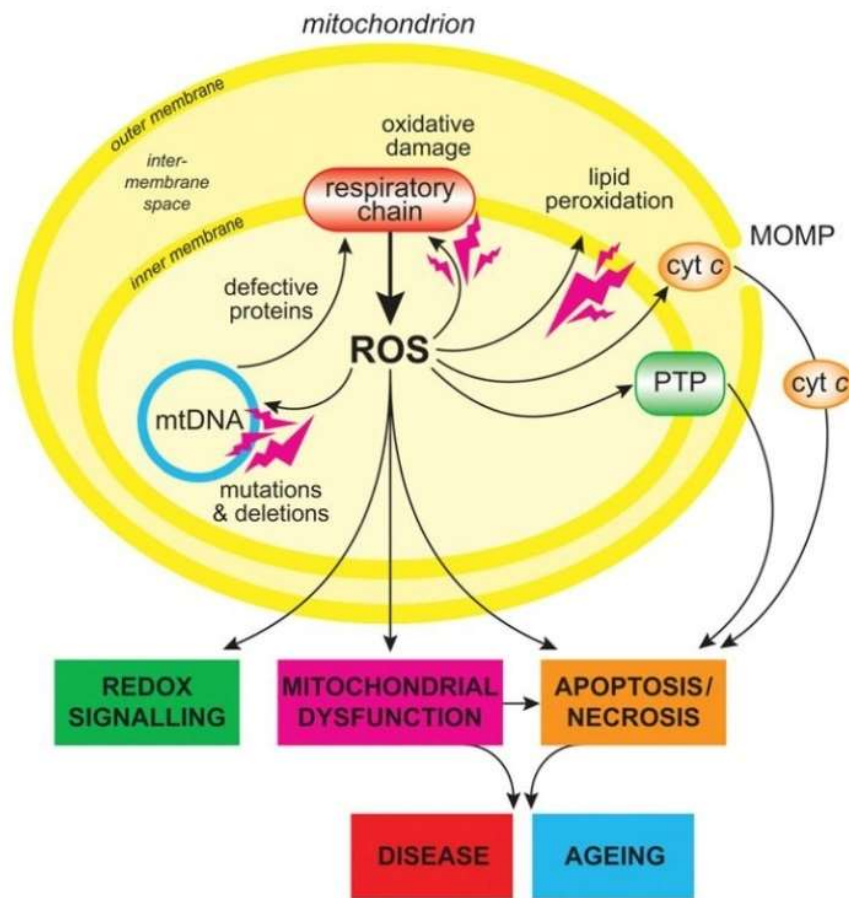


**Figure 1.4** Impairment in ROS control can give rise to several pathologies (modified from [37] Murphy et al., 2009).

Another important process for nanoparticles toxicity assessment inside cells is apoptosis. This process, also known as ‘programmed cell death’ is an important control mechanism for the total number of cells inside the human body. During apoptosis, the cell shrinks and condenses (blebbing), the cytoskeleton collapses, the nuclear envelope disassembles, and the nuclear DNA breaks up into fragments. Most importantly, the cell surface undergoes alterations, displaying properties that cause the dying cell to be rapidly phagocytosed either by a neighboring cell or by a macrophage. The intracellular machinery responsible for apoptosis is similar for all animal cells and depends on a family of proteases called caspases. Caspases are usually synthesized as inactive precursors, called pro-caspases, activated by cleavage at specific aspartic

acids by other caspases. Once activated, they cleave and activate other pro-caspases, resulting in an amplifying proteolytic cascade that induces apoptosis [38, 39]. Apoptosis is extremely complex, therefore its full description can be extremely challenging. A common activation method is by receptor-mediated oligomerization of caspase 8 (**Figure 1.5**). When the Fas ligand (FasL), a transmembrane protein expressed on cytotoxic T lymphocytes, binds to its receptor (FasR) on target cells, the new complex binds directly to the adaptor protein FADD, activating caspase 8. Caspase 8 in turn activates the Bid protein, responsible for the release of cytochrome c from the mitochondria to the cytoplasm, therefore activating the caspase cascade [39].

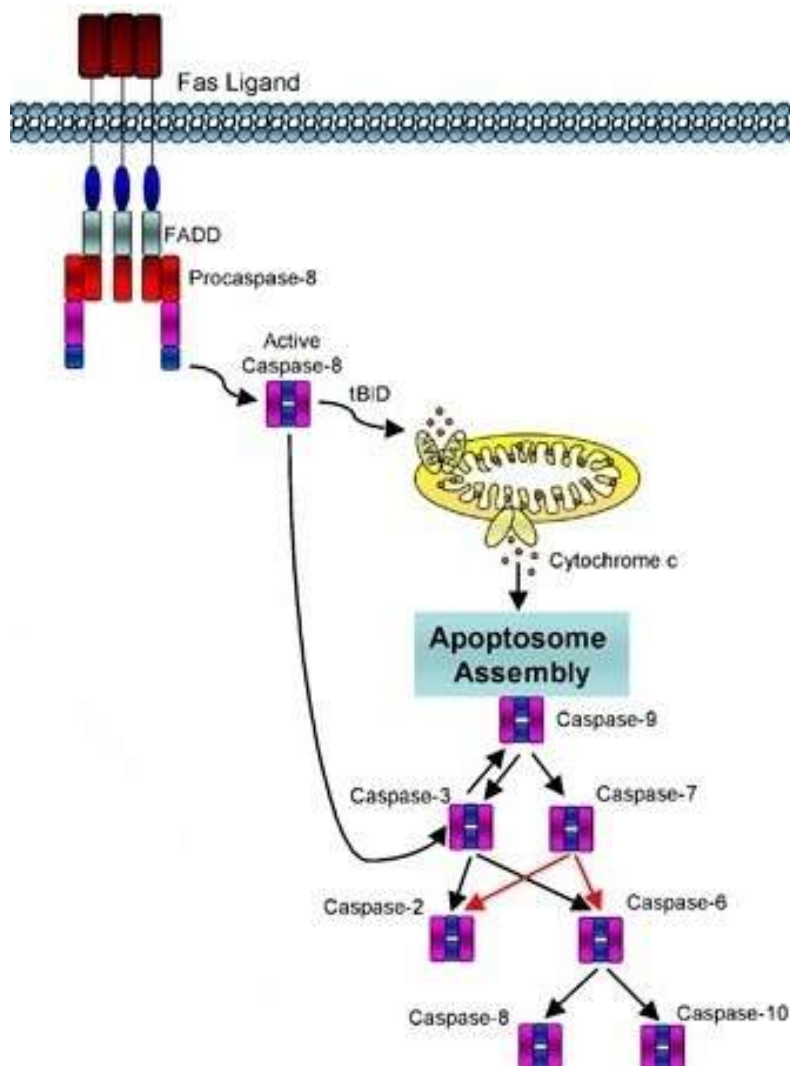


**Figure 1.5** The molecular mechanism of apoptosis (modified from [39] Cullen et al. (2009)).

The process described above is known as the extrinsic pathway, as activation starts outside the cell. An intrinsic pathway is also available, in which an injured mitochondrion releases cytochrome c in the cytoplasm activating the caspase cascade (**Figure 1.6**).

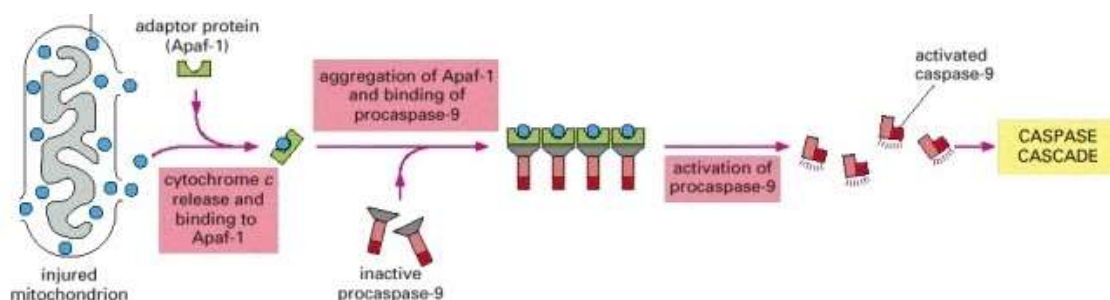


**Figure 1.6** The intrinsic activation pathway (modified from [38] Alberts et al. (2002)).

Apoptosis can be activated not only for normal cell maintenance, but also as a direct result of stimuli in the surrounding environment, including nanomaterials.

Aside from chemical and molecular determinants, another important aspect about nanotoxicology is the routes of exposure, as the human body has several semi-open interfaces for direct substance exchange with the environment, mainly the skin, respiratory tract and gastrointestinal tract (GIT), as displayed in **Figure 1.7**:

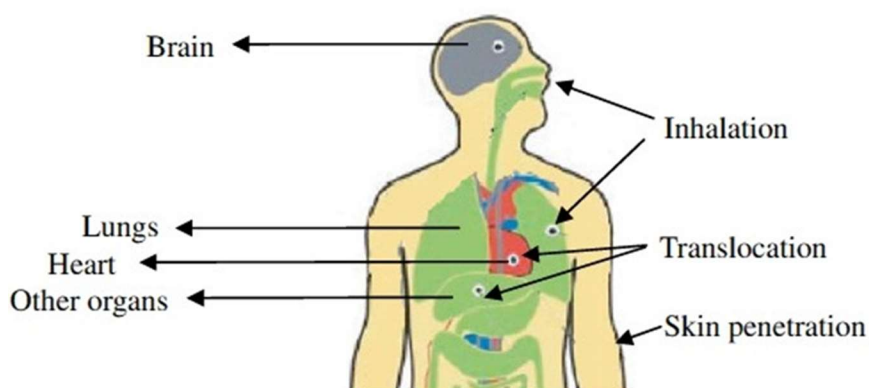


**Figure 1.7** Drawing showing the routes of exposure to nanomaterials (modified from [10] Chen et al. 2011).



Organisms have always faced nanoscale environmental compounds interacting with their exterior barrier but a significant interest in the interactions between NMs and organisms developed because of the increase in the production of engineered nanomaterials. The first step of any interaction between an organism and any compound is its uptake from the environment. Several pathways of absorption exist for human and most animal organisms of which skin is the easiest to reach. Skin absorption of any kind of material can be summarized in two general pathways: along the skin appendages or through the skin outermost layer, the *stratum corneum* (SC). Even though the appendages present only a small portion of skin surface they are considered to contribute and might even be addressed for a directed delivery because of the depth they reach; generally, the *stratum corneum* is assumed to be the main barrier for absorption. Absorption across the SC offers two possible pathways, as shown in **Figure 1.8**: through its cells, known as corneocytes (shown in black) or along the intercellular spaces along its lipid matrix (shown in grey). The latter pathway seems to be most suited for penetration, offering channel-like structures providing higher diffusivity, although it takes longer to reach the target [19, 40, 41].

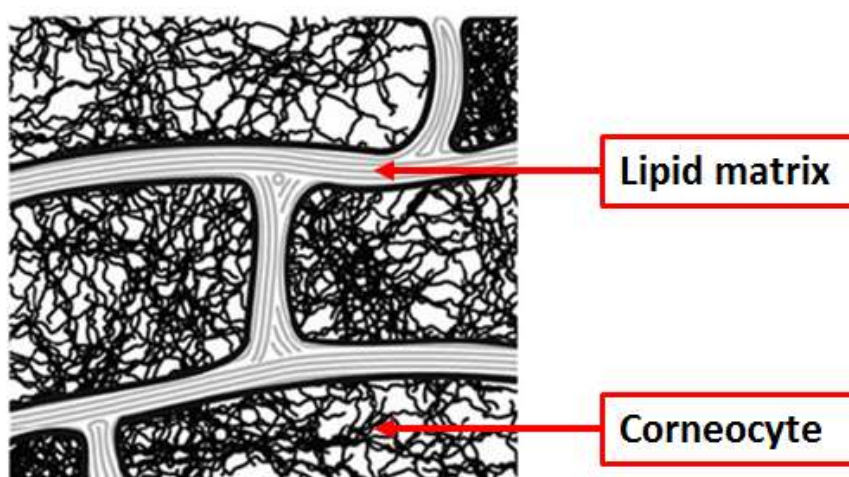


**Figure 1.8** The *stratum corneum* and its pathways for molecule diffusion (modified from [19] Schneider et al. 2009).

The SC can be considered to be a lipoidic compartment whereas the underlying living tissue is a more aqueous environment; hence lipophilic molecules can distribute more easily in the SC and penetration is facilitated. Furthermore, the absorbent needs to fit into the intercellular space and move along the lipid phase or the aqueous phase, respectively, restricting the space available and therefore the size of penetrating species influences the absorption behaviour [42]. As a consequence, the *stratum corneum* acts as the primary protecting layer and may be the rate-limiting barrier to defend against the penetration of most micron sized particles and harmful exogenous toxicants.

Skin exposure to nanomaterials can also occur during the intentional application of topical creams and other drug treatments. Besides skin, the respiratory system serves as a major portal for ambient particulate materials. Pathologies resulting from airborne particle materials have long been researched in occupational and environmental medicine; but, being different from micron sized particles that are largely trapped and cleared by upper airway mucociliary escalator system, nanoparticles can be deposited in the alveoli. After absorption across the lung epithelium, nanomaterials can enter the blood and lymph to reach cells in the bone marrow, lymph nodes, spleen and heart; other targets include the sensory nerve endings embedded in the airway epithelia, followed by ganglia and the central nervous system via axons. Nanomaterials can reach the gastrointestinal tract (GIT) after mucociliary clearance from the respiratory tract through the nasal region, or can be ingested directly in food, water, cosmetics, drugs, and drug delivery devices. The utility of biodegradable nanoparticles in the delivery of oral vaccines has been proposed for antigens known to be susceptible to proteolysis. Apparently studies on toxicity of nanomaterials post-oral ingestion are limited [43, 44, 45, 46].

#### **1.2.4 Current status of nanomaterials regulation**

Because of the concerns over the use of nanotechnology, over the last few years there has been significant debate concerning special government regulation over nanotechnology-based products. The rapid commercialization of

products involving nanotechnology has caught many regulatory agencies off-guard, mainly because of the lack of funding to properly assess the potential toxicity as well as the complete life cycle of nanomaterials. As a consequence, many countries do not have regulations specifically designed to address nanomaterials toxicity. Comprehensive surveillance and regulations for nanomaterials has partially been achieved by the EU and the US [47].

According to the European Commission Environment webpage, **“Nanomaterials are chemical substances or materials that are manufactured and used at a very small scale (down to 10,000 times smaller than the diameter of a human hair). Nanomaterials are developed to exhibit novel characteristics (such as increased strength, chemical reactivity or conductivity) compared to the same material without nanoscale features (...) even though nanomaterials are not per se dangerous, there still is scientific uncertainty about the safety of nanomaterials in many aspects and therefore the safety assessment of the substances must be done on a case-by-case basis.”** In terms of regulatory aspects, the EU regulatory framework is a shared competence between all member states; in this matter the European Commission (EC) and its agencies play a central role, as it is in charge of issuing ‘communications’ on the subject of nanotechnology. As of 2015, the EC has released two documents, one in 2008 and one in 2012. The first one is mostly a legal assessment of how nanomaterials are implemented in the current chemical environment, Health & Safety and product legislation. It concluded that even though nanomaterials were adequately covered, some implementations were needed to address the knowledge gap regarding risk assessments and management methodologies, the adoption of provisions (ex. specific thresholds), better consumer information and increased market surveillance. The 2008 communication was criticized for not being empirical enough; therefore, in 2012, a second review was issued. The new communication gave more attention to the risk and safety assessment issues, addressing the existing knowledge gap and lack of reliable data. It also reviewed how nanomaterials have been addressed in REACH regulations (Registration, Evaluation,

Authorization & Restriction of Chemicals), noticing shortcomings and limitations on the clarity of information relevant to nanomaterials. Regarding environmental legislation, it acknowledged that many issues still had to be addressed because of the significant knowledge gaps. The same report also identified three main types of nanomaterials, defined as: A) Commodity materials, such as carbon black or synthetic amorphous silica, which constitute more than 95% of market and have been extensively used for decades; B) Newly developed medium volume substances, including titanium dioxide and carbon nanotubes, which are under discussion for safety aspects; C) Newly developed low volume substances, most of which are used for technical applications (catalysts, batteries, solar cells etc.). The overall message of this document centered on three main objectives: A) the need for more specific risk assessment procedures; B) the implementation of nanomaterial definition in an appropriate way; C) information-related provisions using REACH as main regulation tool. As a follow up for this review, the European Commission has considered the modification of some of the technical provisions in the REACH Annexes, with a public consultation held until 13 September 2013. Although no amendments have been made so far to the legal text of REACH to incorporate nanomaterials, the European Chemicals Agency (ECHA) has updated its guidance to include nanomaterials. ECHA has also set up a webpage aimed specifically at nanomaterials under REACH, and has updated the International Uniform Chemical Information Database (IUCLID) user manual "Nanomaterials in IUCLID 5" to include instructions on how registrants can report explicitly when a nanoform has been used for testing purposes [48, 49].

The U.S. Food and Drug Administration (FDA) regulates a wide range of products, including foods, cosmetics, drugs, devices, veterinary products, and tobacco products some of which may utilize nanotechnology or contain nanomaterials. Consequently, a nanotechnology task force was formed in August 2006 to determine regulatory approaches to guarantee the development of safe and effective FDA-regulated nanotechnology products. As of 2014, the FDA issued one draft and three final guidance documents related to the use of nanotechnology in regulated products. These three guidance documents

consider A) the application of nanotechnology in FDA-regulated products; B) the safety of nanomaterials in cosmetic products; C) the assessment of the effects of significant manufacturing process changes, including emerging technologies [50]. The first two guidance documents provide an overview of nanomaterials' assessment for industry applications. Guidance document A considers mainly the application of two specific points of view. The first is whether a material or end product is engineered to have at least one external dimension, or an internal or surface structure, in the nanoscale range (approximately 1 nm to 100 nm), the second is whether a material or end product is engineered to exhibit properties, including physical or chemical properties or biological effects, that are attributable to its dimension(s), even if these dimensions fall outside the nanoscale range, up to one micrometer (1,000 nm). These considerations need to be applied not only to new products, but also to manufacturing processes of FDA-regulated products that may need to be altered by said technology. Guidance document B, on the other hand, considers the safety assessment of nanomaterials' safety, physical and chemical properties, toxicology as well as ADME (absorption, distribution, metabolism and excretion) by addressing the routes of exposure, the uptake and absorption, and toxicity testing. It also considers distinctive properties and biological behavior for toxicity testing of cosmetic products containing nanomaterials [51, 52].

Both these main legislations lack information regarding the pharmaceutical field, especially that of drug delivery. While nanomaterials are normally included in the chemicals' legislation in the EU and mostly in the cosmetics assessment in the US, no specific regulations regarding their size-related effects have been considered, even though size is probably the most important in NMs behaviour, as it has direct influence on several other characteristics.

Despite these regulation gaps, as of 2014 nanoformulations have been approved by the FDA, as shown in **Table 1.2** [53, 54, 55]:

**Table 1.2** FDA-approved nanoformulations in the last 15 years (modified from [53] Tinkle et al (2014)).

<b>Tradename</b>	<b>Therapeutic agent</b>	<b>Targeted disease</b>	<b>Manufacturer</b>	<b>FDA Approval Date</b>
<b>PEGASYS®</b>	Peginterferon alfa-2a (polymer–protein conjugate)	Hepatitis B and C	Genentech	2002
<b>Neulasta®</b>	PEG-G-CSF or pegfilgrastim and monomethoxypolyethylene glycol (polymer–protein conjugate)	Chemotherapy-associated neutropenia	Amgen	2002
<b>Eligard®</b>	Leuprolide acetate and PLGH polymer formulation	Advanced prostate cancer	Sanofi	2002
<b>Somavert®</b>	Pegvisomant (PEG-hGH) (polymer–protein)	Acromegaly	Pfizer	2003
<b>Emend®</b>	Aprepitant nanocrystal particles	Chemotherapy-related nausea and vomiting	Merck	2003
<b>Alimta®</b>	Pemetrexed	Non-squamous NSCLC, malignant pleural mesothelioma	Lilly	2004
<b>Macugen®</b>	Pegaptanib (PEG-anti-VEGF aptamer)	Wet age-related macular degeneration	Eyetech	2004
<b>Tricor®</b>	Fenofibrate	Hypercholesterolemia, mixed dyslipidemia, hypertriglyceridemia	Abbott	2004
<b>Abraxane®</b>	Albumin protein-bound paclitaxel	Metastatic breast cancer	Calgene	2005
<b>Elestrin®</b>	Estradiol gel (0.06%) incorporating calcium phosphate nanoparticles	Moderate to severe hot flashes in menopausal women	Biosanté	2006

<b>Mircera®</b>	Methoxy PEG-epoetin beta	Symptomatic anemia associated with CKD	Hoffman La Roche	2007
<b>Cimzia®</b>	Pegylated Fab' fragment of a humanized anti-TNF-alpha antibody	Crohn's disease, rheumatoid arthritis	UCB	2008
<b>Marqibo®</b>	Vincristine	Philadelphia chromosome-negative lymphoblastic leukemia	Talon Therapeutics	2012

## 1.3 Silica Nanomaterials

### 1.3.1 Synthesis methods and characteristics

Silica is the common name for materials composed of silicon dioxide ( $\text{SiO}_2$ ) and exists in different forms: crystalline and amorphous, porous and non-porous, anhydrous and hydroxylated. Quartz is the most common natural crystalline silica compound, but manufactured silica porous crystalline compounds are also available.

Regarding the amorphous forms, silica glass represents the most famous natural type, but many manufactured forms are also available, having attracted interest for applications in a variety of industries. As a bulk material, amorphous silica finds applications as additive to cosmetics, drugs, printer toners, varnishes, and food. As nanosized material, silica nanoparticles have been attracting interest for several biomedical applications (cancer therapy, DNA transfection, drug delivery, and enzyme immobilization) due to their biocompatibility, low toxicity and scalable synthetic availability. Their size, porosity, crystallinity and shape can be finely tuned for diverse applications; their surface can also be easily modified and controlled to achieve specific drug or chemical loading, as well as site-specific targeting. The possibility to combine

these properties makes silica nanoparticles a desirable platform for biomedical imaging, assaying, therapeutic delivery, monitoring and ablative therapies [56, 57]. To meet the demand of these applications, several synthesis techniques have been developed; most of them exploit sol–gel processing at 25°C with careful control of the reactant to solvent ratios or the use of templates to control particles size. The main silica synthesis techniques are described in **Table 1.3**:

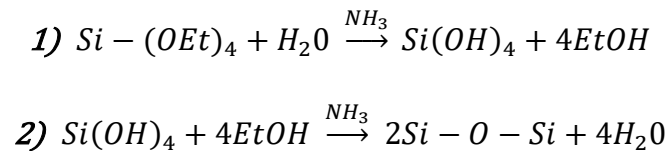
**Table 1.3** The different types of silica nanoparticles that can be obtained by reaction in aqueous solution (modified from [56] Napierska et al (2010)).

Silica particle type	Synthesis method
<b>Stöber/ Colloidal silica</b>	Prepared by controlled hydrolysis and condensation of tetraethylorthosilicate (TEOS) in ethanol with catalytic amounts of water and ammonia. This procedure can be used to obtain monodisperse spherical amorphous silica particles with tuneable size and porosity
<b>Silica gel</b>	Obtained by destabilisation of a silica sol, it's an open 3-D network of aggregated sol particles.
<b>Precipitated silica</b>	Formed by destabilization and precipitation of a silica gel
<b>Mesoporous silica</b>	Obtained by a supramolecular assembly of silica around surfactant micelles, amphiphilic polymers such as triblock- copolymers or quaternary alkyl ammonium compounds. These organic supramolecular templates are evacuated from the mesopores by calcination, a controlled combustion process leading to oxidation and decomposition of the template molecules into small volatile products such as NO <sub>x</sub> , CO <sub>2</sub> and H <sub>2</sub> O, which can leave the pores.

The Stöber method was first developed in 1968, when Werner Stöber prepared silica particles in the range of 0.05–2 μm through the hydrolysis and condensation of alkyl silicates under alkaline conditions in alcoholic solutions



[58]. It continues to be a widely employed method for synthesizing silica nanoparticles, as it avoids the use of templates to form solid particles [59]. To synthesize Stöber silica, tetraethylorthosilicate (TEOS) or other silicates are combined in a water/alcohol/ammonia solution and agitated to form particles, whose size depends on the concentration of the solvents and silicate additives (**Equation 1.1**).



**Equation 1.1** The two-step process (1) hydrolysis and (2) condensation to form colloidal silica.

There have been many investigations of the kinetics and characterization of Stöber process generated particles in order to precisely control their size, shape, and uniformity. For example, Nozawa et al. (2005) studied the rate of addition of TEOS vs. the resulting size of synthesized particles [60]. The particle size decreased with an increase in the rate of addition of the TEOS, and precisely controlling the rate of addition produced uniform particles. Further experiments with Stöber type processes have demonstrated that controlling the ratio of solvent/TEOS permits fine control of particle size [61]. A completely different synthesis route of amorphous silica involves the use of silicon tetrachloride ( $\text{SiCl}_4$ ) in vapour phase. Silicon tetra- chloride is oxidized in a hydrogen flame at temperatures above  $1000^\circ\text{C}$  and polymerized into an amorphous non-porous nanopowder with very low bulk density and high specific surface area, typically 200 to 300  $\text{m}^2/\text{g}$ . This material is called pyrogenic or fumed silica, referring to the special synthesis conditions (**Figure 1.9**).

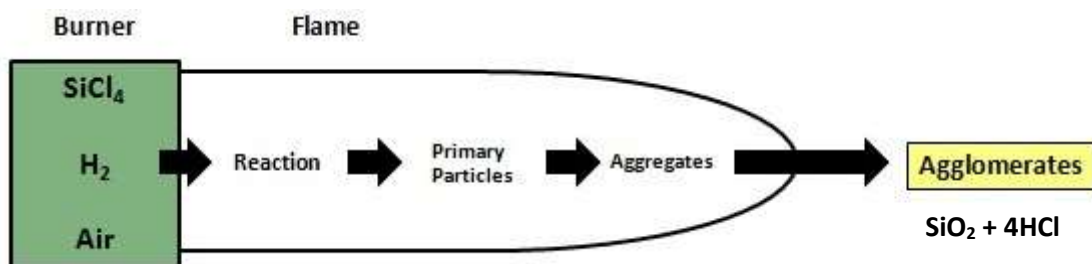


**Figure 1.9** Schematics of the reaction used to obtain fumed silica.

Both fumed and colloidal silica are produced in tonnage quantities, arguably making them the most abundant synthetic nanoparticles on Earth.

### 1.3.2 Relationship between characteristics and toxicity

Amorphous silica is generally considered 'safe' by the FDA, and amorphous silica nanoparticles are often used as negative controls in toxicity studies of nanocrystalline quartz. However, depending on the manufacturing process, amorphous silica has a wide range of physico-chemical properties that determine its industrial applications. These properties also determine silica interaction with and within cells, therefore even subtle differences can modulate the toxicity and modes of action, thus making the results difficult to interpret and compare. In the case of amorphous silica nanoparticles, establishing a reliable toxicological pathway is challenging. While crystalline silica is well-defined structurally, amorphous silica lacks long-range order, with its structures strongly dependent on kinetic and environmental factors. These factors are manifested principally as differences in the siloxane framework architecture, which consists of combinations of closed siloxane rings, shown in **Figure 1.10** [56, 62].

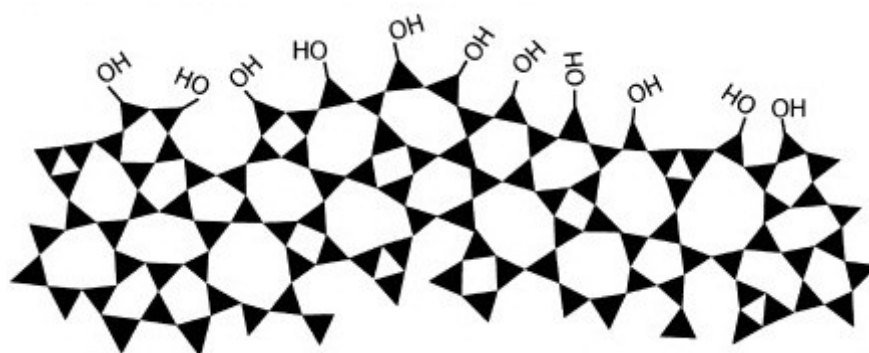


**Figure 1.10** Siloxane rings that constitute the architecture of amorphous silica (modified from [62] Zhang et al. 2012).

The diversity of possible structures and toxicological behaviours, in tandem with their unique physico-chemical properties, makes amorphous silica particles a target for toxicological studies, as to date knowledge about the potential hazard they represent for human health is still limited. Searching through the literature, it is clear that, until recent years, toxicological research into silica particles focused mainly on crystalline silica, especially natural forms such as quartz, cristobalite and tridymite, and the particulate matter generated through industrial exposure (sandblasting, ceramics, cement manufacture, construction). This trend is directly connected to silicosis and other detrimental respiratory effects that crystalline silica causes when inhaled in excessive amounts, causing lung inflammatory diseases, increased susceptibility to infection, as well as lung cancers. Silicosis, in particular, is a generally progressive fibrotic lung disease, exemplified by the development of nodules composed of silica particles surrounded by whorled collagen in concentric layers, with macrophages, lymphocytes, and fibroblasts in the periphery. As comparison, amorphous silica has been far less studied than the crystalline form; consequently, the mechanisms of amorphous silica toxicity at the cellular and molecular levels are still unclear. However, the growing abundance and industrial applications of nanotechnology has resulted in a recent shift of toxicological research towards amorphous silica nanoparticles [62, 63]. Following this new trend, different *in vitro* and *in vivo* studies on amorphous silica NPs have been published.

Relevant *in vitro* and *in vivo* studies are summarized in **Table 1.4** and **Table 1.5** respectively.

**Table 1.4** Summary of relevant *in vitro* studies regarding silica particles.

Research group	Published study
<b>Rancan et al. (2012) [64]</b>	Investigated skin penetration and cellular uptake of 40-200 nm amorphous silica particles with positive and negative surface charge. Partial particle aggregation was observed upon NPs transfer in physiological media, as well as size-dependent uptake inside HaCaT skin cells. Functionalization of the particle surface with positively charged groups enhanced <i>in vitro</i> cellular uptake as well as tendency of particles to form aggregates, leading to lower internalization ratios.
<b>Kato et al (2013) [65]</b>	Investigated the effect of amorphous silica particles of 50, 100, and 200 nm on the Caco-2 intestinal cell line. Particles were incubated in fasted-state and fed-state gastric and intestinal fluids; size, intracellular transport, membrane permeability, and cytotoxicity were evaluated. Silica particles were shown to agglomerate in fed-state intestinal fluids, inhibiting particles absorption and transport; however, they did not observe any cytotoxicity when the average size was larger than 100 nm, independent of the fluid and the concentration.
<b>Park et al. (2013) [66]</b>	Negatively charged [NC] and weakly negatively charged [WNC] silica NPs of 20 nm and 100 nm size were used to investigate cytotoxicity and reactive oxygen species (ROS) generation on keratinocytes, as well as skin irritation and skin sensitization on HSEM (Human Skin Equivalent Model) and mouse skin.

	<p>Smaller size (20 nm) NC silica NPs proved to be more toxic than the larger size particle (100 nm). They also observed an effect of surface charge in cytotoxicity and ROS generation, by showing that the NC silica NPs (20 nm) were more toxic than the WNC silica NPs (20 nm), suggesting the importance of surface charge in silica NPs-induced toxicity.</p>
<p><b>Kim et al. (2015) [67]</b></p>	<p>Employed 20–200 nm monodisperse spherical silica nanoparticles to study size, dose, and cell-type dependent cytotoxicity in A549 human lung carcinoma cells, HepG2 human hepatocarcinoma cells and NIH/3T3 mouse embryo fibroblasts. Cytotoxicity were found to be size-, dose- and cell type dependent; 60 nm particles were preferentially endocytosed by cells and, at high doses, caused a disproportionate decrease in cell viability.</p>

**Table 1.5** Summary of relevant *in vivo* studies regarding silica particles.

<b>Research group</b>	<b>Published study</b>
<b>Yoshida et al. (2015) [68]</b>	Observed that in mice silica nanoparticles with sizes smaller than 100 nm were more likely to cause consumptive coagulopathy, pregnancy complications and immune-modulating effects in mice compared to silica particles with sizes larger than 100 nm. Consequently, they examined the relationship between the surface properties of 70 nm amorphous silica nanoparticles with and without amino surface modification and their interactions with proteins in biological fluids as well as their toxicity by mice intravenous administration of 2 mg/mouse for up to 24 hours. They concluded that surface modification with amino groups prevented toxicity compared to the non-modified particles, as no effect could be detected by assays of platelet counting, clotting time assessment and activated partial thromboplastin Time (APTT) in mice.
<b>Kim et al. (2015) [69]</b>	Investigated the potential toxicity and the No Observed Adverse Effect Level (NOAEL) and target organ(s) of negatively charged 20-100 nm colloidal silica particles after 90 day-oral administration in rats at 500 mg/kg, 1,000 mg/kg and 2,000 mg/kg. Up to the highest tested concentration, no animal deaths were observed, and no treatment-related clinical changes or histopathological findings were observed in any of the experimental groups. Moreover, no difference in toxic effects from chronic exposure to 20 or 100 nm silica NPs was observed, indicating that the NOAEL would most likely be 2,000 mg/kg without any identifiable target organ in rats of either sex.

Despite these various *in vitro* and *in vivo* nanotoxicity studies in the assessment of silica particles toxic effects, there is still a substantial lack of available investigations, as well as a full understanding of the cellular and molecular toxic property of these particle, prompting more work to be done on the matter.

## **1.4 Skin – A Major Target of Nanomaterials**

### **1.4.1 Structure and function**

Skin is the largest organ of the human body, and can be described as a complex, inhomogeneous laminate composite material that is often subjected to large deformations. Skin is organized in three different layers, as illustrated in **Figure 1.11**. The most external one is the epidermis, which serves as a barrier between the external environment and the internal parts of the human body. Under the epidermis is located the dermis, which confers flexibility and is responsible for skin's mechanical behaviour. The inner layer is the hypodermis, which acts as an energy reserve and has a role in skin plasticity [70, 71].

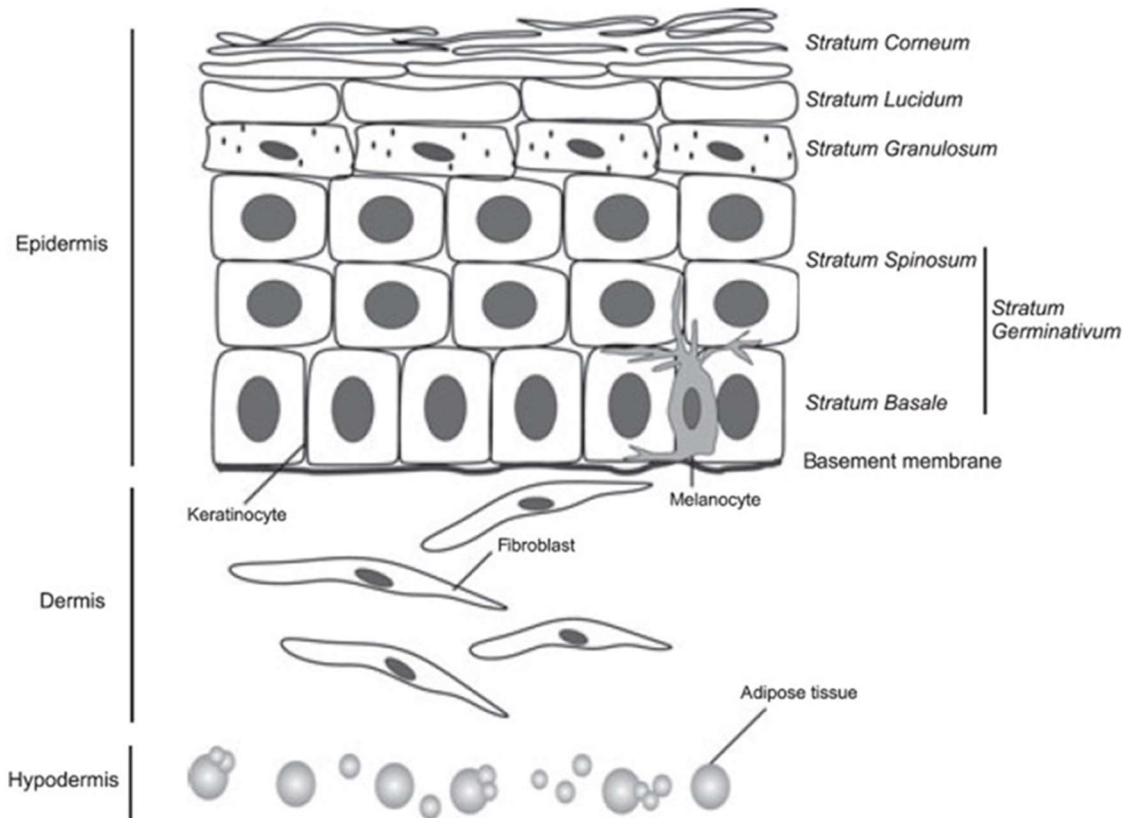


**Figure 1.11** Drawing of the skin tissue and main components of cells. At the bottom is the hypodermis, consisting of adipose cells; the next layer up is the dermis, consisting of fibroblasts; at the top is the epidermis consisting of viable and nonviable keratinocytes and melanocyte (from [70] Brohem et al. 2011).

Each skin layer has diversified functions mediated by different types of cells. Epidermis is formed mainly by keratinocytes, organized in multiple layers. These cells are generated from the *stratum basale*, the innermost part of epidermis, and move upwards through the different strata while enduring defined stages of differentiation. They will eventually fully differentiate into keratinocytes and die on the outermost layer of the epidermis, the *stratum corneum* [70], which is mainly responsible for the barrier function of the skin. Epidermis also contains other types of cells, namely: melanocytes, which confer skin its pigmentation by transferring melanin to the keratinocytes in the final sublayer of the *stratum lucidum*; Merkel cells, which are thought to play a sensory role [72, 73]; Langerhans cells, which play an important role in the skin



immune response [74, 75]. Between the epidermis and the underlying dermis lies the basement membrane, formed by collagen IV, glycosaminoglycans and proteoglycans. The basement membrane has three primary functions:

- it anchors the two layers to each other;
- it controls molecules' traffic in both directions;
- it is able to bind numerous cytokines and growth factors [76].

The dermis, located under the basement membrane, is formed by collagenous materials, such as elastin fibres, fibronectin and hyaluronic acid, all known as the ECM (extracellular matrix), mixed together with dermal fibroblasts (which are responsible for the production of the ECM), immune system cells, nerve endings, hair follicles, blood vessels and endothelial cells [77, 78]. Associated with the dermis and the epidermis are skin appendages, serving different functions. The sweat glands regulate body temperature by secreting sweat on the skin surface, while the sebaceous glands keep skin and hair moisturized by secreting sebum; hair follicles are important in re-epithelialization during wound healing, nails protect the distal phalanx and the fingertips [79]. **Figure 1.11** represents only a schematic overview of skin structure. In reality, the three layers are connected to each other by complex interactions between individual cells with the neighbour cells and the ECM. The connections between layers of the skin can be maintained partially by different mechanical forces applied to the epidermis, which are transmitted to the dermis through the basement membrane [70, 71].

#### **1.4.2 The *stratum corneum*, its composition and barrier function**

As said before, the skin permeation barrier is localized in the outermost layer of epidermis, the *stratum corneum* (SC). It was not too long ago that the SC was considered just a 'graveyard of insoluble keratin fibrils', a lifeless skeleton of what were previously keratinocytes that had completed the upward journey through the layers of the epidermis prior to their shedding by desquamation. Only the ability to harvest the SC intact and separate it from the rest of

epidermis led to the belief that it was a wrap-like film structure important for barrier function. The subsequent investigations based on this principle helped the progressive recognition of the many physiological functions that occur in this particular layer [77].

The SC is made up of a collection of cellular-like structures, with an individual structure being named corneocyte, which originates during the upward migration of a keratinocyte. A stepwise sequence of active biological processes occurs that involves synthesis and activation of specific structural proteins, lipids and enzymes, and formation of structures all of which impact directly upon SC health and functional integrity [77]. The real differentiation process begins in the *stratum granulosum*, where keratinocytes become flattened and gradually differentiate into corneocytes. Corneocytes contain certain types of organelles, namely keratohyalin granules, which stock proflaggarin, and lamellar bodies (LBs), which transport precursor lipids, protease enzymes, and cAMP. These organelles undergo lysozomial degradation, and the lipid precursors in the LBs, shown in **Table 1.6**, are released in the lipid phase of the SC by exocytosis and subsequently transformed into fatty acids, cholesterol and ceramides, which will form a bilayer that will comprise the intercellular lipid membrane [77].

**Table 1.6** Lipid conversion in the *stratum corneum*. The table summarizes the precursor lipids present in the lamellar bodies, which undergo lysozomial degradation, thus freeing the precursors in the lipid phase of the SC. From there, they are enzymatically converted in ceramides, fatty acids and cholesterol (edited from [77] Del Rosso et al. 2011).

Precursor Lipid	Enzymatic Conversion	Final Stratum Corneum Lipid
Glucosylceramide	B-glucosylcerebrosidase	Ceramides
Phospholipid	Phospholipase	Fatty Acids
Cholesterol Sulfate	Steroid Sulfatase	Cholesterol

These three types of lipids are really important, because their properties are directly related to the *stratum corneum* barrier function. Ceramides are the most abundant class, and are structurally heterogeneous, as shown in **Figure 1.12**. Ceramide 1 consists of 30- to 34-carbon  $\omega$ -hydroxyacids amide-linked to sphingosine bases with linoleic acid ester-linked to the  $\omega$ -hydroxyl group; Ceramide 2 consists of long, mostly 24-, 26- and 28-carbon, normal fatty acids amide-linked to sphingosine and dihydrosphingosine bases; Ceramide 3 contains the same long-chain normal fatty acids, but they are linked to phytosphingosine bases. Ceramides 4 and 5 both contain  $\alpha$ -hydroxyacids amide linked to sphingosines and dihydrosphingosines; the main difference is that Ceramide 4 contains predominantly 24- through 28-carbon hydroxyacids, whereas Ceramide 5 contains predominantly  $\alpha$ -hydroxypalmitic acid [78].

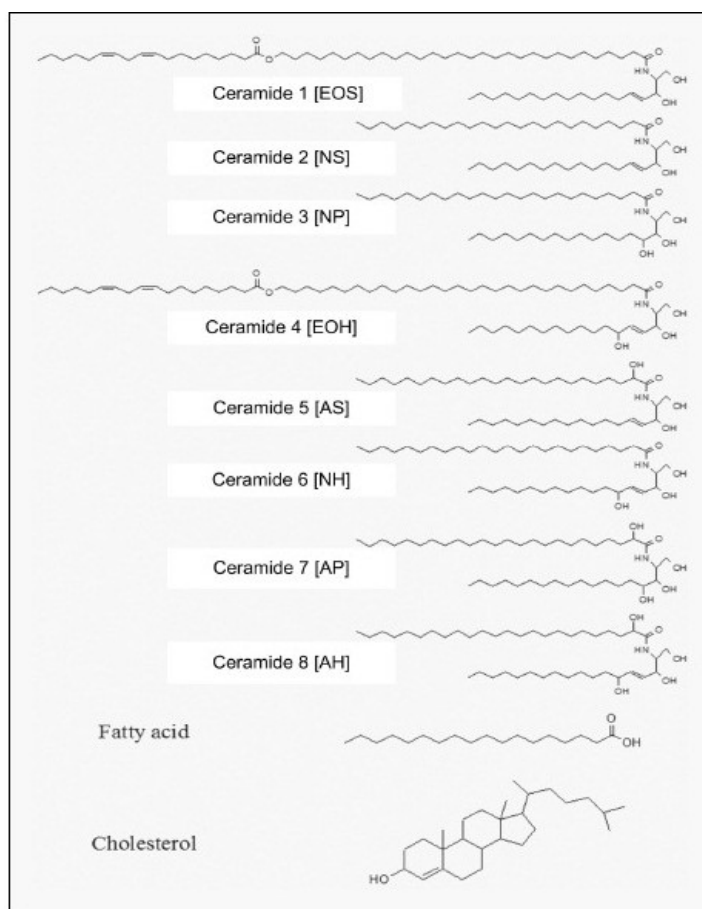


**Figure 1.12** The structure of ceramides, fatty acids and cholesterol (modified from [78] Lee et al. 2006).

Fatty acids are almost entirely saturated, straight-chained and longer than 18 carbons, with the most abundant ones being 22-24 carbon length. Together with ceramides, they confer the *stratum corneum* its rigidity [79, 80]. To plasticize these otherwise rigid membranes, cholesterol plays a fundamental role, as it can increase or decrease fluidity, based on its proportion and the nature of the other components. **Figure 1.13** displays a schematic distribution of ceramides, fatty acids and cholesterol inside the *stratum corneum*.

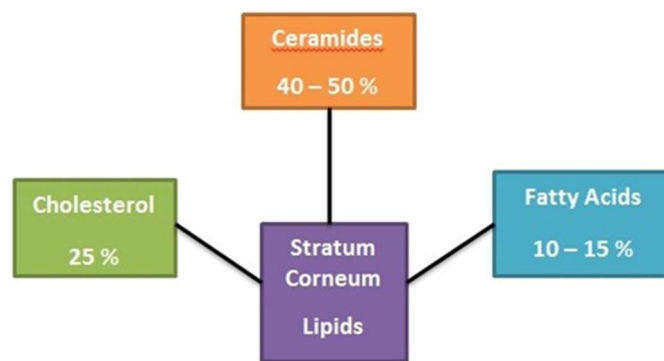


**Figure 1.13** Major SC lipid content by weight. Ceramides are the most abundant lipids, being approximately 40-50% of total, followed by cholesterol and fatty acids.

During the differentiation process, inside the corneocytes proflaggarin is converted into the protein flaggarin, which subsequently migrates at the periphery of the corneocyte and intermingles with keratin filaments to form filament-matrix complex. This matrix is cross-linked by the action of calcium-dependent transglutaminases to: a) the extracellular cornified envelope (CE), a 15-20 nm thick structure composed of structural proteins and a covalently bound lipid monolayer made of long-chain ceramides, that provides external protection for the corneocytes; b) the corneodesmosomes, formed by proteins, especially desmocollins and desmoglein, that anchor the corneocytes within the *stratum corneum* and that are directly related to the desquamation process. The whole differentiation process is schematized in **Figure 1.14**.

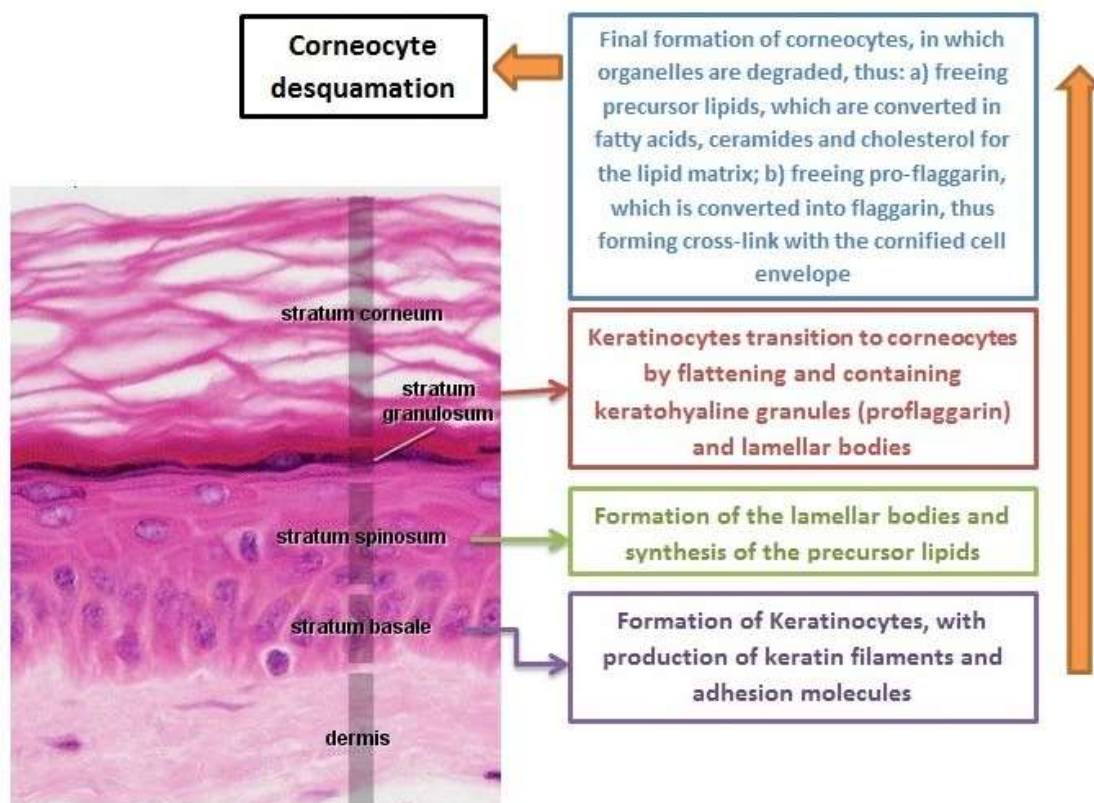


**Figure 1.14** Steps in the formation of the *stratum corneum*. Starting from the *stratum basale*, keratinocytes undergo a stepwise differentiation process that ends with corneocyte desquamation on the *stratum corneum*. (Skin Image from [http://php.med.unsw.edu.au/embryology/index.php?title=File:Adult\\_epidermis\\_histology\\_01.jpg](http://php.med.unsw.edu.au/embryology/index.php?title=File:Adult_epidermis_histology_01.jpg))

The process described above can be viewed as a ‘bricks and mortar’ model, where the flattened corneocytes represent the bricks, while the lamellar lipid membrane represents the mortar between the bricks [77].

In addition to the permeability barrier function, it is important to remember that the *stratum corneum* also plays fundamental roles in other critical functions such as antimicrobial defence, hydration of viable epidermis, UV defence, antioxidant defence and the formation of a mechanical barrier, as shown in **Figure 1.15** [78]. Due to structural heterogeneity, both corneocytes and the lipid membranes contribute to the defence functions. Extracellular lipids usually act as permeability, antioxidant and microbial barrier, while corneocytes act as UV and mechanical barriers [78]. Despite this division, all of these functions are

closely interrelated, so if there's any change in one, all the others could undergo some modifications as well.

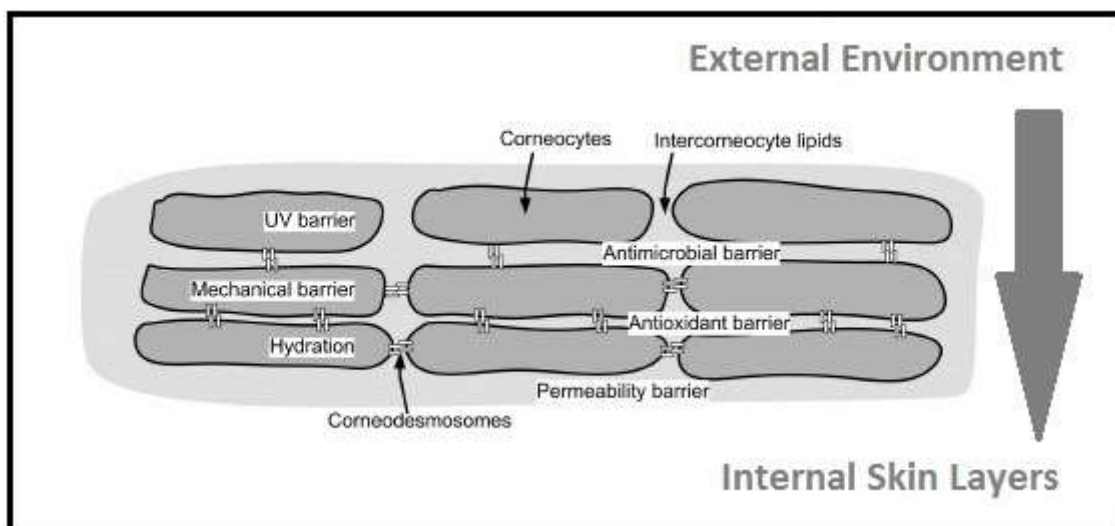


**Figure 1.15** The bricks and mortar model with the various functions of the SC (modified from [78] Lee et al. 2006).

As skin is the major site for NMs exposure, *in vitro* and *in vivo* skin models have been used to assess NPs toxicity. *In vitro* models include classic 2D cell culture, *ex vivo* tissues and 3D culture, while *in vivo* refers to the use of animal models. Each of these techniques have their own advantages and disadvantages, therefore must be chosen carefully depending on the intended study purpose. 2D cell culture, also known as monolayer culture, is conventionally used for drug testing; it consists of cell lines grown on a flat surface in medium supplemented with growth stimulating compounds. 2D culture is a well-established method that has been in use since the beginning of the 20<sup>th</sup> century. It also has limitations, such as lack of cell–cell and cell–extracellular matrix (ECM) signalling that occurs in the *in vivo* environment [81]. *Ex vivo* tissues consist of excised specimens of animal and human skins. Such models have been widely used to test drug permeation in the skin. Despite being full thickness skin, they have their own limitations, as animal *ex vivo* tissues present difference compared with human *ex vivo* tissues; nude mouse skin, for

example, is too leaky to be a reliable substitute of the human skin. Even human *ex vivo* tissues can cause practical problems, especially in terms of availability, variability and quality. Furthermore, the excised pieces of human skin represent dead tissue that is not suitable for toxicity evaluation of drug delivery systems [82]. 3D models of skin epidermis are a promising alternative to the animal experiments and *ex vivo* human skin samples. Unlike excised skin samples, the cell models are viable and they can be used to study specific biological responses to the treatments [82]. However, most of the currently commercially available skin equivalents are based on static culture systems emulating human epidermis only, or combining epidermis and dermis in full-thickness skin equivalents. None of the existing systems comprises functional and physiologically important elements, such as an immune system, vasculature or skin appendices. Such incorporation needs to be implemented in an appropriate culture system with a constant oxygen and nutrient supply and with controlled levels of toxic metabolites [83]. Because of their complexity, long periods of time are necessary for full model growth; such models may also present practical difficulties when the intended use is the toxicological assessment of particle behavior, as using assays such as MTT or LDH might prove challenging. *In vivo* models remains the best in terms of complexity compared to the human body, but ethical and practical reasons call for the constant diminishment on the use of such models. Despite their advantages and disadvantages, all these models are of major importance in several fields of study, including nanomaterials testing.

Murray et al. (2013) [84] for example, used human epidermal keratinocytes (HEK) and murine epidermal cells (JB6 P+) for *in vitro* testing of dextran-coated super-magnetic iron oxide nanoparticles (SPIONs) of different sizes (15–50 nm) and manufacturers in relation to their cytotoxicity and internalization. By using this method, they found that HEK cells exposed to 20 nm particles resulted in a decrease of viability, while the 15 and 50 nm particles were not cytotoxic. They also showed that HEK cells were capable of internalizing the 15 and 20 nm but not 50 nm. Cohen et al. (2013) [85] used skin explants cultivated on polycarbonate slides to assess the biological effects of topically applied copper

oxide (CuO) nanoparticles by assays of light and electron microscopy, as well as biochemical tests including MTT, ELISA and caspase 3 assays. With this method, they showed that nanoparticles were more toxic than micro sized particles, and their effects were stronger when supplied in growth medium than in topical application. They also found that topically applied CuO nanoparticles induced inflammatory cytokine secretion and necrosis, especially in epidermis deprived of its protective cornea. Choi et al. (2014) [86] used the commercially available 3D human skin model KeraSkin™ to assess skin corrosion and irritation upon treatment with zinc and titanium oxide nanoparticles by assay of cytotoxicity and cytokine release. They found no decrease of viability after exposure to nanomaterial for pre-determined threshold level, which was 15% after 60 minutes exposure in corrosion test and 50% after 45 minutes exposure in the irritation test. Korani et al. (2013) [87] used guinea pigs to determine the morphological changes and pathological abnormalities on the tissues following dermal treatment with silver nanoparticles (AgNPs). They showed a close correlation between dermal exposure and tissue levels of Ag NPs; they also demonstrated that tissue uptakes happened in dose dependent manner with ranking kidney>muscle>bone>skin>liver>heart >spleen.

#### **1.4.3 Basic principles of *in vitro* tissue culture**

Tissue culture was first established in the last years of XIX century, when Wilhelm Roux, a German zoologist working in Innsbruck (Austria), first removed a section of the medullary plate of an embryonic chicken and maintained it in a warm saline solution for several days [88]. From there, tissue and cell culture has matured from a simple and microscope-driven observational science to an indispensable technology in many branches of the life sciences, with roots set deep in both industry and academia. They provide the basis for studying the regulation of cell proliferation, differentiation and product formation in carefully controlled conditions. They have also provided the means to define almost the entire human genome, and to dissect the pathways of intracellular and intercellular signalling [89].



Originally, tissue culture was regarded as the culture of whole fragments of explanted tissue, which was considered to maintain at least part of its histological integrity. Now the term includes organ culture as well, but also, and most importantly, cell culture, where tissue is dispersed mechanically or enzymatically and the resulting cells are propagated as a suspension or attached monolayer [56]. Literally thousands of different cell lines have been derived from human tissues. Many of these originate from normal tissues and exhibit a definable, limited doubling potential; others may be propagated continuously, either having gone through an engineered or spontaneous genetic change, or having been developed from tumour tissue [90].

Cell cultures have lost their histotypic architecture, and often the associated biochemical properties; consequently, they are not only devoid of structural organisation, but also do not reach a steady state unless specific conditions are achieved. These specific conditions mainly involve:

- **Substratum:** a surface where cells can attach and spread; the type used depends on the cell type, with optically clear negatively charged polystyrene being the one almost universally used by research labs.
- **Medium:** represents the diffuse environment, and is often chosen empirically, especially for primary cell lines.

Culture medium comprises all types of soluble molecules - nutrients and salts, hormones and growth factors; it must supply all essential nutrients for cell metabolism, proliferation and growth [91]. These include 1) biosynthetic precursors for cell anabolism, 2) catabolic substrates for energy metabolism, 3) vitamins and trace elements for catalytic function, 4) electrolytes for catalytic and physiological functions. An example of such catalytic and physiological functions is the maintenance of pH and osmolarity within acceptable limits. In addition to those components, animal serum, such as Foetal Bovine Serum (FBS) is frequently added. FBS and related sera, in general, are an extremely complex mixture of low and high molecular weight biomolecules with different, physiologically balanced growth-promoting and growth-inhibiting activities. The

main components and major functions of FBS in culture media are summarized in **Table 1.7**:

**Table 1.7** Main components and properties of FBS (modified from [91] Gstraunthaler et al., 2003).

Main Components	Biological functions
Albumin	Providing hormonal factors stimulating cell growth and proliferation
Cholesterol	
Cortisone	Providing stabilizing and detoxifying agents to maintain pH and inhibit proteases
Glucose	
Haemoglobin	Transport proteins
Thyroxine, trijodo-thyronine	Providing attachment and spreading factor

FBS has become the standard supplement of cell culture media; in most cases, it is used at concentrations of 10% (v/v), although this may vary for specific applications.

#### **1.4.4 Interaction of culture medium and biological fluids with nanomaterials**

When NMs enter a biological fluid, for example blood, proteins and other biomolecules rapidly compete for binding to the NMs surface, leading to a formation of a dynamic protein layer, called protein corona (PC). This layer critically defines the biological identity of the particle, as cells interact with the entire nanoparticle–protein corona complexes rather than with the bare entity of

nanoparticle (**Figure 1.16**). Protein coronas have been experimentally identified and characterised using a range of techniques, which include polyacrylamide gel electrophoresis (SDS-PAGE), tandem liquid chromatography-mass spectrometry (LC-MS/MS), proteomics, differential centrifugal sedimentation and Western blotting. These research efforts have revealed differential affinity or binding strength of each protein member of the plasma, serum or other body fluids onto specific type of nanoparticle surface, leading to the formation of 'hard' and 'soft' corona proteins. From these studies, it is believed that within the first seconds or minutes after immersion of NPs into biological fluids a soft protein corona is formed. This corona dynamically evolves over time due to the Vroman effect [92]: mobile and abundant proteins first interact with the surface of the particle, but over time they are replaced with less mobile proteins that have a higher affinity for the surface and subsequently evolve into a hard PC. That may consequently change the NPs properties, affecting biological responses and NPs bio-distribution [92, 93, 94].

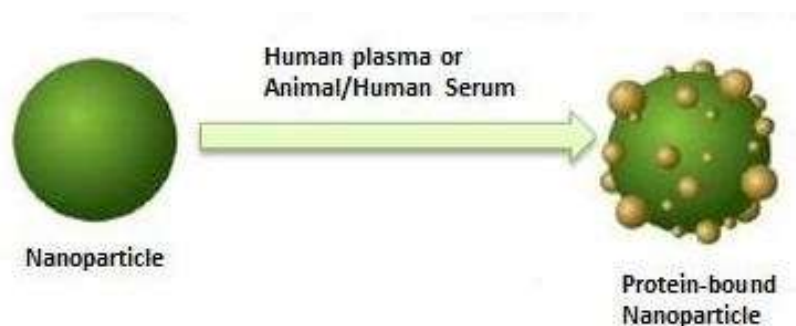


**Figure 1.16** The principle behind protein corona formation (Modified from [88] Aggarwal et al., 2009).

Not surprisingly, protein corona has been found not only to change its composition, but also its physical character over time, being loosely bound at first and gradually transitioning into a more tightly bound protein layer over the course of several days. Changes in composition are influenced by NPs properties such as size, hydrophobicity, charge and surface chemistry, as

reported in **Table 1.8**. The composition of the protein corona has been studied in an attempt to elucidate its role in governing NP interactions with, and their biological impact on mammalian cells.

**Table 1.8** Major effect of NPs properties on corona formation (from [95] Aggarwal et al. 2009).

NPs Properties that influence protein binding	Effect
<b>Surface Charge</b>	Neutral particles have slower opsonisation than charged particles
<b>Hydrophobicity</b>	Hydrophobic particles are opsonised more quickly than hydrophilic particles
<b>Size</b>	Influences the amount of bound proteins

The majority of studies examining the influence of protein binding on uptake have been conducted either by pre-incubating particles with bulk serum/plasma, or by pre-incubating particles with individual proteins or attaching individual proteins to the surface of the particles, and by evaluating uptake by macrophages. This research has showed that neutrally charged particles have a distinctively slower opsonization rate than charged particles, demonstrating a direct correlation between surface charge and protein binding [95]. Formation of the protein corona on NPs in mammalian growth media also leads to changes in hydrodynamic diameter and zeta potential. Lundqvist et al. analyzed the protein corona composition on polystyrene (PS) NPs incubated in human serum for one hour, and found that the native size and surface chemistry of NPs affected the nature of the resulting corona. A detailed analysis of the protein corona composition is necessary for evaluating changes in surface properties and the putative presence of opsonization candidates that could affect NPs uptake and

toxicity in mammalian cells [93]. Mortensen et al. (2013) [93] results indicate that *in vitro* each protein corona comprised more than 30 detectable proteins confirming the complex and dynamic nature of the NPs protein corona, and illustrating that the original surface chemistry of the NPs composition significantly impacts the resulting protein corona.

Aggarwal et al. (2009) [95] reported that in current preclinical testing of pharmaceutical molecules, evaluation of plasma protein binding is recognized as an important element in an assessment of drug efficacy, safety, and disposition, as well as pharmacokinetics and pharmacodynamics of the drug inside the body. The composition of the protein corona on a given particle, at a given time, depends on the concentrations and kinetic properties of the proteins found in plasma. Therefore, it is important to not only determine which proteins are adsorbed onto the surface of the nanoparticle, but also understand the binding affinities and stoichiometry. They reported that kinetic studies on solid lipid nanoparticles (SLNs) showed that initial protein binding was predominated by albumin, replaced over time by fibrinogen, which was then replaced by IHRP (inter- $\alpha$ - trypsin inhibitor family heavy chain-related protein) and apolipoproteins. They have also reported that with increasing plasma concentrations, the amount of fibrinogen on the SLNs surface decreased while the amount of apolipoproteins steadily increased. At high concentrations of plasma, fibrinogen can be displaced within seconds, if not fractions of a second, by apolipoproteins.

Just as the properties of a nanoparticle influence the protein binding profile, the binding profile influences biodistribution, as it can cause, for example, a change in nanoparticle size and surface charge. These changes affect the internalization process of these nanoparticles into macrophages and the overall distribution throughout the body [95]. The presence of protein corona affects cellular responses toward the particles in a complex manner. Aggarwal et al. (2009) [95] reported that binding of opsonins such as IgG, complement factors, and fibrinogen are said to promote phagocytosis and the eventual removal of the particles from systemic circulation via cells of the RES, whereas

dysopsonins such as albumin are said to promote prolonged circulation times in the blood. Lesniak et al. (2012) [96] used 50 nm SiO<sub>2</sub> NPs to observe how the absence and presence of preformed protein corona change their biological fate. To do so, they used NPs in the presence and absence of serum to perform cell uptake studies. 'Bare' NPs were internalised at higher extent by human cells and more strongly adhered to the cell membrane compared to those with presence of pre-formed corona. 'Bare' NPs were found engulfed in vesicles and lysosomes, and also as free particles in the cytosol and as aggregates in the proximity of the plasma membrane. The particles with pre-formed corona on the other hand, were enclosed in vesicles along the endolysosomal pathway. The work further revealed that the protein identity of the corona is determined by the environment in which the NPs were found. Investigations of the post-cell exposure protein corona of the recovered particles revealed a very different protein composition. For the NPs exposed to cells in the serum-containing medium (presence of pre-formed corona), the major members of the corona were the serum proteins immunoglobulins, complement proteins and apolipoproteins, while in the serum-free medium ('bare' NPs) the most abundant proteins were cytosolic proteins, components of cytoskeleton and membrane-associated proteins. The protein composition of the corona governs the nanoparticle - cell interactions and in turn, the biological fates and potential *in vivo* roles of the particles. Adsorption of a particular protein identity in relatively high abundance on the particle surface could trigger key biological processes in the forms of cell uptake, activation of unique cellular signalling pathways as well as scavenging of biomolecules. Kinetics of nanoparticle – protein association and dissociation, along with the simultaneous exchange of the bound proteins with 'free' proteins in the surrounding fluid, may also influence the nanoparticle interactions with biological surfaces and receptors. In unique cases, proteins can undergo conformational and/ or orientation changes upon particle binding, which could result in the presentation of a new epitope, thus modifying the biological functions of the nanoparticles and in a number of circumstances lead to disease pathogenesis [92].

## 1.5 Conclusions

As described in this literature review, there has been a great development in NMs applications and toxicity assessment over the last few years. Despite these advancements, more research is needed to further understand the relation between nanomaterials characteristics in biological media and toxicity upon contact with cells, tissues and organs. To achieve such knowledge, the study of molecular mechanisms of uptake and toxicity, the improvement of *in vitro* models, as well as studying the toxicity in relation to the NMs characteristics will be fundamental in the next few years. Providing further evidence supporting *in vivo* studies will also contribute to fill the gaps in nanomaterials' regulation, thus leading to even better development on safe nanoformulations.

## **2 AIMS AND OBJECTIVES**

### **2.1 Aims**

This project is part of NANODRUG, a research consortium funded by the European Commission, Marie Curie Actions, Seventh Framework Programme, Initial Training Network (grant agreement number: 289454). The scientific aim of the NANODRUG consortium was to develop and characterize a selected set of nanomaterials and to study their suitability as drug delivery systems targeting inflammatory skin diseases. As part of the NANODRUG consortium, the main aim of this project was the toxicity assessment of nanoparticles in relation to their physico-chemical properties, with focus on fumed and colloidal amorphous silica particles because of their unique physical and chemical properties and potential application as carrier for drug delivery through topical route.

#### **2.1.1 Research hypothesis**

Size and characteristics influence nanoparticles and submicroparticles toxic potential.

### **2.2 Objectives**

#### **2.2.1 Objective 1: Characterization of silica particles behaviour in cell culture medium**

The availability of studies focusing on amorphous silica is still limited, due to the variable synthesis methods used by different laboratories as well as their mouldable physical and chemical properties. For this study, amorphous fumed and colloidal silica nanoparticles of different size were sourced from commercial suppliers without further treatment and characterized, in order to make the results more reproducible and easy for comparison across different laboratories. Because all nanomaterials interact with biomolecules in biological fluids upon contact with them, undergoing changes in their surface structure as well as their biological interaction, *in vitro* study of interaction between silica particles and



biomolecules was investigated. Silica particles were tested in different media used for culturing of different cells in order to gain information regarding media composition effect on particle behaviour, focusing on the effect of Foetal Bovine Serum (FBS) as this is widely used in cell culture *in vitro*. Further information was also gathered regarding particle shape and stability in biological media. The results obtained were assessed for relationship between characteristics and toxicity of the silica particles.

### **2.2.2 Objective 2: Toxicological assessment of silica particles *in vitro* in human skin cells**

As the focus for the use of silica nanoparticles in this project is for drug delivery through topical application, particle behaviour upon contact with skin cells was investigated *in vitro* by toxicological assessment of fumed and colloidal silica particles on four different types of human skin cells: HaCaT and K17 keratinocytes, BJ fibroblasts and Human Dermal Fibroblasts (HDF). Multi-parameter assays were performed on each cell type to establish the toxicity potential of the silica particles in relation to their size, dose and the sensitivity of different cell types.

### **2.2.3 Objective 3: Delineation of toxicity mechanisms in relation to silica particle size**

Because of its variable structure, establishing a reliable toxicity pathway for amorphous silica has proven to be challenging. The assessment of silica toxicity via multi-assays proved necessary in delineate the mechanisms of cell-type, particle size- and dose-dependent toxicity. These assays included cell viability, cell membrane damage, morphology changes, cellular uptake and induction of apoptosis, and cell death gene expression.

#### **2.2.4 Objective 4: Assessment of the effect of serum on silica particle behaviour in cell culture medium and toxicity potential**

As introduced before, animal serum, such as Foetal Bovine Serum (FBS) is frequently added to cell culture media in *in vitro* cell culture to mimic *in vivo* conditions. As in *in vivo* conditions any type of nanoscale material that enters in contact with biological fluids is quickly enveloped in biomolecules competing for binding on the nanomaterial surface, in *in vitro* conditions a similar effect occurs for nanomaterials dispersed in serum-rich culture media. The adsorption of such biomolecules on the surface of nanomaterials can alter their surface reactivity, thus influencing their size, stability in suspension and, most importantly, their interaction with cells. Consequently, in this study the effect of FBS on silica particle behaviour in cell culture media and on their toxicity potential upon treatment of skin cell lines has been investigated.

#### **2.2.5 Collaboration with partners to achieve the overall objectives of the NANODRUG consortium**

The NANODRUG consortium brings together six academic groups and two industrial teams as full partners, distributed over a total of six European Union member states. The consortium brings together groups with a very interdisciplinary expertise ranging from polymer synthesis and characterisation, computational modelling and physicochemical characterisation of materials to bioavailability, nanoparticles formulation, drug distribution and nanotoxicity, genetics, drug delivery and clinical dermatology. As part of researcher development, collaborations with consortium and external partners were one of the most important overall objectives of the programme, as a means to develop awareness of value of working together to benefit research and to maximise the potential for impact (i.e. publications).

## 2.3 Research Approach

The research approach taken for implementing the aims and objectives of the project is illustrated in **Figure 2.1**.

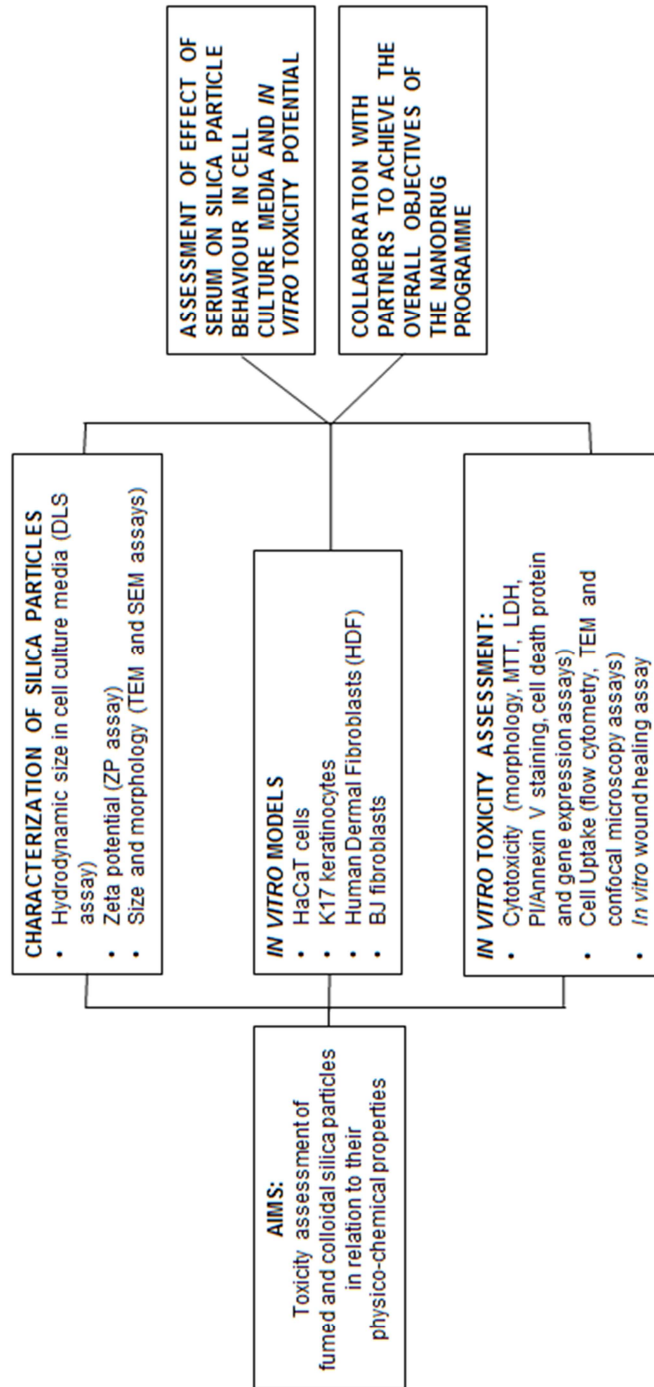


**Figure 2.1** An overview of the research approach used in this study.

## 3 MATERIALS AND METHODS

### 3.1 Materials

In this section, a list of the materials used in this study is provided for further reference. Each table summarises a specific materials category: nanomaterials, cell lines and related media/supplements, cell-based assay reagents. **Table 3.1** reports amorphous and colloidal silica particles purchased and used for this study.

**Table 3.1** Nanomaterials used in this study.

Material name	Supplier	Catalogue Number
SiNP7 (amorphous)	Sigma Aldrich	S5130
SiNP14 (amorphous)	Sigma Aldrich	S5505
SiNP20 (colloidal)	Sigma Aldrich	420875
SiNP70 (colloidal)	Postnova Analytics	Z-PS-SIL-GFP-0,07
SMP200 (colloidal)	Postnova Analytics	Z-PS-SIL-GFP-0,2
SMP500 (colloidal)	Postnova Analytics	Z-PS-SIL-GFP-0,5

**Table 3.2**, on the other hand, reports all the information regarding the cell lines used for the cell-based experiments, including the media and the supplements used for cell growth.

**Table 3.2** Cell lines, media and supplements.

Material name	Supplier	Catalogue Number
HaCaT cells	CLS (Germany)	CLS 300493
BJ Fibroblasts	ATCC (American Type Culture Collection)	BJ (ATCC® CRL-2522™)
HDF (Human Dermal Fibroblasts)	Gibco®	C-013-5C
K17	Queen Mary University	N/A
Phosphate Buffered Saline	Sigma Aldrich	P4417-100TAB
DMEM/F-12 medium	Gibco®	31330-038
Medium 106 (for HDF)	Gibco ®	M-106-500
EpiLife™ Medium (for K17)	Gibco®	M-EPI-500-CA
Fetal Bovine Serum	Gibco®	VX10108165
LSGS (supplement for Medium 106)	Gibco ®	S-003-10
HKGS (supplement for EpiLife Medium)	Gibco ®	S-001-5
Penicillin/Streptomycin 100UI/ml	Gibco®	15070-063
Trypsin/EDTA 10X	Gibco®	15400-054
Trypsin-EDTA 0.05%	Gibco ®	25300-054
Trypsin Neutralizer Solution (TNS)	Gibco®	R-002-100

**Table 3.3** reports the reagents used for the cell-based assays, such as cell viability, membrane damage, apoptotic cell death and fluorescent staining, as well as those used for molecular biology experiments.

**Table 3.3** Cell-based and molecular biology assay reagents.

<b>Material name</b>	<b>Supplier</b>	<b>Catalogue Number</b>
MTT reagent (3-(4,5-dimethylthiazol-2-yl)-2,5-diphenyltetrazolium bromide)	Sigma Aldrich	M2128-500MG
Dimethyl Sulfoxide	Sigma Aldrich	D5879-500ML
LDH assay kit	Sigma Aldrich	TOX7-1KT
Annexin V/FITC conjugate	Gibco®	APOAF-50TST
Propidium Iodide	Sigma Aldrich	P4170-10MG
RNeasy Mini Kit	QIAGEN	74104
QIAshredder	QIAGEN	79654
RT <sup>2</sup> First Strand Kit (12)	QIAGEN	330401
RT <sup>2</sup> SYBR Green ROX FAST Mastermix (12)	QIAGEN	330622
RT <sup>2</sup> Profiler™ PCR Array	QIAGEN	PAHS-212Z
PFA Stock Solution (10 ml, 16% in water)	Alfa-Aesar	43368
Draq7™	CST	#7406
Hoechst 33342	Invitrogen	H3570
ActinRed™ 555	Invitrogen	R37112
Vybrant AlexaFluor 594 Lipid Raft Labelling Kit	Invitrogen	V34405
Cell Proliferation Reagent (WST-1)	Roche	11-644-807-001
Apo-ONE Homogeneous Caspase 3-7 Assay	Promega	G7792

## 3.2 Characterization of Nanoparticles

Due to the importance and relevance of NMs characteristics in biological studies, they need to be subjected to physico-chemical characterization. Several techniques have been developed in order to analyze particle shape and size as well as size distribution and stability in solution. The most commonly used techniques include Dynamic Light Scattering (DLS), Zeta-Potential (ZP) and Electron Microscopy (EM) [97]. DLS is the most widespread light scattering technique, performing nano-scale characterization by analyzing patterns resulting from light scattered by particles moving under Brownian motion. ZP measures the relation between charge and flocculation for particles in a solution. EM, on the other hand, offers high resolution images of the particles within a sample, gathering information on both size and morphology [97, 98].

All these techniques have limitations and disadvantages: DLS has limited capability to analyze particles in polydisperse or heterogeneous systems; ZP results tend to be biased towards larger, higher scattering particles; EM requires time-consuming sample preparation. Consequently, in order for the data to be validated, these techniques should be used together when characterizing nanoparticles.

### 3.2.1 Dynamic light scattering (DLS)

Dynamic Light Scattering (DLS) has been a well-established method for the last 40 years. In monodispersed systems, it measures Brownian motion and relates it to the size of particles in a sample suspension. Brownian motion can be defined as the random motion of particles suspended in a fluid resulting from their collision with the quick-moving atoms and molecules in the gas or liquid which constitutes the sample fluid. Brownian motion is fundamental for DLS analysis because it allows the use of the Stokes-Einstein equation (**Equation 3.1**), which relates the velocity of a particle in solution to its hydrodynamic radius.

$$D = \frac{kT}{6\pi\eta\alpha}$$

- **D**: Diffusion velocity
- **k**: Boltzmann constant
- **T**: Temperature
- **η**: Viscosity
- **α**: Hydrodynamic radius

**Equation 3.1** The Stokes-Einstein equation.

The diffusion velocity in the Stokes-Einstein relation is inversely proportional to the radius of the particle; the random movement of the particles and the related movement speed are used to determine particle size. Larger particles move slower than smaller particles, therefore minimal movement and particle positions should be very similar. For smaller particles, on the other hand, the amount of movement and particle positions are very variable. Through analysis of the resultant exponential correlation function, particle size as well as dispersion index can be calculated [97, 98].

DLS systems are typically composed of six components (**Figure 3.1**) including laser, cell, detector, attenuator, correlator and computer. A laser (1) is used as the light source to illuminate the sample solution; while most of the laser beam will pass straight through the sample, a small portion is scattered by the particles in the solution. A cell (2) is used to allocate the sample inside the system. It can be made of different materials (plastic, glass, quartz) depending on the type of sample and the analysis to be performed. A detector (3) is used to measure the intensity of the scattered light. Even though it could be placed theoretically in every available position, as light from the sample scatters in all directions, detectors in DLS systems are normally positioned at either 173° or 90°. Moreover, for the detector to make a successful measurement, light must be within a specific energy range, in order to avoid overloading. Because of this, an attenuator (4) is used to regulate the intensity of the laser and therefore the



intensity of the scattering. A correlator (5) then translates the scattering intensity signal to a digital signal, which is then passed to a computer (6) where dedicated software will analyze the data and derive size information.

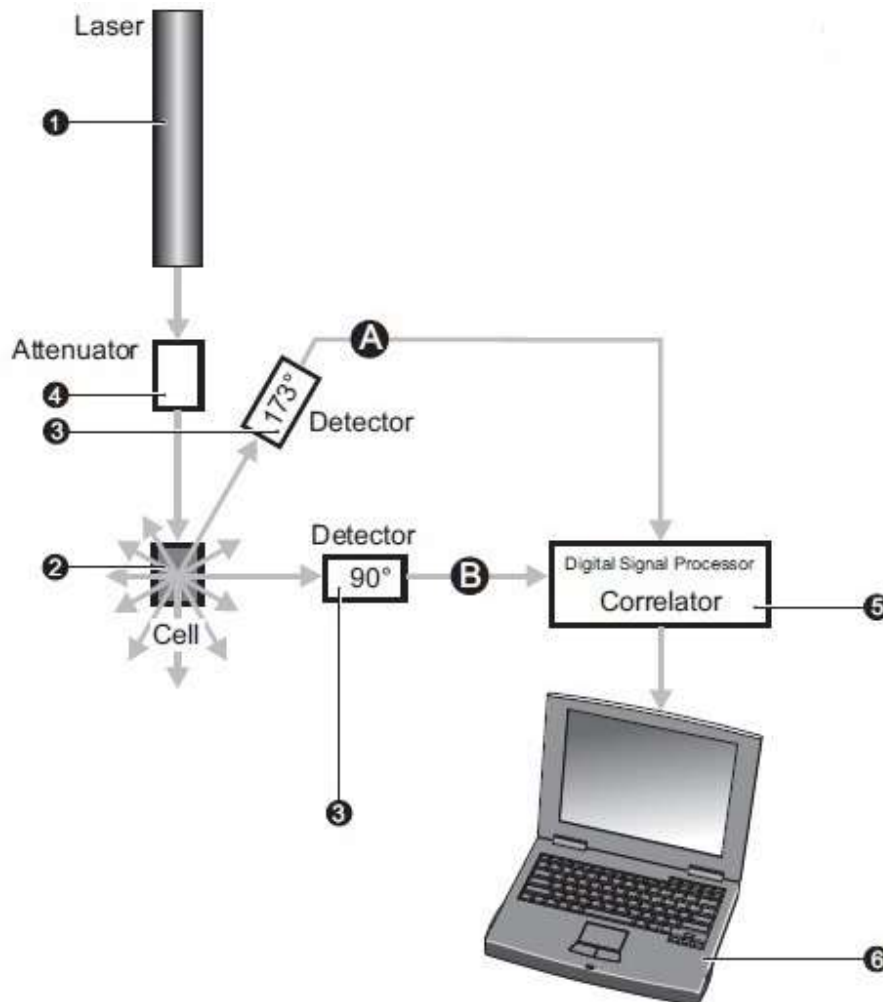


**Figure 3.1** The DLS measuring system has six components: a laser (1), a cell (2), a detector (3), an attenuator (4) a correlator (5) and a computer (6) (modified from [98] Malvern Zetasizer User Guide).

Within the instrument, the correlator plays the most pivotal role. It measures the degree of similarity between two signals over very short periods of time (microseconds and nanoseconds). Based on the values obtained, a correlation function of signals over time can be drawn, in which 1 = perfect correlation and

0 = no correlation. The measured intensity fluctuations are directly related to the movement of particles in solution, and are therefore directly related to the Stoke-Einstein equation described before. Consequently, the correlation function is directly related to particle size, as the intensity signal for smaller particles fluctuates more rapidly than for larger particles and as a result, the correlation decreases at a faster rate (**Figure 3.2**) [98].

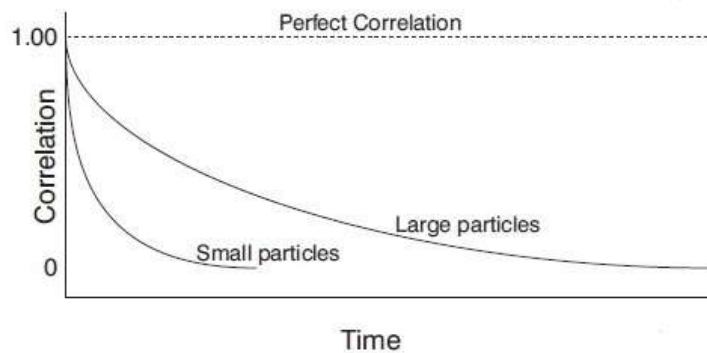


**Figure 3.2** The correlation function measures the similarity between signals over very short periods of time; the decay rate is directly related to particle size (modified from [98] Zetasizer User Guide).

After correlation function has been measured, algorithms inside the DLS system software will extract the decay rates for a number of size classes to produce a size distribution graph (**Figure 3.3**).

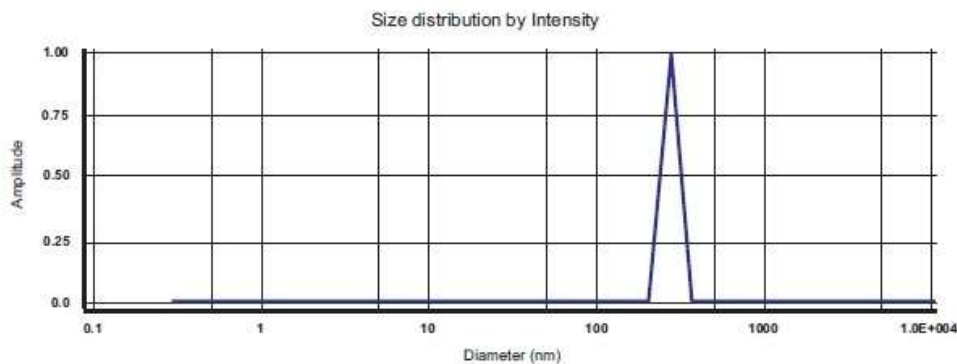


**Figure 3.3** Size distribution graph derived from the correlation function (modified from [98] Zetasizer User Guide).

Dynamic Light Scattering (DLS) was used to determine the particles size distribution and their dispersion pattern in DMEM/F-12, EpiLife™ and 106 media, which were used to culture different types of cells. The particles were diluted in the media at concentrations relevant to the study of nanoparticles effect on cells (10-200 µg/ml). To study the stability of the particles over time during incubation at temperatures relevant to cell culture and sample storage, only the top part of the nanoparticle solution was taken for DLS assay. Three or five measurements were made for each sample using Zetasizer (Malvern, Worcestershire, UK) at 25 °C with 173° detector. Before particle analysis, the DLS profiles of cell culture media were acquired for the presence of background molecule clusters, which could interfere with the samples measurement.

### **3.2.2 Zeta potential**

Zeta Potential (ZP) is a technique that determines whether the particles contained in a liquid tend to flocculate (agglomerate) or not. It is measured by performing an electrophoresis experiment and measuring the velocity of particle movement using Laser Doppler Velocity (LSV) in a sample when an electrical field is applied. The basic principle behind ZP can be viewed in **Figure 3.4**. The development of a net charge at the particle surface affects the distribution of ions in the surrounding interfacial region, resulting in an increased concentration of counter-ions close to the surface. This phenomenon can be described as electrical double layer, and exists around each particle inside the sample. The liquid layer surrounding the particles exists as two parts: an inner region (Stern layer), where ions are strongly bound, and an outer region (diffuse layer), where ions are much less attached. Part of the diffuse layer exists as a boundary (the surface of hydrodynamic shear or slipping plane) where ions and particles form a stable identity. As a direct consequence, when a particle moves, the ions within the boundary move with it, whereas ions outside the boundary do not travel with the particle. The potential inside the boundary is known as Zeta Potential [98].

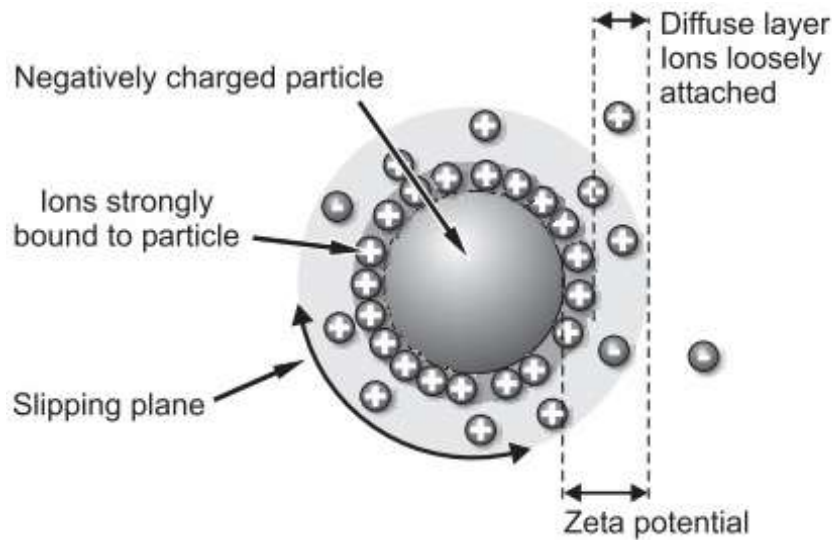


**Figure 3.4** The basic principle of zeta potential (modified from [98] Zetasizer User Guide).

Zeta potential (ZP) is particularly useful to get information on the potential stability of a colloidal system. A colloidal system can be defined as the fine dispersion of one of the three state of the matter (gas, liquid, solid) in one of the others. For ZP the two colloidal systems that can be measured are solid dispersed in liquid and liquid dispersed in liquid (emulsions). If all the particles in suspension have large negative or positive ZP they will repel each other, and therefore there will be no tendency to flocculate. However, if ZP levels are low, it means that there is no force to prevent the particles from coming together and flocculate. The general dividing line between stable and unstable suspensions is generally taken at either +30 mV or -30 mV; particles more positive than +30 mV or more negative than -30mV are generally considered stable [98].

An important consequence of the existence of electrical charges on the surface of particles is that they will exhibit electro-kinetic effects under the influence of an applied electrical field. Four different effects can be described depending on the way motion is induced:

- 1) Electrophoresis: movement of charged particles relative to their suspension liquid under the influence of an electrical field;

- 2) Electro-osmosis: movement of a liquid relative to a stationary charged surface under the influence of an electric field;
- 3) Streaming potential: electric field generated when a liquid is forced to flow past a stationary charged surface;
- 4) Sedimentation potential: electric field generated when charged particles move relatively to a stationary field.

As said before, for ZP measurements electrophoretic mobility is measured. To do so, a micro-electrophoresis system consisting of a cell equipped with a positive and negative electrode, where potential is applied, is used to load the sample inside the ZP system (**Figure 3.5**).

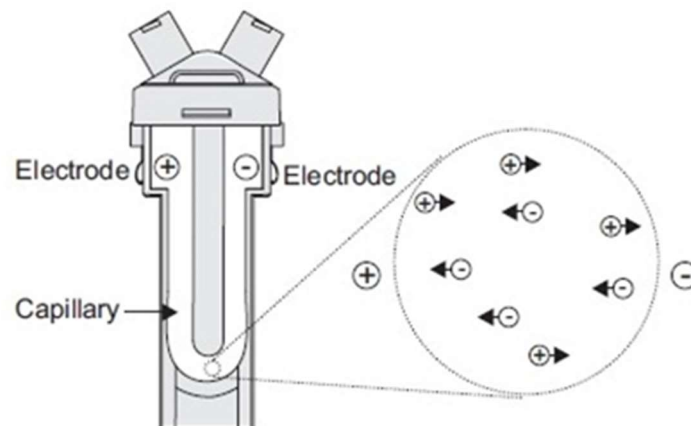


**Figure 3.5** The cell system used to measure zeta potential is equipped with a positive and negative electrode, where potential is applied (modified from [98] Zetasizer User Guide).

When an electric field is applied across an electrolyte, charged particles suspended in the electrolyte are attracted towards the electrode of opposite charge. Viscous forces acting on the particles tend to oppose this movement. When equilibrium is reached between these two opposing forces, the particles move with constant velocity [98].

The velocity of the particle is dependent on the following factors:

- Strength of electric field or voltage gradient;
- The dielectric constant of the medium;
- The viscosity of the medium;
- The zeta potential.

With this knowledge zeta potential of the particle can be obtained by application of the Henry equation (**Equation 3.2**), which is:

$$U_E = \frac{2\varepsilon z f(Ka)}{3\eta}$$

- **z** : Zeta potential;
- **U<sub>E</sub>** : Electrophoretic mobility;
- **ε**: Dielectric constant;
- **η**: viscosity;
- **f(K<sub>a</sub>)** : Henrys function. Two values are generally used as approximations for the f(K<sub>a</sub>) determination - either 1.5 or 1.0.

**Equation 3.2** The Henry equation.

Because electrophoretic determinations of zeta potential are commonly made in aqueous media and moderate electrolyte concentration, f(K<sub>a</sub>) approximation of 1.5 is normally used. This is referred as the Smoluchowski approximation; zeta potential calculations for systems that fit the Smoluchowski model is straightforward [98].

The system used to measure ZP is in practice very similar to the one used by DLS systems, and consists of seven components (**Figure 3.6**): a laser (1), used to provide the light source to illuminate the particles within the sample. For ZP measurements the light source is split, in order to provide an incident and a reference beam. A cell (2) holds the sample solution. When an electric field is applied to it, any particles moving will cause the intensity of the light detected to

fluctuate with a frequency proportional to the particle speed. A detector (3) sends the information to a digital signal processor (4) and then to a computer (5), where the system software produces a frequency spectrum from which ZP is calculated. As for the DLS system measurement, the scattered light must be in a specific range for the detector to make a successful measurement, therefore an attenuator (6) is used to regulate the intensity of the laser and the scattering. In order to compensate and correct any variations in the cell wall thickness and the dispersant refraction compensation optics (7) are installed within the scattering beam path in order to guarantee the alignment of the beams.

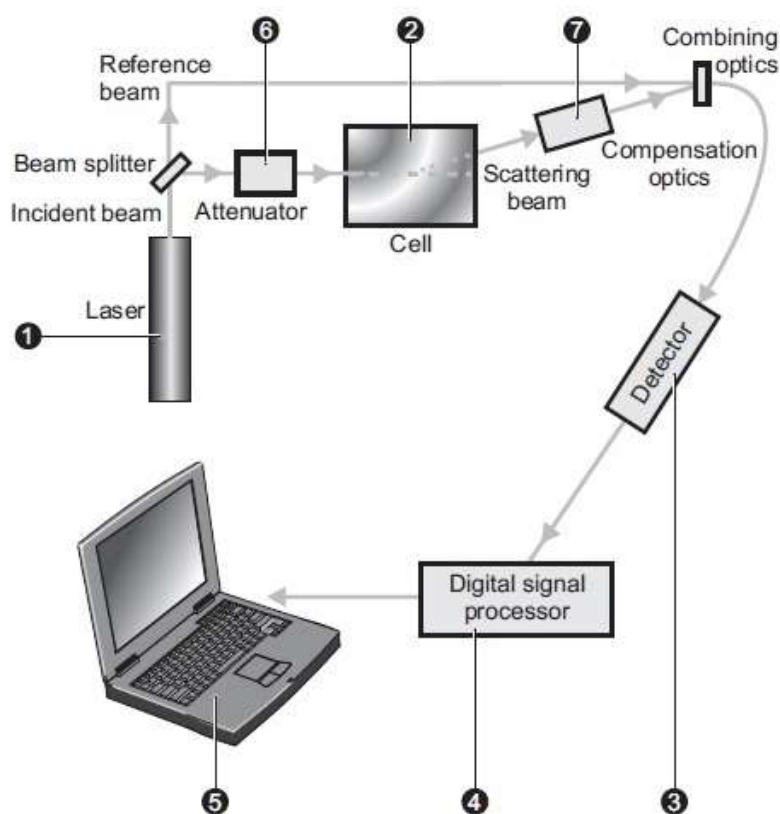


**Figure 3.6** A schematic version of the ZP measurement system including a laser (1), a cell (2), a detector (3), a digital signal processor (4), a computer (5), an attenuator (6) and compensation optics (7) (modified from [98] Zetasizer User Guide).

Zeta Potential was used to determine surface charge for colloidal silica particles. Each sample was dispersed in DMEM/F-12 medium with 10% FBS (CM-10%) and 0% FBS (CM) at 100 µg/ml for 24 h at 4°C (storage conditions) and analyzed with Zetasizer (Malvern, Worcestershire, UK). Five cycles of measurements were taken to derive an average zeta potential for each sample.

### **3.2.3 Electron microscopy (scanning electron microscopy and transmission electron microscopy)**

Electron microscopy (EM) over the years has proven an extremely valuable tool for several research applications, including nanomaterials analysis. It involves the use of a beam of electrons and a series of electric or electromagnetic fields to achieve higher resolution imaging compared to light or optical microscopes. Visible light, used by optical and light microscopes, makes it impossible to resolve points in an object closer together than a few hundred nanometers. Electrons, on the other hand, exhibit similar, albeit shorter wavelengths than those found in light. The various forms of electron microscopy have several areas of application [99, 100].

Transmission electron microscopy (TEM) is a stationary beam method applied to a wide range of materials (**Figure 3.7**). It is composed of an electron optical column, a vacuum system, lens for focusing and deflecting the beam, a high voltage generator for electron source, and control software. It typically comprises an operating console placed for the operator; the microscope may also be fully enclosed to reduce interference from environmental sources or operated remotely [100].



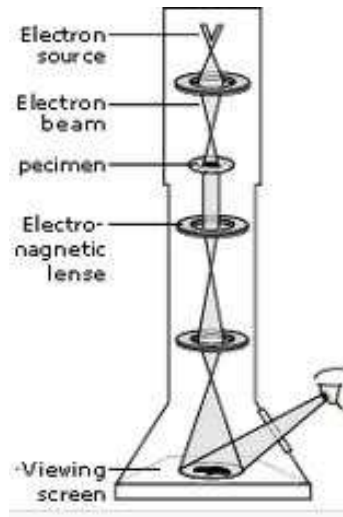


**Figure 3.7** The basics of TEM (from

<http://www.nobelprize.org/educational/physics/microscopes/tem/>).

The electron column includes elements analogous to those of a light microscope. The light source is an electron gun built into the column. The lenses used are electromagnetic lenses, which allow the focal length to be changed by changing the current through the lens coil. Instead of the eyepiece or ocular, a fluorescent screen and/or a digital camera are used by the operator. The electron beam emerges from the electron gun, and passes through the sample, transmitting electrons that are collected, focused, and projected onto the viewing device at the bottom of the column. The entire electron path from gun to camera must be under vacuum. As the electron beam emerges (on the downward side of the specimen), two other electronic lenses (electromagnetic fields) influence its path. First, a minutely focused objective lens spreads the concentrated beam created by the condenser lens. Then, a projector lens “captures” the resultant image, which is recorded on the fluorescent screen as a picture [100, 101]. TEM has proved invaluable to examine the ultrastructure of metals, as it is able to detect dislocations in the crystal lattice fairly easily; it’s been equally useful in life sciences applications, for examining plant, bacteria or animal tissue. One limitation of the TEM is that samples need to be very thin, otherwise electrons are scattered or absorbed rather than transmitted. In order

to be able to examine relatively thick samples, scanning electron microscope (SEM) was developed [100, 101, 102].

SEM (**Figure 3.8**) is the most popular of the microscopic techniques due to the simplicity of interpretation of most of the images and the ease of specimen preparation. In SEM, electrons are focused in a small-diameter spot on the sample surface; said focused spot is then used to scan in two perpendicular directions, thus covering a specific area. The intensities of the signals created by the interactions between the beam electrons and the sample are measured and then mapped as variations in brightness on the image display. The secondary electron (SE) signal is the most frequently used signal. It varies with the topography of the sample surface much like an aerial photograph: edges are bright while recesses are dark. The ratio of the size of the displayed image to the size of the area scanned on the specimen gives the magnification [100, 101]. In SEM, the optical column is shorter than TEM, as the only lenses needed are those above the sample used to focus the electrons into a fine spot on the sample surface. The sample chamber, however, is larger because the SEM technique does not impose any restriction on specimen size other than chamber size. The electron gun and lenses are similar to those of a transmission electron microscope [100, 102].

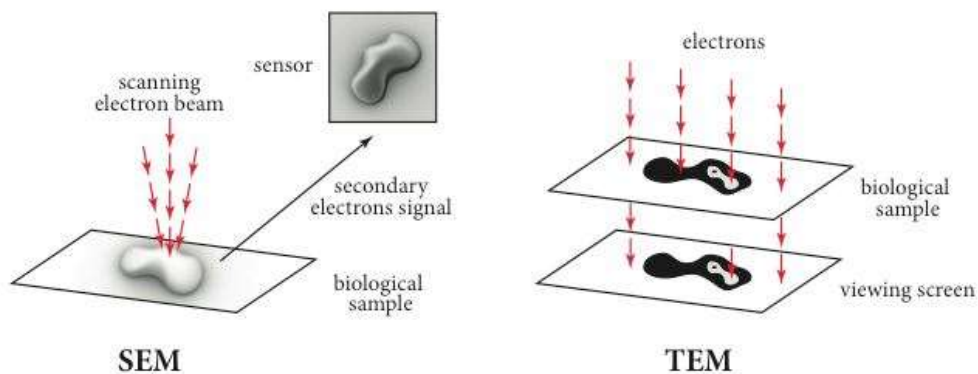


**Figure 3.8** The difference between SEM and TEM (from <http://bsp.med.harvard.edu/node/221>).

To summarize, the most important differences between a transmission electron microscope and a scanning electron microscope are:

- While TEM uses a broad static beam, the SEM beam is focused to a fine point and scans line by line over the sample surface in a rectangular pattern;
- Voltages are much lower in SEM than in TEM because sample penetration is not necessary;
- In SEM, the sample does not need to be thin, thus simplifying specimen preparation.

Scanning Electron Microscopy (SEM) and Transmission Electron Microscopy (TEM) were used to establish silica particles morphology structure and distribution in water. Each sample was dispersed in deionized water at a concentration of 10-25 µg/ml. For SEM imaging, a drop of each sample suspension was placed on a silicon chip, dried in air, and coated with Au/Pd or carbon. For TEM imaging, a drop of the sample suspension was placed on a carbon-formvar coated grid and dried in air. Each sample was then analyzed at different magnifications using Philips XL30 SFEG SEM and Philips CM20 TEM (Philips, Netherlands).

### **3.3 Cytotoxicity Assessment**

#### **3.3.1 Cell lines used for the assays**

Thousands of different cell lines, either primary or immortalized, have been derived from human tissues throughout the years depending on the intended use. Whereas primary cells are normally isolated from tissue and then proliferated and sub-cultured for a specific amount of time, immortalized cells can proliferate indefinitely. Immortalized cells are generally obtained by virus-mediated genome modification or by isolation of cells from tumorigenic tissue, which makes them more prone to malignancy and related problems [103].

An exception is represented by HaCaT cells, a line developed at the end of the Eighties by the Cancer Research Center in Heidelberg. Instead of using viruses such as SV40 for immortalization, Petra Boukamp and her research group used a method based on temperature and calcium levels to achieve immortalization without inducing tumorigenic effects. Full thickness human body skin was obtained from the distant periphery of a melanoma located on the upper half of the back of a 62-year old male patient. Cells were then isolated from tissue, suspended in MEM medium with low levels of Ca<sup>2+</sup> and sub-cultured at 38.5 °C in order to increase cell proliferation. The first subculture, after reaching confluency, was split with a high cell density ratio (1:2) for the following three passages. By the fourth passage, density was no longer critical and the resulting cell line was designated 'HaCaT' to denote its origin from human keratinocytes and the growth conditions used to establish it. After the fourth passage, proliferation continued steadily, allowing the researchers to passage the cells for over 140 times, becoming completely independent from Ca<sup>2+</sup> and temperature levels after the tenth passage [104]. Because they are characterized by an altered phenotype, though without tumorigenic effects, after their development HaCaT cells have been used for different applications, from 3D skin grafting to *in vitro* toxicity evaluation.

Because of their properties, as well as being an established model for *in vitro* keratinocyte studying, HaCaT cells were chosen as the main cell line to use for this study. In order to gain additional information on comparison between other skin cell lines, three additional lines were chosen to perform experiments on cell viability, apoptosis and morphology studies: BJ fibroblasts, Human Dermal Fibroblasts (HDF) and K17 keratinocytes. The BJ cell line was first obtained in the Nineties from the foreskin of a healthy new-born male. They have a normal diploid karyotype, and can be cultured up to 70 passages. They are not immortalized, and are telomerase negative. BJ cells have been used for different studies in cellular and molecular biology, especially for telomerase studies as well as transfection host [105, 106]. Human Dermal Fibroblasts (HDF) is a primary cell line purchased from Gibco® derived from adult skin (single donor), capable of at least 12 doublings [107]. K17 keratinocytes were

kindly provided by Prof. David Kelsell (Queen Mary University of London – Centre for Cell Biology and Cutaneous Research). The cells were prepared following the protocol by Storey et al. [108].

### **3.3.2 Cell culture**

As said before (see Introduction) cell culture can be defined as the mechanical or enzymatic dispersion of tissue followed by the propagation of the resulting cells as a suspension or attached monolayer. Cell cultures have lost their histotypic architecture, and often the associated biochemical properties; therefore, they do not reach a steady state unless specific conditions are achieved. These specific conditions mainly involve a surface where cells can attach and spread (the substratum) and, most importantly, a diffuse environment that must supply all the essential nutrients for cell metabolism, proliferation and cell growth (the medium). To mimic *in vivo* conditions and achieve physiologically balanced growth-promoting and growth-inhibiting activities, animal serum is frequently added, as it contains low and high molecular weight compounds such as albumin, cholesterol, cortisone, endotoxin, glucose, thyroxine, haemoglobin, insulin, and triiodothyronine.

For HaCaT cells and BJ fibroblasts, cells were suspended in DMEM/F-12 culture medium supplemented with 10% FBS and antibiotics (penicillin 100 units/ml, streptomycin 100 µg/ml), then seeded at a density of  $5 \times 10^5$  cells/cm<sup>2</sup> in flasks and incubated at 37°C in a humidified atmosphere with 5% CO<sub>2</sub> and 95% air. The cells were sub-cultured every 3 days by trypsinisation with trypsin coupled with ethylene diamine tetra acetic acid (trypsin-EDTA).

For K17 keratinocytes, cells were suspended in Epilife™ culture medium supplemented with antibiotics (penicillin/streptomycin 5000U/ml) and HKGS (Human Keratinocyte Growth Supplement), an ionically-balanced supplement containing bovine pituitary extract (BPE), recombinant human insulin-like growth factor-I, hydrocortisone, bovine transferrin, and human epidermal growth factor. Cells were then seeded at a density of  $5 \times 10^5$  cells/cm<sup>2</sup> in flasks and incubated

at 37°C in a humidified atmosphere with 5% CO<sub>2</sub> and 95% air. The cells were sub-cultured every 4-5 days by trypsinisation with trypsin coupled with ethylene diamine tetracetic acid (trypsin-EDTA).

For HDF fibroblasts, cells were suspended in Medium 106 culture medium supplemented with antibiotics (penicillin/streptomycin 5000U/ml) and LSGS (Low Serum Growth Supplement), a solution containing foetal bovine serum, basic fibroblast growth factor, heparin, hydrocortisone, and epidermal growth factor. Cells were then seeded at a density of  $3 \times 10^5$  cells/cm<sup>2</sup> in flasks and incubated at 37°C in a humidified atmosphere with 5% CO<sub>2</sub> and 95% air. The cells were sub-cultured every 4-5 days by trypsinisation with trypsin coupled with ethylene diamine tetra acetic acid (trypsin-EDTA).

### **3.3.3 Cell viability and membrane damage assays**

The reduction of tetrazolium salts from weakly colored aqueous solutions to brightly colored derivatives known as formazans has been the basis of many biochemistry applications for more than half a century. This widespread application is due to the unique physico-chemical properties of these compounds, which depends on the positively charged quaternary tetrazole ring core containing four nitrogen atoms surrounded by three variable aromatic structures usually containing phenyl groups (**Figure 3.9**). This variability has generated several tetrazolium compounds with different properties, which have been used both qualitatively and quantitatively for many biological measurement systems. All these compounds have a common chemistry principle, which involves a mild reduction reaction; as a direct consequence, the tetrazole ring inside the compound is displaced, prompting the transformation into colored formazan salts [109].

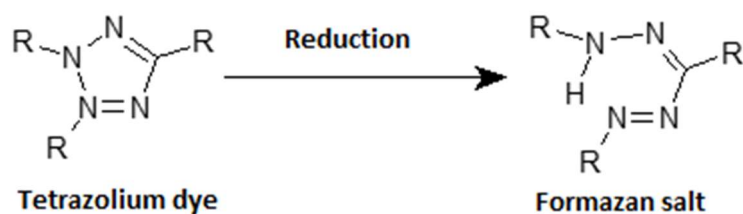


**Figure 3.9** The general structure of the tetrazolium dyes and the formazan salts.

There are two categories of tetrazolium salts. The first one, which includes 3-(4,5-dimethylthiazol-2-yl)-2,5-diphenyltetrazolium bromide (MTT), forms insoluble formazan salts upon reduction by NAD(P)H-dependent oxidoreductases and hydrogenases of metabolically active cells. In order for the assay to be measurable, the salts must be solubilized using solvents such as DMSO or acidified isopropanol. The second one, which comprises WST-1, does not require any kind of stabilization of the medium in the sample, as the formazan salt that is formed is soluble. This difference in the two categories is given by the aromatic variable groups in each compound: whereas MTT has a positively charged moiety, which improves lipophilicity and gives it the ability to form large needle-like structures inside the cell/tissue, WST-1 and the related compound have their phenyl moieties capped with negatively charged sulfonate groups, which improves solubility but also hinders movement ability of these compounds across cell membranes (**Figure 3.10**) [110].

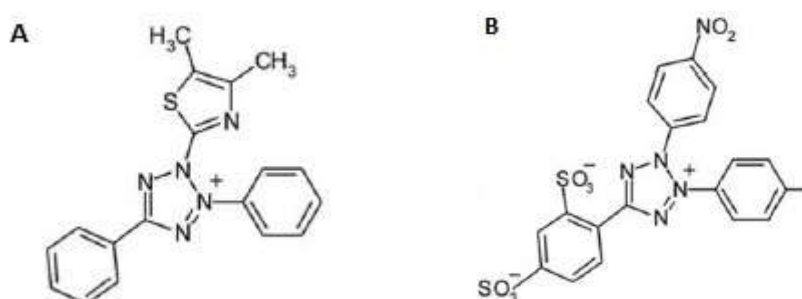


**Figure 3.10** The structures of MTT (A) and WST-1 (B).

Because of this difference, MTT and WST-1 reaction location inside cells is different; whereas MTT is readily internalized by exploiting the plasma membrane potential and reduced intracellularly, WST-1 is reduced at the cell surface because of its poor penetration capability. **Figure 3.11** shows a schematic representation of the two different mechanisms of action: whereas MTT is reduced intracellularly by NADH, WST-1 is reduced by trans-plasma membrane electron transport (via electron carrier 1-methoxyPMS) using NADH derived from the TCA cycle as a reducing agent.

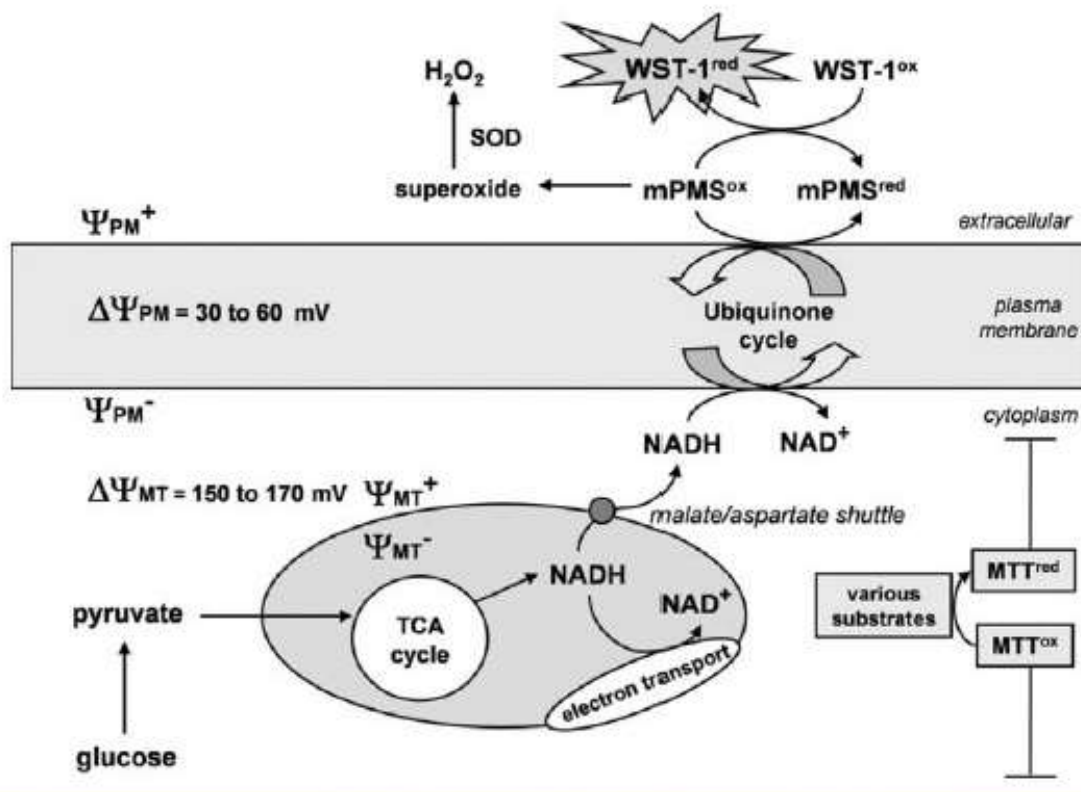


**Figure 3.11** The mechanism behind MTT and WST-1 reduction by cells (modified from [109] Berridge et al., 2005).

In practice, both assays involve the use of microplates, where cell proliferation is measured under the assumption that dye reduction will be proportional to the number of viable cells in the exponential growth phase [109]. The general purpose of these assays is to measure viable cells in a relatively high-



throughput way (96-well plates) without the need for elaborate cell counting. The most common use is the measurement of the cytotoxicity of drug at several concentrations, with the results expressed against IC<sub>50</sub>, the concentration needed to inhibit growth in 50% of cell population, or LD<sub>50</sub>, (LD stands for lethal dose), the amount of a material needed to kill 50% of the cell population [110, 111].

For this work, MTT has been used to measure viability in HaCaT keratinocytes and BJ fibroblasts, while WST-1 has been used on K17 keratinocytes and HDF fibroblasts. For MTT assay cells were seeded at a density of  $1 \times 10^4$  cells/well in 96-well plates and cultured in full medium until 70% confluency was reached. The medium was then replaced with 200  $\mu$ l of silica particle suspension at 10-200  $\mu$ g/ml. Cells incubated with particle-free culture medium were used as control. After 24 h treatment, cells were washed twice with PBS. The plate was then incubated with 100  $\mu$ l of MTT [3-(4, 5-Dimethylthiazol-2-yl)-2, 5-diphenyltetrazolium bromide] solution (1 mg/ml) for 2 h at room temperature in the dark. The formazan salt crystals were solubilised with 100  $\mu$ l of DMSO. After 20 minutes further incubation at room temperature, the absorption was recorded using a Thermo Scientific Varioskan plate reader (Thermo Fisher Scientific, US) at a wavelength of 570 nm. For WST-1, cells were seeded at a density of  $2 \times 10^4$  cells/well in 96-well plates and cultured in full medium until 70-80% confluency was reached. The medium was then replaced with 100  $\mu$ l of silica particle suspension at 10-200  $\mu$ g/ml. Cells incubated with particle-free culture medium were used as control. After 24 h treatment, the plate was treated with 10  $\mu$ l of WST-1 for 4 h at 37 °C, then read using a Thermo Scientific Varioskan plate reader (Thermo Fisher Scientific, US) at 450 nm (sample reading) and 600 nm (background reading).

Another important assay for studying the interaction between nanomaterials and cells is the LDH assay. Lactate dehydrogenase, also known as LDH, is an oxidoreductase enzyme found extensively in body tissues that catalyzes the interconversion of lactate and pyruvate (**Figure 3.12**).

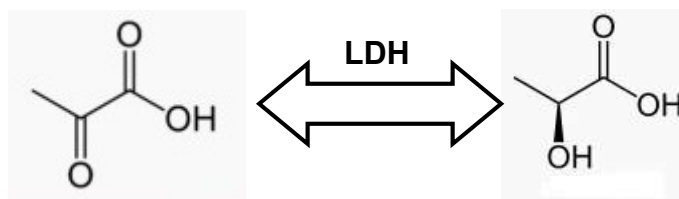


**Figure 3.12** The LDH enzyme catalyzes the interconversion between pyruvate (left) and lactate (right).

When cells are lethally injured, LDH is released in the surrounding external medium. Because LDH is a fairly stable enzyme, its release can be measured as a marker for necrotic cell death by using NAD, which is reduced to NADH by LDH in a reaction that can be detected colorimetrically (450 nm) [112].

For this study, HaCaT cells were prepared and treated as described for MTT assay. After treatment, 50% of supernatant from each well was transferred from each well to a new plate, where it was treated with 100  $\mu$ l LDH reagent for 20 minutes at room temperature. LDH release was then detected using Thermo Scientific Varioskan plate reader (Thermo Fisher Scientific, US) at 490 nm. A background reading was taken at 690 nm as instructed by the manufacturer; the final value was obtained by subtracting the reading at 690 nm from the reading at 490 nm. The cells remained attached and were used for MTT assay as described above.

Beside LDH release, membrane damage can be assessed by using propidium iodide (PI). Propidium iodide has the ability to stain the nucleus of membrane-compromised cells only, as it is membrane-impervious and generally excluded from viable cells. After treatment of both K17 keratinocytes and HDF with colloidal silica 10-200  $\mu$ g/ml for 24 hours, PI at 5  $\mu$ g/ml was added to the wells and incubated for 20 minutes at room temperature. Untreated cells were used as negative control, while cells incubated with Triton X-100 0.025% for 15 minutes were used as positive control. Triton X-100 was chosen as positive control because it is widely used to lyse cells or to permeabilize the membranes of living cells. After treatment with PI, cells were washed with PBS and fixed using a solution of paraformaldehyde 4%. The nuclei were then stained with

Hoechst 33342 at 0.1 mg/ml for 10 minutes at room temperature. For cell counting, a wide field fluorescence microscope (Zeiss Axiovert; Jena, Germany) was used. Image acquisition and post-acquisition analysis were performed using Morphostrider software (Exploranova; La Rochelle, France). Using an objective 10x, images were acquired using the adequate filter cubes for Hoechst and PI. Sixteen fields (840.4 x 640.3  $\mu\text{m}$ ) per well were acquired in order to image a large surface of the well. In the post-analysis process, both Hoechst- and PI-labeled cells were counted and the ratio of the number of PI-labeled cells versus the number of Hoechst-labeled cells was calculated.

### **3.3.4 Phase contrast microscopy for cell imaging**

Phase contrast is an optical contrast technique for making unstained phase objects visible under an optical microscope. Cells that appear inconspicuous and transparent in bright field can be viewed in high contrast and rich detail using a phase contrast microscope. This technique finds several applications, the main one consisting of producing high-contrast images of transparent samples, such as living cells (usually in culture), microorganisms, thin tissue slices, lithographic patterns, fibers, latex dispersions, glass fragments, and subcellular particles (including nuclei and other organelles). The technique of phase contrast microscopy was developed in the 1930s by the Dutch physicist Frits Zernike. After the technique was brought into use in 1942, Zernike was awarded the Nobel Prize in Physics in 1953 [113, 114].

The phase contrast microscope (Figure **3.13**) uses the fact that the light passing through a transparent part of the sample travels slower and therefore is shifted compared to the uninfluenced light. This difference in phase is not visible to the human eye; however, the change in phase can be increased to half a wavelength by a transparent phase-plate in the microscope, thereby causing a difference in brightness making the transparent object shine out in contrast to its surroundings [115].

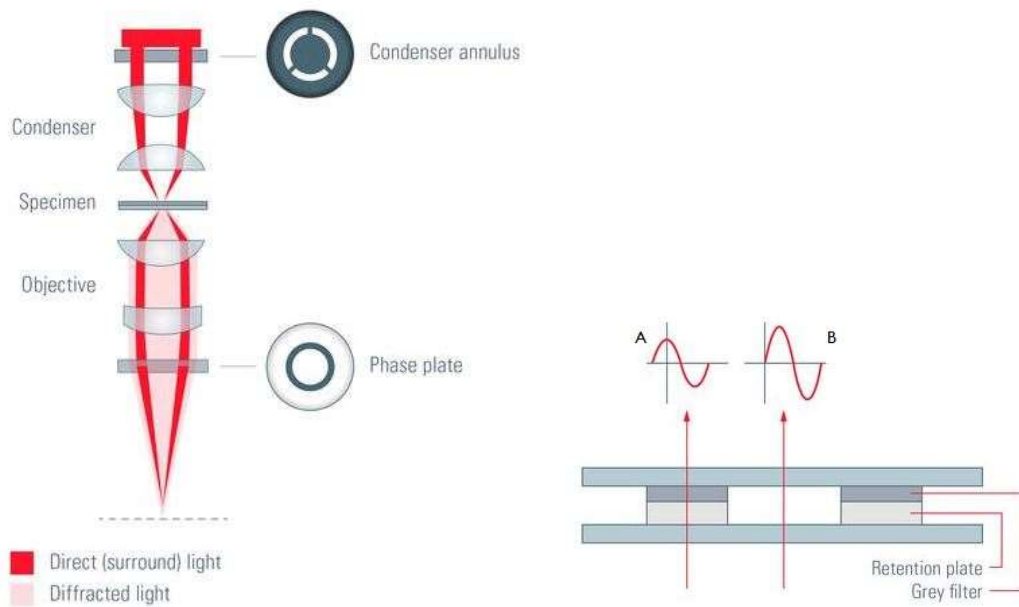


**Figure 3.13** The structure of a phase contrast microscope and its phase ring. The portion of light that passed the specimen without experiencing diffraction passes the phase ring (A), whereas the retention plate retards the phase of the non-diffracted light to allow interference with the light waves that experienced phase shift and diffraction by passing the sample (B) (from [113] <http://www.leica-microsystems.com/science-lab/phase-contrast/>).

The key elements of a phase contrast microscope are the condenser annulus (1) and the phase plate (2). The condenser annulus is placed in the front focal plane of the condenser and limits the angle of the penetrating light waves. The phase plate lies in the back focal plane of the objective and has a phase ring made of a material that dims the light passing through it and changes its phase by modifying the light's wavelength ( $\lambda$ ) by  $\lambda/4$ . The ring shaped light that passes the condenser annulus is focused on the specimen by the condenser. Portions of the ring shaped light are diffracted by optically dense structures of the specimen (e.g. plasma membranes, organelles etc.) and experiences a phase shift of approximately  $\frac{1}{4} \lambda$  (usual for biological specimen). This phase shifted/diffracted light bypasses the phase ring and is hardly affected by it. The phase ring is a central component of a phase contrast microscope, usually located in the rear focal plane of the objective. Composed of a grey filter and a

retention plate; the grey filter dims the light to avoid irradiation, the retention plate retards the phase of the non-diffracted light to allow interference with the light waves that experienced phase shift and diffraction by passing the specimen. The portion of light that passes the sample without experiencing diffraction passes the phase ring. In contrast, the direct ring shaped light from the condenser annulus will hit the phase ring, which will dim the direct light and cause a phase shift (usually advanced by  $\frac{1}{4} \lambda$  or retarded by  $\frac{3}{4} \lambda$  for positive phase contrast). As the total phase shift between the light refracted by the sample and the light that passed the phase ring will be up to  $\frac{1}{2} \lambda$ , destructive interference will occur. Optically dense structures will consequently appear darker (in positive phase contrast) [113, 114, 115].

Cell morphology was examined before and after treatment with colloidal silica particles 25-100  $\mu\text{g/ml}$  in medium with 10% FBS (CM-10%) and 0% FBS (CM) at 24 hours. Phase contrast cell images were taken at 20X magnification using Leica DFC 295.

### **3.3.5 Flow cytometry assays for cell uptake of particles and apoptosis assay**

Flow cytometry is a technology that simultaneously measures and analyzes multiple physical characteristics of single particles (cells) as they flow in a fluid stream through a collimated beam of light, usually a laser. The measured properties include size, granularity (internal complexity), and relative fluorescence intensity. A flow cytometer is made up of three main systems: fluidics, optics, and electronics. The fluidics system transports particles in a stream to the laser beam for interrogation; the optics system consists of lasers, which illuminate the particles in the sample stream, and optical filters, which direct the resulting light signals to the appropriate detectors; the electronics system converts the detected light signals into electronic signals that can be processed by the computer [116]. In the flow cytometer, particles carried through the laser intercept scatter laser light. The extent of light scatter depends on the physical properties of the particle measured, namely its size and internal

complexity. For cellular samples, affecting factors are also the cell membrane, the nucleus, and any granular material inside the cell. Cell shape and surface topography also contribute to the total light scatter. Forward-scattered light (FSC) is proportional to cell-surface area or size. FSC is a measurement of mostly diffracted light and is detected just off the axis of the incident laser beam in the forward direction. FSC provides a suitable method of detecting particles greater than a given size independent of their fluorescence. Side-scattered light (SSC), on the other hand, is proportional to cell granularity or internal complexity. SSC is a measurement of mostly refracted and reflected light that occurs at any interface within the cell where there is a change in refractive index. SSC is collected at approximately 90 degrees to the laser beam by a collection lens and then redirected by a beam splitter to the appropriate detector. Correlated measurements of FSC and SSC can allow for differentiation of cell types in a heterogeneous cell population [116].

Flow cytometry was used to detect cellular uptake of particles and study cell necrosis and apoptosis. Measurement of nanomaterials cell uptake by flow cytometry is relatively easy, as the only requirement is the use of fluorescent labeled samples. The particles inside of cells will react with the lasers inside the cytometer system; however, no quantitative or uptake mechanism information can be gained using this technique.

This technique could also provide information on cell death mechanisms, such as necrotic or apoptotic cell death. Whereas apoptosis is accompanied by water loss, cell shrinkage, and nuclear fragmentation, necrosis is characterized by rapid cytoplasmic swelling, plasma membrane rupture and organelle breakdown. Consequently, apoptotic and necrotic cells differ in light scatter patterns; apoptotic cells give lower forward scatter and higher side scatter values than viable cells, reflecting the smaller size and different nucleus/cytoplasm consistency. Apoptosis has been characterized by different criteria, such as caspase activation and, most importantly, different kinetics of phosphatidylserine (PS) exposure on the plasma membrane [117]. PS is an important component of the cell membrane; normally restricted to the inner

leaflet of the membrane, it moves transversely across the bilayer to the outer leaflet of the plasma membrane. Phosphatidylserine exposure has several potential biological consequences, most importantly as the basis to detect apoptotic cell death. Annexin V is a  $\text{Ca}^{2+}$  dependent phospholipid-binding protein with high affinity for PS; as a direct consequence, this protein can be used as a sensitive probe for apoptotic cell death. As translocation of PS to the external cell surface is not unique to apoptosis, but occurs also during necrosis, analysis has to be performed in conjunction with a dye to establish integrity of the cell membrane. To do so, Annexin V, properly conjugated with FITC for cell staining evaluation, is used to treat cells together with Propidium Iodide. Whereas Annexin V binds to phosphatidylserine in the membrane of cells, PI binds to the cellular DNA in cells where the cell membrane has been compromised, thus providing discrimination between apoptosis and necrosis [116, 117, 118].

To measure particle uptake, HaCaT cells were seeded in 24-well plates at  $5 \times 10^4$  cells/well overnight, then incubated with FITC-labelled SiNP7, SiNP14, SiNP70, SMP200, SMP500 in CM-10% and CM for 24 h, then collected by trypsinization and centrifugation. The data containing 10000 events were acquired and displayed as side scattering (SSC) vs forward scattering (FSC) to distinguish intact cells from debris, using BD Accuri C6 Flow Cytometer (BD, San Jose, CA, USA). The intact cells were then analyzed for FITC intensity using the Accuri C6 software. The difference of FITC intensity between cells indicates the difference in silica particles uptake.

For necrosis and apoptosis detection, cells were seeded and treated in the same conditions as for particle uptake. The cells were then re-suspended in PBS containing Annexin V-FITC (0.025 mg/ml) and propidium iodide (0.01 mg/ml), and incubated at room temperature for 10 minutes in dark. Cell viability and apoptosis were quantified using the BD Accuri TM C6 Flow Cytometer (BD, San Jose, CA, USA). The data containing at least 10000 events were acquired and displayed as SSC vs FSC to distinguish intact cells from debris. The intact cells were then further analyzed for FITC and PI intensity, respectively, to

quantify apoptotic and necrotic cell death. The maximum intensity of PI and FITC obtained from 90% of cells without particle treatment were set to distinguish PI positive, FITC positive and PI/FITC double positive cells. Cells with FITC and PI double negative staining were designated as healthy cells, PI positive and FITC negative as necrotic cells, PI negative and FITC positive as early apoptotic cells, PI and FITC double positive as late apoptotic cells.

### **3.3.6 TEM imaging for cellular uptake**

As described before, the size of nanoparticles allows them to pass through biological barriers and enter cells. As this may result in permanent cell damage, the quantitative study of the relationship of NPs internalization, cellular location and cytotoxicity is crucially important and can be achieved by utilization of Transmission Electron Microscopy (TEM). *In vitro*, the results of cell imaging are often qualitatively compared to cell line responses measured by standard viability and genotoxicity assays. However, effective quantification of the real number of particles internalized by the cells remains quite challenging, as well as time and cost consuming [119, 120]. For sample preparation, employing resin embedding with only chemical fixation (including osmium tetroxide) enables visualization of the main cellular structures without contrast from the NPs themselves being obscured by heavy metal stains, allowing easy NPs localization. Quantification of NP uptake within thin sections of cells is also possible, however random sampling procedures or correlation to higher throughput techniques are required to measure a population of whole cells [121].

For this study, HaCaT cells were seeded in a 6-well plate at  $3 \times 10^5$  cells/well, cultured overnight and then treated with colloidal silica at 25  $\mu\text{g}/\text{ml}$  for 24 h. Each sample was then scraped from the plate, fixed with 2% glutaraldehyde in 0.1 M sodium cacodylate buffer (pH 7.4), and kept at 4°C for 24 h. Cells were then postfixed with 1% osmium tetroxide /1% potassium ferrocyanide for 1 hour at room temperature and stained en bloc with 5% aqueous uranyl acetate overnight at room temperature, dehydrated, and embedded in Taab epoxy resin



(Taab Laboratories Equipment Ltd., Aldermaston, UK). Ultrathin sections were stained with lead citrate and recorded using a Megaview 3 digital camera and iTEM software (Olympus Soft Imaging Solutions GmbH, Münster, Germany) in a Jeol 100-CXII electron microscope (Jeol UK Ltd., Welwyn Garden City, UK).

### 3.3.7 Confocal microscopy

Confocal microscopy has proved to be a quite popular technique in recent years, as it allows getting high-quality images from samples prepared for conventional fluorescence microscopy. It is proving to be one of the most important advances ever achieved, with a growing number of applications in cell biology for both fixed and living cells and tissues. Compared with conventional optical microscopy, confocal microscopy offers several advantages:

- Ability to control depth of field;
- Elimination or reduction of background information away from the focal plane (that leads to image degradation);
- Capability to collect serial optical sections from thick specimens.

The basic key is the use of spatial filtering techniques to eliminate out-of-focus light or glare in samples whose thickness exceeds the immediate plane of focus [122]. In a confocal microscope, light emitted by an excitation source, usually a laser system, passes through a pinhole and an excitation filter before being reflected by a dichromatic mirror and scanned across the sample. As a consequence, secondary fluorescence is emitted from points on the sample (in the same focal plane) and passed back through the dichromatic mirror; the fluorescence then passes through a second pinhole aperture positioned in front of the detector (a photomultiplier tube) (**Figure 3.14**).

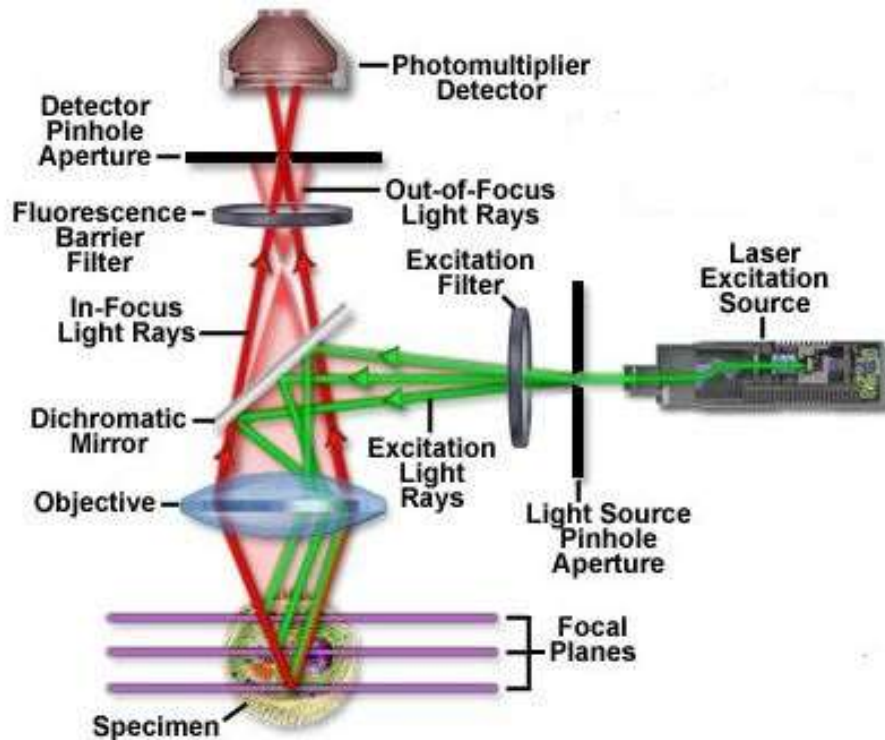


**Figure 3.14** The basic structure of a confocal microscope (modified from [122] <http://www.olympusfluoview.com/theory/confocalintro.html>).

The significant amount of fluorescence emission that occurs at points above and below the objective focal plane is not confocal with the pinhole and forms extended airy disks in the aperture plane. Because only a small fraction of the out-of-focus fluorescence emission is delivered through the pinhole aperture, most of this extraneous light is not detected by the photomultiplier and does not contribute to the resulting image [122, 123].

The primary advantage of laser scanning confocal microscopy is the ability to produce serially thin optical sections through fluorescent sample restricted to a well-defined plane. Contrast and definition are dramatically improved due to the reduction in background fluorescence. With most modern confocal microscopies, sections are not restricted to the x-y plane, but can also be collected in vertical sections in the x-z and y-z planes (parallel to the microscope optical axis). In practice, vertical sections are obtained by combining a series of x-y scans taken along the z-axis, and then projected in a

view of fluorescence intensity, as it would appear should the microscope hardware have been capable of physically performing a vertical section. In complex samples, interconnected structural elements can be difficult to discern; however, once a sufficient number of sections has been gathered, they can be further processed into a three-dimensional representation using computational techniques. This approach is now in common use to help elucidate the numerous interrelationships between structure and function of cells and tissues in biological investigations [122, 123].

In order to gain additional information on particle localization inside different cell lines,  $2 \times 10^4$  HDF fibroblasts and K17 keratinocytes were seeded in 8-well chamber slides (Ibidi, Germany) and cultured until confluency at 37 °C. Treatment with SiNP70, SMP200 and 500 at 10 µg/ml was then carried out for 2 and 24 h at 37 °C. After incubation the particles were removed and the cells first fixed with 4% PFA (Alfa-Aesar, Germany) for 15 minutes, than stained with ActinRed and Hoechst 33342 by incubating the cells for 30 minutes and 10 minutes respectively. Visualization of the samples was performed using Zeiss LSM510 laser scanning confocal microscope equipped with 4 lasers (405 nm violet diode; 458/477/488/514 nm 4-line Argon; 543 nm HeNe; 633 nm HeNe). Images were acquired using the objective Plan Apochromat 63x/1.4 Oil DIC and the following laser excitation and emission filters settings (**Table 3.4**):

**Table 3.4** Excitation/Emission outputs of the fluorescent dyes and silica particles.

	<b>Excitation laser (power output)</b>	<b>Emission filters</b>
<b>Hoechst</b>	405 nm (10%)	BP 420-450
<b>FITC-NPs</b>	488 nm (10%)	BP 520-550
<b>Alexa 555</b>	543 nm (100%)	BP 560-620

### 3.3.8 Wound healing assay

Cell migration plays an essential role in a variety of biological processes, including embryonic development, homeostasis, immune responses, wound healing and cancer metastasis; it is a complex process that in recent years has attracted the interest of researchers from diverse disciplines in biology. This interest is due different factors, such as:

- The consistent amount of knowledge that has been gathered on the components and interactions of the macromolecular machinery of cell movement, as well as its related signaling pathways;
- The use of efficient model organisms for *in vivo* studies on cell migration biology;
- The use of sophisticated imaging and genetic approaches.

Wound healing is a dynamic and complex process involving a series of coordinated events, including bleeding, coagulation, initiation of an acute inflammatory response to the initial injury, regeneration, migration, proliferation and remodeling. The repair process usually begins immediately after injury and goes through similar phases of healing in all tissues; however, specialized tissues (e.g. liver, skeletal tissue and the eye) have their own distinctive forms and follow separate pathways. As most of the repair processes are common for all tissues, the related pathways are very similar. They usually involve a carefully and precisely regulated cascade that correlates with the appearance of different cell types in the wound during distinct phases of the healing process. Timing and interactions between the components taking part in the wound healing process are different for acute and chronic wounds; the main phases remain nevertheless the same. Acute tissue repair, which is triggered by tissue injury, can be describes as four time-dependent phases:

1. Coagulation and hemostasis, beginning immediately after injury;
2. Inflammation, which begins shortly after the first step;
3. Proliferation, which includes the major healing processes;

#### 4. Wound remodeling, in which scar tissue is formed.

Wound treatment and its medical complications remain one of the most prevalent and economically challenging healthcare issues in the world, therefore development of appropriate therapeutics, such as wound healing-enhancing nanomaterials, is necessary to satisfy the unmet clinical need. [124, 125, 126].

The wound-healing assay is one of the earliest developed methods to study cell migration *in vitro*. It's a method based on observation of cell migration into an artificial wound created on a cell monolayer. Although not an exact duplication of *in vivo* cell migration, this method mimics to some extent migration of cells in wound healing. In comparison with other popular *in vitro* methods, the wound-healing assay is particularly suitable for studies of directional cell migration and its regulation. Migration of the cells is regulated by both the extracellular matrix (ECM) surrounding the cells as well as intercellular interactions in the case of epithelial and endothelial cells. The effects of each of these factors on directional cell migration can be studied using the wound healing method. The wound-healing assay is probably the simplest method to study cell migration *in vitro*, as it only requires common and inexpensive supplies found in most cell culture labs. It involves the creation of an artificial wound on a properly confluent monolayer of cells, followed by the capture of images at the beginning and regular intervals during cell migration. The images acquired will then be compared in order to determine the different rate of wound closure across different samples. There are a number of disadvantages and limitations of the *in vitro* scratch assay compared to other available methods. It takes a relatively longer time to perform than some other methods, as one to two days are needed for the formation of cell monolayer and then up to several days for cell migration to close the scratch. Moreover, relatively large amount of cells and chemicals will be required for the assay if performed in a tissue culture dish. Despite these limitations, the wound-healing assay is still often the method of choice to analyze cell migration [124, 127].

To analyze cellular migration following treatment with colloidal silica *in vitro*, HaCaT cells were seeded at a density of  $2 \times 10^4$  cells/well in fibronectin-coated 96-well plates, supplemented with 1% (v/v) penicillin, 1% (v/v) streptomycin and 10% (v/v) FBS and cultured for 48 h at 37 °C to achieve confluent monolayer. Culture medium was then replaced with starvation medium (0.5% FBS) to incubate overnight. Each well was then treated with particle suspension or particle-free starvation medium for 5 h at 37 °C. After incubation, particles were removed and the wells were washed twice with PBS. Wounds were created by cutting through the center of the cell monolayer in the well with a pipette tip. The detached cells were washed away using PBS and the wells were re-coated with fibronectin (10µg/mL in starvation medium) for 1 hour at 37 °C. At this point (t=0), the first images were taken on In Cell Microscope 2000 (GE Healthcare) (objective 2x), then cells were washed and maintained in starvation medium for cell migration monitoring up to 72h. Scratch areas were quantified using the AxioVision software (Carl Zeiss). Wound areas were normalized by the initial area (n= 8 images).

### **3.3.9 Western blot**

Western Blot is an important technique in cell and molecular biology, as it allows the identification of specific proteins from a complex mixture extracted from cells. To do so, it exploits four elements: 1) separation by size, 2) transfer to a solid support, 3) marking of the target protein using a proper primary antibody, 4) use of a secondary antibody that binds to the primary antibody to visualize the target protein. In Western Blot the mixture of proteins is separated based on molecular weight through gel electrophoresis. These results are then transferred to a membrane, producing a band for each protein. The membrane is then incubated with labeled antibodies specific to the protein of interest. The unbound antibody is washed off leaving only the bound antibody to the protein of interest. The bound antibodies are then detected by developing the film. As the antibodies only bind to the protein of interest, only one band should be

visible. The thickness of the band corresponds to the amount of protein present; therefore doing a standard can indicate the amount of protein present [128].

Cell lysates are the most common form of sample used for Western blot. After protein extraction, its concentration is measured using a spectrophotometer, thus allowing the measurement of the mass that is being loaded into each well by the relationship between concentration, mass, and volume. Western blot uses two different types of agarose gel: a stacking gel and a separating (or resolving) gel. The stacking gel is slightly acidic (pH 6.8) and has a lower acrylamide concentration, which has poor separation properties but allows proteins to form thin, sharply defined bands. The separating gel is basic (pH 8.8) with higher polyacrylamide content, thus making its pores narrower and causing protein separation by their size, as smaller proteins travel faster than larger proteins. After electrophoresis, the separated proteins are transferred to a membrane. The transfer is performed using an electric field oriented perpendicular to the surface of the gel, causing proteins to move out of the gel and onto the membrane. The membrane, the solid support, is an essential part of this process. Two types of membrane are commonly used: nitrocellulose and polyvinylidene fluoride (PVDF). Nitrocellulose has retention as well as high protein affinity, but does not allow the membrane to be used for re-probing. PVDF membranes, on the other hand, provide better mechanical support and allow the blot to be re-probed and stored. However, they produce higher background and therefore must be washed carefully. After blocking of non-specific binding by treatment with Bovine Serum Albumin (BSA), the primary antibody is added to the membrane to bind the target protein. The membrane is then detected using the label antibody, which is detected by the signal it produces corresponding to the position of the target protein (**Figure 3.15**). This signal is captured on a film which is usually developed in a dark room [128].

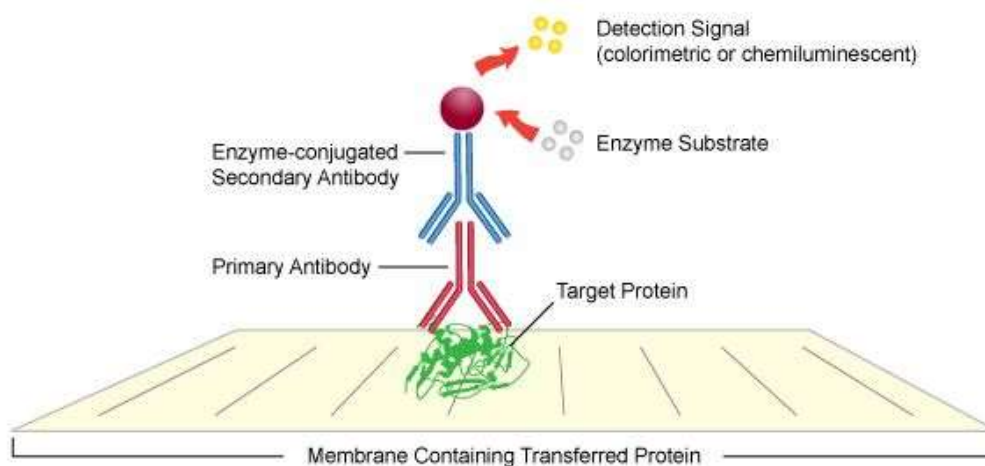


**Figure 3.15** The detection mechanisms in western blot (from [http://www.leinco.com/general\\_wb](http://www.leinco.com/general_wb)).

It is very important to remember that Western blot is typically considered a semi-quantitative technique, as it provides a relative comparison of protein levels, but not an absolute measure of quantity. This is due to two factors: 1) the variations in loading and transfer rates between the samples in separate lanes as well as separate blots. These differences will need to be standardized before a more precise comparison can be made. 2) The detection signal is not linear across the concentration range of samples [128].

To study the effect of colloidal silica on caspase 3, which is involved in apoptotic cell death regulation, HaCaT cells were seeded at  $7 \times 10^5$  cells/well in 6-well plates overnight, and then treated with SiNP20-70 and SMP200-500 at 10-100  $\mu\text{g/ml}$  in CM-10% for 24 hours. After treatment, cells were washed with PBS, collected by centrifugation and shock-frozen by immersion in liquid nitrogen for two minutes. The samples were kept at  $-80^\circ\text{C}$  until needed. Following cell lysis, a 4% stacking gel and a 13% resolving gel were prepared (BioRad Mini-PROTEAN Tetra cell kit, BioRad, US), and Cellular proteins from each sample were then loaded into the wells. Protein standard was loaded into the first and last wells. The gel was run at 90 V until the bottom of the gel was reached. The proteins separated on the gel were then transferred overnight to Hybond C (Hybond-C extra, Amersham, Bucks, UK) at 25 V. Subsequently, the membrane



was stained with Ponceau S (Sigma Aldrich, US) to confirm transfer of proteins and standards. Membrane were then rinsed twice in Tris-Buffered Saline and Tween 20 solution (TBS-T), then blocked for 1 h in blocking buffer. The membrane was then incubated for 2 h with in house-raised rabbit anti-human caspase-3 primary antibody. After careful rinsing and blocking, incubation for 1 hour with HRP-conjugated Goat anti-rabbit IgG secondary antibody (DAKO, Sigma) was performed. Antibody bound proteins were visualised using the ECL analysis system (Amersham, UK) using Kodak Biomax XAR film. Films were developed on a Compact X4 Xograph Imaging System.

Despite being one of the most common procedures in biochemical labs, Western blotting has several disadvantages. Besides being semi-quantitative, Western blot can only be performed if primary antibodies against the protein of interest are available. Western blot can also be challenging to perform without proper training, and is time-consuming. An alternative to this technique is represented by direct measurement of caspase3/7 using fluorescence-based kits such as the Apo-ONE® Homogeneous Caspase-3/7 Assay (Promega, UK). Following rapid and efficient lysis/permeabilization of cultured mammalian cells, pro-fluorescent substrate rhodamine 110, bis-N-CBZ- L-aspartyl-L-glutamyl-L-valyl-L-aspartic acid amide (Z-DEVD-R110), is cleaved as a direct consequence of caspase-3/7 activity. Subsequent excitation at 499nm makes the rhodamine 110 leaving group intensely fluorescent. The emission maximum is 521nm. In this study, the Apo-ONE® Homogeneous Caspase-3/7 Assay was used to detect caspase activity in K17 keratinocytes and HDF following treatment with colloidal silica 10-200 µg/ml. Staurosporine, an anti-cancer drug routinely used in apoptosis assays, was used at 1-100 µM as positive control. Fluorescence intensity and optical density were measured using Gemini EM Microplate Reader (Molecular Devices, US).

### **3.3.10 Molecular pathway analysis**

Study of cellular response to external stimuli at molecular levels, such as protein and gene expression, have provided important advances in many areas

of fundamental and applied biology. The latest technique development in gene expression profiling allows studying specific subset of target genes, or thousands of genes at once, thus creating a global picture of gene expression of an organism under a given condition. There are several techniques available to evaluate gene expression, such as Northern Blot, ribonuclease protection assay (RPA), serial analysis of gene expression (SAGE), reverse transcription-polymerase chain reaction (RT-PCR), quantitative real-time polymerase chain reaction (qRT-PCR), PCR arrays, and microarrays. Among these techniques, Northern blot analysis remains a standard method for detection and quantitation of mRNA levels despite the advent of more robust techniques [129].

In the last two decades, real-time PCR has become widely used in biomedical science research, and a reliable method to determine the expression level of target genes. It is a highly sensitive and quantitative method for the determination of copy number of PCR templates, such as DNA or cDNA. Its wide dynamic range makes real-time PCR the preferred choice for the simultaneous quantification of both rare and abundant genes in the same sample. Although a number of kits and reagents for real-time PCR are commercially available, the basic principle behind the technique is relatively simple and the same for all [130, 131]. There are two types of real-time PCR, a probe-based one and intercalator-based one. Probe-based real-time PCR, also known as TaqMan™ PCR (**Figure 3.16**), requires a pair of specific primers and a fluorogenic probe complementary to the target sequence. The probe is an oligonucleotide with a reporter dye attached to the 5' end and a quencher dye attached to the 3' end. Until it is hydrolyzed, the quencher and the fluorophore remain separated by the probe itself; consequently, the reported dye is partially quenched and emits only background fluorescence. During PCR, the probe anneals specifically between the primers to an internal region of the PCR product. When the polymerase carries out the extension of the primer and replicates the template to which the TaqMan™ is bound, the probe is cleaved, releasing the reporter molecule away from the close vicinity of the quencher thus increasing the fluorescence. This process repeats in every cycle and does not interfere with the accumulation of PCR product [132].

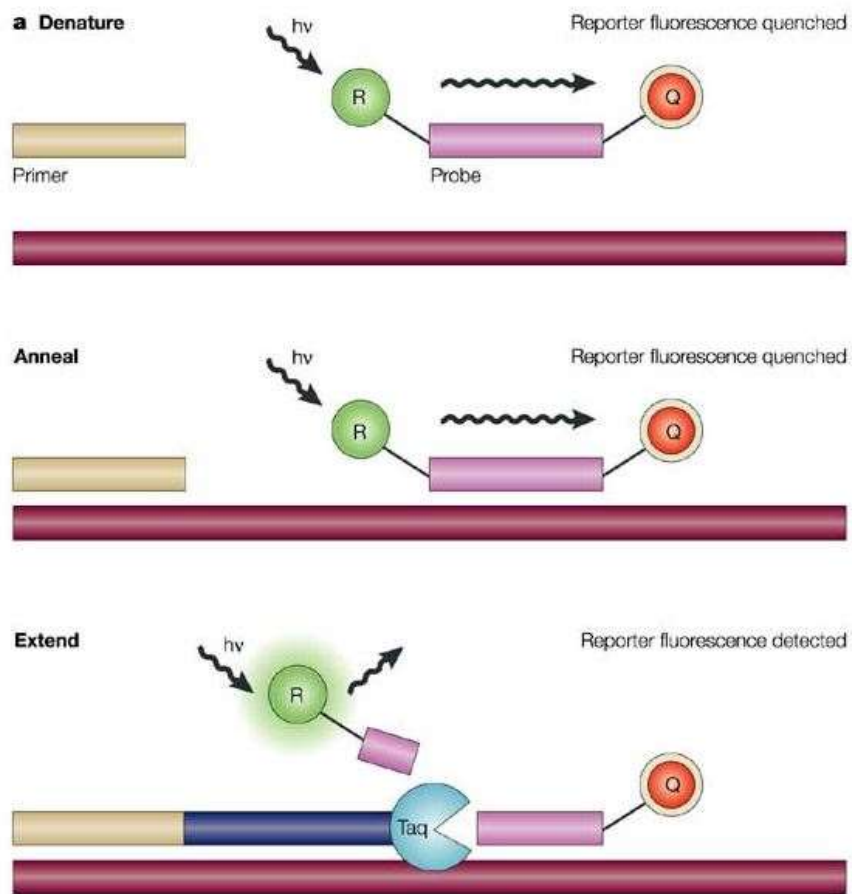


**Figure 3.16** The principle for Taqman™ RT-PCR (modified from [http://www.nature.com/nrd/journal/v3/n9/fig\\_tab/nrd1496\\_F1.html](http://www.nature.com/nrd/journal/v3/n9/fig_tab/nrd1496_F1.html)).

The intercalator-based method requires the use of a dye such as SYBR Green (Figure 3.17), which binds to newly synthesized double-stranded DNA by intercalating between base pairs and generates fluorescence only when bound to DNA. Detection of the fluorescent signal occurs during the PCR cycle at the end of either the annealing or the extension step when the greatest amount of double-stranded DNA product is present. SYBR Green-based detection is the least expensive and easiest method available for real-time PCR; however, as SYBR Green detects any double-stranded DNA non-specifically, the reaction must contain a combination of primers and master mix that generates a single gene-specific amplicon without producing any non-specific secondary products.

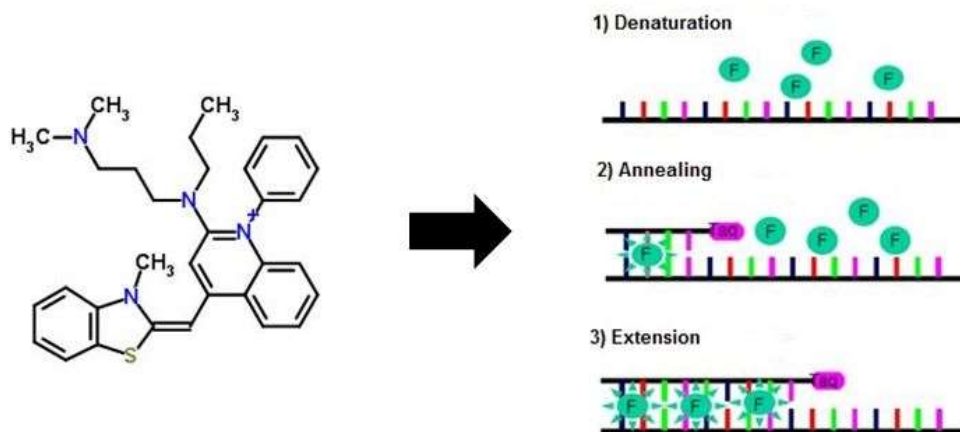


**Figure 3.17** SYBR Green and its intercalation inside dsDNA (modified from <http://img.guidechem.com/pic/image/163795-75-3.png> and <http://eng.bioneer.com/products/geneexpression/qPCRArrayService-detection.aspx> ).

Both methods require the same equipment: a thermal cycler, equipped with a sensitive camera that monitors the fluorescence in each sample at frequent intervals during the PCR, as well as software for data collection and analysis. The principle behind real-time PCR consists of three steps (**Figure 3.18**): 1) total RNA isolation, 2) reverse transcription to cDNA, and 3) PCR [131, 133].

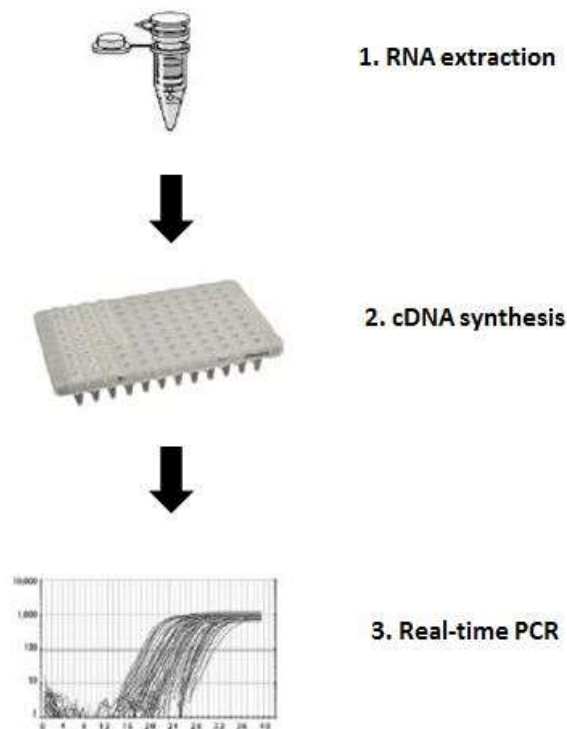


**Figure 3.18** The three steps involved in real-time PCR (modified from QIAGEN RT-PCR Handbook).

Total RNA isolation refers to the extraction of RNA from biological samples. Extracting high-quality RNA might prove challenging, as this nucleic acid is labile and is rapidly degraded by ubiquitous RNases which occur naturally in all cells and are released following cell lysis, the first essential step of RNA extraction. To avoid this problem, modern day kits include buffers containing specific molecules, such as the highly denaturing guanidine-thiocyanate, which immediately inactivates RNases to ensure purification of intact RNA. Following lysis and proper homogenization of the sample, a number of approaches to RNA extraction are available, although the most commonly used are based on a solid phase approach such as column-binding purification combined with microspin technology. Reverse transcription involves the use of the enzyme reverse transcriptase to generate single-stranded complementary DNA (cDNA) from the extracted RNA. Reverse transcriptases (RTs) use an RNA template

and a short primer complementary to the 3' end of the RNA to direct the synthesis of the first strand cDNA which can be used directly as a template for real-time PCR. Alternatively, the first-strand cDNA can be made double-stranded using DNA Polymerase I and DNA Ligase [134, 135].

To understand the molecular pathway of silica-induced apoptotic cell death,  $6 \times 10^5$  HaCaT cells/well were seeded in 6-well plates and cultured until 70% confluence was reached. Each well was then treated with SiNP20 10-50  $\mu\text{g/ml}$  in CM-10% for 24 h. After incubation, particles were removed and cells harvested by trypsinization and centrifugation. The resulting pellets were allowed to completely dry, then dislodged and treated with 350-700  $\mu\text{l}$  RLT Buffer (RNeasy Total RNA Extraction Kit, QIAGEN, UK). The lysate was then centrifuged 2 minutes into a QIAshredder spin column (QIAGEN, UK), and resuspended in 1 volume of 70% ethanol. The mix was then transferred in an RNeasy spin column and centrifuged 15 s at  $\geq 8000 \times g$  ( $\geq 10,000$  rpm). After centrifugation, the flow-through was discarded, then 700  $\mu\text{l}$  Buffer RW1 (RNeasy Total RNA Extraction Kit, QIAGEN, UK) was added to the spin column, then centrifuged for 15 s at  $\geq 8000 \times g$  ( $\geq 10,000$  rpm). This step was repeated again twice using 500  $\mu\text{l}$  Buffer RPE (RNeasy Total RNA Extraction Kit, QIAGEN, UK); after that, 30-50  $\mu\text{l}$  of RNase free water were added and the samples were centrifuged at full speed for 1 min to collect the purified RNA. RNA purity and concentration was verified by using Pico100<sup>TM</sup> (Picodrop, UK). After verification, approximately 0.8  $\mu\text{g}$  RNA/sample were mixed with RNase-free water and Buffer GE (RT<sup>2</sup> First Strand Kit, QIAGEN, UK) and put in Techne TC-512 thermocycler (Bibby Scientific, UK) for 5 min at 42°C. After that, samples were placed in ice for 1 minute, and then mixed with 5x Buffer BC3, Control P2, RE3 Reverse Transcriptase, RNase-free water (RT<sup>2</sup> First Strand Kit, QIAGEN, UK); the mix was incubated at 42°C for exactly 15 min, then immediately at 95°C for 5 min. In the end, 91  $\mu\text{l}$  of RNase-free water were added to each sample. The samples were then mixed with 2x RT<sup>2</sup> SYBR Green ROX FAST Mastermix (QIAGEN, UK) and RNase-free water, and loaded in Cell-Death Pathway-Finder RT<sup>2</sup> Profiler PCR Array (QIAGEN, UK) using QIAgility automated sample loading (QIAGEN, UK) to minimize operator-related

loading errors. The loaded ring was then sealed with Rotor-Disc Heat-Sealing Film (QIAGEN, UK) and placed inside Rotorgene Q100 (QIAGEN, UK). The samples were run for 10 minutes at 95°C, then for 40 cycles of 15s/95°C – 30s/60°C. The collected data were then analyzed using the Rotorgene Software.

### **3.3.11 Statistics**

All experiments were performed at least three times and one of the representative experiment data was presented. For MTT and LDH assays, the mean values of three replicates were expressed as percentage of negative control (cells without treatment) with standard deviation (mean  $\pm$  SD). Two-tailed unpaired t-test and one-way ANOVA were used for comparison of differences between samples and the control. The differences were considered significant when  $p \leq 0.05$ .

## 4 RESULTS

### 4.1 Fumed Amorphous Silica

#### 4.1.1 Characteristics in suspension

In order to determine the particles' size, solubility and stability in cell culture media, fumed silica particles suspended in media with 10% FBS (CM-10%) and 0% FBS (CM) were characterized by Dynamic Light Scattering (DLS) at 0 and 24 h after incubation at 4°C (storage conditions). The resultant hydrodynamic ( $H_d$ ) size of the particles in the suspensions was compared with the given size of the respective silica particles (**Table 4.1**) while their dispersion properties were assessed by observation of their polydispersion index (PDI). Particle-free CM-10% and CM were used as background controls (**Table 4.2**). The particles average size in CM-10% was larger than that in CM, suggesting that the presence of larger clusters was attributable to FBS proteins. 24 h incubation resulted in an increase in average size and PDI.

**Table 4.1** Characteristics of fumed silica (see Appendices for full Sigma Aldrich specification sheets).

	<b>SiNP7</b>	<b>SiNP14</b>
<b>Given size (nm)</b>	7	14
<b>Surface area (m<sup>2</sup>/g)</b>	390±40	200±25

The DLS assay of fumed silica 7 (SiNP7) and 14 nm (SiNP14) at 25-100 µg/ml suspended in CM-10% and CM was performed. In CM-10% both SiNP7 and SiNP14 showed an  $H_d$  size around 20 nm and PDI 0.4 and 0.3 respectively, when measured at 25 µg/ml 0 h (**Table 4.3**). The increase of incubation time to 24 h had little effect while increasing particle concentration to 100 µg/ml resulted in an increase in PDI, indicating the tendency of particle aggregation. In CM (**Table 4.4**), on the other hand, the  $H_d$  size/PDI increased to 677 nm/0.6



and 375 nm/0.7 for SiNP7 and SiNP14 respectively when measured at 0 h, while the particles  $H_d$  size and PDI became much smaller with extension of incubation time to 24 h and increase of concentration to 100  $\mu\text{g/ml}$ , suggesting that these particles were unstable when suspended in CM due to formation of aggregates, which appeared larger for SiNP7 than SiNP14.

**Table 4.2** DLS assay of particle-free CM-10% and CM. Particle-free media was measured in order to detect background molecule clusters after 0 and 24 h incubation at 4 °C (storage conditions). Results are expressed as Average size (Average (nm)), to indicate the size of measured clusters, and polydispersion index (PDI) to indicate stability of the clusters in solution. Average size was measured lower in CM due to the different amount of proteins and other serum components. Five measurements were performed for each sample using Malvern Zetasizer.

Culture Media	0 h		24 h	
	Average (nm)	PDI	Average (nm)	PDI
CM-10%	19	0.4	26.4	0.6
CM	4.4	0.3	9.3	0.5

**Table 4.3** DLS assay of fumed silica in CM-10%. SiNP7 and SiNP14 were analysed at 25 and 100 µg/ml after 0 and 24 h incubation at 4 °C (storage conditions). Results are expressed as Average size (Ave. (nm)), to indicate the size of measured clusters, and polydispersion index (PDI) to indicate stability of the clusters in solution. Five measurements were performed for each sample using Malvern Zetasizer.

NPs in CM-10%	25 µg/ml				100 µg/ml			
	0 h		24 h		0 h		24 h	
	Ave. (nm)	PDI	Ave. (nm)	PDI	Ave. (nm)	PDI	Ave. (nm)	PDI
SiNP7	20	0.4	19	0.4	20	0.4	24.4	0.4
SiNP14	20.2	0.3	19.4	0.4	20.4	0.4	19.3	0.4

**Table 4.4** DLS assay of fumed silica in CM. SiNP7 and SiNP14 were analysed at 25 and 100 µg/ml after 0 and 24 h incubation at 4 °C (storage conditions). Results are expressed as Average size (Ave. (nm)), to indicate the size of measured clusters, and polydispersion index (PDI) to indicate stability of the clusters in solution. Five measurements were performed for each sample using Malvern Zetasizer.

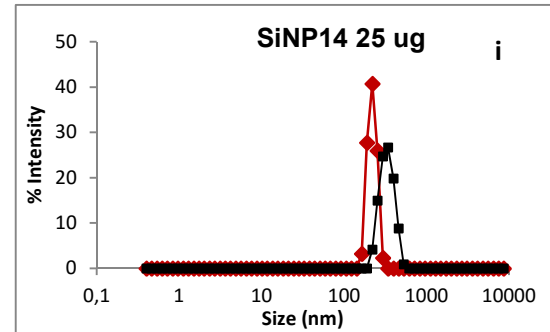
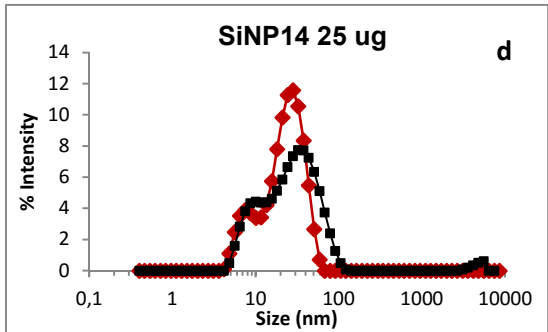
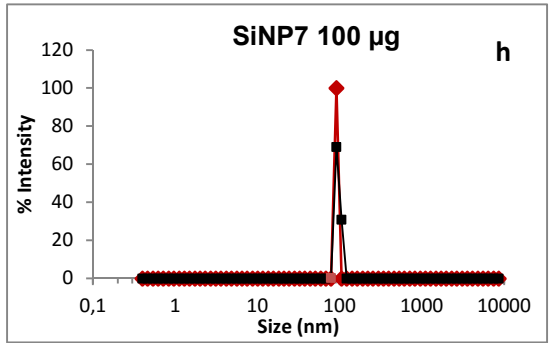
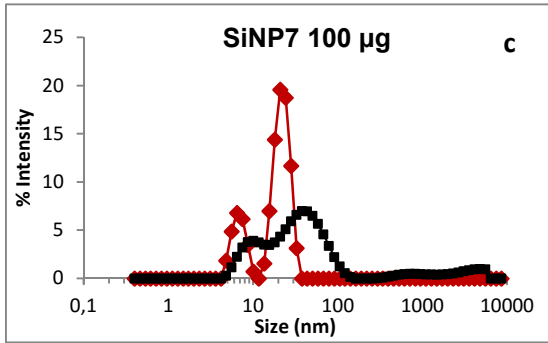
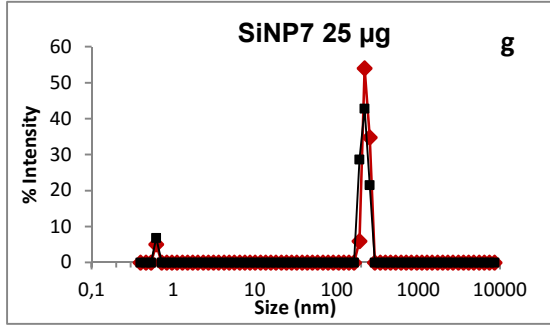
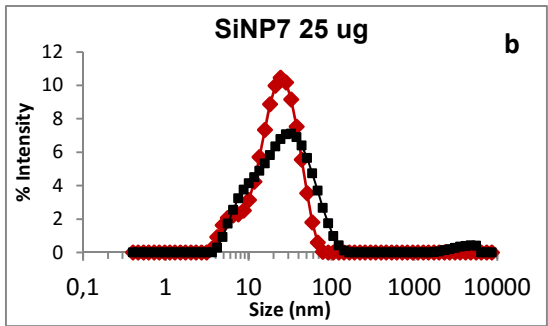
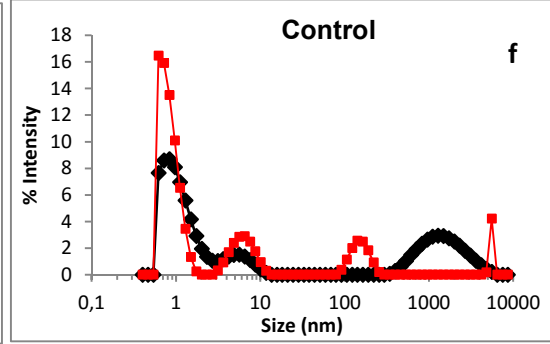
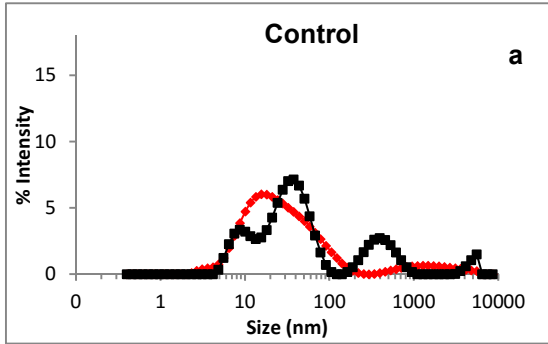
NPs in CM	25 µg/ml				100 µg/ml			
	0H		24H		0H		24H	
	Ave. (nm)	PDI	Ave. (nm)	PDI	Ave. (nm)	PDI	Ave. (nm)	PDI
SiNP7	677	0.6	543	0.3	325.4	0.5	500.1	0.4
SiNP14	375	0.4	259	0.1	276.2	0.3	304	0.2

The dispersion behavior of the particles in cell culture media could be better demonstrated by showing the DLS profile (**Figure 4.1 a-I**). The dispersion patterns for SiNP7 and SiNP14 in CM-10% were very different from that of the background particles, although they shared a similar average particles size (**Table 4.1 and 4.2**). The difference in the dispersion profiles of silica particles in CM-10% and CM indicated the interaction of the particles with FBS components, whereas the wider size distribution after 24 h incubation presented evidence of instability of the particles in the suspensions (**compare black with red line for each particle profile**).

LEGEND: - 0 h; -24 h

CM-10%

CM



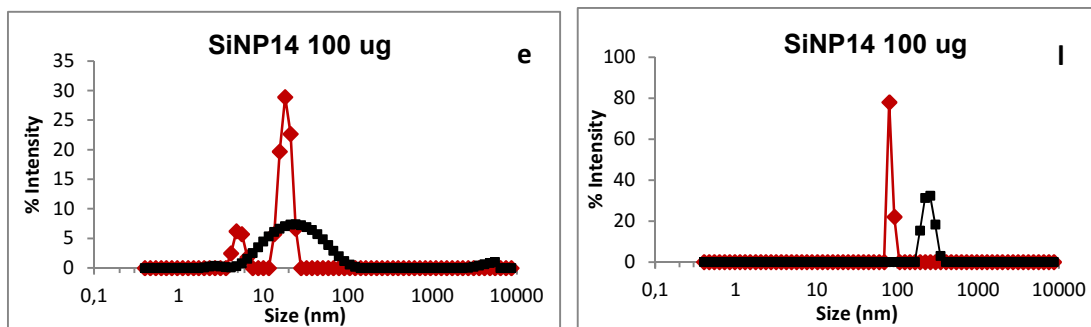


**Figure 4.1** DLS profiling of particle dispersion patterns in CM-10% and CM. a, f: culture media presenting background particles; b, c, d and e: dispersion patterns of SiNP7 and SiNP14 in CM-10%; g, h, i and l: dispersion patterns of SiNP7 and SiNP14 in CM.

To get confirmation of DLS analysis and gain information on particle shape, SEM imaging of SiNP7 at 10  $\mu\text{g}/\text{ml}$  in water was performed (**Figure 4.2**). The particles were shown as round-shaped, forming chain-like structures with size far beyond the given size, confirming formation of aggregates consistent with the DLS measurement for particles suspended in CM (**Figure 4.1, d-f**).

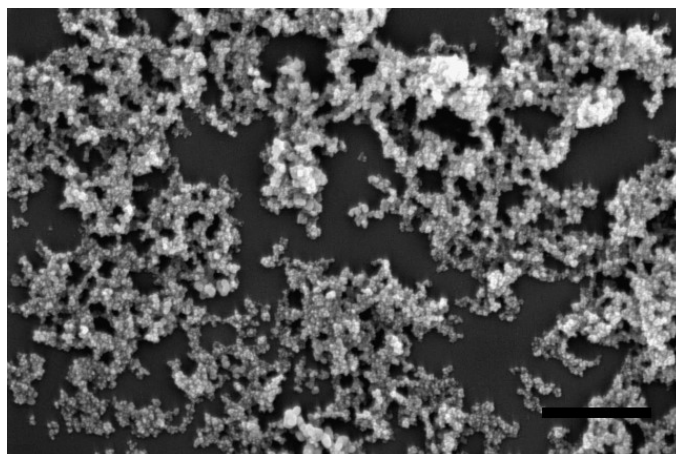


**Figure 4.2** SEM Imaging of SiNP7. SEM imaging in water at 10  $\mu\text{g}/\text{ml}$  was performed using Philips XL30 SFEG. Scale bar: 1  $\mu\text{m}$ .

### 4.1.2 *In vitro* cytotoxicity assessment and induction of apoptotic cell death

Human skin HaCaT cells were used to examine the cytotoxic potential of fumed silica nanoparticles by assays of cell viability (MTT) and flow cytometry detection of necrotic and apoptotic cell death. Cellular uptake was also examined to provide insights into the relationship between particle internalization/subcellular location and cytotoxicity. All the assays were performed on particle-free cultures as reference and cells treated with SiNP7 and SiNP14 at 10-200  $\mu\text{g/ml}$  in CM-10% or CM. After 24 h treatment, a significant effect of both SiNP7 and SiNP14 on cell viability could only be detected in the absence of FBS at concentrations  $\geq 50 \mu\text{g/ml}$  (Figure 4.3).

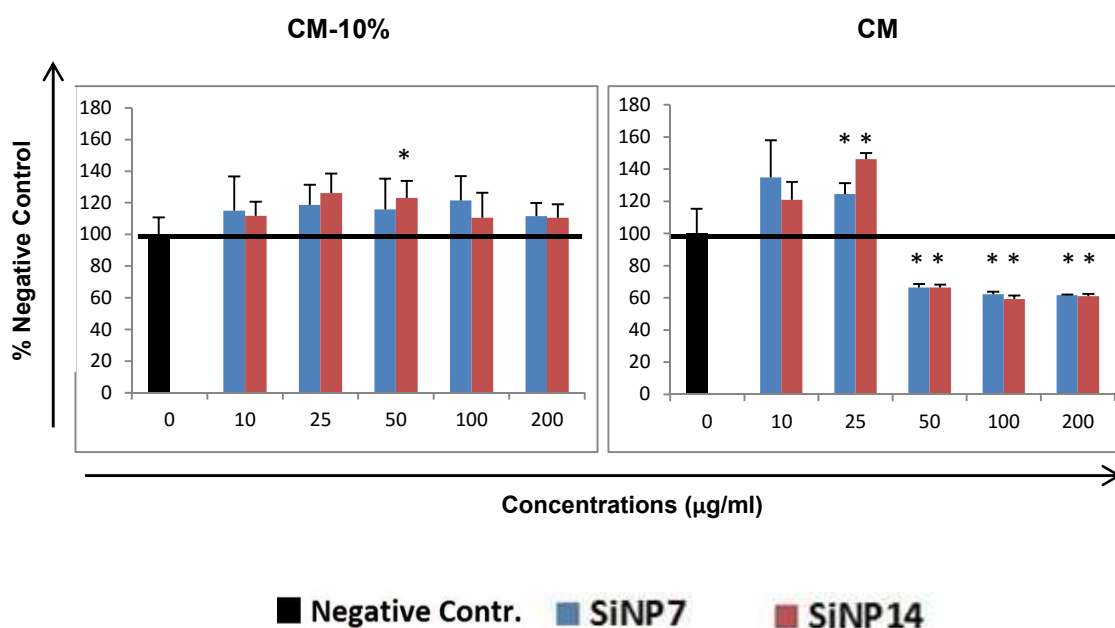


**Figure 4.3** Effect of fumed silica nanoparticles on cell viability in HaCaT cells assessed by MTT assay. HaCaT cells were treated with SiNP7 and SiNP14 in CM-10% and CM and cell viability was assessed at 24 h treatment. Results were expressed as percentage of negative control, indicating increase/decrease of cellular metabolism in particle-treated samples compared with cellular metabolism in particle-free control. Black line serves as reference for normal cellular activity. Each particle concentration was tested in triplicates and the results analysed by one-way ANOVA and Student's t-test. Statistically significant results ( $p < 0.05$ ) are marked with an asterisk (\*) on top of the corresponding bar.

To assess whether the cytotoxicity of SiNP7 and SiNP14 was due to the particles' cellular uptake, HaCaT cells were treated for 24 h and then subjected to flow cytometry for semi-quantification of silica NPs cellular uptake. The profiles of cellular uptake of silica nanoparticles are displayed in **Figure 4**. The shift of peaks to the right indicated cellular uptake of the fluorescent particles. A weak concentration-dependent increase of cellular uptake of both SiNP7 and SiNP14 was detected when tested in CM-10%, while the uptake was much greater when tested at  $\geq 50 \mu\text{g/ml}$  in CM (**Figure 4.4** and **Table 4.5**). These data suggested that the cytotoxicity of SiNP7 and SiNP14 was correlated with their cellular uptake.

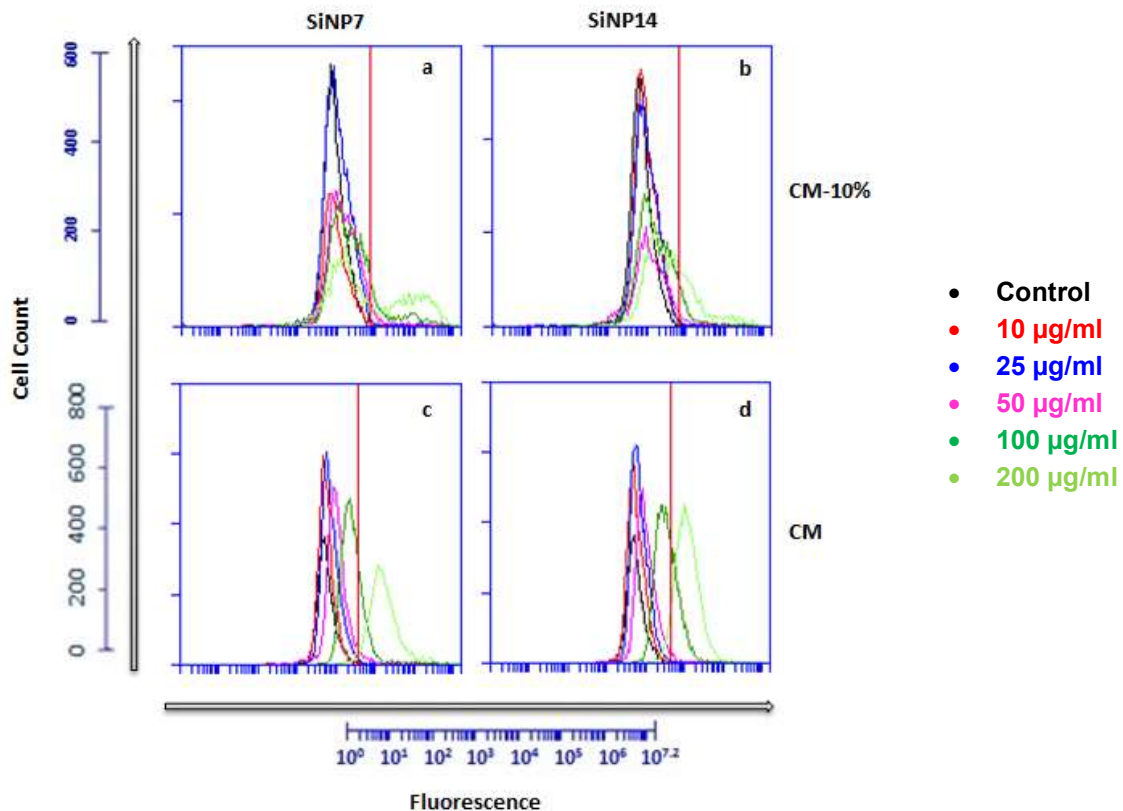


**Figure 4.4** Flow cytometry assay of cellular uptake of fumed silica nanoparticles. HaCaT cells were treated with the particles at 10-200  $\mu\text{g/ml}$  in CM-10% and CM for 24 h. Results are expressed as number of cells vs. detected fluorescence. The red line separates the left part of the graph, which indicates non-fluorescent cells associated with particle-free cells, from the right part of the graph, which shows fluorescence positive cells associated with silica particles uptake.

**Table 4.5** Flow cytometry quantification of silica nanoparticles' cellular uptake. The results as shown in Figure 4.4 were qualitatively analyzed using BD CSampler software as described in the methods section. Each value of the table corresponds to the percentage of fluorescence detected by the flow cytometer and previously expressed as cell count vs. fluorescence.

	Uptake in CM-10%		Uptake in CM	
	SiNP7	SiNP14	SiNP7	SiNP14
<b>Negative Control</b>	N/A	N/A	N/A	N/A
<b>10 µg/ml</b>	0.5%	0.5%	0.2%	0.1%
<b>25 µg/ml</b>	0.8%	0.6%	0.6%	0.2%
<b>50 µg/ml</b>	4.8%	5.2%	5.1%	1.7%
<b>100 µg/ml</b>	14.3%	9%	24.3%	32.5%
<b>200 µg/ml</b>	39.6%	29.5%	97.6%	93.6%

The results of cellular uptake obtained by flow cytometry were partially confirmed by TEM imaging on HaCaT cells, in collaboration with Dr. David Dinsdale and Prof. Marion MacFarlane, MRC toxicology unit, Leicester (UK). Cells were treated with Silica 7 25 µg/ml in CM-10%, fixed and analyzed by TEM at different magnifications. The TEM images showed no evidence of cellular uptake at this concentration (data not shown), consistent with the data from the flow cytometry assay.

To investigate the toxicity mechanism of fumed silica nanoparticles on HaCaT cells, Annexin V/FITC and Propidium Iodide (PI) double staining and subsequent flow cytometry were employed to detect necrotic and apoptotic cell death. As shown in **Figure 4.5**, approximately 90% of untreated cells were not stained with PI and Annexin V/FITC when cultured in particle-free CM-10% and CM. In CM-10% both SiNP7 and SiNP14 at 5-25 µg/ml induced a slight increase in FITC-positive and PI/FITC double positive staining cells in a concentration-dependent manner. In contrast, when tested in CM, both SiNP7 and SiNP14 induced a great increase of FITC positive and PI/FITC double



positive staining cells (**Figure 4.6**), indicative of apoptotic cell death. The induction of apoptotic cell death by the silica nanoparticles was detected at the lowest concentration and reached more than 90% at the highest concentration tested. These results suggested that in HaCaT cells the toxicity of fumed silica NPs, as detected by the MTT assay, was via induction of apoptosis.

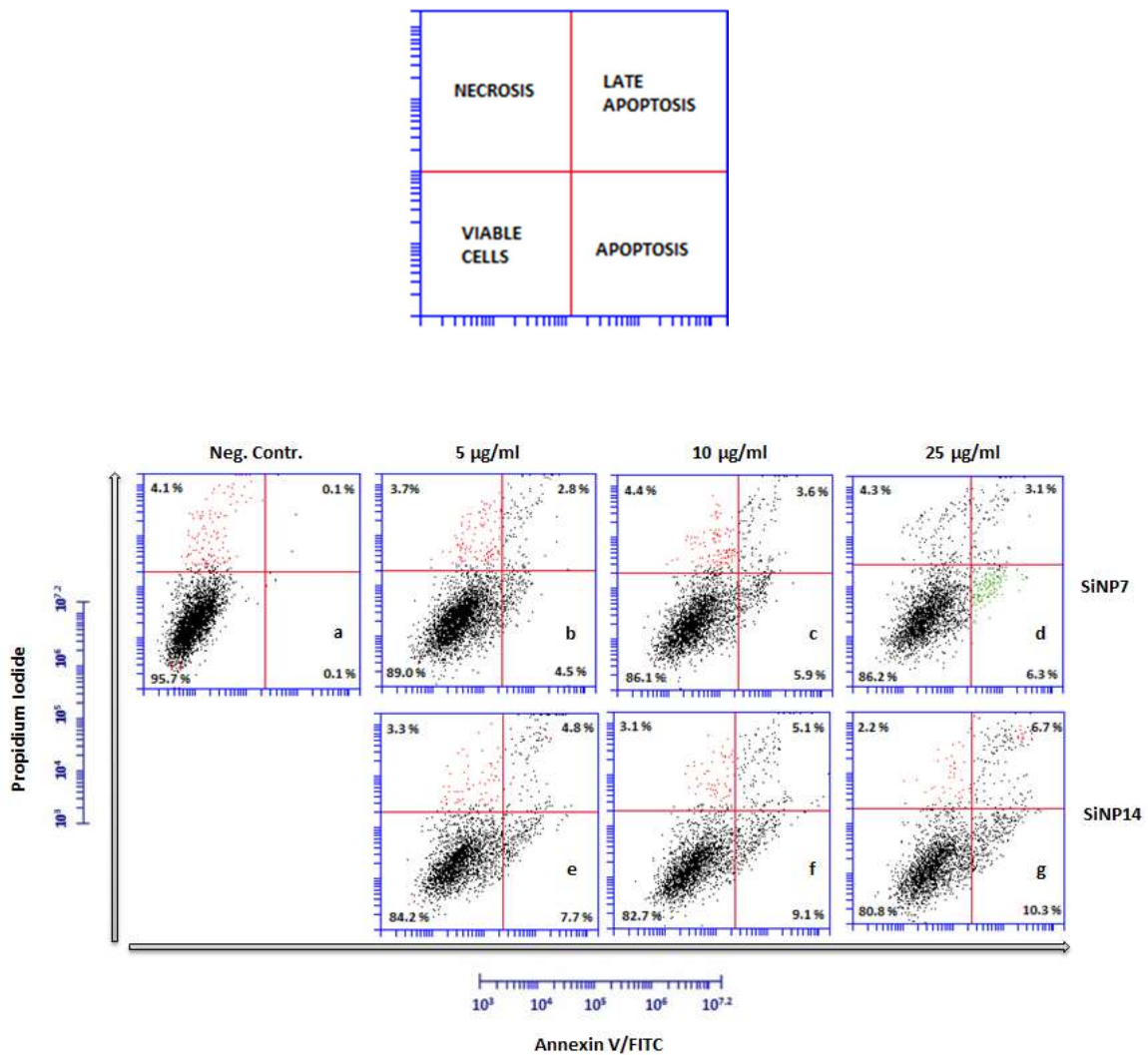


**Figure 4.5** Apoptosis assay of fumed silica in CM-10%. HaCaT cells were treated with SiNP7 and SiNP14 at 5-25 µg/ml in CM-10% for 24 h. Following treatment, double staining with propidium iodide (PI) and Annexin V/FITC was performed and using BD Accuri C6 flow cytometer. For each sample 10.000 events were recorded, and the results expressed as PI fluorescence vs. Annexin V/FITC fluorescence. In each quadrant, quantification is reported as percentage of detected fluorescence.

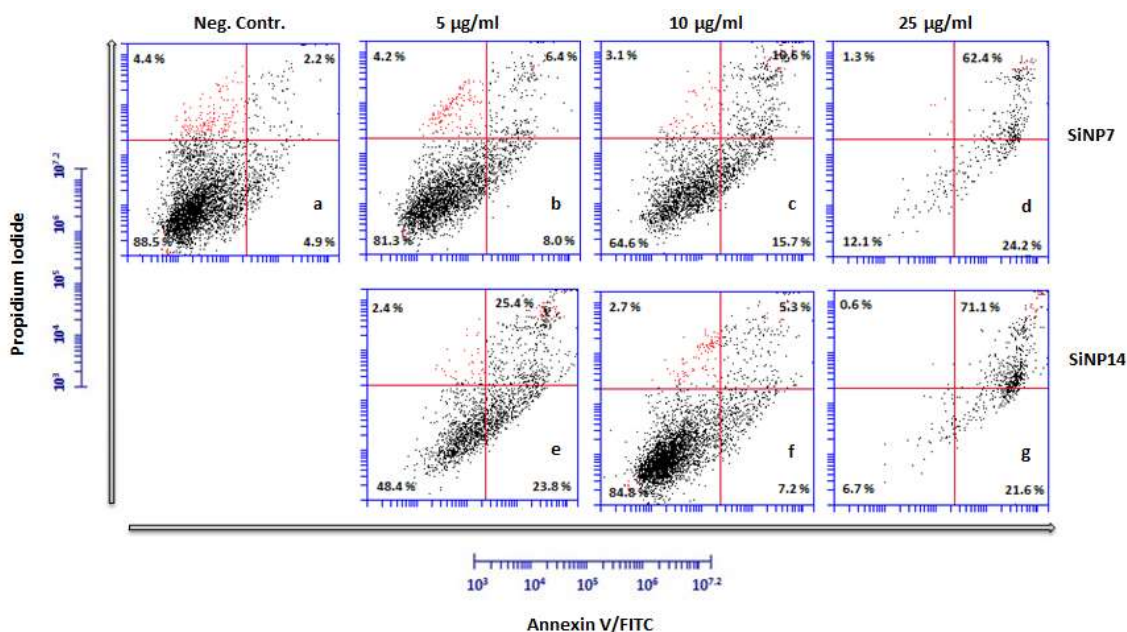


**Figure 4.6** Apoptosis assay of fumed silica in CM. HaCaT cells were treated with SiNP7 and SiNP14 at 5-25 µg/ml in CM for 24 h. Following treatment, double staining with propidium iodide (PI) and Annexin V/FITC was performed and using BD Accuri C6 flow cytometer. For each sample 10.000 events were recorded, and the results expressed as PI fluorescence vs. Annexin V/FITC fluorescence. In each quadrant, quantification is reported as percentage of detected fluorescence.

## 4.2 Colloidal Amorphous Silica

### 4.2.1 Characteristics in suspension

In order to determine particles' size and behaviour in different media, Dynamic Light Scattering (DLS) was performed to determine their hydrodynamic ( $H_d$ ) size and their dispersion properties, indicated by the polydispersion index (PDI). As silica particles may behave diversely in different testing media, in this study colloidal amorphous silica particles were characterized in five different cell culture media at concentrations that were used for assessing their cellular effects. The tested media included DMEM/F-12 with 10% (CM-10%), 0.5% (CM-0.5%) and 0% (CM) FBS, plus EpiLife™ medium and Medium 106, as these media were used for culturing different types of cells in this research. Particle-free media were analysed as background controls for pre-existing clusters of

biomolecules such as sugars, aminoacids and proteins that might interfere with the measurement of added particles. As shown in **Table 4.6**, pre-existing clusters were detected in all the tested media. The clusters appeared to be similar in size in CM-10%, CM-0.5% and Medium 106, while they appeared smaller in CM and larger in EpiLife™ Medium. The difference in size of the particles detected in the culture media reflects the difference of their composition.

**Table 4.6** DLS assay of cell culture media. Five different types of media were used for particle dispersion: CM-10% (DMEM/F-12 + 10% FBS), CM-0.5% (DMEM/F-12 + 0.5% FBS), CM (DMEM/F-12 + 0%FBS), EpiLife™ Medium, and Medium 106. Particle free media were analysed as background controls after 0 and 24 h incubation at 4 °C (storage conditions). Results are expressed as Average size (Average (nm)), to indicate the size of measured clusters, and polydispersion index (PDI) to indicate stability of the clusters in solution. Five measurements were performed for each sample using Malvern Zetasizer.

Neg. Contr.	0 h		24 h	
	Average (nm)	PDI	Average (nm)	PDI
CM-10%	19	0.4	26	0.6
CM-0.5%	18	0.4	26	0.2
CM	4	0.3	9	0.5
EpiLife™	71	0.5	119	0.3
Medium 106	17	0.4	17	0.4

SiNP20, SiNP70, SMP200 and SMP500 at 25-100 µg/ml were suspended in cell culture media and analysed at 0 and 24 h after incubation at 4°C (storage conditions). To gain insights into the stability of the particles in the suspensions over time, the size of the particles detected by the DLS were compared with their given size by the material supplier (**Table 4.7**).

**Table 4.7** Characteristics of colloidal silica (see Appendices for full Sigma Aldrich and Postnova Analytics specification sheets).

	<b>SiNP20</b>	<b>SiNP70</b>	<b>SMP200</b>	<b>SMP500</b>
<b>Manufacturer</b>	Sigma-Aldrich	Postnova Analytics	Postnova Analytics	Postnova Analytics
<b>Given size (nm)</b>	20 nm	70 nm	200 nm	500 nm
<b>Surface area (m<sup>2</sup>/g)</b>	198-258	43	15	6

When suspended in CM-10% at 25, 50, 100 µg/ml (**Table 4.8**), all the 4 particles showed an average  $H_d$  size different from their given one. For SiNP20, the  $H_d$  size was 3-5 times larger with PDI 0.3-0.5, depending on the concentration. The increase in size suggested that SiNP20 might either form aggregates or adsorb proteins in the culture medium. For SiNP70, SMP200 and SMP500, their  $H_d$  size was smaller than their given one when measured at 25 µg/ml, whereas when measured at higher concentrations, SiNP70 became slightly larger with SMP200 unchanged and SMP500 smaller as compared with their given size. The big size decrease of SMP500 when measured at 24 h after suspension was associated particle sedimentation, which was readily visualized. According to the consistency between the DLS data and their given size, SiNP70 and SMP200 have better colloidal stability than SiNP20 and SMP500.

**Table 4.8** DLS assay of colloidal silica in CM-10%. SiNP20, SiNP70, SMP200 and SMP500 were analysed at 25, 50 and 100 µg/ml after 0 and 24 h incubation at 4 °C (storage conditions). Results are expressed as Average size (Ave. (nm)), to indicate the size of measured clusters, and polydispersion index (PDI) to indicate stability of the clusters in solution. Five measurements were performed for each sample using Malvern Zetasizer.

CM-10%	25 µg/ml				50 µg/ml				100 µg/ml			
	0H		24H		0H		24H		0H		24H	
	Ave. (nm)	PDI	Ave. (nm)	PDI	Ave. (nm)	PDI	Ave. (nm)	PDI	Ave. (nm)	PDI	Ave. (nm)	PDI
SiNP20	61	0.5	91	0.5	145	0.3	131	0.3	96	0.4	119	0.3
SiNP70	38	0.5	35	0.6	90	0.3	88	0.3	96	0.3	93	0.3
SMP200	128	0.7	93	0.7	197	0.3	195	0.2	208	0.2	202	0.2
SMP500	50	1.00	48	1.00	312	0.8	147	0.7	426	0.4	216	0.7

When suspended in CM-0.5%, SiNP20, SiNP70 and SMP200 were all larger than their given size (**Table 4.9**). The size increase was more than 5 folds for SiNP20 and just over 1 fold for SiNP70 and SMP200. These data suggested that the size increase could be either due to particle aggregation for the small SiNPs or adsorption of proteins for the larger particles. For SMP500, the  $H_d$  size was very close to its given size.

**Table 4.9** DLS assay of colloidal silica in CM-0.5%. Particles were analyzed at 25, 50 and 100 µg/ml after 0 and 24 h incubation at 4 °C (storage conditions). Results are expressed as Average size (Ave. (nm)), to indicate the size of measured clusters, and polydispersion index (PDI) to indicate stability of the clusters in solution. Five measurements were performed for each sample using Malvern Zetasizer.

CM-0.5%	25 µg/ml				50 µg/ml				100 µg/ml			
	0H		24H		0H		24H		0H		24H	
	Ave. (nm)	PDI	Ave. (nm)	PDI	Ave. (nm)	PDI	Ave. (nm)	PDI	Ave. (nm)	PDI	Ave. (nm)	PDI
<b>SiNP20</b>	122	0.2	148	0.2	92	0.2	98	0.2	155	0.3	159	0.3
<b>SiNP70</b>	121	0.2	119	0.2	112	0.1	112	0.11	201	0.3	127	0.1
<b>SMP200</b>	287	0.01	266	0.08	221	0.2	216	0.3	264	0.01	255	0.03
<b>SMP500</b>	491	0.1	511	0.3	320	0.6	241	0.7	499	0.06	455	0.1

Moreover, when suspended in CM, all the particles exhibited  $H_d$  size very close to their given size (**Table 4.10**), suggesting no particle aggregation and biomolecule adsorption. It could be seen from **Table 4.9** and **4.10** that the PDI was  $\leq 0.2$  for SiNP70, SMP200 and SMP500, while it was higher for SiNP20, suggesting lower colloidal stability in culture medium for the smallest nanoparticles.

**Table 4.10** DLS assay of colloidal silica in CM. Particles were analyzed at 25, 50 and 100 µg/ml after 0 and 24 h incubation at 4 °C (storage conditions). Results are expressed as Average size (Ave. (nm)), to indicate the size of measured clusters, and polydispersion index (PDI) to indicate stability of the clusters in solution. Five measurements were performed for each sample using Malvern Zetasizer.

CM	25 µg/ml				50 µg/ml				100 µg/ml			
	0H		24H		0H		24H		0H		24H	
	Ave. (nm)	PDI	Ave. (nm)	PDI	Ave. (nm)	PDI	Ave. (nm)	PDI	Ave. (nm)	PDI	Ave. (nm)	PDI
<b>SiNP20</b>	19	0.4	19	0.5	20	0.4	20	0.5	29	0.5	22	0.4
<b>SiNP70</b>	73	0.07	73	0.07	75	0.02	81	0.07	71	0.05	72	0.03
<b>SMP200</b>	193	0.08	190	0.04	244	0.15	343	0.17	183	0.02	184	0.01
<b>SMP500</b>	527	0.23	498	0.02	505	0.01	478	0.05	492	0.03	473	0.02

In EpiLife™ Medium (**Table 4.11**), the  $H_d$  size of SiNP20, SiNP70 and SMP200 increased in the order of SiNP70>SiNP20>SMP200, while the  $H_d$  size of SMP500 showed little difference from its given size. Particle agglomeration and sedimentation could be detected for SiNP20 and SiNP70; SMP200 showed a  $H_d$  size more than 1 fold larger than its given size, while SMP500 showed a  $H_d$  size (530/488) compatible with the one given by the manufacturer and good dispersion (0.2). This sharp difference in particle behaviour was associated with different media composition, as shown in the negative control DLS measurement, where size average and PDI were higher compared with other media (71/119, 0.5-0.3).

**Table 4.11** DLS assay of colloidal silica in EpiLife™ Medium. Particles were analyzed at 50 µg/ml after 0 and 24 h incubation at 4 °C (storage conditions). Results are expressed as Average size (Ave. (nm)), to indicate the size of measured clusters, and polydispersion index (PDI) to indicate stability of the clusters in solution. Three measurements were performed for each sample using Malvern Zetasizer.

EpiLife™ Medium	50 µg/ml			
	0H		24H	
	Ave. (nm)	PDI	Ave. (nm)	PDI
SiNP20	123	0.6	130	0.9
SiNP70	1215	0.3	3688	1.0
SMP200	314	0.1	362	0.2
SMP500	530	0.1	488	0.2

The particles  $H_d$  size in Medium 106 were displayed in **Table 4.12**. SiNP20 again showed  $H_d$  size more than 4 folds larger than it given size, while SiNP70 retained its given size. The  $H_d$  size of the two SMPs was much smaller than expected with high PDIs, indicating unstable colloidal status.



**Table 4.12** DLS assay of colloidal silica in Medium 106. Particles were analyzed at 50 µg/ml after 0 and 24 h incubation at 4 °C (storage conditions). Results are expressed as Average size (Ave. (nm)), to indicate the size of measured clusters, and polydispersion index (PDI) to indicate stability of the clusters in solution. Three measurements were performed for each sample using Malvern Zetasizer.

Medium 106	50 µg/ml			
	0H		24H	
	Ave. (nm)	PDI	Ave. (nm)	PDI
SiNP20	109	0.3	119	0.2
SiNP70	97	0.2	100	0.2
SMP200	188	0.4	166	0.6
SMP500	87	1.0	48	1.0

Further analysis was performed after 24 h incubation at 37°C (**Table 4.13**) for CM-10% and CM in order to mimic cellular growth conditions. Such analysis showed similar data compared with CM, but high aggregation in CM-10%.

**Table 4.13** DLS assay of colloidal silica in CM-10% and CM after 24 h at 37°C. Results are expressed as Average size (Ave. (nm)), to indicate the size of measured clusters, and polydispersion index (PDI) to indicate stability of the clusters in solution. Five measurements were performed for each sample using Malvern Zetasizer.

37°C	50 µg/ml			
	CM-10%		CM	
	Ave. (nm)	PDI	Ave. (nm)	PDI
24H				
<b>SiNP20</b>	813	0.6	28	1.0
<b>SiNP70</b>	69	0.6	87	0.2
<b>SMP200</b>	135	0.6	213	0.04
<b>SMP500</b>	54	1.0	468	0.1

Additional information on particle stability in solution was sought by Zeta Potential (ZP) analysis of particles at 100 µg/ml. All particles exhibited a weak negative zeta potential (**Table 4.14**) in CM. When suspended in CM-10%, a slight decrease in ZP was detected for the particles  $\geq 70$  nm. These results suggested that due to the weak zeta potential, these particles could be unstable in CM-10% and CM, which could have implications in the mechanism of their cytotoxicity.

**Table 4.14** Zeta potential assay of colloidal silica in CM-10% and CM. Particles were examined at 100 µg/ml using Malvern Zetasizer. Three measurements were performed for each sample using Malvern Zetasizer.

	CM-10%	CM	SiNP20	SiNP70	SMP200	SMP500
CM-10%	-10	N/A	-13	-14	-10	-12
CM	N/A	-11	-13	-18	-19	-14

SEM and TEM were employed to gain information on the shape of particles and to confirm their size as measured by DLS. Initial imaging of particles in CM and CM-10% proved difficult in determination of particle size, due to intrinsic problems during sample preparation linked to the sugars inside the media (data not shown). Subsequently, all the particles were analysed by SEM (**Figure 4.7**) and TEM (**Figure 4.8**) in deionized water at 25  $\mu\text{g/ml}$  to avoid any more background noise. Both imaging studies highlighted the differences in shape between SiNP20, SiNP70, SMP200 and SMP500. In the SEM images, it was observed that SiNP70, SMP200 and SMP500 all retained a perfect spherical shape and size consistent with their given size, while SiNP20 appeared rod shaped and larger than its given size, suggesting the formation of aggregates that was further confirmed by the TEM imaging. In TEM images, SiNP20 showed very distinct signs of agglomeration, making particle size measurement challenging. The rest of the images confirmed that the spherical shape and size of SiNP70, SMP200 and SMP500 were correlated with their given size.

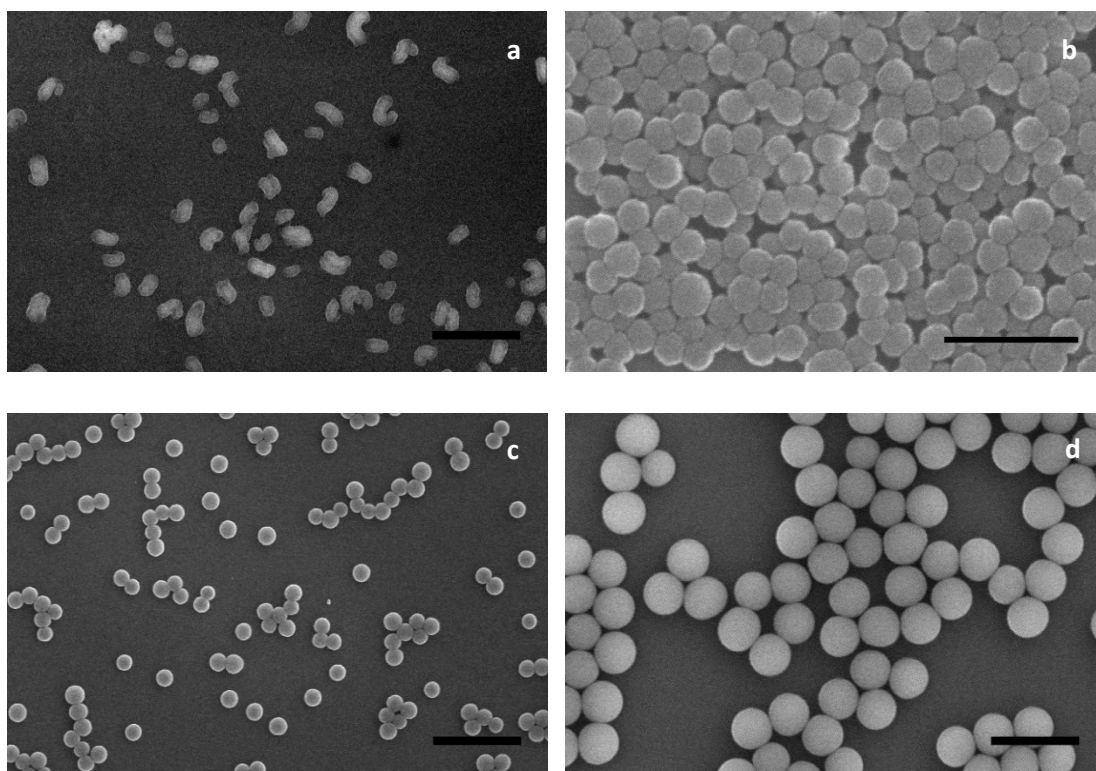


**Figure 4.7** SEM imaging of colloidal silica particles. a: SiNP20; b: SiNP70; c: SMP200; d: SMP500. Particles were analysed in deionized water at 25  $\mu\text{g/ml}$  using Philips XL30 SFE. Scale bar: 1  $\mu\text{m}$ .

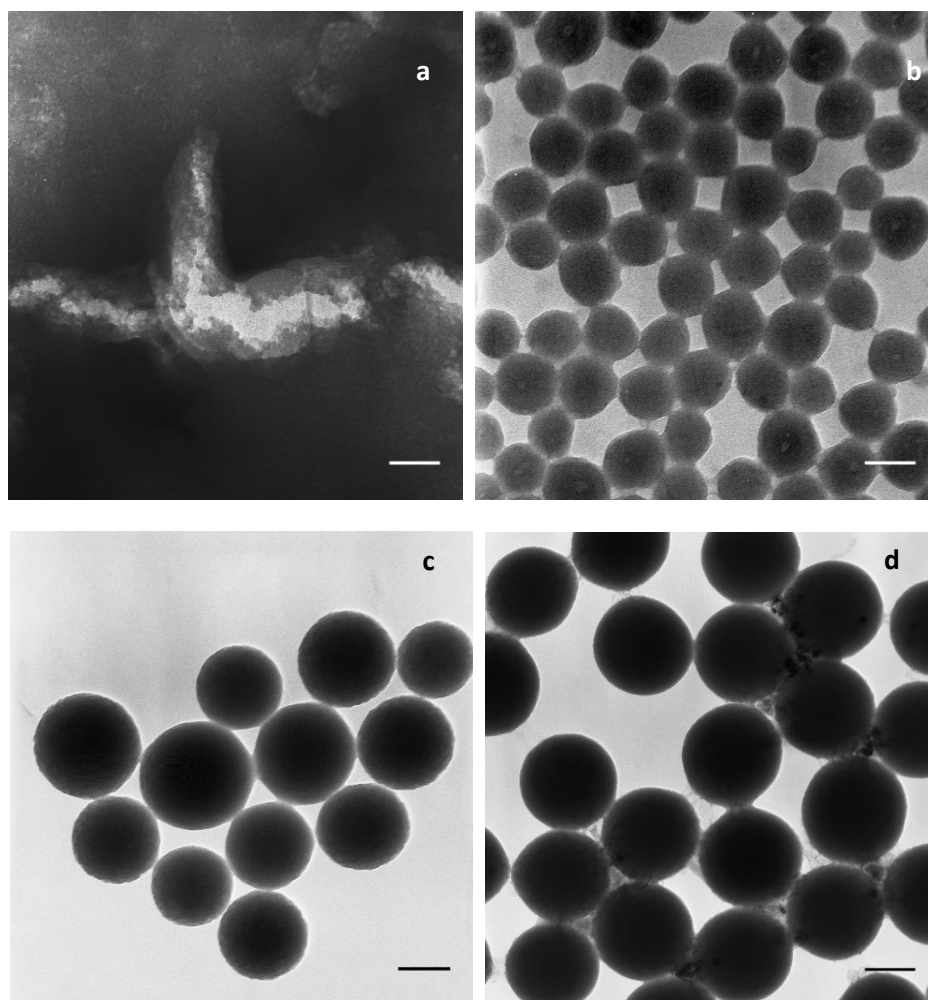


**Figure 4.8** TEM imaging of colloidal silica particle in water. a: SiNP20; b: SiNP70; c: SMP200; d: SMP500. Particles were analysed in deionized water at 25  $\mu\text{g/ml}$  using Philips CM20 TEM (Philips, Netherlands). Scale Bar: 100 nm.

#### 4.2.2 *In vitro* cytotoxicity assessment and wound healing induction on HaCaT cells

**(a) Effects on Cell Viability and Membrane Damage.** In order to assess the cytotoxic potential of colloidal silica particles *in vitro*, human skin HaCaT cells were initially employed. The cells were treated with colloidal silica at 25-100  $\mu\text{g/ml}$  in CM-10%, CM-0.5% and CM, then analysed for cell viability, membrane damage and morphology changes using MTT, LDH and phase contrast microscopy assays. When tested in CM-10%, SiNP20 induced a dose-dependent (15-60%) reduction in cell viability at  $\geq 25 \mu\text{g/ml}$  (**Figure 4.9, blue**

**bars in a**), which was accompanied with a notable increase in LDH release (**Figure 4.9, blue bars in b**), suggesting that cytotoxicity was due to loss of cell membrane integrity. In the same conditions SiNP70 showed a 30% increase in cell viability at 25-50  $\mu\text{g/ml}$  (**Figure 4.9, red bars in a**). The similar remarked effects were also detected for SiNP20 in CM-0.5% and CM (**Figure 4.9, blue bars in c, d, e and f**). On the other hand, SiNP70 only caused a dose-dependent reduction of cell viability and increase of LDH release when tested in CM (**Figure 4.9, red bars in e and f**), while SMP200 and SMP500 had little effect regardless of the test media (**Figure 4.9, green and purple bars**). These results provided evidence that colloidal silica toxicity is size-dependent.

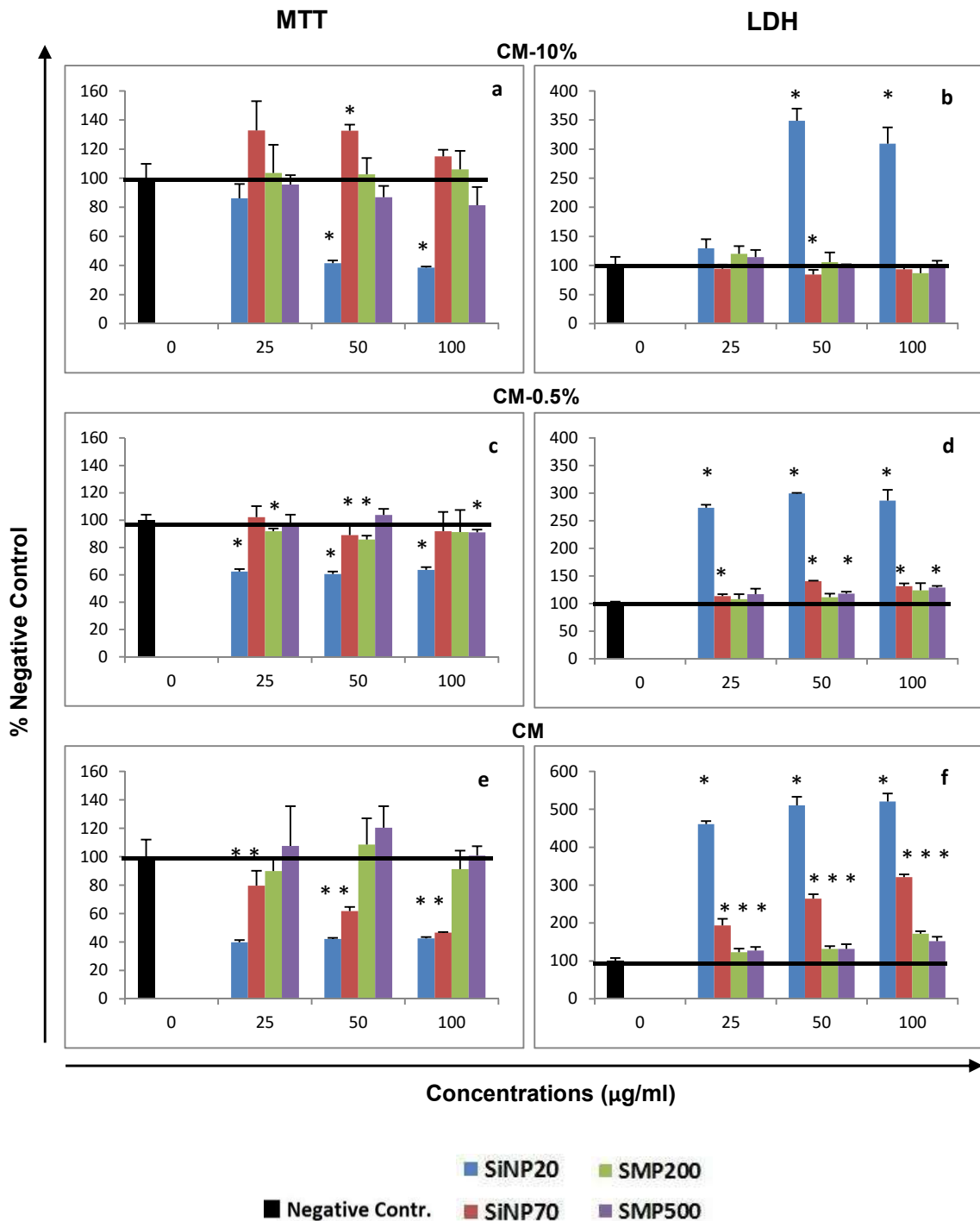


**Figure 4.9** MTT and LDH assays on HaCaT cells following 24 hours treatment with colloidal silica. a, b: cells treated with particles in CM-10%; c, d: cells treated with particles in CM-0.5%; e-f: cells treated with particles in CM. Results were expressed as percentage of negative control, black line serves as reference for normal activity. Each particle concentration was tested in triplicates and the results analysed by one-way ANOVA and Student's t-test. Statistically significant results ( $p < 0.05$ ) are marked with an asterisk (\*) on top of the corresponding bar.

**(b) Effect on morphology.** The difference in morphology between control cells and those treated with colloidal silica for 24 hours were readily observed using phase contrast light microscopy. Control cells maintained in CM-10% showed an adherent growth pattern and morphology with rounded nuclei and membrane projections as indicated by the arrows in **Figure 4.10 (a)**. This feature of cell morphology was associated with active cell growth. Control cells maintained in CM, on the other hand, exhibited an adherent feature with relatively larger nuclei (**Figure 4.10, f compared with a**), which could indicate the blockage of cell division. In CM-10%, SiNP20 caused detachment of cells from the culture surface in a concentration- dependent manner; the remaining attached cells showed irregular shape in CM-10% (**Figure 4.10, b compared with a**). Cells treated with SiNP70 showed very similar morphology as compared with control cells but much higher cell density (**Figure 4.10, c compared with a**), indicative of active cell growth. SMP200 also induced a similar morphological change to SiNP70, although cell density was much lower (**Figure 4.10, d compared with c**). Cells treated with SMP500 showed a flattened morphology, reflecting the impact of the substantial sedimentation of these large particles (**Figure 4.10, e compared with a**). In CM, SiNP20 again caused detachment of cells from the culture surface in a concentration- dependent manner; the remaining attached cells displayed much smaller nuclei (**Figure 4.10, g compared with f**). Cells treated with SiNP70 showed lower density with cell morphology resembling to cells treated with SiNP20 (**Figure 4.10, h compared with g**), suggesting a comparable mechanism of cytotoxicity. Cells treated with SMP200 and SMP500 showed a flattened morphology, reflecting once again the impact of the substantial sedimentation of these large particles (**Figure 4.10, i and j compared with f**). Nonetheless, these cells retained a relatively high density, suggesting that treatment with SMP200 and SMP500 had little effect on cell viability.

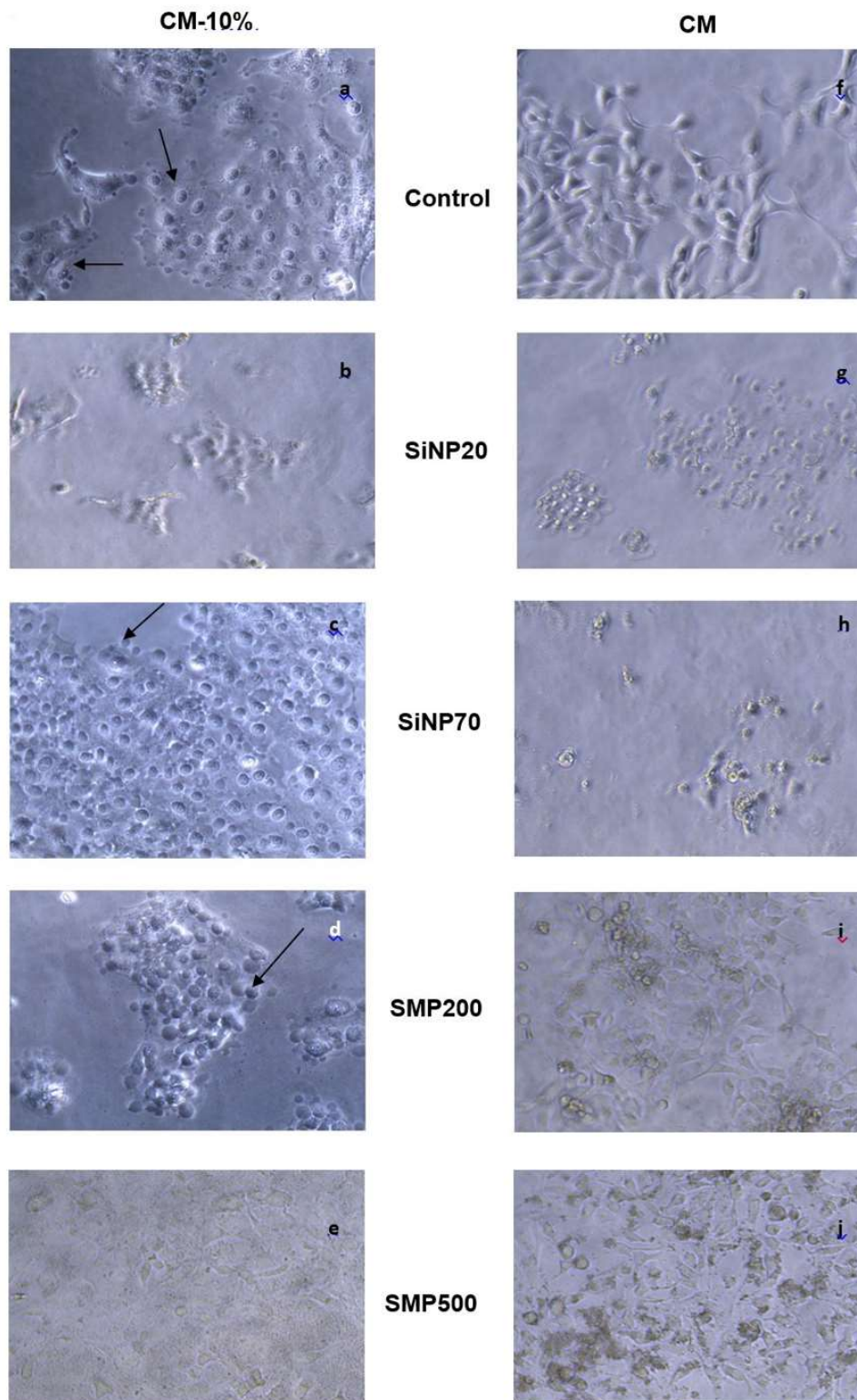


**Figure 4.10** Phase contrast imaging of HaCaT cells after 24 h treatment with colloidal silica. a, f: Untreated cells; b, g: cells treated with SiNP20; c, h: cells treated with SiNP70; d, i: cells treated with SMP200; e, j: cells treated with SMP500. Arrows in images a, c, d indicate cellular proliferation in the corresponding sample.



**(c) Cellular Uptake and subcellular location.** In order to investigate whether silica size-dependent toxicity was associated with cellular uptake of the particles, flow cytometry and TEM imaging were performed. **Figure 4.11** and **Table 4.15** present the flow cytometry profiles of cellular fluorescence intensity and semi quantification of fluorescent positive cells after 24 h treatment with fluorescent particles. The shift of peaks for cells treated with silica of different size to the right of control cells indicates a dose-related increase of cellular uptake of particles. SiNP20 was excluded from this assay as it was not FITC-labelled. When tested in CM-10%, cell uptake was detected for all particles at 25-200  $\mu\text{g/ml}$  and appeared to be higher for SMPs than SiNP70, which was associated with sedimentation of the larger particles in cell culture. When tested in CM on the other hand, the uptake increased markedly with 99-100% of cells being fluorescent positive with silica at 25  $\mu\text{g/ml}$ . Further increase of concentration to 200  $\mu\text{g/ml}$  resulted in a decrease of cell count; the effect was more pronounced for SiNP70, which could be due to the size-dependent toxicity.

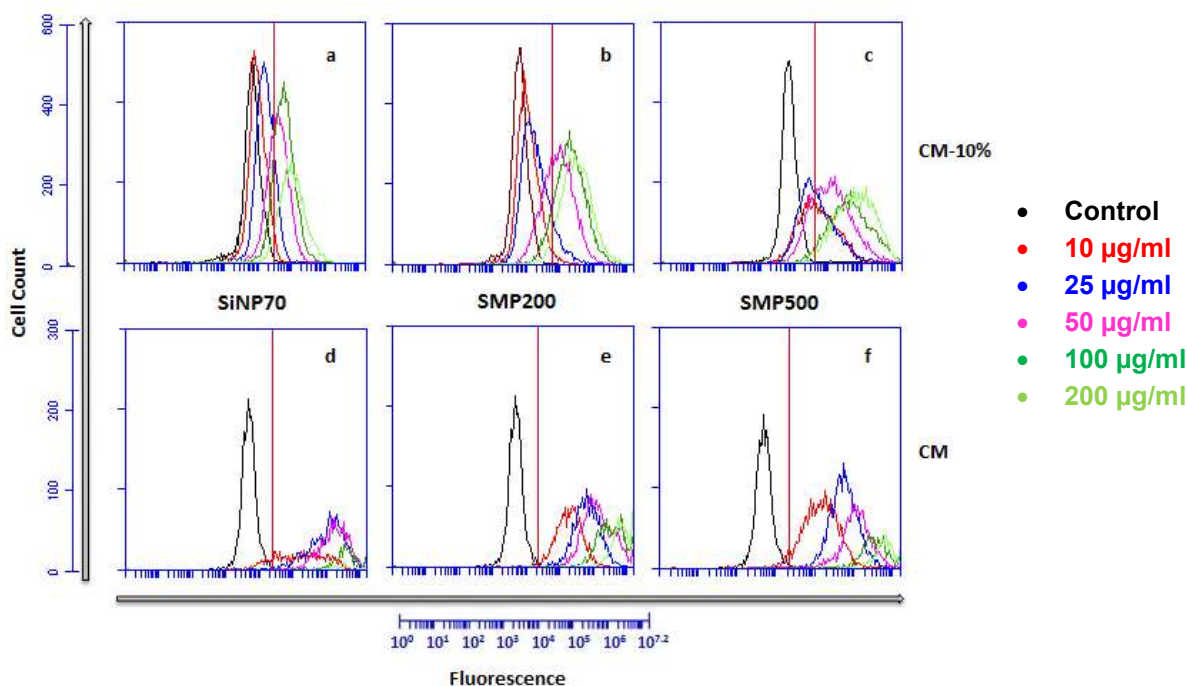
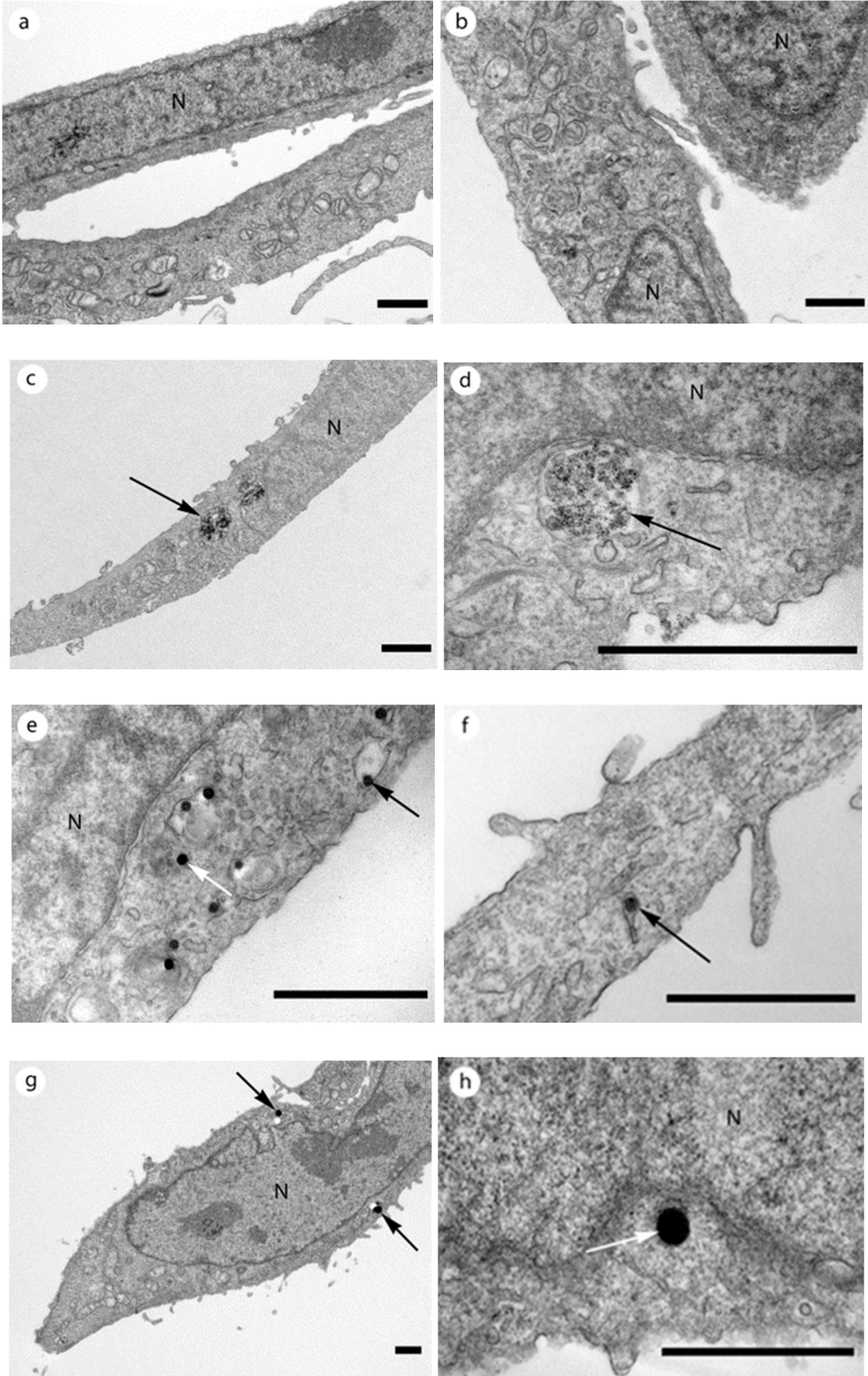


**Figure 4.11** Cellular uptake of colloidal silica measured by flow cytometry. HaCaT cells were treated with colloidal silica at 25-200  $\mu\text{g/ml}$  for 24 h in CM-10% and CM. Results are expressed as number of cells vs. detected fluorescence. The red line separates the left part of the graph, which indicates non-fluorescent cells associated with particle-free cells, from the right part of the graph, which shows fluorescence positive cells associated with silica particles uptake.

**Table 4.15** Flow cytometry quantification of silica nanoparticles' cellular uptake. The results as shown in Figure 4.11 were qualitatively analyzed using BD CSampler software as described in the methods section. Each value of the table corresponds to the percentage of fluorescence detected by the flow cytometer and previously expressed as cell count vs. fluorescence.

	SiNP70		SMP200		SMP500	
	CM-10%	CM	CM-10%	CM	CM-10%	CM
<b>Negative Control</b>	N/A	N/A	N/A	N/A	N/A	N/A
<b>10 µg/ml</b>	2.6%	84.3%	2.1%	98.7%	52.8%	95.5%
<b>25 µg/ml</b>	15.7%	99.3%	11.4%	99.8%	48.7%	99.7%
<b>50 µg/ml</b>	64.9%	99.8%	63.5%	99.9%	76.8%	99.3%
<b>100 µg/ml</b>	84.2%	99.5%	88.3%	99.9%	96.1%	99.6%
<b>200 µg/ml</b>	93.6%	99.1%	95%	99.3%	97.9%	99.6%

To confirm cellular uptake of colloidal silica as well as investigate their cellular location, HaCaT cells were treated with all particles at 25 µg/ml for 24 hours in CM-10% and analyzed by TEM imaging (**Figure 4.12**). Untreated HaCaT cells showed a well-defined cytoplasmic and nuclear ultrastructure, whereas cells treated with silica particles showed evidence of particle uptake. SiNP20 was mostly observed in multi-vesicular bodies/merged endosomes. The lack of a defined shape of these nanoparticles is consistent with SEM and TEM characterization and can be linked to particle agglomeration. SiNP70, SMP200 and SMP500, on the other hand, retained their spherical shape and were found mostly in intracellular vacuoles (**indicated by black arrows in e-g & i- j**) and also free in cytoplasm (**indicated by white arrows in e, h, j**). None of the particles were found in nuclei.



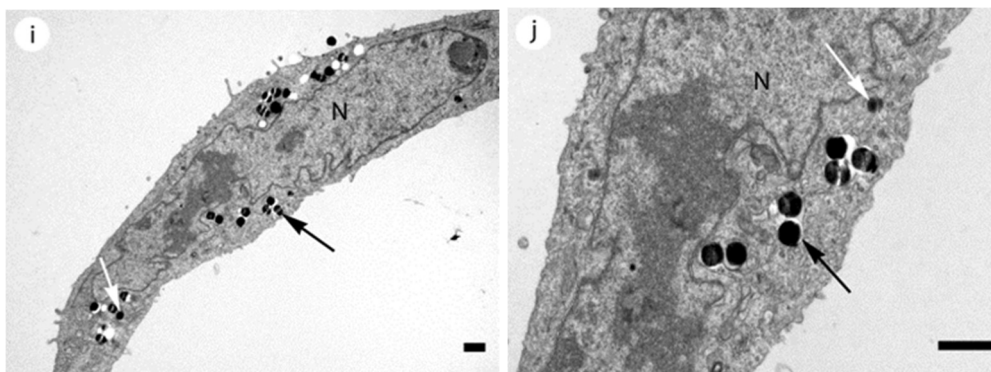


**Figure 4.12** Uptake of colloidal silica inside HaCaT cells measured by TEM imaging. HaCaT cells were treated with particles at 25  $\mu\text{g/ml}$  for 24 h in CM-10%. a,b: untreated cells; c, d: cells treated with SiNP20; e, f: cells treated with SiNP70; g, h: cells treated with SMP200; i, j: SMP500. Scale bar: 1 $\mu\text{m}$ . Black/white arrows indicate the corresponding particle in each image, while N=nucleus. Images taken by Dr. David Dinsdale, MRC Toxicology Unit (Leicester, UK).

**(d) Effect on wound healing.** The effect observed in phase contrast imaging for SiNP70 and SMP200 in CM-10% suggested that silica could have the potential to promote cell growth in a size dependent manner. As cell growth plays a critical role in wound healing, silica particles were further investigated for their effect on wound healing *in vitro* using HaCaT cells in collaboration with Dr. Lino Ferreira and Michela Comune at CNBC (Centre of Neuroscience and Cell Biology), Coimbra (Portugal). As observed via light microscopy, cell migration to the wound area was relatively low for untreated cells (**Figure 4.13, a-d**), whereas cell migration was promoted by all silica particles (**e-t**). A size-, concentration- and time-dependent effect in promoting wound closure was demonstrated using the AxioVision (Carl Zeiss) software. The maximum effect was achieved at 25  $\mu\text{g/ml}$  for all particles at 72 hours (**Figure 4.14**). For SiNP20 and SMP200 (**Figure 4.14, a and c**), further increase in concentration resulted in significant toxicity as observed under light microscopy (data not shown). For SiNP70 and SMP500 (**b and d**), the slowdown of wound closure at 50-200  $\mu\text{g/ml}$  could also be due to cytotoxicity.

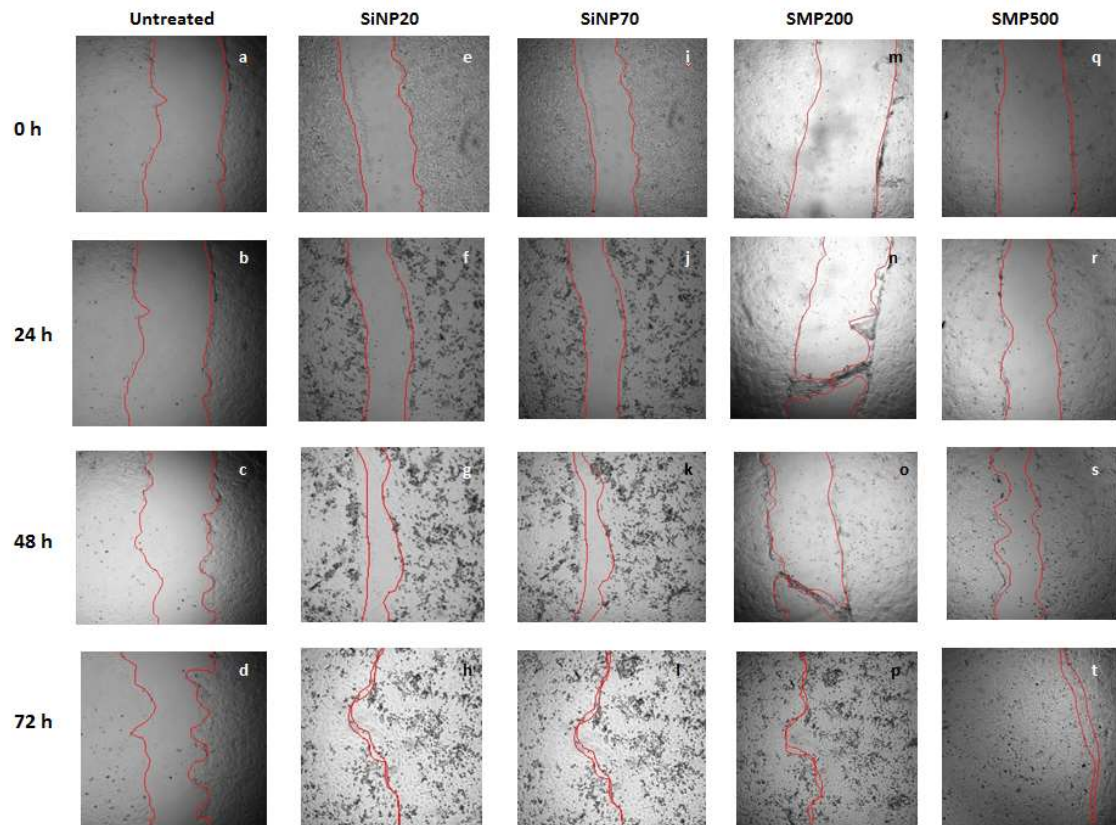


**Figure 4.13** *In vitro* wound healing assay for HaCaT cells treated with colloidal silica (microscopy imaging). Cells were treated 0, 24, 48 and 72 h with colloidal silica 5-200  $\mu\text{g/ml}$  in CM-0.5%. Images show effect at 25  $\mu\text{g/ml}$ . a, d: untreated cells; e, h: cells treated with SiNP20; i, l: cells treated with SiNP70; m, p: cells treated with SMP200; q, t: cells treated with SMP500.

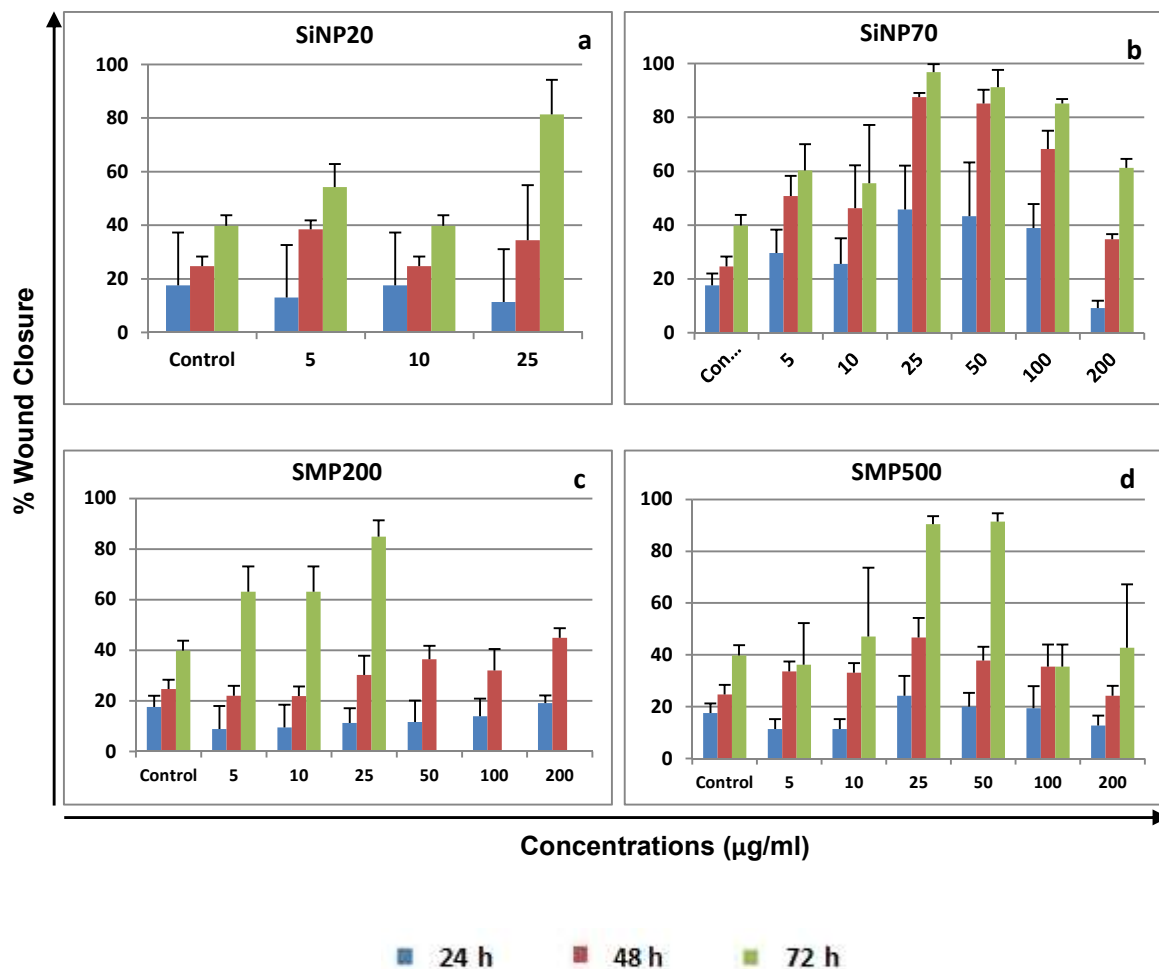
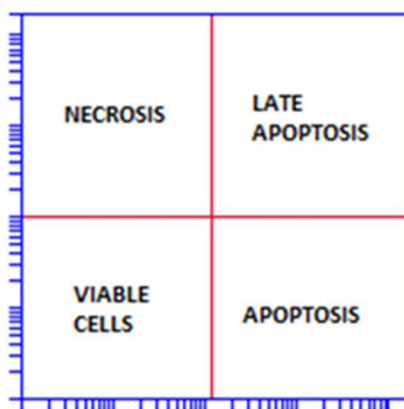


**Figure 4.14** *In vitro* wound healing assay for HaCaT cells treated with colloidal silica. Cells were treated 24, 48 and 72 h with colloidal silica 5-200 µg/ml in CM-0.5%. Results are expressed as percentage of wound closure in particle-treated samples compared with particle-free culture.

**(e) Expression pattern change of cell death genes in response to SiNP20.**

In order to understand the mechanism of colloidal silica cytotoxicity, cells treated with all particles at 10-50 µg/ml for 24 hours were also assessed for induction of necrotic and apoptotic cell death by Annexin V/FITC – Propidium Iodide (PI) staining and subsequent flow cytometer analysis. More than 90% of control cells (cultured in CM-10% and CM without particle treatment) were PI and FITC negative (**Figure 4.15, a-e**). SiNP20 10-50 µg/ml in CM-10% induced a concentration-dependent increase in FITC positive and PI/FITC double positive cells, indicative of apoptosis (**b-d**). On the other hand, SiNP70,

SMP200 and SMP500 did not induce any forms of cell death when tested in CM-10% (data not shown). In CM, however, all particles caused toxicity as indicated by an increase in floating cells observed under the microscope. Owing to severe toxicity, not enough cells could be recovered from the samples treated with SiNP20 for the assay, while enough cells were recovered after treatment with larger particles. SiNP70, SMP200 and SMP500 appeared to induce size- and concentration-dependent increases in PI/FITC double positive cells (**Figure 4.15, f-h, i-k, and l-n**), indicative of apoptotic cell death, with SiNP70 being most toxic.





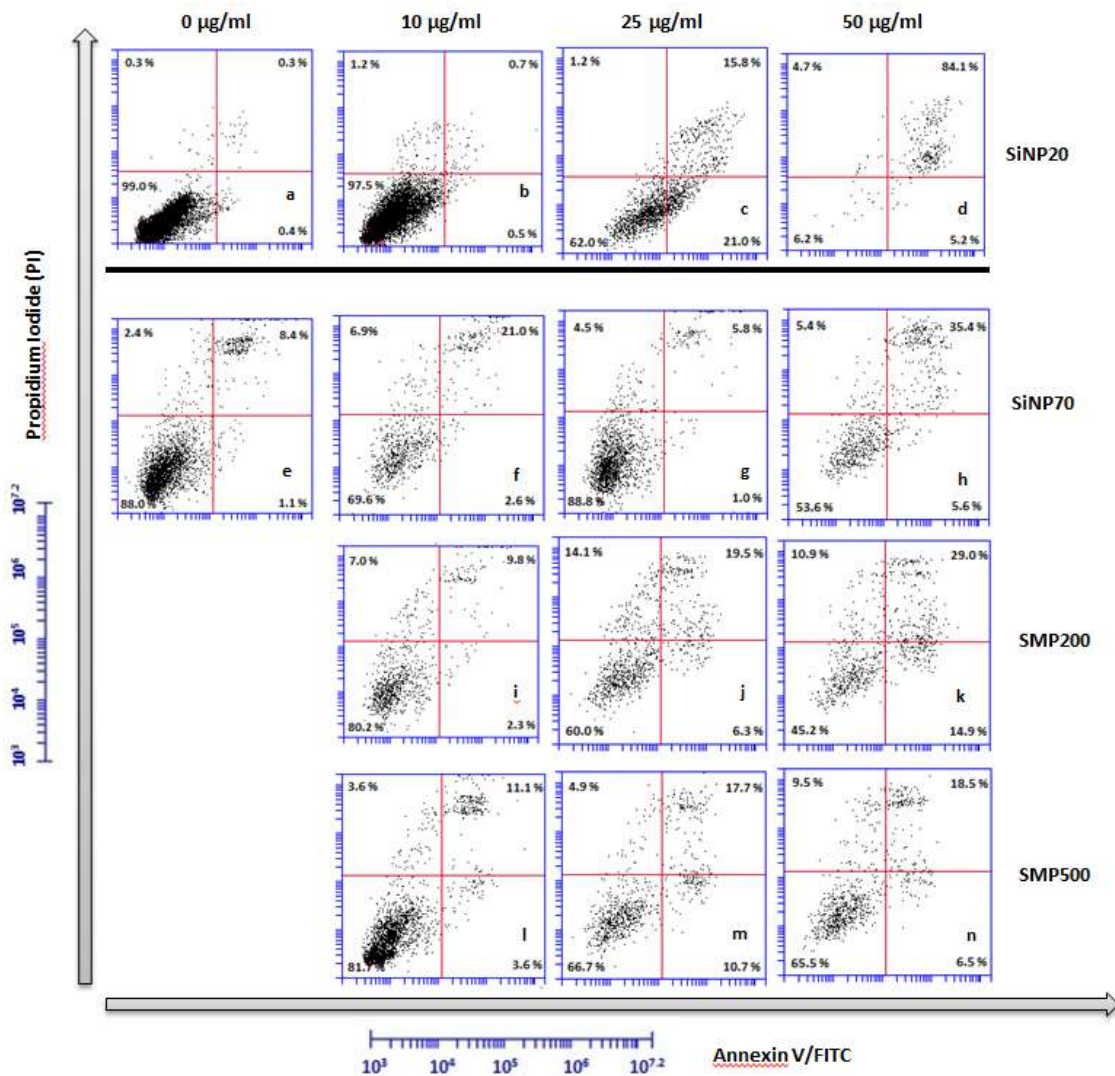


**Figure 4.15** Annexin V/FITC – PI staining of HaCaT cells treated with colloidal silica to detect apoptotic cell death. Cells were treated with colloidal silica 10-50 µg/ml; only CM-10% measurement is shown for cells treated with SiNP20 (b-d), while CM measurements are shown for cells treated with SiNP70, SMP200 and SMP500 (f-n). Following treatment, double staining with propidium iodide (PI) and Annexin V/FITC was performed and using BD Accuri C6 flow cytometer. For each sample 10.000 events were recorded, and the results expressed as PI fluorescence vs. Annexin V/FITC fluorescence. In each quadrant, quantification is reported as percentage of detected fluorescence.

Confirmation of apoptotic cell death was obtained by Western Blot analysis, in collaboration with Dr. Xiao Ming Sun and Prof. Marion MacFarlane, MRC Toxicology Unit, Leicester (UK). HaCaT cells were treated with colloidal silica at



10-100  $\mu\text{g/ml}$  in CM-10% to induce a concentration dependent apoptotic cell death as detected by flow cytometry (**Figure 4.15, b-d**). Proteins were then extracted and the samples were analyzed for the apoptosis specific cleavage of caspase 3. Caspase 3 is part of the caspase family responsible for the caspase-dependent pathways of apoptosis. It is activated by the apoptosome caspase 9/APAF-1. In its activated form it cleaves caspase 2, 6, 8, 10 at the cytoplasm, thus playing a major role in the initial steps of cell death [136]. The degradation of this protein has been associated with apoptosis. As shown in **Figure 4.16**, no caspase 3 degradation was detected in all samples except for sample 4, which was treated with SiNP20 at 50  $\mu\text{g/ml}$  and presented caspase-3 degradation product p17, suggesting activation of apoptosis. This was in accordance with flow cytometry data, as the strongest apoptotic effect was detected in the same conditions. Not enough cells could be retrieved for protein extraction from sample 5, meaning that the toxic effect of SiNP20 is too high at 100  $\mu\text{g/ml}$ .

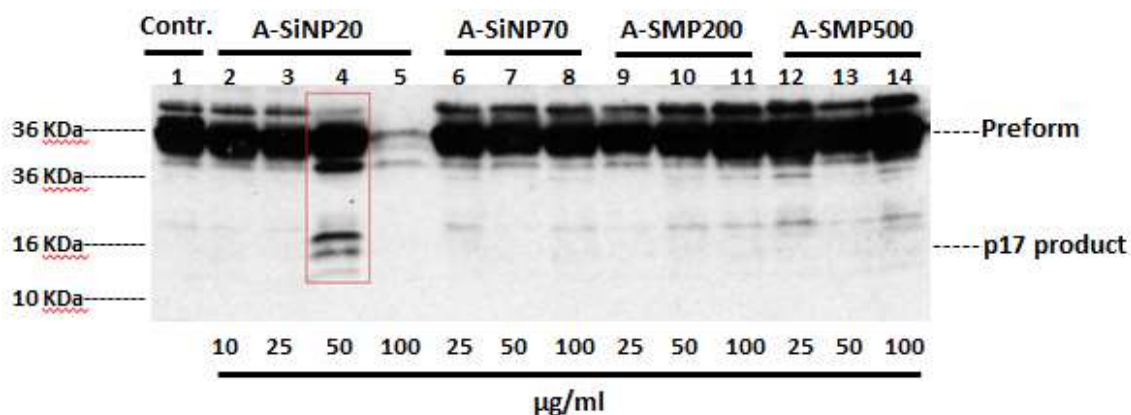


**Figure 4.16** Western blot analysis of caspase 3 in cells treated with colloidal silica in CM-10% for 24 h. Caspase 3 inactive preform is located in the 36 kDa row, while p17 product is located in the 16 kDa row. Image taken by Dr. Xiao Ming, MRC Toxicology Unit (Leicester, UK).

To further explore the molecular mechanism by which silica particles initiate apoptotic cell death in HaCaT cells,  $6 \times 10^5$  cells treated for 24 h with SiNP20 at 10, 25 and 50  $\mu\text{g/ml}$  in CM-10% were subjected to the Human Cell Death

PathwayFinder™ PCR Array assay, which allows to profile the expression of 84 key genes important for the central mechanisms of cellular death: apoptosis, autophagy, and necrosis. The array also includes 5 housekeeping genes, which were Actin (*ACTB*), Beta-2-microglobulin (*B2M*), Glyceraldehyde-3-phosphate dehydrogenase (*GAPDH*), Hypoxanthine phosphoribosyltransferase 1 (*HPRT1*), Ribosomal protein, large, P0 subunit (*RPLP0*). This assay involved total RNA extraction, cDNA synthesis and quantitative PCR (qPCR).

RNA purity before cDNA synthesis was assessed using Picodrop Q100, and expressed as  $A_{260}/A_{280}$  (purity) and  $A_{260}/A_{230}$  (impurities) (**Table 4.16**). The  $A_{260}/A_{280}$  ratio of 1.5-2 is required for specific gene expression assay, while  $A_{260}/A_{230}$  ratio  $\geq 1.0$  indicates cDNA purity. The data shown in **Table 4.16** and **Table 4.17** suggested that all cDNA synthesis products were of sufficient quantity and purity for subsequent real-time PCR assay.

**Table 4.16** Quality of the cDNA synthesis from total RNA extracted from HaCaT cells treated with SiNP20 of different concentrations.

<b>Sample Name</b>	<b>cDNA concentration (ng/μl)</b>	<b>A<sub>260</sub>/A<sub>280</sub> (Purity)</b>	<b>A<sub>260</sub>/A<sub>230</sub> (Impurities)</b>
A1 (Plate A, Neg. Contr.)	156.7	2.080	1.668
A2 (Plate A, SiNP20 10 μg/ml)	160.2	1.998	1.641
A3 (Plate A, SiNP20 25 μg/ml)	163.5	1.911	1.464
A4 (Plate A, SiNP20 50 μg/ml)	157.2	1.989	1.670
B1 (Plate B, Neg. Contr.)	140.5	2.032	1.589
B2 (Plate B, SiNP20 10 μg/ml)	116.7	1.998	0.967
B3 (Plate B, SiNP20 25 μg/ml)	156.4	2.015	1.335
B4 (Plate B, SiNP20 50 μg/ml)	123.2	1.971	1.569
C1 (Plate C, Neg. Contr.)	144.8	2.017	1.204
C2 (Plate C, SiNP20 10 μg/ml)	151.5	2.025	1.431
C3 (Plate C, SiNP20 25 μg/ml)	149.9	2.009	1.238

**Table 4.17** Mean concentrations of cDNA synthesized from total RNA extracted from HaCaT cells treated with SiNP20 of different concentrations. For A), B), C) n° replicates = 3, for D) n° replicates = 2. SD indicates the standard deviation for each sample.

<b>Samples</b>	<b>cDNA concentration Mean ± SD (ng/μl)</b>
A) Control	147 ±8.4
B) SiNP20 10 μg/ml	143±23
C) SiNP20 25 μg/ml	157±6.8
D) SiNP20 50 μg/ml	135±20

The raw real-time PCR data were analyzed with the QIAGEN Data Analysis Web Portal (QIAGEN, UK) and expressed as fold-change for each gene. The fold change was derived from the normalized gene expression in the test samples divided the normalized gene expression in the control samples. The fold change greater or less than two fold was defined as up-regulation or down-regulation for a given gene. As it can be seen in **Figure 4.17**, a change of gene expression pattern was induced by the SiNP20 treatment at different concentrations. At 10 μg/ml, only 5 genes were up-regulated with the rest down regulated (**a**). The up-regulated genes included 3 housekeeping genes, namely actin (*ACTB*), Hypoxanthine phosphoribosyltransferase 1 (*HPRT1*) and ribosomal protein, large, P0 (*RPLP0*), and two cell death regulator genes, *ATP6V1G2* and *PARP1* (**Table 4.18**). The 116 KDa protein PARP1 is located in the nuclei and activated in cells experiencing stress and/or DNA damage. *ATP6V1G2*, a component of H<sup>+</sup> transporting, lysosomal vacuolar ATPase (V-ATPase), mediates acidification of intracellular compartments, which is necessary for protein sorting, zymogen activation, receptor-mediated

endocytosis, and synaptic vesicle proton gradient generation [137]. More genes were up-regulated by SiNP20 at 25  $\mu\text{g/ml}$  (**Figure 4.17, b**), while the majority of genes were down regulated by further increase the concentration to 50  $\mu\text{g/ml}$  (**Figure 4.17, c**). The different down-regulation at 10 and 50  $\mu\text{g/ml}$  were linked with early and late apoptosis respectively as seen **Figure 4.15**. The full list of examined genes and related fold changes are listed in **Table 4.18**.

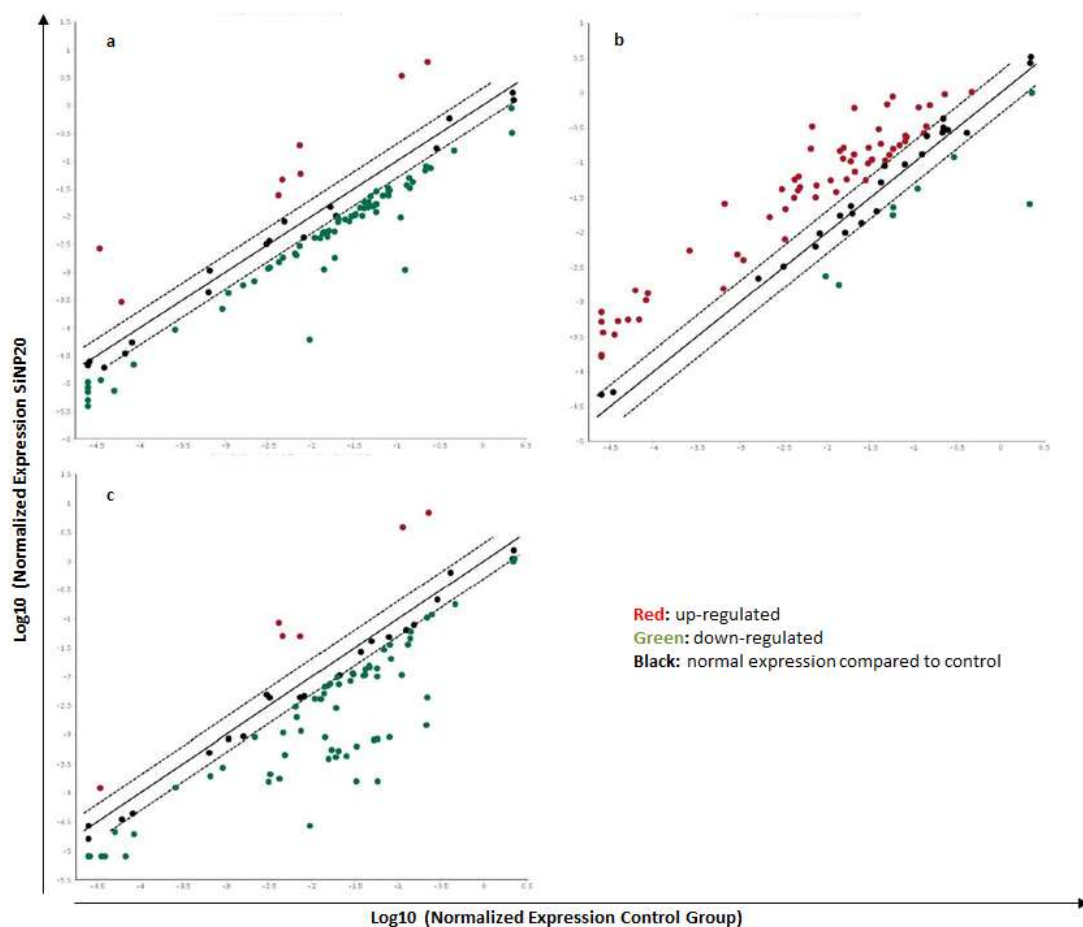


**Figure 4.17** Gene expression scatter plots following HaCaT 24 h treatment with SiNP20 10-50  $\mu\text{g/ml}$  in CM-10%. Results are expressed as Log10 of normalized expression. a: SiNP20 10  $\mu\text{g/ml}$ ; b: SiNP20 25  $\mu\text{g/ml}$ ; c: SiNP20 50  $\mu\text{g/ml}$ . Down-regulated are indicated in green, while red indicates up-regulated genes. Black central line indicates unchanged gene expression. The dotted lines indicate the selected fold regulation threshold (fold =  $\pm 2$ ).

**Table 4.18** Effect of SiNP20 on the expression of mRNAs involved in apoptosis regulation. Full names of the corresponding genes were given with symbols included in brackets; values in red indicate genes up-regulated  $\geq 2$  folds; values in green indicates genes down regulated more than 2 fold; gene descriptions were obtained through UniProt and GENE bank at National Centre for Biotechnology Information (NCBI).

Gene name / Symbol	Description	Expression in SiNP20 10 $\mu\text{g/ml}$	Expression in SiNP20 25 $\mu\text{g/ml}$	Expression in SiNP20 50 $\mu\text{g/ml}$
C-abl oncogene 1 ( <b>ABL1</b> )	Proto-oncogene for a non-receptor tyrosine kinase involved in a variety of cellular processes, including response to stress	-6.34		-3.08
V-akt murine thymoma viral oncogene homolog 1 ( <b>AKT1</b> )	Apoptosis suppressor, phosphorylates and inactivates components of the apoptotic machinery	-2.81	2.38	-3.07
Apoptotic peptidase activating factor 1 ( <b>APAF1</b> )	Its related protein is involved in the initiation of apoptosis	-2.86	7.50	-2.19
Amyloid beta (A4) precursor protein ( <b>APP</b> )	Cell surface receptor and transmembrane precursor protein that is cleaved to form different peptides	-2.72		-2.07
Autophagy related 12 homolog (S. cerevisiae) ( <b>ATG12</b> )	Involved in autophagy	-2.58		
Autophagy related 16-like 1 (S. cerevisiae) ( <b>ATG16L1</b> )	Part of a large protein complex that is necessary for autophagy	-3.34	2.01	-3.31
Autophagy related 3 homolog (S. cerevisiae) ( <b>ATG3</b> )	Encodes a ubiquitin-like-conjugating enzyme involved in autophagy	-3.34		-2.10

Autophagy related 5 homolog (S. cerevisiae) ( <b>ATG5</b> )	Involved in autophagy	<b>-3.80</b>	<b>7.55</b>	<b>-3.79</b>
ATPase, H <sup>+</sup> transporting, lysosomal 13kDa, V1 subunit G2 ( <b>ATP6V1G2</b> )	Encodes a component of vacuolar ATPase (V-ATPase), which mediates intracellular acidification of cells	<b>4.78</b>	<b>23.70</b>	
BCL2-associated X protein ( <b>BAX</b> )	Forms a heterodimer with BCL2, and functions as an apoptotic activator	<b>-4.29</b>		<b>-2.35</b>
B-cell CLL/lymphoma 2 ( <b>BCL2</b> )	Encodes an integral outer mitochondrial membrane protein that blocks the apoptotic death	<b>-3.14</b>	<b>7.55</b>	<b>-2.38</b>
BCL2-related protein A1 ( <b>BCL2A1</b> )	Reduction of the release of pro-apoptotic cytochrome c from mitochondria and block caspase activation	<b>-2.53</b>	<b>3.72</b>	
BCL2-like 1 ( <b>BCL2L1</b> )	Regulation of outer mitochondrial membrane channel (VDAC) opening	<b>-2.81</b>	<b>2.80</b>	<b>-4.13</b>
BCL2-like 11 ( <b>BCL2L11</b> )	Apoptotic activator	<b>-2.65</b>	<b>10.36</b>	<b>-2.13</b>
Beclin 1 ( <b>BECN1</b> )	Involved in autophagy regulation	<b>-2.92</b>	<b>3.34</b>	<b>-2.60</b>
Baculoviral IAP repeat containing 2 ( <b>BIRC2</b> )	Apoptosis inhibition by binding to tumor necrosis factor receptor-associated factors TRAF1 and TRAF2	<b>-2.92</b>	<b>2.55</b>	<b>-2.37</b>
Bcl2 modifying factor ( <b>BMF</b> )	Binds BCL2 proteins and functions as an apoptotic activator	<b>-4.16</b>	<b>5.25</b>	<b>-3.36</b>

Chromosome 1 open reading frame 159 ( <b>C1orf159</b> )	Unknown	<b>-3.34</b>	<b>48.84</b>	<b>-3.39</b>
Caspase 1 ( <b>CASP1</b> )	Induction of apoptosis	<b>-2.99</b>	<b>24.25</b>	<b>-2.14</b>
Caspase 2 ( <b>CASP2</b> )	Apoptosis-related cysteine peptidase	<b>-3.38</b>	<b>15.46</b>	<b>-4.13</b>
Caspase 3 ( <b>CASP3</b> )	Apoptosis-related cysteine peptidase, cleaves and activates caspases 6, 7 and 9, and the protein itself is processed by caspases 8, 9 and 10	<b>-2.95</b>	<b>5.43</b>	<b>-2.75</b>
Caspase 6 ( <b>CASP6</b> )	Downstream enzyme in the caspase activation cascade	<b>-2.55</b>	<b>29.45</b>	<b>-2.77</b>
Caspase 7 ( <b>CASP7</b> )	Apoptosis-related cysteine peptidase	<b>-2.81</b>		<b>-57.63</b>
Caspase 9 ( <b>CASP9</b> )	Apoptosis-related cysteine peptidase	<b>-2.72</b>		<b>-20.14</b>
Coiled-coil domain containing 103 ( <b>CCDC103</b> )	Protein homodimerization activity	<b>-2.55</b>	<b>13.55</b>	<b>-4.32</b>
CD40 molecule ( <b>CD40</b> )	TNF receptor superfamily member 5, receptor on antigen-presenting cells of the immune system	<b>-2.79</b>	<b>13.42</b>	<b>-24.09</b>
CD40 ligand ( <b>CD40LG</b> )	Protein expressed on the surface of T cells, regulates B cell function by engaging CD40		<b>6.48</b>	
CASP8 and FADD-like apoptosis regulator ( <b>CFLAR</b> )	Regulator of apoptosis structurally similar to caspase-8	<b>-3.54</b>	<b>10.51</b>	<b>-39.96</b>



COMM domain containing 4 ( <b>COMMD4</b> )	Inhibits nuclear factor kappaB (NF-kappaB), a transcription factor affecting apoptosis	-2.14	13.90	
Cathepsin B ( <b>CTSB</b> )	Involved in the proteolytic processing of amyloid precursor protein (APP)	-4.76	-3.23	-5.73
Cathepsin S ( <b>CTSS</b> )	Lysosomal cysteine proteinase	-2.47		
Cylindromatosis ( <b>CYLD</b> )	Turban tumor syndrome; deubiquitinating enzyme	-2.92		-2.15
Defensin, beta 1 ( <b>DEFB1</b> )	Antimicrobial peptide implicated in the resistance of epithelial surfaces to microbial colonization	-2.76		
DENN/MADD domain containing 4A ( <b>DENND4A</b> )	C-myc promoter-binding protein	-3.15		-3.00
DNA fragmentation factor, 45kDa, alpha polypeptide ( <b>DFFA</b> )	Substrate for caspase-3; triggers DNA fragmentation during apoptosis	-3.35	3.01	-2.26
Dihydropyrimidinase-like 4 ( <b>DPYSL4</b> )	N/A		8.19	-8.38
Eukaryotic translation initiation factor 5B ( <b>EIF5B</b> )	Initiation of translation	-3.65	4.30	
Estrogen receptor 1 ( <b>ESR1</b> )	Ligand-activated transcription factor	-3.91	15.63	-4.36
Fas ( <b>FAS</b> )	TNF receptor superfamily, member 6; contains a death domain, shown to play a central role in	-2.32	3.54	

	apoptosis			
Fas ligand ( <b>FASLG</b> )	Induction of apoptosis by binding to FAS	<b>-2.37</b>	<b>28.31</b>	<b>-3.08</b>
Forkhead box I1 ( <b>FOXI1</b> )	Transcription factor; specific function unknown		<b>13.61</b>	<b>-4.78</b>
Glucosidase, alpha; acid ( <b>GAA</b> )	Degradation of glycogen to glucose in lysosomes	<b>-3.09</b>	<b>2.98</b>	<b>-3.12</b>
Growth arrest and DNA-damage-inducible, alpha ( <b>GADD45A</b> )	Environmental stress response	<b>-11.62</b>	<b>-2.65</b>	<b>-10.44</b>
UDP-N-acetyl-alpha-D-galactosamine:polypeptide N-acetylgalactosaminyltransferase 5 ( <b>GALNT5</b> )	N/A	<b>-3.58</b>	<b>2.00</b>	<b>-3.65</b>
Growth factor receptor-bound protein 2 ( <b>GRB2</b> )	Involved in the signal transduction pathway	<b>-2.29</b>		<b>-3.16</b>
HSPB (heat shock 27kDa) associated protein 1 ( <b>HSPBAP1</b> )	Encodes a protein that binds toHsp27, which is involved with cell growth and differentiation	<b>-2.76</b>	<b>-7.82</b>	<b>-2.69</b>
Huntingtin ( <b>HTT</b> )	Widely expressed and is required for normal development	<b>-2.62</b>	<b>5.05</b>	<b>-2.67</b>
Interferon, gamma ( <b>IFNG</b> )	Antiviral, immunoregulatory and anti-tumor properties; potent activator of macrophages	<b>-3.03</b>	<b>9.54</b>	<b>-4.34</b>
Insulin-like growth factor 1 (somatomedin C) ( <b>IGF1</b> )	Involved in mediating growth and development	<b>-2.80</b>	<b>20.97</b>	<b>-2.10</b>
Insulin-like growth factor 1	Highly overexpressed in malignant tissues	<b>-2.94</b>	<b>4.42</b>	<b>-3.86</b>

receptor ( <b>IGF1R</b> )	where it functions as an anti-apoptotic agent by enhancing cell survival			
Insulin ( <b>INS</b> )	Glucose uptake	<b>-3.54</b>	<b>20.49</b>	<b>-3.08</b>
Immunity-related GTPase family, M ( <b>IRGM</b> )	Regulation of autophagy	<b>-2.94</b>	<b>6.70</b>	
Junctophilin 3 ( <b>JPH3</b> )	Component of junctional complexes between the plasma membrane and endoplasmic/sarcoplasmic reticulum	<b>-4.98</b>	<b>6.92</b>	<b>-3.08</b>
Kv channel interacting protein 1 ( <b>KCNIP1</b> )	Member of the family of cytosolic voltage-gated potassium (Kv) channel-interacting proteins (KCNIPs)	<b>-6.83</b>	<b>10.88</b>	<b>-2.41</b>
Myelin associated glycoprotein ( <b>MAG</b> )	Involved in the myelination process	<b>-2.95</b>	<b>28.25</b>	<b>-3.08</b>
Microtubule-associated protein 1 light chain 3 alpha ( <b>MAP1LC3A</b> )	Microtubule-associated proteins which mediate the physical interactions between microtubules and components of the cytoskeleton	<b>-2.73</b>	<b>6.51</b>	<b>-15.77</b>
Mitogen-activated protein kinase 8 ( <b>MAPK8</b> )	Activated by tumor-necrosis factor alpha (TNF-alpha) to induce apoptosis	<b>-2.97</b>	<b>3.34</b>	<b>-52.06</b>
Myeloid cell leukemia sequence 1 (BCL2-related) ( <b>MCL1</b> )	Anti-apoptotic protein member of the Bcl-2 family	<b>-3.01</b>		<b>-50.23</b>
Nuclear factor of kappa light polypeptide gene enhancer in B-cells 1 ( <b>NFKB1</b> )	Involved in a wide variety of biological functions		<b>3.40</b>	<b>-30.42</b>
Nucleolar protein 3 ( <b>NOL3</b> )	Anti-apoptotic protein; down-regulates caspase 2, caspase 8		<b>9.08</b>	<b>-10.79</b>

	and tumor protein p53			
Olfactory receptor, family 10, subfamily J, member 3 ( <b>OR10J3</b> )	Recognition and G protein-mediated transduction of odorant signals		<b>13.86</b>	<b>-3.21</b>
Poly (ADP-ribose) polymerase 1 ( <b>PARP1</b> )	Regulation of differentiation, proliferation, tumor transformation, regulation of cell recovery from DNA damage	<b>7.75</b>	<b>6.22</b>	<b>-6.55</b>
Poly (ADP-ribose) polymerase 2 ( <b>PARP2</b> )	Caralysis of a poly(ADP-ribosyl)ation reaction	<b>-2.03</b>	<b>2.73</b>	<b>-68.30</b>
Phosphoinositide-3-kinase, class 3 ( <b>PIK3C3</b> )	Autophagy-related	<b>-2.14</b>	<b>6.41</b>	<b>-38.29</b>
Poliovirus receptor ( <b>PVR</b> )	Transmembrane glycoprotein; mediates cell attachment to the extracellular matrix	<b>-2.88</b>	<b>2.54</b>	<b>-87.65</b>
<b>RAB25</b>	Member RAS oncogene family; controls the return of internalized membrane-associated moieties to the cell surface	<b>-3.15</b>		<b>-147.76</b>
Ribosomal protein S6 kinase, 70kDa, polypeptide 1 ( <b>RPS6KB1</b> )	Signaling to promote protein synthesis, cell growth, and cell proliferation. Activity has been associated with human cancer	<b>-3.48</b>	<b>2.43</b>	<b>-64.61</b>
S100 calcium binding protein A7A ( <b>S100A7A</b> )	Inflammatory response		<b>12.79</b>	
Synuclein, alpha ( <b>SNCA</b> )	non A4 component of amyloid precursor; involved in signaling and membrane trafficking		<b>39.12</b>	<b>-3.36</b>

Spermatogenesis associated 2 ( <b>SPATA2</b> )	Cellular differentiation	<b>-3.48</b>	<b>5.51</b>	<b>-45.11</b>
Sequestosome 1 ( <b>SQSTM1</b> )	Functions as a scaffolding/adaptor protein in concert with TNF receptor-associated factor 6 to mediate activation of NF-kB in response to upstream signals		<b>-2.42</b>	
Synaptonemal complex protein 2 ( <b>SYCP2</b> )	Part of the synaptonemal complex, which links homologous chromosomes during the prophase of meiosis	<b>-156.33</b>	<b>-4.07</b>	<b>-355.10</b>
Transmembrane protein 57 ( <b>TMEM57</b> )	Unknown		<b>2.42</b>	
Tumor necrosis factor ( <b>TNF</b> )	Cytokine involved in a wide spectrum of biological processes including apoptosis		<b>13.77</b>	
Tumor necrosis factor receptor superfamily, member 10a ( <b>TNFRSF10A</b> )	Receptor that transduces cell death signal and induces cell apoptosis			<b>-2.01</b>
Tumor necrosis factor receptor superfamily, member 11b ( <b>TNFRSF11B</b> )	Osteoblast-secreted decoy receptor that functions as a negative regulator of bone resorption		<b>2.41</b>	
Tumor necrosis factor receptor superfamily, member 1A ( <b>TNFRSF1A</b> )	One of the major receptors for the tumor necrosis factor-alpha; mediates apoptosis and functions as a regulator of inflammation	<b>-2.58</b>	<b>2.29</b>	<b>-3.25</b>
Tumor protein p53 ( <b>TP53</b> )	Tumor suppressor protein responding to cellular stresses, thereby inducing		<b>2.19</b>	<b>-362.14</b>

	apoptosis			
TNF receptor-associated factor 2 ( <b>TRAF2</b> )	Associates with, and mediates the signal transduction from members of the TNF receptor superfamily	<b>-3.44</b>	<b>-2.54</b>	<b>-205.61</b>
Thioredoxin-like 4B ( <b>TXNL4B</b> )	Mitotic division	<b>-3.06</b>	<b>3.35</b>	
Unc-51-like kinase 1 (C. elegans) ( <b>ULK1</b> )	Serine/threonine-protein kinase involved in autophagy in response to starvation	<b>-12.60</b>		<b>-15.68</b>
X-linked inhibitor of apoptosis ( <b>XIAP</b> )	Member of a family of apoptotic suppressor proteins sharing the conserved baculovirus IAP repeat, necessary for their anti-apoptotic function	<b>-10.42</b>		<b>-6.61</b>
Actin, beta ( <b>ACTB</b> )	Involved in cell motility, structure, and integrity	<b>26.44</b>	<b>4.12</b>	<b>29.61</b>
Hypoxanthine phosphoribosyltransferase 1 ( <b>HPRT1</b> )	Central role in the generation of purine nucleotides through the purine salvage pathway	<b>5.77</b>		<b>20.41</b>
Ribosomal protein, large, P0 ( <b>RPLP0</b> )	Encodes a ribosomal protein that is a component of the 60S subunit	<b>29.68</b>		<b>33.70</b>

#### 4.2.3 *In vitro* toxicity potential in other human skin cells

To investigate whether the size-dependent toxicity of silica particles as detected in HaCaT cells is cell type dependent, the same group of colloidal silica particles of different size was assessed for cytotoxicity potential in three more human skin cell types including K17 keratinocytes, Human Dermal Fibroblasts (HDF) and BJ fibroblasts.

**Size-dependent toxicity on K17 keratinocytes and Human Dermal Fibroblasts (HDF).** The cell type dependent effects of the colloidal silica were further investigated in additional human keratinocytes and fibroblast cell lines in collaboration with Dr. Xavier Vigé and Dr. Sara Vicente in Sanofi Chilli-Mazarin (France). Assays of cytotoxicity, namely WST-1, Caspase 3/7 activity and Propidium Iodide measurement were conducted using the same cell culture and treatment conditions that have been tested for HaCaT cells.

In K17 keratinocytes, WST-1 assay was used to assess cell viability. After 24 hours treatment with colloidal silica at 5-200  $\mu\text{g/ml}$ , a clear size- and concentration-dependent effect was detected (**Figure 4.18**). SiNP20 caused a 50% reduction of cell viability at 25  $\mu\text{g/ml}$ , with the lowest effect concentration of 10  $\mu\text{g/ml}$ . For SiNP70, a 20% reduction of cells viability was detected at 200  $\mu\text{g/ml}$ , the highest concentration tested. For larger silica, on the other hand, SMP200 showed up to 20% increase in viability with the effect not following dose-dependent pattern, whereas SMP500 showed a reduction of cell at 10-25  $\mu\text{g/ml}$  and an increase of cell viability at 100-200  $\mu\text{g/ml}$ .

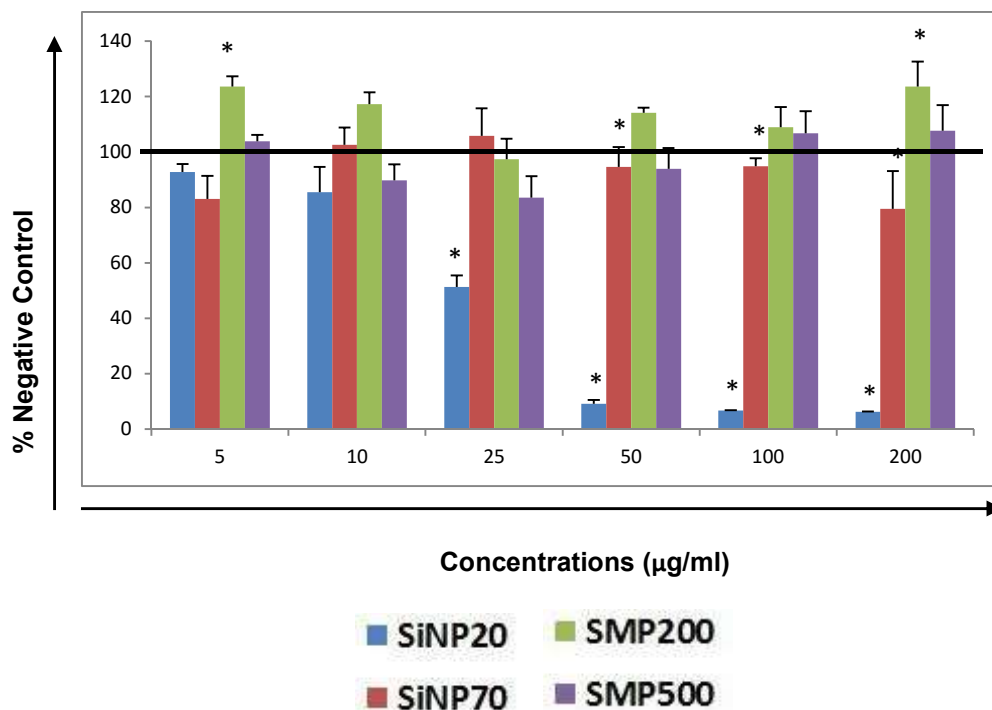


**Figure 4.18** WST-1 analysis of cell viability in K17 keratinocytes treated with colloidal silica. Cells were treated with colloidal silica 10-200 µg/ml for 24 h. Results were expressed as percentage of negative control; black line serves as reference for normal activity. Each particle concentration was tested in triplicates and the results analyzed by one-way ANOVA and Student's t-test. Statistically significant results ( $p < 0.05$ ) are marked with an asterisk (\*) on top of the corresponding bar.

The toxicity potential of colloidal silica in K17 cells was further characterized using the Propidium Iodide (PI) assay after 24 h treatment with Triton X-100 0.025% as positive control. Triton X-100 was chosen because it is widely used to lyse cells or to permeabilize the membranes of living cells. In this study the increase of PI would give indication of cell membrane damage and necrotic cell death. As expected, staurosporine induced an 80% increase of PI staining cells. As consistent with the effect in cell viability, SiNP20 induced a dose-dependent increase of PI, while the other particles had little effect in PI uptake (**Figure 4.19**).



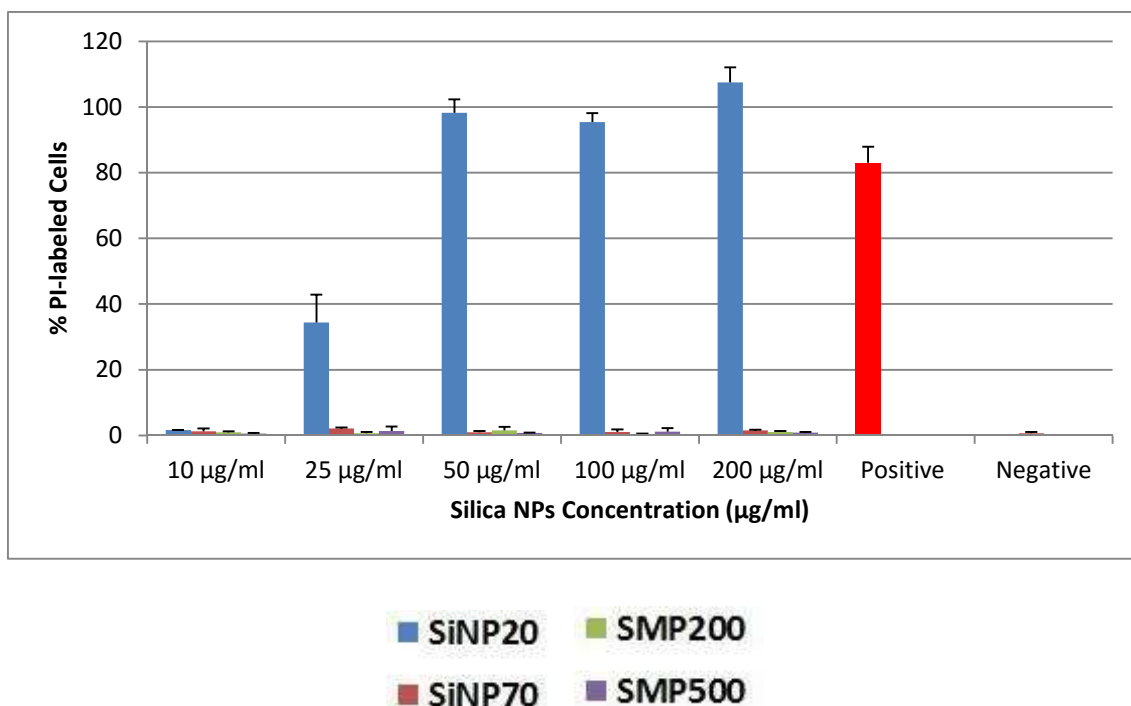


**Figure 4.19** Propidium Iodide measurement of K17 keratinocytes after treatment with colloidal silica. Cells were treated with colloidal silica at 10-200 µg/ml for 24 hours, plus Triton X-100 0.025% for 15 minutes at 37 °C as positive control.

To investigate whether the cytotoxicity of colloidal silica in K17 involved apoptotic cell death through activation of the caspase pathway, the cells were subjected to the analysis of caspase 3/7 activity (**Figure 4.20**). For this assay, staurosporine 10 µM was also added as positive control. Staurosporine was chosen because it is routinely used in apoptosis assays, as it induces apoptotic cell death by two different pathways, one caspase-dependent and one caspase independent [138]. As expected, the positive control showed a high level (more than 5 folds) induction of the caspase 3/7 activity. As consistent with its effect in reduction of cell viability, SiNP20 at 10 µg/ml induced an induction of the caspase activity, while the inhibitory effect at 100 µg/ml was consistent with the loss of cell viability and subsequent loss of total proteases observed in **Figure 4.18** and **Figure 4.19**. Little to no effect was detected for the rest of the particles, consistent with the lack of toxicity as detected by the WST-1 and PI assays.

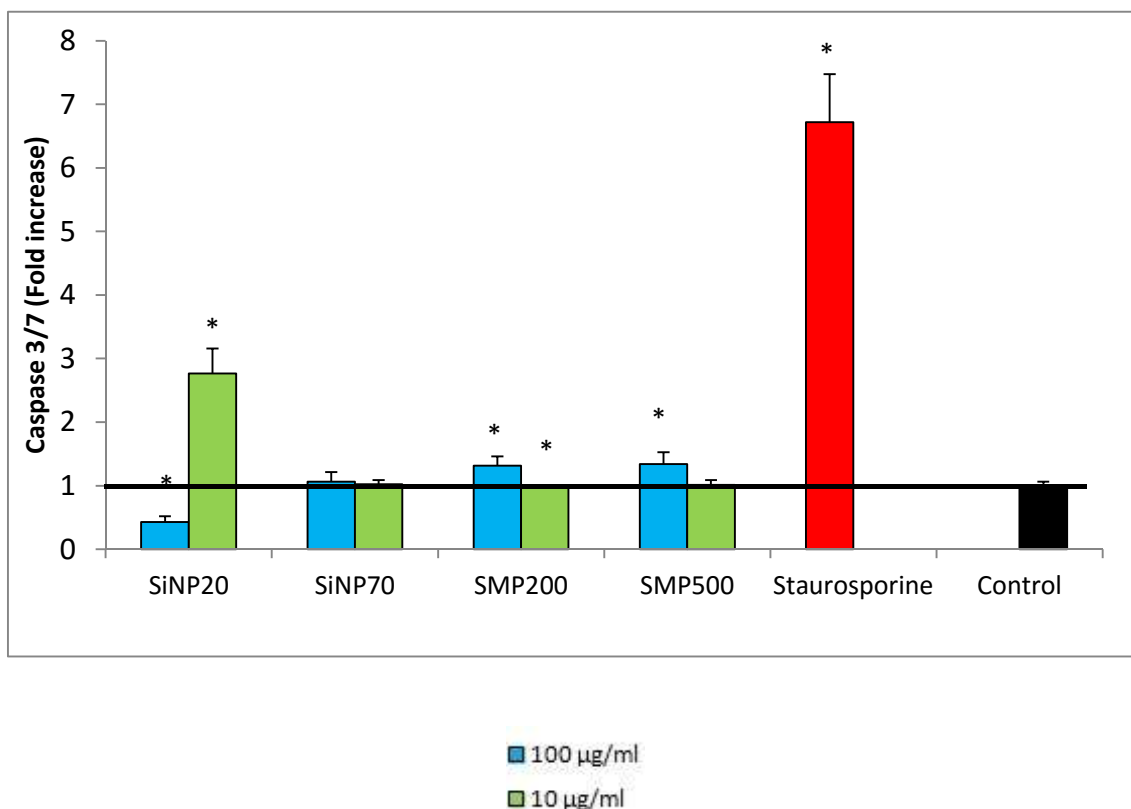


**Figure 4.20** Caspase 3/7 assay on K17 keratinocytes treated with colloidal silica. Cells were treated with colloidal silica at 10 and 100 µg/ml for 24 hours, plus staurosporine 10 µM as positive control, for 6 hours at 37°C. Results were expressed as fold increase of caspase 3/7; black line serves as reference for normal activity. Each particle concentration was tested in triplicates and the results analysed by one-way ANOVA and Student's t-test. Statistically significant results ( $p < 0.05$ ) are marked with an asterisk (\*) on top of the corresponding bar.

To take the advantage of the confocal microscopy technique developed in the collaborator's lab in Sanofi, the mechanism of silica toxicity in relation to particle internalization in K17 cells was further investigated. Cells were treated with fluorescent silica particles 70-500 nm at 10 µg/ml, double stained with Hoechst 33342 and ActinRed™, and then subjected to confocal imaging to establish particles internalization and their localization inside cells. SiNP20 was excluded from the test as they were not FITC labelled. After 2 hours of treatment, K17 keratinocytes showed a low level of particles' internalization, with most of the particles being seen outside the cells and only a few clusters located inside cells (**Figure 4.21, a-c**). After 24 hours there was an increased uptake for all

particles, which were found clustering around the nuclei in a size-independent manner, meaning more uptake was detected for SMP200 and SMP500 than SiNP70 (**Figure 4.21, d-f**). As shown in the Z-stacks, which combine multiple images taken at different focus distances in order to achieve a greater depth of field (DOF), no particles could be detected inside the nuclei for all three sized particles (**Figure 4.22**).

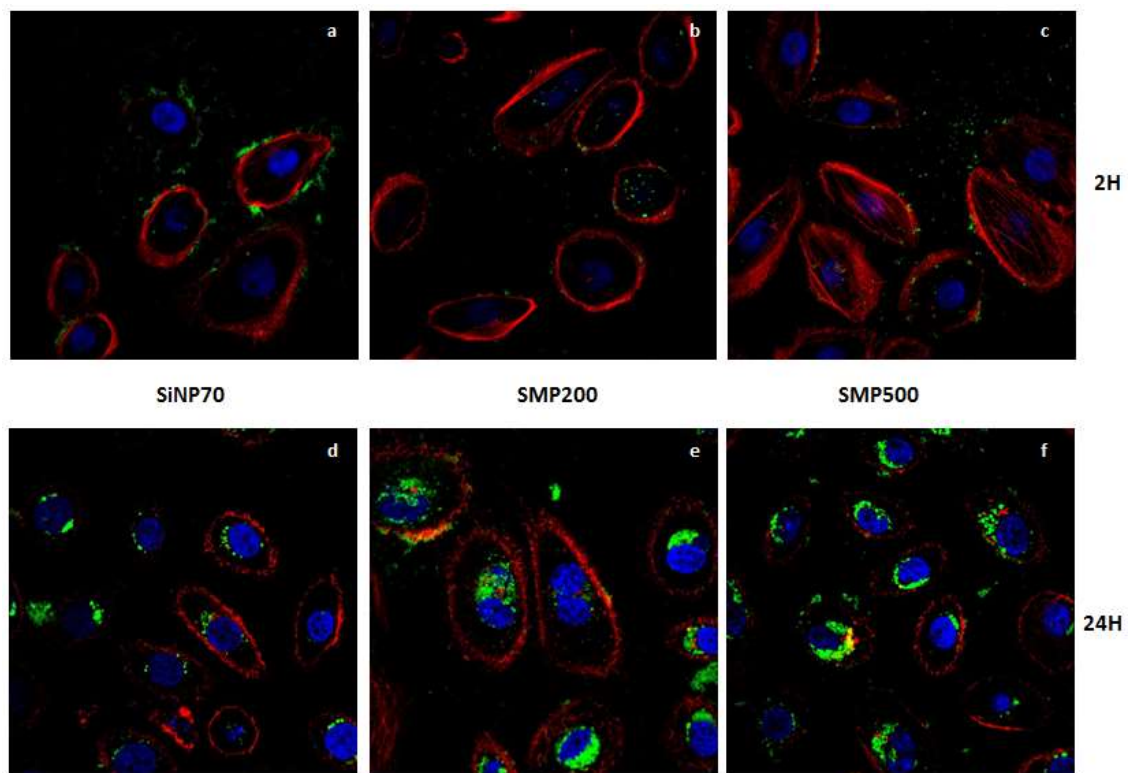


**Figure 4.21** Confocal microscopy imaging of K17 keratinocytes treated with colloidal silica. Cells were treated with FITC-particles (green) at 10  $\mu\text{g}/\text{ml}$  and co-stained with Hoechst 33342 for nuclei (blue) and actin (red).

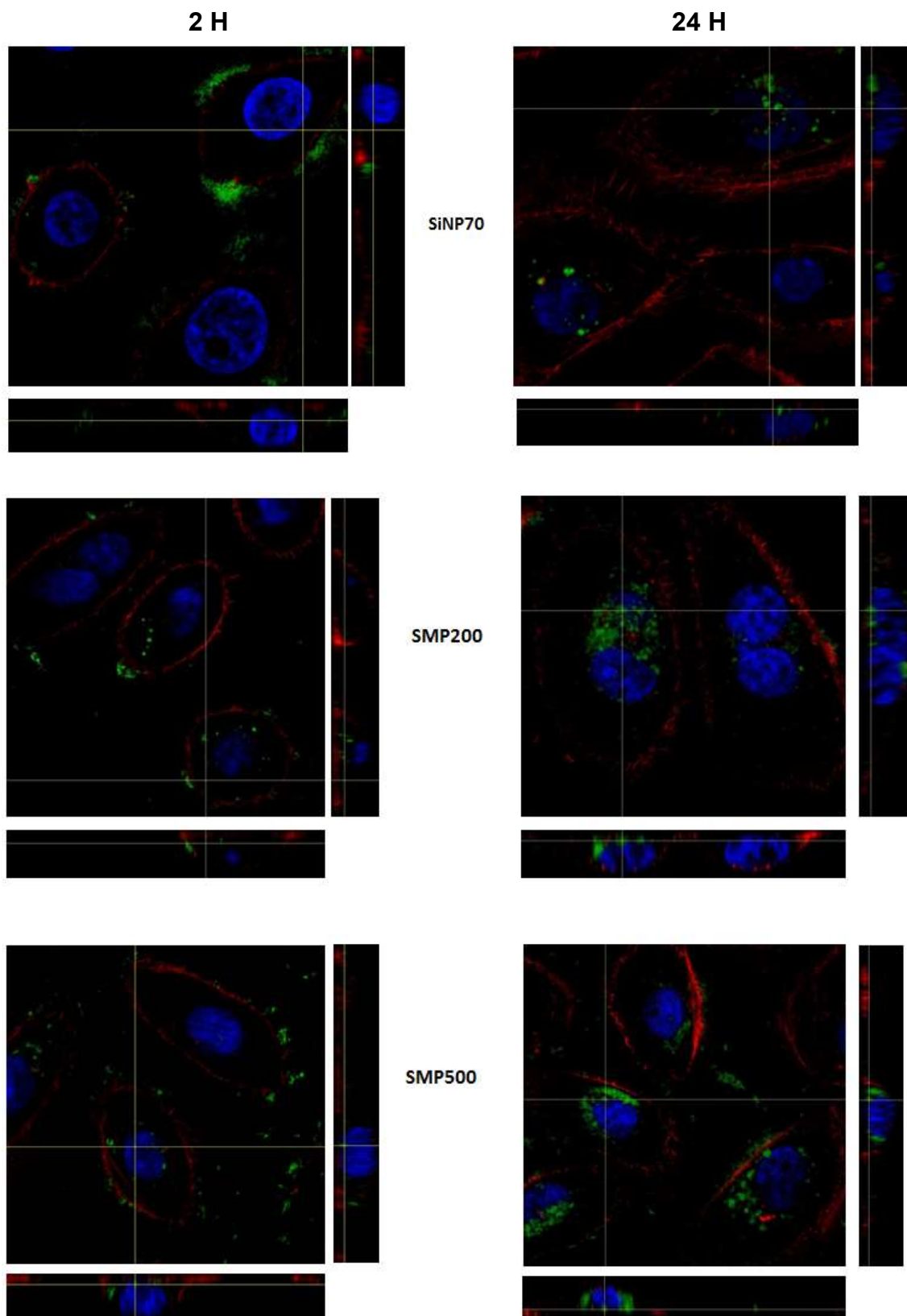


**Figure 4.22** Z-Stacks of K17 keratinocytes treated with colloidal silica.

The same assays used on K17 keratinocytes were exploited also to examine the toxic effects of colloidal silica on Human Dermal Fibroblasts (HDF). WST-1 assay showed that after 24 h treatment at 10-200  $\mu\text{l/ml}$ , only SiNP20 induced a concentration dependent reduction of cell viability, with 100  $\mu\text{l/ml}$  being the lowest effect concentration, whereas SiNP70, SMP200 and SMP500 showed little effect (**Figure 4.23**).

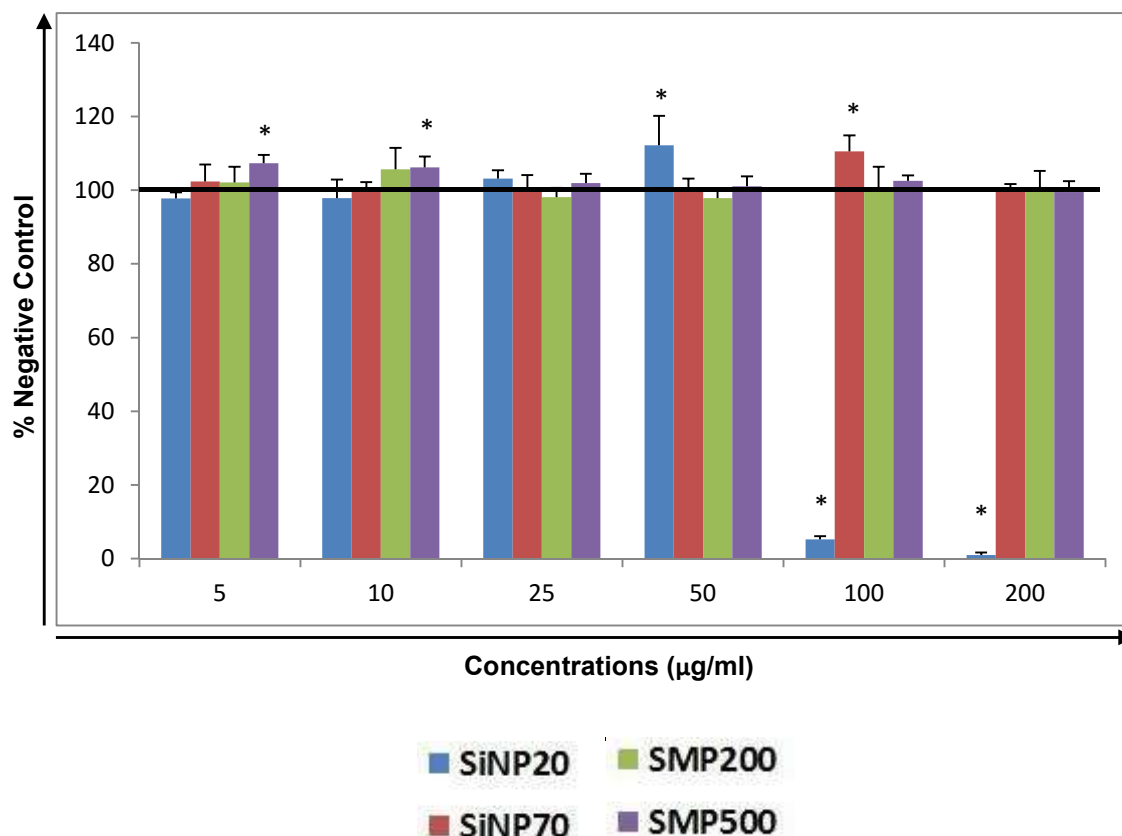


**Figure 4.23** WST-1 analysis of HDF fibroblasts treated with colloidal silica. Cells were treated with colloidal silica at 10-200  $\mu\text{g/ml}$  for 24 h at 37 °C. Results were expressed as percentage of negative control; black line serves as reference for normal activity. Each particle concentration was tested in triplicates and the results analysed by one-way ANOVA and Student's t-test. Statistically significant results ( $p < 0.05$ ) are marked with an asterisk (\*) on top of the corresponding bar.

The toxicity potential of the colloidal silica particles in the HDF cells was further characterized by the Propidium Iodide (PI) uptake assay. Cells were treated

with the particles at 10-200  $\mu\text{g/ml}$  for 24 h, with Triton X-100 0.025% as positive control. Again, Triton X-100 induced a significant increase of PI uptake. Only SiNP20 induced a significant increase in PI uptake at the concentrations that induced significant reduction of cell viability (**Figure 4.24**). The other particles, on the other hand, showed no detectable effect on cellular uptake of PI.

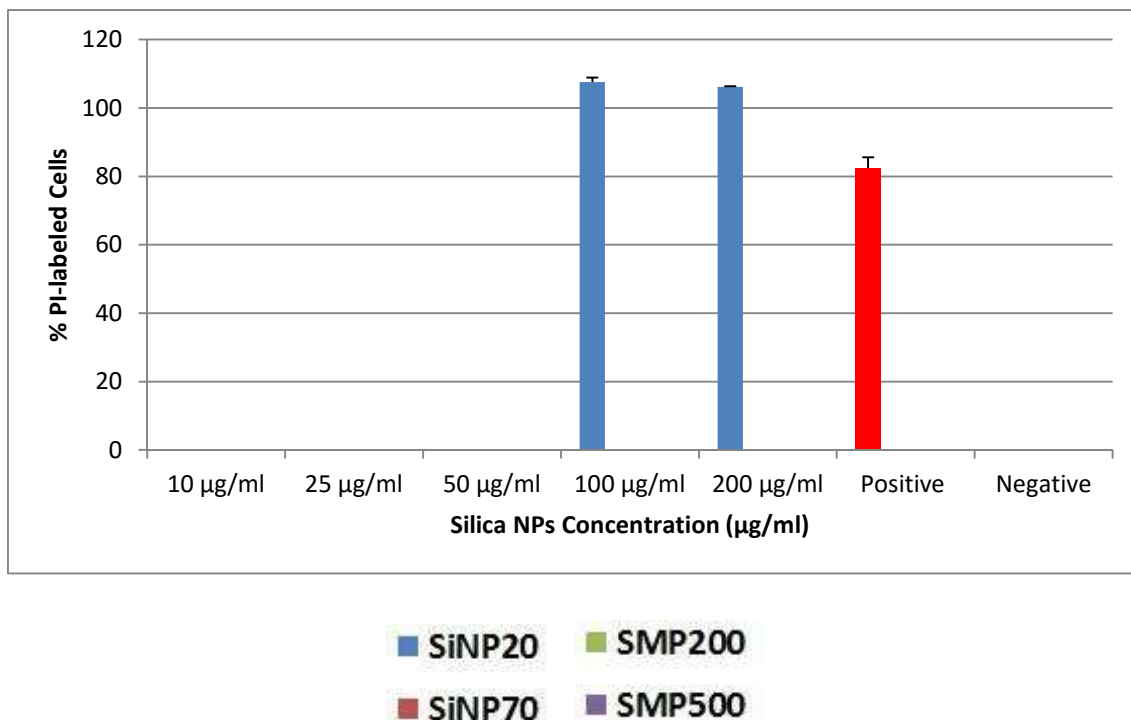


**Figure 4.24** Propidium Iodide measurement of HDF after treatment with colloidal silica. Cells were treated with colloidal silica 10-200  $\mu\text{g/ml}$  for 24 h, with Triton X-100 0.025% positive control.

Whether apoptotic cell death was involved in the toxicity of the colloidal silica particles in HDF cells was also investigated by the caspase 3/7 activity assay. As shown in **Figure 4.25**, it appeared that only treatment for 24 h with SiNP20 at 10  $\mu\text{g/ml}$  induced an increase of caspase 3/7 activity, while an inhibition was detected for SiNP20 at 100  $\mu\text{g/ml}$ , which is co-occurrence with the substantial reduction of cell viability. Treatment with other particles, on the other hand, was not associated with the induction of the caspase 3/7 activity (**Figure 4.25**).

Positive control staurosporine was tested at different concentrations (1, 10, 100  $\mu\text{M}$ ); however, no effect could be detected of HDF. As positive control showed a negative effect, more experiments need to be performed to establish whether the colloidal particles can induce toxicity in the HDF cells through activation of caspase 3/7.

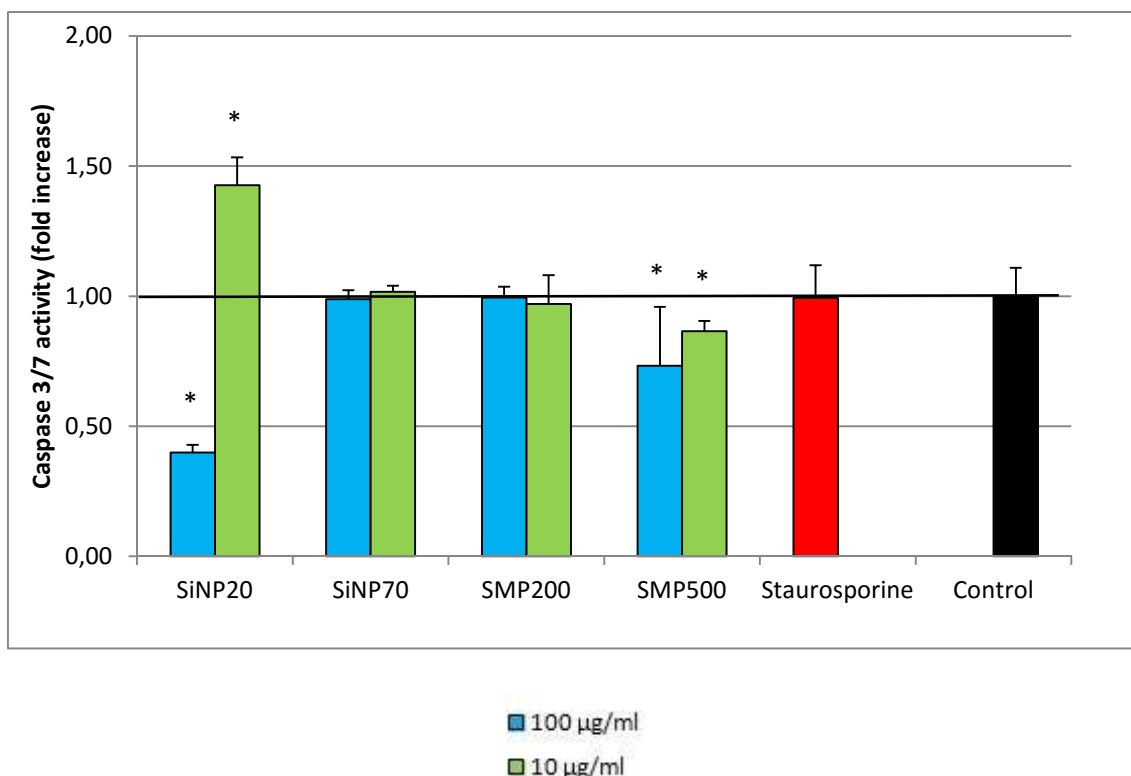


**Figure 4.25** Caspase 3/7 assay on HDF treated with colloidal silica. Cells were treated with colloidal silica at 10-100  $\mu\text{g/ml}$  for 24 h at 3°C, with staurosporine 10  $\mu\text{M}$  as positive control. Results were expressed as fold increase of caspase 3/7; black line serves as reference for normal activity. Each particle concentration was tested in triplicates and the results analyzed by one-way ANOVA and Student's t-test. Statistically significant results ( $p < 0.05$ ) are marked with an asterisk (\*) on top of the corresponding bar.

The cellular uptake and subcellular location of colloidal silica in HDF cells was also investigated by confocal imaging. As seen in K17 keratinocytes, cellular uptake of the silica particles observed after 2 h incubation (**Figure 4.26 a-c**) showed no internalization, with particles located outside the cells. After 24 hours

treatment (**Figure 4.26 d-f**), active uptake could be observed for all particles, but no specific localization could be detected, as NPs appeared to be free in the cytoplasm (**Figure 4.27**).

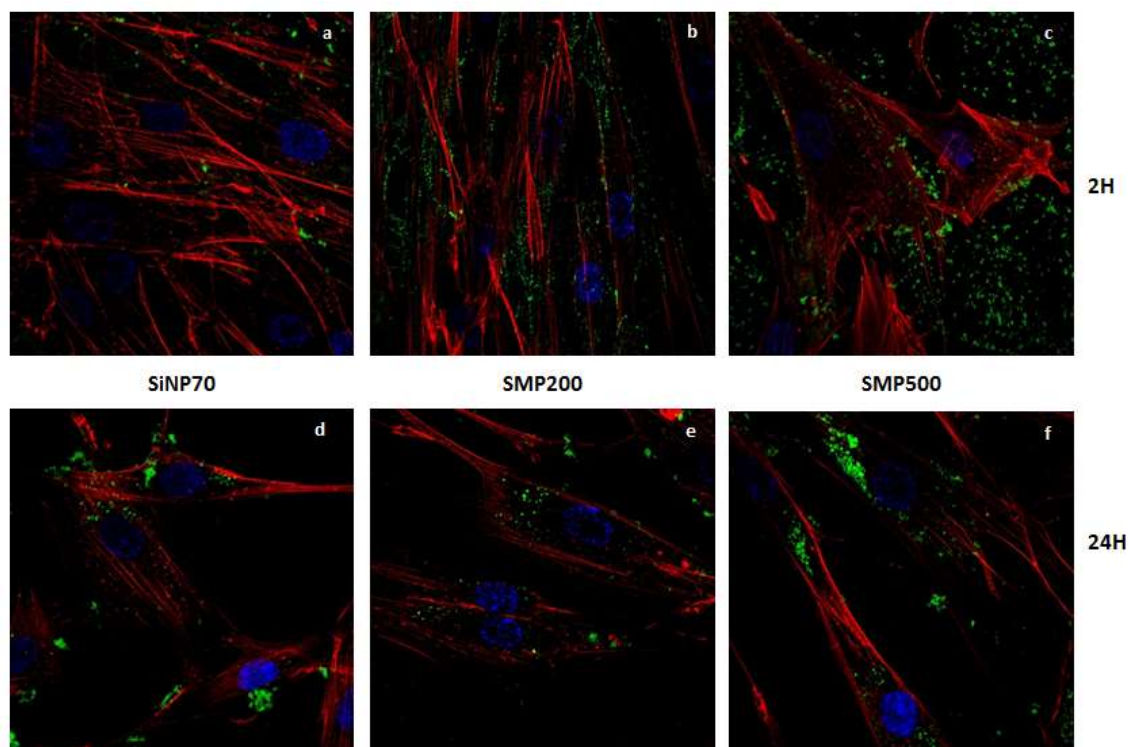


**Figure 4.26** Confocal microscopy imaging of HDF fibroblasts. Cells were treated with FITC-particles (green) at 10 µg/ml for 24 h. Cells were co-stained with Hoechst 33342 for nuclei (blue) and actin (red). No specific localization could be detected, as particles appeared to be free in the cytoplasm.



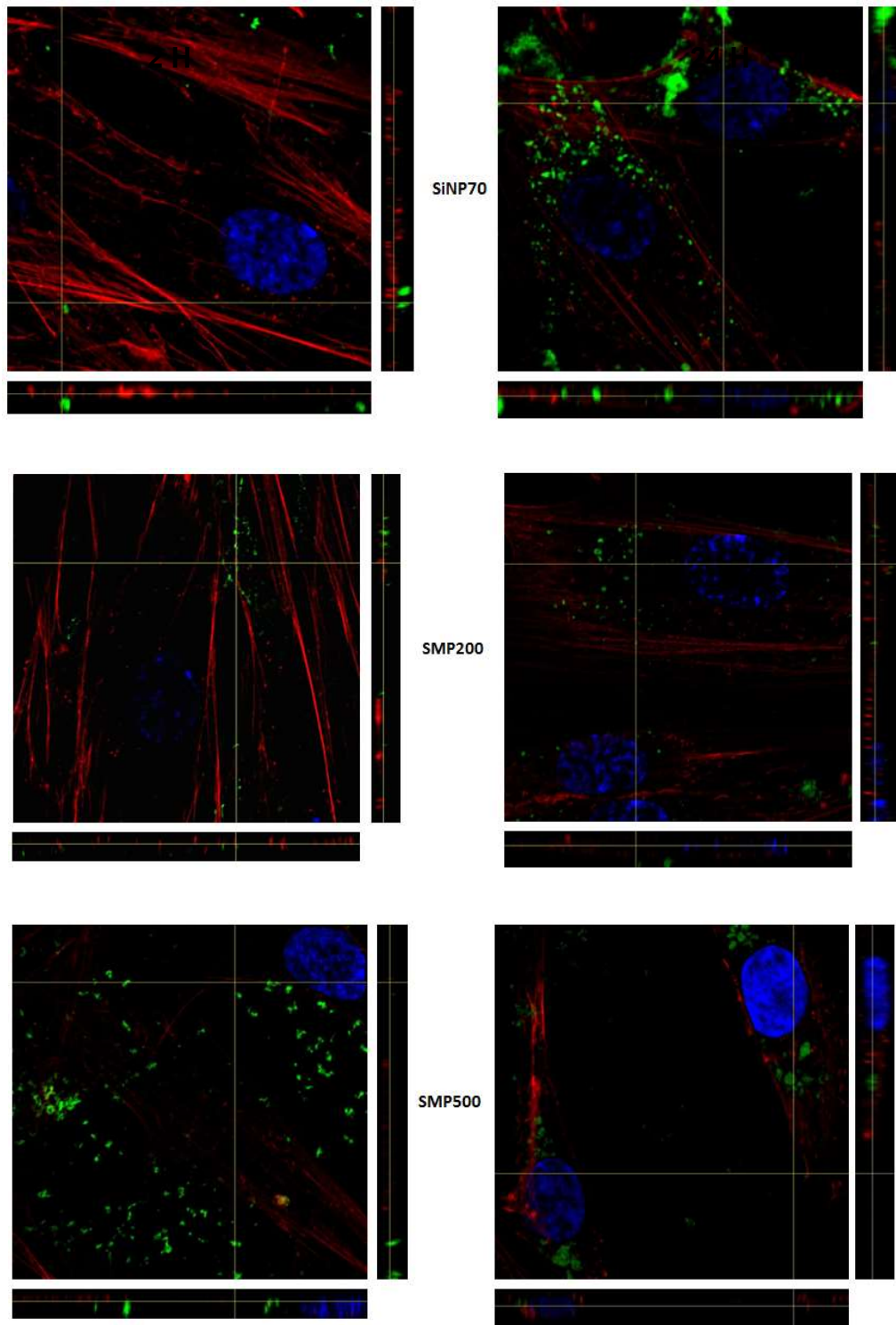


**Figure 4.27** Z-Stacks of HDF treated with colloidal silica. Laser scanning of cells previously treated with FITC-labelled silica particles and double stained with Hoechst 33342 for nuclei (blue) and actin (red) revealed that particles are mostly free inside the cytoplasm, making exact localization difficult; none reached the nuclei.

**Size-dependent toxicity of silica in BJ fibroblasts.** The toxicity of colloidal silica of different size was assessed by MTT and LDH assays after treatment of BJ fibroblasts for 24 h of treatment at 25-100 µg/ml. Like in HaCaT cells, colloidal silica particles were tested in CM-10%, CM-0.5 and CM. As assessed by MTT and LDH assays, no effects were detected for all the particles when tested in CM-10%, while some dose-dependent effects were detected for SiNP20 in CM-0.5% and for both SiNP20 and SiNP70 in CM (**Figure 4.28**). The discrepancy between the results of MTT and LDH could be due to the low metabolism of cells maintained in CM.

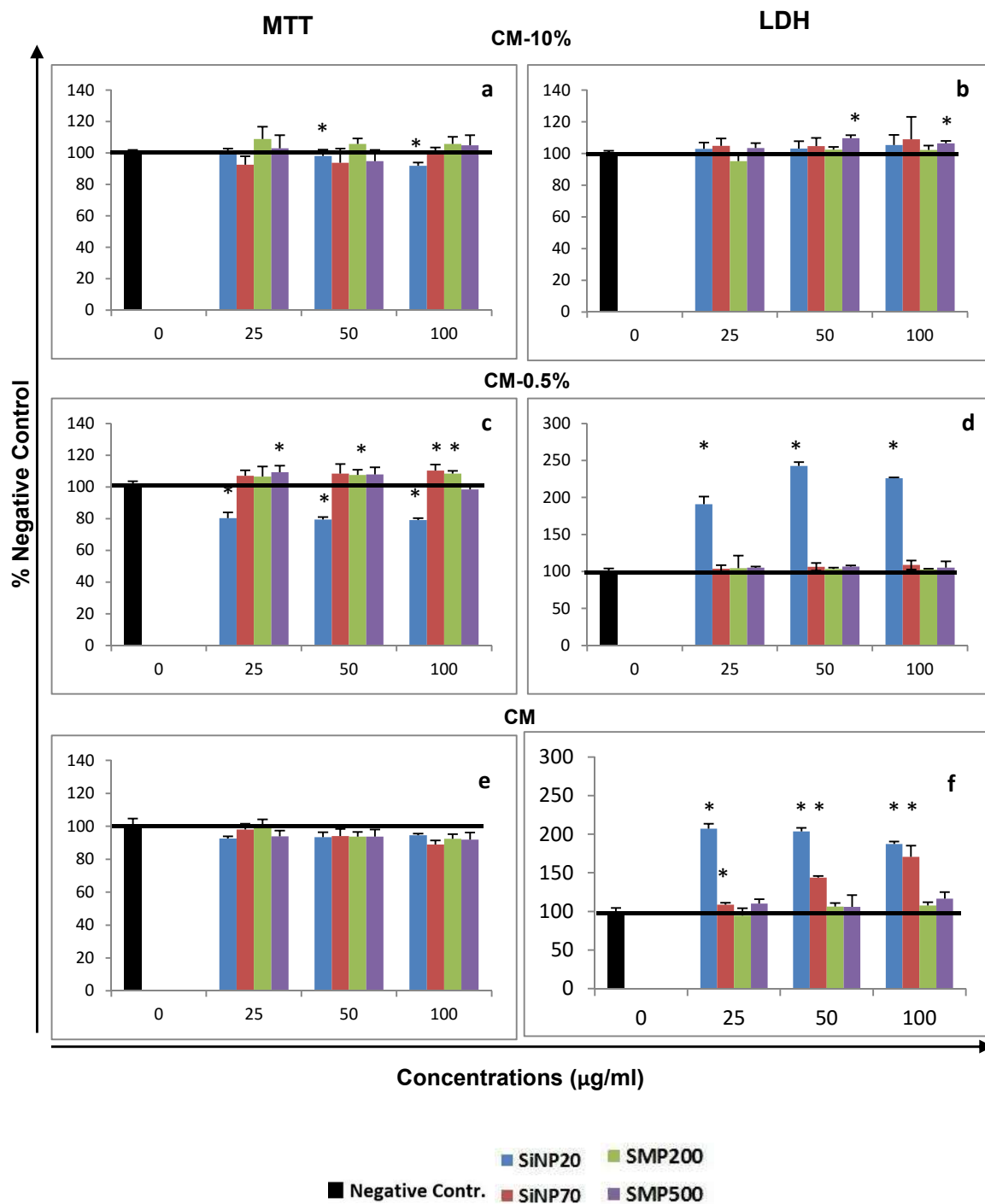


**Figure 4.28** MTT and LDH assay of BJ fibroblasts after treatment with colloidal silica. Cells were treated with particles at 25-100 µg/ml for 24 h in CM-10%, CM-0.5% and CM. a, b: treatment in CM-10%; c, d: treatment in CM-0.5%; e, f: treatment with CM. Results were expressed as percentage of negative control; black line serves as reference for normal activity. Each particle concentration was tested in triplicates and the results analysed by one-way ANOVA and Student's t-test. Statistically significant results ( $p < 0.05$ ) are marked with an asterisk (\*) on top of the corresponding bar.

The effect of colloidal silica was also examined using phase contrast imaging. BJ Fibroblasts treated with SiNP20-70 at 50 µg/ml in CM-10% and CM for 24 hours were assessed for shape and density variations. As shown in **Figure 4.29**, cells maintained in CM-10% exhibited a density of around 70% confluence and signs of active growth features that have been seen in HaCaT cells (**Figure 4.10, a compared with Figure 4.29, a**), while cells maintained in CM showed a much lower density (**Figure 4.29, d compared with a**), suggesting a low level of metabolism/growth potential. Particle-treated samples showed notable shape variations, especially cells treated with SiNP20, where a significant loss of shape could be detected both in CM-10% and CM (**Figure 4.29, a compared with b and e compared with d**). These morphological changes were not associated with the loss of cell viability and membrane damage as seen in **Figure 4.28**. For SiNP70 a much lower cell density as compared with control cells was observed (**Figure 4.29, c compared with a**), which was inconsistent with the result in the MTT assay (**Figure 4.28, a**), indicating the low sensitivity of the MTT assay. Based on the results from the LDH and phase contrast microscopy assays, it was evident that the toxicity of the colloidal silica in BJ fibroblast was size- dependent and the effects were not detectable in the presence of FBS.

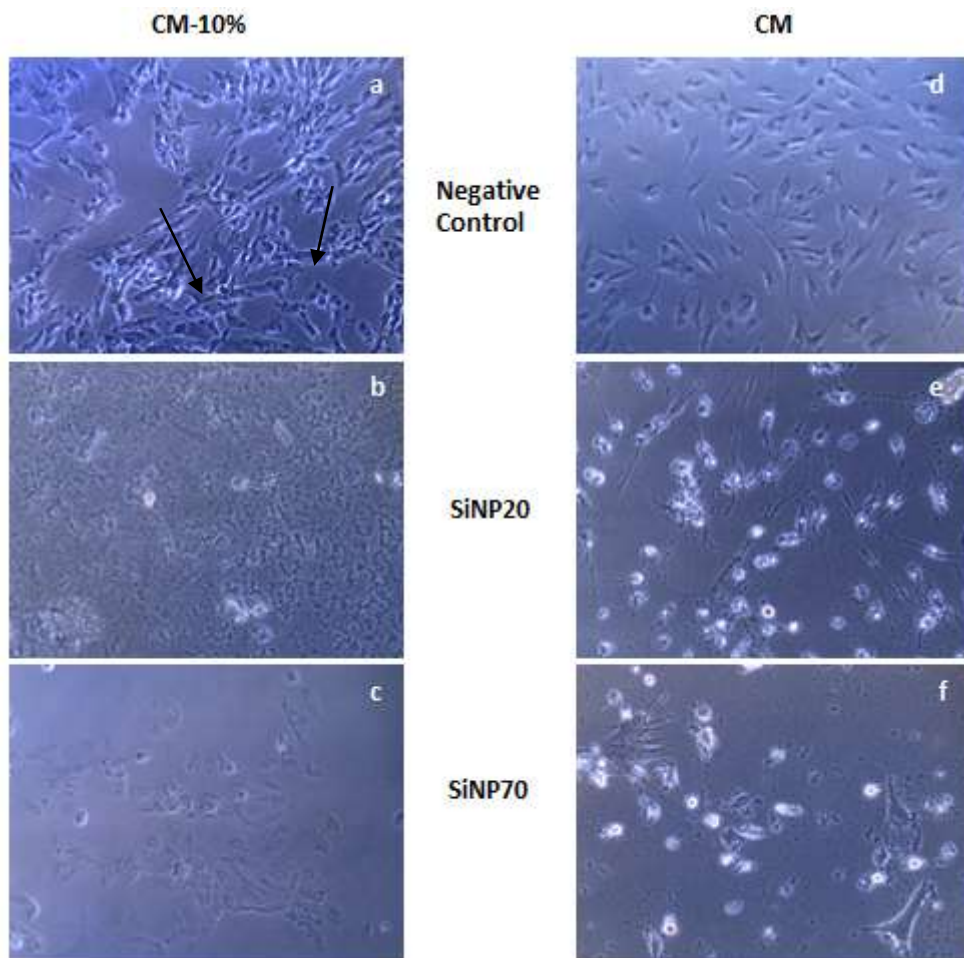


**Figure 4.29** Phase contrast imaging of BJ fibroblasts cells treated with SiNP20-70. Cells were treated with particles at 50  $\mu\text{g}/\text{ml}$  for 24 h in CM-10% and CM. Arrows in image a indicate cellular proliferation in the corresponding sample.

Based on the study of the colloidal silica particles in human keratinocyte and fibroblast cells, it appeared that the order of the toxicity follows is SiNP20>SiNP70>SMP200 >SMP500.

## 5 DISCUSSION

### 5.1 Silica particles dispersion properties in biological media depend on size, media composition and temperature

As *in vivo* and *in vitro* toxicology studies involve delivery of testing materials in aqueous biological media, size, as well as aggregation/agglomeration state of the materials under physiological conditions are fundamental parameters to be determined prior to toxicological studies [139]. The terms “agglomerate” and “aggregate” are widely used to describe the status of NMs in liquid suspensions. Despite the fact that each term has its own specific meaning, they are frequently interchanged at will, which results in conflicting definitions in national and international standards, thus creating problems with communication of results in reports and research papers. To avoid such confusion, in this study “agglomeration” will be defined as an assemblage of particles which are firmly bound and therefore not readily dispersed, whereas “aggregation” will be defined as an assemblage of particles loosely attached by contact at their corners and edges, thus easy to re-disperse [140]. The aggregation/agglomeration and subsequent sedimentation of nanoparticles raises concerns when considering size-, time-, and dose-dependent toxicity [141]. Experimental determination of NPs aggregation/agglomeration state is possible thanks to techniques such as Dynamic Light Scattering (DLS).

The determination of particles surface charge when introduced into aqueous solutions is also of the uttermost importance, as almost all mode of exposure in toxicology studies involve particles interaction with aqueous biological fluids, whose characteristics, such as ionic strength, pH and composition, contribute to the modification of particle behaviour in suspension. Measuring zeta potential often provides insight both on dispersion stability of the particle in suspension as well as information about their aggregation/agglomeration behaviour [142, 143]. Zeta potential is a measure of the magnitude of the electrostatic or charge repulsion/attraction between particles. If all the particles in suspension have large negative or positive ZP they will repel each other, thus preventing any agglomeration/aggregation. However, if ZP levels are low, no force will be able

to prevent the particles from coming together and aggregate [98]. Beside DLS and ZP, high resolution imaging techniques such as Scanning electron microscopy (SEM) and/or transmission electron microscopy (TEM) are considered as gold standard to assess particles shape, morphology, size range, agglomeration state, surface morphology [46].

A key factor to take into consideration when characterizing NMs in biological media is the potential interaction with proteins as this leads to formation of a protein corona (PC), thus altering their surface properties and reactivity. The majority of *in vitro* tests of NPs are performed using bovine serum, mainly because of its availability and traditional use in many assays, as well as for economic reasons. Another fact to consider is the culture medium characteristics, such as ionic strength, pH and composition, as they contribute to the modification of particle behaviour in suspension, and therefore the nature of their interaction with cells [144].

In this study, all the silica materials tested were characterized in different cell culture media with different bovine serum concentrations to gain information on average size, aggregation/agglomeration state, colloidal stability, shape, as well as the effect that serum and media composition had on particle stability. The selection of manufactured fumed silica and colloidal silica particles of different size allowed the differentiation of silica particles form- and size-dependent effects.

When analysed by DLS, SiNP7 and SiNP14 showed aggregation in CM, while in CM-10% their size and PDI increased compared to their given size. Such effect could be the result of protein corona formation, thus suggesting the role of FBS in improving colloidal stability for these particles. TEM imaging in deionised water showed chain-like structure compatible with aggregation as well. Such findings were previously described [145, 146]; Irfan et al. (2014) [145], having tested the same particles in medium by assays of DLS, TEM and ZP, found that while fumed silica 7 and 14 dispersed well in culture medium, they also had the tendency to form aggregates very quickly. They linked this effect to low zeta potential, which was measured to be around -9. A similar effect was described

by Sun et al. (2015) [146]; they used pristine, calcinated, rehydrated and doped fumed silica to assemble a library of fumed silica nanoparticles in order to study the relationship of surface silanol display to pro-inflammatory responses in macrophages and murine lung. Regarding pristine fumed silica, they tested them in a) water, b) a mixture of PBS + Bovine Serum Albumin (BSA) + 1,2-Dipalmitoyllecithin (DPPC), c) RPMI 1640 medium +10% serum. They found that fumed silica were better dispersed in medium rather than water and PBS/BSA mixture, which was linked to protein corona formation actually improving fumed silica colloidal stability. TEM characterization also showed a 'string of pearl-like structures', compatible with particle aggregation.

Regarding colloidal silica, in CM the size of all particles was consistent with their given size. However, when dispersed in CM-10% at concentrations above 50 µg/ml, all the particles with the exception of SMP500 were measured larger than their known size. The same increase in particle size could also be detected for all particles suspended in CM-0.5% and Medium 106. The ratio of size difference as measured in CM-10%, CM-0.5% and Medium 106 vs CM was in the order SiNP20>SiNP70>SMP200>SMP500. SiNP20 had the biggest size alteration, compatible with particle agglomeration, which was not associated with a change in zeta potential, suggesting that non-electrostatic protein adsorption could be the cause for size change. For SiNP70 and SMP200, on the other hand, the slight size increase could be due to the formation of protein corona. In the last few years, protein corona formation has gained so much importance that in the future it may be used for NPs classification [147, 148]. Despite the increasing interest, only very recent contributions have addressed the question of how NPs-protein coronas form, evolve with time and affect colloidal stability [149, 150]. Until recently, the main reason for colloidal instability of nanoparticles has been assumed to be cell culture medium, in particular its high ionic strength, capable of reducing particles' surface potentials. On the other hand, proteins had been generally assumed to enhance the dispersion of NPs in culture medium [151]. Nevertheless, in the last decade studies demonstrated size-dependent protein absorption. Roach et al. (2006) [152] used 15-165 nm silica spheres treated with bovine serum albumin (BSA)



and bovine fibrinogen (Fg) to assess protein-NP surface interactions and protein binding affinity, with focus on NPs surface curvature variations. They found that while binding affinity and saturation values were similar for both proteins, a size-dependent difference in orientation/conformation was detected, with albumin increasingly less ordered on larger particles, while fibrinogen became more denatured upon binding to smaller particles, suggesting that smaller particles cause protein alteration when PC is forming. Orts-Gil et al. (2013) [153] scrutinized the short and long term colloidal stability of silica nanoparticles (SNPs) and silica–poly(ethylene glycol) nanohybrids (Sil–PEG) in a protein model system using Bovine Serum Albumin (BSA) dispersed in PBS. Using such method, they showed that pristine silica nanoparticles formed small clusters with BSA after some minute's incubation in BSA/PBS solution, while after several hours the formation of large agglomerates was observed. In contrast, Sil–PEG hybrid nanoparticles were able to resist BSA adsorption and persisted as single NPs in a BSA–PBS suspension even after 48 h incubation. They explained such results as BSA acting as a 'bridge' between particles, as uncoated particles showed a stronger tendency to agglomerate. The data obtained in CM-10%, CM-0.5%, CM and Medium 106 were all in agreement with such studies [152, 153], as a size-dependent surface adsorption could be observed.

About SMP200 and SMP500 protein binding properties in different media, a previous study by Puddu et al. (2013) [154] demonstrated a shift of the dominant binding mechanism toward electrostatic interactions on larger silica particles. Using silica particles of 28, 82, 210 and 500 nm, they investigated the adsorption capability of each particle towards three different types of peptides. They found size-dependent protein adsorption, with binding mechanism for larger particles based on hydrogen-bonding interactions. This current study seemed consistent with this observation, as zeta potential for larger particles was reduced in CM-10%, suggesting the occurrence of electrostatic interaction between the particles and biomolecules. The sedimentation observed for SiNP20 and SiNP70 in EpiLife™ medium can be linked to the difference in composition compared with other media, as shown in the increased average

size measured for particle-free EpiLife™ medium by DLS. Such assertion is corroborated by direct comparison of DMEM/F-12 and EpiLife™ medium composition. The amount as well as the composition of inorganic salts is different, with EpiLife™ medium containing higher amounts as well as being characterized by different inorganic salts, such as magnesium chloride ( $\text{MgCl}_2 \times 6\text{H}_2\text{O}$ ), potassium chloride (KCl), sodium meta silicate ( $\text{Na}_2\text{SiO}_3 \times 9\text{H}_2\text{O}$ ) and sodium phosphate dibasic ( $\text{Na}_2\text{HPO}_4 \times 7\text{H}_2\text{O}$ ). Such differences have a direct influence on the ionic strength of the medium, thus affecting particle behaviour once dispersed. Inorganic ions play an important role in determining the aggregation and electro-kinetic behaviour of NPs. Ions with charge opposite to that of the NPs surface charge (counter ions) can attenuate the effect of repulsion by neutralizing the particle surface charge. Increase in the counter ion concentration normally causes an increase in zeta-potential values towards zero, thus facilitating particle aggregation. Ions charged similarly to the surface charge of NPs (co-ions) can also play important role in affecting the charge and aggregation behaviour of NPs. Approach of co-ions close to the surface of the particles causes an increase of the electro kinetic potential, thus imparting surface charges (more negative or more positive) by preferential adsorption [155].

Another important factor often overlooked during particle characterization is temperature. Temperature can influence protein corona composition, as evidenced that the composition of the protein corona formed upon NP exposure to heat-inactivated proteins (preheating at 56 °C) and non-heat-inactivated proteins is different [156]. However, effects on the protein corona when temperature is close to physiological temperature have not yet been studied in detail. Studying such effects may be relevant for NPs *in vivo* applications, as human body temperature can vary significantly. Normally human body temperature ranges from 35.8 to 37.2 °C depending on different parts of the body [157]. If protein adsorption onto the surface of NPs depends on the body temperature, it may also result in a significant effect on the cellular uptake of NPs *in vivo*. Therefore, in this study a DLS measurement of colloidal silica following incubation in medium at 37 °C was included, in order to mimic the *in*

*vitro* conditions used for cell-based assays as well as to mimic the mean human body temperature. While no difference could be detected for particles in CM as compared with their given size, particles in CM-10% showed an increase in average size that was associated with protein adsorption on the particle surface which was temperature dependent as the changes were only detected at 37°C but not 4°C. Such effect was previously demonstrated with different NPs [158, 159]. Mahmoudi et al. (2013) tested the effect of temperature on protein composition on 3-20 nm FePt NPs following treatment with Human Serum Albumin (HSA) and apo-transferrin (apo-Tf) at 9, 22, and 43°C; they also incubated larger FeO<sub>x</sub> NPs with positive, negative charge and neutral surfaces in foetal bovine serum (FBS) at 10-50°C [158]. They found that the increase of temperature resulted in an increase of protein affinity for binding to the surface of particles, thus leading to an increase in protein corona thickness. The amount of proteins in the corona was highest around 40 °C. In contrast, Mu et al. (2012) analysed amorphous silica Ludox SM-30 (20 nm) at 37°C in both water and DMEM medium with 10% FBS [159]. They found that while in water the particles were monodispersed with an average size around 14 nm, in DMEM the NPs suspension showed an average size of approximately 500 nm, indicating particle agglomeration which was consistent with the results from the current study.

SEM and TEM imaging confirmed the spherical shape and size of SiNP70, SMP200 and SMP500 as reported previously by Al-Rawi et al. (2011) [160]. For SiNP20, the elongated shape as well as the agglomeration detected was also previously reported by Mu et al. (2012) [159].

The fact that fumed SiNP7 and SiNP14 could disperse well in CM-10% but colloidal SiNP20 showed agglomeration could be linked to the original physical state and characteristics of the particles before dispersion in media. SiNP7 and SiNP14 are both ultrafine nanopowders with desiccant properties, which cause them to swell inside aqueous solutions [161]. SiNP20, on the other hand, was a clear aqueous solution containing Na<sup>+</sup> as a counter-ion to increase particle stability due to the high surface reactivity of the particles. While re-suspension

of SiNP7 and SiNP14 would have caused swelling, thus affecting their size and surface reactivity, re-suspension of SiNP20 in media without its counter-ions would have caused an imbalance in particle stability, which resulted in aggregation/agglomeration.

## **5.2 Silica particles uptake into HaCaT cells is endocytosis-related**

Cellular uptake of NMs is of paramount importance, as the targets for many therapeutic compounds are localized in the subcellular compartments [162, 163]. However, to achieve entrance inside the cells, NMs must be capable of efficient translocation across the plasma membrane, since the function of the barrier is to regulate which compounds enter into the cells. As efficient uptake of NMs is of central importance to nanomedicine applications, a deeper understanding of the biological pathways for cellular internalization of nutrients and solutes can facilitate the development of nanomaterials with precise intracellular targeting and enhanced therapeutic outcomes [162, 164].

In this study, cellular uptake in HaCaT cells occurred for both fumed and colloidal silica in a concentration-dependent manner. While fumed silica uptake was relatively low at concentrations  $\leq 100$   $\mu\text{g/ml}$ , colloidal silica was readily taken up by HaCaT cells at  $\geq 25$   $\mu\text{g/ml}$ . Such effect was previously described by Zhang et al (2012) [62], who addressed the fate of both fumed silica and Stöber silica nanoparticles tested at 25  $\mu\text{g/ml}$  in BEAS-2B lung epithelial cells and THP-1 monocytes. They observed relatively low uptake for fumed silica, while Stöber silica were readily taken up by both cell types. In this study such effect was further investigated by assessing the intracellular location of both fumed and colloidal silica. While TEM imaging of SiNP7 showed that cells were devoid of particles, SiNP20 were mostly observed as clusters in multi-vesicular bodies, while SiNP70, SMP200 and SMP500 were more often isolated in small vacuoles. Most of colloidal silica were observed in membrane-bound organelles regardless of size but some were free in cytoplasm.

This difference in cellular localization was observed as well by Zhang et al. (2012) [62]. Using TEM imaging, they demonstrated that fumed silica NPs in BEAS-2B and THP-1 cells were mostly associated with the external cell surface membrane, with few fumed silica nanoparticles inside the cells. Stöber silica NPs, on the other hand, were readily internalized and did not collect on the outer surface. The lack of membrane-bound fumed silica in this study can be linked to cell type difference, as BEAS-2B are lung epithelial cells and THP-1 are monocytes. The difference might also be linked to different culture conditions, such as the use of Foetal Bovine serum (FBS). In this current study FBS appeared to partially prevent the uptake, as the uptake was more pronounced in CM rather than CM-10%. This effect might be due to the fact that, when placed in a complex biological environment, nanoparticles interaction with the proteins in the medium and the formation of a protein corona can 'screen' the functional groups on the surface of nanoparticles, thus preventing non-selective cellular uptake of nanoparticles [165]. Nowak et al. (2013) [166] reported on the effect of serum proteins on the uptake of 20 nm monodispersed nanoparticles. Uptake rate of the particles was demonstrated to be lower in the presence of serum proteins compared to serum free conditions. The presence of colloidal particles free in the cytoplasm might be due to insufficient degradation of particles inside the lysosomal environment, where they could remain through late stage lysosomal digestion until release into the cytoplasm.

The considerations regarding the location of colloidal silica is further corroborated by previous studies, which showed that silica particles and some other types of nanoparticles were often observed in lysosomes [167] and in some cases were also found free in the cytoplasm [168]. Ye et al. (2013) [167] selected three industrially made SiO<sub>2</sub> particles of 50 nm, 100 nm and 200 nm to investigate their ability of nanoparticles to access and transport across the blood brain barrier (BBB). To do so they used the particles to treat *in vitro* endothelial hCMEC/D3 cells, and then examine them by extensive TEM imaging. They found that all tested nanomaterials entered the endothelial cell monolayer and accumulated along the endo-lysosomal pathway. Herd et al. (2011) [168] used three types of amine-terminated Stöber silica nanomaterials

of different shapes, namely spheres (178 nm), worms (232 nm × 1348 nm) and cylinders (214 nm × 428 nm) to study *in vitro* the influence of geometry of silica nanomaterials on cellular uptake and toxicity on epithelial A549 cells and phagocytic RAW264.7 murine macrophages. They found that geometry did not play a dominant role in the modes of toxicity and uptake of these particles, while a concentration- and cell-type dependent toxicity of all particle types could be observed. The presence of particles either free in the cytoplasm or co-localized within highly acidic lysosomal compartments suggests lysosomal escape or an indication of different stages of lysosome maturation.

The uptake of non-functionalized silica particles and their location in both the lysosomal compartment and free in the cytoplasm suggests that non-specific endocytosis could be the mechanism of uptake for these particles. Such affirmation is due to inconclusive assessment of uptake mechanisms using pathway-specific inhibitors. Use of Cytochalasin D, Dynasore, Nocodazole, Filipin and Polyinosinic acid did not provide any type of information regarding specific preferential pathways, such as caveolae-mediated or clathrin-mediated endocytosis. These observations are further corroborated by previous studies [31, 32]. Huang et al. (2010) [169] used three different shaped monodisperse mesoporous silica nanoparticles of 100, 240 and 540 nm to study the effects of particle shape on cellular uptake and behaviour using A375 human melanoma cells. They found that smaller particles had a greater impact on different aspects of cellular function including cell proliferation, apoptosis, cytoskeleton formation, adhesion and migration. They also found that particles were readily taken up by A375 cells and encapsulated into vesicular or cytosolic compartments. From the TEM images, they concluded that MSNs were first internalized in A375 cells by non-specific cellular uptake and merged with endosomes. Subsequently the MSN particles escaped from the endosomes and entered the cytoplasm. Chu et al. (2011) [170] used 50 nm and 400 nm Stöber silica NPs plus 10 and 20 nm industrially made silica NPs to study *in vitro* the interaction of silica nanoparticles (NPs) with human cell lines H1299 human lung carcinoma cell, HONE1 human nasopharyngeal carcinoma cell, NE083 human oesophageal epithelial cell, NL20 human bronchial epithelial cell and

HEK293 human embryonic kidney cell. Using three time-points (3 hours, 10 hours, 48 hours) they assessed particle uptake to determine the mechanism for both pathways. For all particles and cell type tested most of the NPs were found in mono-dispersed form in endolysosomes or cytoplasm after 3 hours incubation; after 10 hours and further to 48 hours, more and more clustering of multiple NPs appeared in the endo-lysosomes, while very few single particles were found in the cytoplasm. The observation of a large amount of membrane bounded NPs inside the cells, together with the fact that no specific coating was deposited on the NP surface, suggested nonspecific endocytosis as the major mechanism for the cellular uptake of the nanoparticles. They also studied the excretion pathway by incubating with particle-free medium for 1 hour after the maximum uptake period (48 + 1 hour). Taking into consideration the dynamic nature of endocytosis and exocytosis, they observed a notable difference between the amount of silica nanoparticles inside and outside the cells, with most of the NP aggregates in the organelles disappearing but with some single NP left in the cytoplasm. Based on these observations they concluded that NP clusters in lysosomes were more easily excreted by the cells when compared to the single NP in cytoplasm.

Taken together, existing data suggest that the cellular uptake of silica particles could be cell type-dependent via non-specific endolysosomal pathways that have a broad range of shape and size selections. Different locations between SiNP20 and SiNP70, SMP200, SMP500 also suggest the role of particle size in the internalization pathway. Further study will be needed to firmly establish cellular uptake pathways of silica particles in both CM-10% and CM, as well as assess their fate post-uptake.

### **5.3 Modulation of silica size dependent toxicity by FBS**

Due to the many different forms of NPs produced in a wide variety of applications, study of the effects of nanomaterial exposure to the human body is of paramount importance. Studies using *in vitro* and *in vivo* models to delineate size-dependent effects of silica particles have been increasingly documented.

However, the relevance of particle size in toxicity has not been established, which was partially due to the variations in physico-chemical properties of particles used by different groups.

When studying *in vitro* the potential toxicity of NPs, assays assessing cell viability and cellular membrane damage were often employed in combination to gain initial assessment of toxicity potential of the testing materials [171, 172]. More assays were needed to gain insights into the mechanisms of the toxicity. In this study, silica particles were initially assessed by MTT/WST-1 and LDH/PI staining for their effects on cell viability and membrane damage respectively. HaCaT cells were used as a model to assess the effect of fumed and colloidal silica previously characterized in culture medium, thus allowing the correlation of cytotoxicity to their size as well as the presence or absence of FBS. The study clearly demonstrated size- and dose-dependent toxicity of colloidal silica in the order SiNP20 $\geq$ SiNP70 $\geq$ SMP200 $\geq$ SMP500 respectively. For both forms of silica particles, cytotoxicity was detected in the absence of FBS, while in CM-10% the toxicity was detected for colloidal SiNPs but was absent for fumed SiNPs, thus providing evidence that serum modulates silica toxicity which is silica-type dependent.

Although many studies indicate that nanoparticles are more toxic than their larger counterparts, the size-dependent mode of action is still elusive. Size-selective cellular internalization is one of the speculations for the toxicity of nanoparticles. Zhu et al. (2013) [173], for example, investigated the cellular uptake efficiency, mechanism and cytotoxicity of silica nanoparticles (SNPs) with different sizes (55.6, 167.8, 306.7 nm) in HeLa cells. They found that cellular uptake efficiency was size-dependent, in the order 55.6  $\geq$  167.8  $\geq$  307.6 nm; however, no toxicity could be detected after 48 hours. While providing evidence for size-dependent uptake of particles, the lack of toxicity is in contrast with other reports on size-dependent toxicity of silica particles of similar size, thus suggesting a different size-related mode of action. Li et al. (2011) [174] compared the potential cytotoxicity induced by amorphous silica particles of 19, 43, 68 and 498 nm *in vitro* using HepG2 human hepatoma cells. Investigation of



cell viability found that cytotoxicity generated by silica particles strongly depended on particle size and administered dose, with smaller silica particle producing higher toxic effect. Lu et al. (2011) [175] investigated the cytotoxicity of 7–50 nm silica nanoparticles in human HepG2 hepatoma cells, using normal human L-02 hepatocytes as a control. They found that silica nanoparticles were also cytotoxic in a dose- and time-dependent manner. Dose-dependent toxicity has also been observed in previous studies. Ahmad et al. (2011) [176] used 14 nm silica nanoparticles to assess reactive oxygen species (ROS) mediated apoptosis in human liver cell line HepG2. They found that treatment 5–200 µg/ml caused cytotoxicity and oxidative stress above 25 µg/ml, suggesting dose-dependent toxicity.

The influence of FBS on particle cellular uptake and toxicity has been previously discussed. For fumed SiNPs, the toxicity and cellular uptake were only significant in the absence of FBS. For colloidal silica, on the other hand, it seemed that it was the toxicity but not cellular uptake was size-dependent. Such difference might be due to the desiccant capability of fumed silica, which may be able to adsorb proteins on their surface in a different fashion compared to colloidal silica. It is likely that, after cellular internalization and digestion of corona proteins, colloidal silica particles regain their primary size so that the smaller particles can access the binding side of intracellular structures/molecules, and interfere with cell survival programme, leading to cell death. The agglomeration/aggregation of SiNP7, SiNP14, SiNP20 and SiNP70 in culture medium, as well as the sedimentation of SMP200 and SMP500 on the surface of cells in culture suggests that they may cause toxicity via strong physical contact with cells, triggering cell death signals. As the characteristics of NPs may be affected by the chemistry of their surroundings, caution needs to be taken in interpreting *in vitro* studies. The composition of inorganic and biological moieties of FBS used in *in vitro* culture is different from human serum, and thus could have a different effect on the toxicity of silica particles [94].

Size-dependent toxicity of silica particles was also proved true in many different *in vivo* models. Several studies showed that silica nanoparticles particles

elicited higher toxicity than their larger counterparts. Nemmar et al. (2014) [177] used amorphous silica particles 50 nm and 500 nm at 0.5 mg/kg to demonstrate induction of systemic inflammation and coagulation events in mice through intraperitoneal injection. They linked size-dependent effects to internalization in platelets, oxidative stress and cytolysis. Brown et al. (2014) [178] used rats as model to perform the pulmonary instillation of silica particles 50 nm and 200 nm, which caused an acute inflammatory response. However, the magnitude of the response was influenced by the media used for particles dispersion, suggesting that silica particles should be dispersed in media more compatible with body fluids, for example using human serum instead of FBS. Hassankhani et al. (2014) [179] demonstrated that silica particles of 10-15 nm caused toxicity in mice to various tissues including liver, kidney, lung, and testis through oral route, although larger particles were not included for comparison. It was also interesting to note that when intra-peritoneally administered in mice, mesoporous silica nanoparticles caused more damage to systemic immunity than colloidal silica particles of similar size [180]. All the particles tested in this current study also appeared to cause cytotoxicity through induction of apoptosis.

#### **5.4 Silica induction of apoptotic cell death is size- and dose-dependent**

The internalization and accumulation of particles could ultimately lead to the loss of cell viability, which could be the outcome of cell death via different mechanisms, such as necrosis and apoptosis. Necrosis is a form of traumatic cell death that results from acute cellular injury. Apoptosis, also known as 'programmed cell death', on the other hand, consists of a series of biochemical events that lead to characteristic morphology and intracellular changes, followed by cell death [181]. Such changes include membrane blebbing, cell shrinkage, nuclear fragmentation, chromatin condensation, chromosomal DNA fragmentation, and global mRNA decay. While apoptosis is highly regulated and controlled process during an organism's lifecycle, necrosis is caused by factors

external to the cell or tissue, such as infection, toxins, or trauma, which result in the unregulated digestion of cell components [182]. Both pathways can be triggered by the interaction between cells and nanomaterials. Although the importance of understanding such cellular and molecular pathways in relation to nanoparticle exposure has been recognized, only few studies in recent years have started to shed light on such mechanisms [183].

In this study, the mechanism silica cytotoxicity was preliminarily assessed by detection of necrosis and apoptosis. Using the optical microscopy technique of phase contrast imaging to assess morphology changes of cells following silica treatment proved useful in obtaining real time information on cellular response to the treatment. Although the technique does not have the resolution to see individual nanoparticles, it has been widely applied to image morphology changes of the cells and tissues for any sign of pathology [184, 185]. The size- and dose-dependent cellular effect of silica in CM and CM-10% detected by phase contrast imaging was very much comparable with the cytotoxicity detected by the MTT and LDH. The effects observed on cells treated with SiNP20 and SiNP70, such as cell shrinkage and becoming rounded, were associated with apoptosis. The induction of apoptotic cell death was previously reported in the literature for different types of nanoparticles [48, 49]. Lee et al. (2014) [186] investigated the effects of silver nanoparticles (AgNPs) on NIH/3T3 mouse embryonic fibroblasts to explore the potential application of these nanoparticles in consumer products. After 24 hours of AgNPs treatment, the changes in cell morphology were examined using phase-contrast microscopy. They found significant morphological changes characteristic of apoptotic cell death in NIH 3T3 cells exposed to AgNPs, including cell shrinkage, few cellular extensions and increased floating cells. Alarifi et al. (2013) [187] investigated the cytotoxicity, oxidative stress, and apoptosis caused by ZnO nanoparticles in human skin melanoma (A375) cells. They found that after 24 and 48 hours treatment, cells treated with different concentrations of ZnO NPs changed into a spherical shape and detached from the surface, which was associated with induction of apoptosis in A375 cells.

To validate the induction of apoptosis as detected by phase contrast imaging, double staining with Annexin V and Propidium Iodide for flow cytometry was performed. Annexin V has high affinity to phosphatidylserine, which translocates from the inner layer to the outer layer of cell membrane during apoptosis, while Propidium iodide (PI) is a DNA intercalating agent that penetrates cells only with a damaged cell membrane, normally associated with necrosis. In late apoptosis, cells become positive for both Annexin and PI staining due to the plasma membrane becoming permeabilized as a direct consequence of phosphatidylserine (PS) on the cell surface [188].

In this study, a dose-dependent toxicity was demonstrated for both fumed and colloidal silica, in the order SiNP7  $\geq$  SiNP14 and SiNP20  $\geq$  SiNP70  $\geq$  SMP200  $\geq$  SMP500. For both particle types, the occurrence of late apoptosis, as indicated by double positive Annexin V/PI-stained, was more accentuated in CM, thus providing further evidence of the role of serum in attenuating toxicity. Detection of apoptosis induced by nanoparticles has also been reported previously [51, 52]. Jia et al. (2013) [189] used paclitaxel (PTX)-loaded mesoporous silica (MSNs) to treat MCF-7 breast cancer cells and found a dose-dependent increase of late apoptosis, which was associated with critical particle pore size. Laha et al. (2014) [190] used 30 nm CuO NPs to investigate apoptosis in MCF7 breast cancer cells. They found that after 24 hours treatment, the majority of cells were in a late apoptosis; such effect was linked to the cleavage of Poly (ADP-ribose) polymerase (PARP), a nuclear protein activated in cells experiencing stress and/or DNA damage, de-phosphorylation of Bcl-2-associated death promoter (BAD) (which has a role in apoptosis activation), and increased cleavage product of caspase 3.

Although the mechanisms and morphologies of apoptosis and necrosis differ, there is overlap between these two processes. Necrosis and apoptosis represent morphologic expressions of a shared biochemical network. Whether a cell dies by necrosis or apoptosis depends in part on the nature of the cell death signal, the tissue type, the developmental stage of the tissue and the physiologic milieu [191, 192]. Two factors that will convert an ongoing apoptotic

process into a necrotic process include a decrease in the availability of caspases and intracellular ATP [191, 193]. The mechanisms of apoptosis are highly complex and sophisticated, involving two energy-dependent apoptotic pathways: the extrinsic or death receptor pathway and the intrinsic or mitochondrial pathway. The two pathways are linked, and molecules in one pathway can influence the other [189, 194]; both converge on the same execution pathway initiated by the cleavage of caspase 3. Caspase 3, caspase 6 and caspase 7 function as effector caspases, cleaving various substrates that ultimately cause the morphological and biochemical changes seen in apoptotic cells [189]. Caspase 3 is considered the most important of the execution pathway caspases; activated by initiator caspases (caspase 8, caspase 9, or caspase 10), it activates CAD, an endonuclease responsible for chromosomal DNA degradation and chromatin condensation within the nuclei. Caspase 3 also induces cytoskeletal reorganization and disintegration of the cell into apoptotic bodies [192]. In this study, discrimination between apoptosis and necrosis as well as definition of apoptosis pathway has been assessed by Western Blot and gene expression analysis. The size- and dose-dependent detection of activated caspase 3 in HaCaT cells treated with colloidal silica was consistent with both phase-contrast imaging and Annexin V/PI staining, thus giving confirmation about induction of apoptotic cell death as primary toxicity mechanism in HaCaT cells. Constantini et al. (2011) [195] previously reported a similar effect, which compared the uptake and toxicity of amorphous and crystalline silica *in vitro* using MH-S mouse alveolar macrophages. By assay of Western blot after 4 and 8 hours treatment, they found that both crystalline and amorphous silica induced high amounts of cell death in MH-S cells, with a high ratio of cleaved (active) caspase 3, suggesting a similar toxicity mechanism between the two particles. Sun et al. (2011) [196] investigated the cytotoxicity and mitochondrial damage of amorphous silica nanoparticles 43 nm following treatment in HepG2 hepatocellular carcinoma cell line for 24 hours. Detection of caspase 3 by Western blot showed dose-dependent increase in protein levels, which, paired with the released cytochrome c and decreased membrane potential, was linked to apoptosis through mitochondrial pathway.

Further information regarding the molecular pathway to silica-induced apoptotic cell death was obtained by gene expression assay of cells treated with SiNP20 in CM-10%, which revealed a dose-dependent up-regulation/down-regulation of several pro-apoptotic and anti-apoptotic genes, suggesting a dynamic process of apoptosis. The slight change of the gene expression profile induced by 10  $\mu$ l/ml of SiNP20 treatment was consistent with the lack of toxicity. While majority genes appeared down regulated, only 5 genes were up-regulated, including *ATP6V1G2*, *PARP1*, *ACTB*, *HPRT1* and *RPLPO*. With the increase of SiNP20 concentration to 25  $\mu$ g/ml, the majority of cell death genes were up regulated, suggesting that cells were actively engaged in the process of cell death. Among these genes, the well-known pro-apoptotic *CASP* gene family and *FASLG* were predominantly up regulated as compared with the anti-apoptotic *BCL2* gene family and the autophagy *ATG* gene family. This gene expression profile coincided with induction of apoptosis, providing insights into the dominant molecular mechanism of SiNP20 toxicity in HaCaT cells.

The pro-apoptosis genes that were up regulated could be linked to both the extrinsic and intrinsic pathway of apoptosis, as well as the execution pathway (**Table 5.1**). The up-regulation of autophagy regulator genes (*ATG5*, *ATG12*, *IRGM*, *ULK1*, *P53*) also suggested a role of autophagy in the toxicity mechanism induced by SiNP20. Autophagy can be defined as a catabolic mechanism that involves cell degradation of unnecessary or dysfunctional cellular components through the actions of lysosomes, thus allowing degradation and recycling of cellular components [197]. A similar effect was previously reported by Hussain et al. (2012) [198]; using CeO<sub>2</sub> NPs to treat CD14<sup>+</sup> monocytes, they demonstrated a notable increase in toxicity after 20-40 hours exposure, which was associated with both induction of apoptosis and autophagy. While apoptosis was linked to mitochondrial damage and expression of apoptosis-inducing factor (*AIF*), autophagy was linked to the modulation of transcription factor p53. While the exact mechanism was not clear, it was suggested that the accumulation of CeO<sub>2</sub> NPs in endosomes and lysosomes could cause overexpression of genes for vesicle formation or identification of NPs as foreign endosomal pathogens.

**Table 5.1** The main upregulated genes in this study and their related pathways.

<b>Extrinsic Pathway</b>	<b>Intrinsic Pathway</b>	<b>Execution Pathway</b>
FAS	APAF-1	Caspase 3
FASLG	BCL2	Caspase 2
TNF	BAX	Caspase 6
TNFRSF11B	BCL2L1, BCL2L11	PARP1
TNFRSF1A	XIAP	PARP2

Further increase of SiNP20 to 50  $\mu\text{g/ml}$  resulted in a down-regulation of majority genes, which coincided with the onset of late apoptosis. It was interesting to note that the housekeeping genes *ACTB*, *HPRT1* and *PRLP0* were persistently up regulated regardless of the SiNP20 concentration, suggesting that these housekeeping genes play an important role in providing structure support against necrotic cell death.

Gene expression profiles after exposure to amorphous silica particles have been reported in previous studies. Ahamed et al. (2013) [199] investigated the induction of cytotoxicity, oxidative stress and apoptosis by 15 nm SiO<sub>2</sub> NPs following 72 hours exposure in A431 human skin epithelial cells and A549 human lung epithelial cells. Analysis of mRNA expression of apoptotic genes caspase 3 and caspase 9 showed that SiO<sub>2</sub> NPs up-regulated mRNA levels of these genes, which was also linked to increased activity for the corresponding proteins. This, together with increased levels of ROS, was linked to stress-induced apoptosis. Okoturo-Evans et al. (2013) [200] used 20 nm colloidal silica to assess *in vitro* the consequences of exposure of lung to nanoparticles. Following treatment in A549 human lung cancer cells, assessment of protein expression showed that while exposure to NPs was tolerated up to 4 hours, after that specific time notable changes could be detected for apoptosis gene regulation, structural reorganisation and regulation of actin cytoskeleton, unfolded protein response, and proteins involved in protein synthesis (e.g.

ribosomal proteins). Treatment in serum-free medium resulted in a rapid deterioration of the cells, suggesting interaction of serum components with the nanoparticles. Fede et al. (2014) [201] analyzed the effects of Ludox® SM30 and AS30 nanoparticles on gene transcription of A549 cells using microarray analysis. After establishing the non-toxic critical dose at 0.02 mg/ml, they treated cells with said concentration. They found that genes up-regulated in response to Ludox® NPs showed notable impact on vesicle transport, regulation of apoptosis and regulation of transcription from RNA polymerase II promoter. They also showed activation of both intrinsic and extrinsic apoptosis pathway, as well as execution pathway, suggesting transcriptional alterations at a dose of exposure considered non-cytotoxic.

While this study proved that amorphous silica induced the size- and dose-dependent induction of apoptosis, as well as shedding light on the involved mechanisms in HaCaT cells, more work will need to be done to further elucidate the fate of silica particles inside cells, as well as assess different cell lines with similar high-throughput assays to establish any kind of cell-type dependent mechanism of silica toxicity.

### **5.5 Silica particles enhance wound healing *in vitro* in the HaCaT model system**

Keratinocyte proliferation and migration are essential for epidermal repair after injury. *In vivo*, wound repair requires proliferation and migration of both fibroblasts and keratinocytes to re-establish the normal cellular and extracellular matrix composition of skin, as well as the growth of vascular endothelial cells (VECs) to form new blood vessels to supply nutrients to the skin cells [202].

*In vitro*, normal cell growth relies on growth factors. The optimal cell growth is usually achieved by supplementing culture medium with 10% FBS. When FBS concentration is too low, cells cannot achieve optimal growth. For this reason, *in vitro* wound healing assessment through scratch assay is often carried out in culture medium containing 0.5% FBS, which is also referred to as starvation



medium, to minimize cell proliferation, but just sufficient to prevent apoptosis and/or cell detachment. That way it is possible to assess induction of cell growth and migration of the tested materials [203].

Active proliferation of HaCaT keratinocytes was detected by phase contrast imaging in untreated cells as well as those treated with SiNP70 and SMP200. The same morphology of cell growth were detected by Nickoloff et al. (2005) [204], where melanocytes were compared with different melanoma cell lines derived from patient. Rounded structures compatible with cell growth, as well as an enhanced proliferation compared with normal cells could be detected. As it is already known that HaCaT cells are characterized by faster growth compared with other normal phenotype cell lines, the increase in cell number detected in cells treated with SiNP70 and SMP200 was linked to enhanced cellular growth. As shown in the *in vitro* scratch assay, HaCaT cells in CM-0.5% (starvation medium) underwent a slow process of wound closure, which was augmented by all colloidal silica in a dose-dependent manner  $\leq 25 \mu\text{g/ml}$ . Such observation, compared with previously reported toxicity  $\geq 25 \mu\text{g/ml}$ , suggests a threshold between promotion of wound healing and induction of toxicity. As the wounds were created after particles incubation and removal from the culture medium, the effect could only be initiated by colloidal silica internalization inside HaCaT cells. Although all the tested particles showed an ability to promote wound healing *in vitro*, they did not share the same dose- and time-response pattern. Such difference could be related to the different size of the particles, as well as the nature of serum proteins that were carried over by the different particles. The adsorption of proteins by particles can be directed by positively charged areas on the protein surface towards the negatively charged silica surface at conditions allowing specific binding. Consequently, even small variations of characteristics in silica particles could lead to a drastic change in protein adsorbing properties, in selective protein binding and in delivery by silica particles, thus reflecting a different impact on their biological behaviour [205].

Studies on tissue regeneration properties of amorphous silica are scarce. Feng et al. (2007) [206] used silica nanospheres 30-80 nm to assess their potential in

bone regeneration. Using the nanospheres to treat osteoblast-like cells, by assay of MTT and alkaline phosphatase (ALP) they found that cells treated with the nanospheres had higher cell viability as well as higher ALP activity compared to the control, thus suggesting enhanced proliferation. Meddahi-Pellé et al. (2014) [207] used 50 nm Stöber silica to assess their ability to achieve rapid and strong closure and healing of deep wounds in rats skin and liver. They reported a beneficial effect of colloidal silica in skin and liver repair, which could be attributable to the adhesion and haemostasis activity of silica nanoparticles. While the present study using HaCaT cells as model provided further evidence that treatment with colloidal silica could be beneficial for tissue repair, the effects of the particles in promoting cell proliferation and migration warrant further *in vitro* and *in vivo* assessment before exploitation for applications in regenerative medicine could be considered.

## **5.6 Cell-type related toxicological effects of colloidal silica**

In order to identify sensitive cells/organs to nanotoxicity, there has been considerable effort on investigating the potential toxicity of nanoparticles using different cell models [208]. Despite the amount of available studies, inconsistent or conflicting observations have hindered the establishment of cell-type specific mechanism of nanoparticle cytotoxicity [209, 210].

In this study, three additional human skin cell lines were chosen to determine whether the size-dependent toxicity of the chosen colloidal silica particles is cell type specific. These cells were assessed for cell viability, particle uptake and activation of apoptotic pathway after colloidal silica treatment. Although the chosen assays were different from that used for HaCaT study due to the preference of different labs, the results provided insights into the toxicity potential and mechanisms of the same group particles in different cell lines. While K17 keratinocytes was chosen to present a different cell line but with same tissue origin as HaCaT cells, BJ fibroblasts and Human Dermal Fibroblasts (HDF) were chosen to present morphologically different cell types originated from different skin layers as keratinocytes. Fibroblasts are associated

with the dermis, and promote the formation of the connective tissue, which unites the different cell layers. Keratinocytes, on the other hand, occupy the upper layer of skin, the epidermis, therefore are the first to come to contact with any external agent, including nanoparticles.

In this study, the cell-type dependent response to colloidal silica of different size was demonstrated. The particles induced a size- and dose-dependent decrease of cell viability in both K17 and HaCaT keratinocytes with the former more sensitive than the latter. In contrast, in HDF, cytotoxicity was only induced by SiNP20 but not by the larger particles under the different tested conditions. BJ fibroblasts were shown to induce cytotoxicity for both SiNP20 and SiNP70, although at a lower level compared to HaCaT and K17 keratinocytes. The sensitivity difference between cell lines to toxins was previously described by Olschläger et al. (2009) [211] using primary fibroblasts NHDF (Normal Human Dermal Fibroblasts), primary keratinocytes NHEK (Normal Human Epidermal Keratinocytes), 3T3 mouse fibroblasts and HaCaT. While both fibroblast cell lines showed similar sensitivities towards sodium dodecyl sulphate (SDS), primary keratinocytes died at SDS concentrations about three times lower than the toxic concentration derived from the immortal HaCaT cells. The different sensitivity between the cell types used in this study might be due to different levels of paracrine factors, proteins synthesized in response endocrine factors (hormones) to induce changes in neighbouring cells [212]. These factors are important for growth and differentiation both *in vivo* and *in vitro* [213, 214], and low levels of such proteins could lead to lower differentiation and reduced sensitivity [215]. This consideration is further corroborated by the previously discussed wound healing data. In the wound healing experiment, coating wells with fibronectin, a glycoprotein of the extracellular matrix, and prior to HaCaT cell seeding was required for cell adhesion, growth, migration, and differentiation. While no such assay has been performed on fibroblasts, the slower growth, as well as the higher degree of cell differentiation observed in the other assays as well as previously reported in the literature [216, 217, 218] are two key characteristics. Such characteristics distinguish fibroblasts from

keratinocytes and further corroborate the importance of growth and differentiation factors in cellular sensitivity to nanoparticle-induced cytotoxicity.

Another interesting difference between the cell lines is the mechanisms of cell death induced by colloidal silica. While in HaCaT cells this mechanism was associated with apoptosis, in both K17 and HDF the same mechanism was instead associated with necrosis. Such difference could be due to the difference of subcellular locations as detected by confocal imaging. In K17 keratinocytes, the particles were located all around the nuclei, while they were found in the cytoplasm in HDF. The influence of cell-type related particle localization on apoptosis has been previously described [219, 220]. Blechinger et al. (2013) [219] investigated the cell-type dependent cytotoxic response of cells and uptake kinetics of 304 and 310 nm silica nanoparticles. By 24 hours treatment of HUVEC human vascular endothelial and HeLa cervix carcinoma cancer cells they found that cellular destination of SiO<sub>2</sub> particles was cell-type dependent, as particles were found inside the cytoplasm in HUVEC cells and associated with the plasma membrane in HeLa cells. This difference in cellular location was directly linked to cell death results, as treatment with SiO<sub>2</sub> NPs was associated with cell death for HUVEC, whereas no effect could be detected on the viability of HeLa cells. A previous study (2011) [221] by the same group demonstrated that cell death in HUVEC could be linked to induction of necrosis. Wu et al. (2015) [220] investigated the cytotoxic effects of 20 nm silica nanoparticles (SNPs) on MGC80–3 human gastric cancer cells and HeLa cells. After up to 24 hours exposure, they observed significant intake of SNPs in both MGC80–3 and HeLa cells in similar locations. The higher uptake efficiency they observed for MGC80–3 cells was correlated to the higher levels of apoptotic cell death induction, suggesting that particle uptake efficiency also plays an important role in cytotoxicity and in the definition of cell-type toxicological behaviour. Despite the light this study shed on the difference in cell type behaviour after treatment with colloidal silica, more work will need to be done on the issue, especially in the determination of cell death induction mechanism, as well as uptake efficiency and subcellular location.

## 6 CONCLUSIONS

The increased emphasis on nanotechnology and its potential widespread commercial applications over the last two decades has sparked great interest in the potential human health and environmental effects of nanomaterials, most of which is directed towards nanoparticles. If uncontrolled and unregulated, there is some potential that such particles might pose a human health hazard and/or environmental damage. Nanotoxicology research has shown that the interactions between nanoparticles (NPs), submicroparticles (SMPs) and cells are remarkably complex; however, many of the reported results are in contradiction between themselves, therefore there is still considerable debate about the regulation of nanomaterials. The potential key reasons for these conflicts lie in some matters often ignored or barely acknowledged in toxicological studies. Such matters include a) the sedimentation of particles and the absorption of proteins and other essential biomolecules onto their surface; b) the study of toxicity mechanisms taking into consideration of the changeable behaviour of particles in different biological media; c) cell type related toxicity. Addressing the reasons behind the conflicting results of nanotoxicity offers the opportunity to understand better cell-particles interactions, thus decreasing the number of conflicting reports and paving the way for better regulation towards nanomaterials.

Consequently, this study aimed to assess the toxic potential of silica nanoparticles and submicroparticles in relation to their physico-chemical properties. The choice has fallen on amorphous silica particles because despite being one of the most abundant materials on earth with a wide range of industrial applications, including nanoformulations for drug delivery, their toxicity is not well understood and, most importantly, regulated. No specific information is available regarding the effect of surface groups and, most importantly, about the optimal size range to achieve non-toxicity.

For this study, the focus has been on the importance of size in relation to amorphous silica cytotoxic potential. Sedimentation and protein adsorption have also been investigated to provide further evidence on silica stability in

suspension as well as to get insight on their interaction with cells. Consequently amorphous fumed and colloidal silica nanoparticles of different size were sourced from commercial suppliers without further treatment and characterized, in order to make the results more reproducible and easy for comparison across different laboratories. The main cell line used for this study, HaCaT keratinocytes, has been chosen because of its well-characterized behavior, as proven by the several studies in which it was used through the years, as well as for its characteristics, such as rapid growth and immortalized phenotype without tumorigenic activity. The other cell lines chosen for this study provided additional information, especially in regards to cell type related cellular response to silica particle treatment. This study has made the following important findings:

1. Fumed and colloidal SiNPs exhibited different dispersity in cell culture media, as fumed silica showed aggregation in serum-free medium while colloidal silica in the same conditions showed relatively good stability;
2. Fumed SiNPs showed cytotoxicity only in the absence FBS, whereas colloidal SiNPs could induce cytotoxicity also in the presence of FBS;
3. Silica particles exerted toxicity in a size-dependent manner in four human skin cell lines including two cell types;
4. While silica particles toxicity was evidenced to be associated with the induction of apoptotic cell death, sedimentation of larger particle could also have impact on cytotoxicity;
5. Cellular uptake appeared not to be size dependent;
6. Colloidal silica particles could either induce toxicity or promote wound healing in a dose-dependent manner.

This *in vitro* study suggests that 1) SiNP7, SiNP14, SiNP20 may not suitable for biomedical applications due to their instability in biological media and toxicity induction respectively; 2) the potential of silica toxicity could be different *in vivo* as components of FBS used *in vitro* are different from that of human serum; 3) there seems to be dose thresholds for colloidal silica to interfere with different cellular processes such as toxicity and wound healing.

Although this project aimed to assess the toxicity silica particles for drug delivery, this study provided information on a provisional size range suitable for biomedical application of amorphous silica, thus providing new scientific evidence supporting development of new regulations specific for nanomaterials. Modelling the size-dependent effect of silica particles *in vitro* also provided new insights into the size-dependent mode of action, which is of significance for predicting the possible outcome of amorphous silica particles exposure *in vivo*.

## **7 FUTURE PERSPECTIVES**

Despite the new insights provided in this study, more work will need to be done in order to understand the cellular and molecular mechanisms of silica uptake and toxicity in relation to particle size- and cell-type specificity. Further assessment also needs to consider the long-term fate and effect of silica particles after cellular internalization. To achieve this, assays could include:

- Gene and protein expression in different cells in response to cellular uptake of silica particles;
- Detection of exocytosis of silica particles in relationship to their size.

Future work should also focus more on the effect silica particles on cellular proliferation and migration, as these are important cellular processes in wound healing. Therefore, the evidence generated could support the development of advanced silica nanomaterials for tissue regeneration.





## REFERENCES

- 1 – Santamaria A., Historical Overview of Nanotechnology and Nanotoxicology, *Nanotoxicity* 926, 1-12, Humana Press (2012).
- 2 - Taniguchi N., On the basic concept of nano-technology, Proceedings of the international conference of production engineering, Japan Society of Precision Engineering, Tokyo (1974).
- 3 - Drexler K.E., Molecular engineering: an approach to the development of general capabilities for molecular manipulation, *Proc Natl Acad Sci USA* 78(9): 5275–5278 (1981).
- 4 - Drexler K.E. Engines of creation: the coming era of nanotechnology, Random House, New York (1986).
- 5 - Fanfair D., Desai S., Kelty C., The early history of nanotechnology. Produced by the Connexions Project, Module m14504, Rice University, <http://cnx.org/content/m14504/latest/> (2007).
- 6 - Donaldson K., Nanotoxicology, *Occup Environ Med* 61(9):727–728 (2004).
- 7 – Nel A., Xia T., Mädler L.; Li N., Toxic potential of materials at the nanolevel, *Science*, 311, 5761, 622-627 (2006).
- 8 - Thanh N.T.K.; Green L.A.W., Functionalisation of nanoparticles for biomedical applications, *Nano Today*, 5, 3, 213-230 (2010).
- 9 - Algar W.R., Prasuhn D.E., Stewart M.H., Jennings T.L., Blanco-Canosa J.B., Dawson P.E., Medintz I.L., The Controlled Display of Biomolecules on Nanoparticles: A Challenge Suited to Bioorthogonal Chemistry, *Bioconjugate Chem.* 22, 825–858 (2011).
- 10 - Chen Z., Yadghara A.M., Zhao L. and Mi Z., A review of environmental effects and management of nanomaterials, *Toxicological & Environmental Chemistry* Vol. 93, No. 6, 1227–1250 (2011).

- 11** – Yang C.C., Mai Y.W., Thermodynamics at the nanoscale: A new approach to the investigation of unique physicochemical properties of nanomaterials, *Materials Science and Engineering R* 79, 1–40 (2014).
- 12** - Jiang Q., Yang C.C., Size Effect on the Phase Stability of Nanostructures, *Current Nanoscience* 179–200 (2008).
- 13** - Gattoo M.A., Naseem S., Arfat M.Y., Dar A.M., Qasim K., Zubair S., Physicochemical Properties of Nanomaterials: Implication in Associated Toxic Manifestations, *BioMed Research International* Volume 2014, Article ID 498420, <http://dx.doi.org/10.1155/2014/498420> (2014).
- 14** - Powers K.W., Palazuelos M., Moudgil B.M., Roberts S. M., Characterization of the size, shape, and state of dispersion of nanoparticles for toxicological studies, *Nanotoxicology*, vol. 1, no. 1, pp. 42–51 (2007).
- 15** - De Jong W. H., Hagens W.I., Krystek P., Burger M.C., Sips A.J.A.M., Geertsma R. E., Particle size-dependent organ distribution of gold nanoparticles after intravenous administration, *Biomaterials*, vol. 29, no. 12, pp. 1912–1919 (2008).
- 16** - Verma A. and Stellacci F., Effect of surface properties on nanoparticle-cell interactions, *Small*, vol. 6, no. 1, pp. 12–21 (2010).
- 17** - Champion J. A. and Mitragotri S., Role of target geometry in phagocytosis, *Proc Natl Acad Sci USA*, vol. 103, no. 13, pp. 4930–4934 (2006).
- 18** - Kim S. T., Chompoosor A., Yeh Y., Agasti S. S., Solfiell D. J., Rotello V. M., Dendronized gold nanoparticles for siRNA delivery, *Small*, vol. 8, no. 21, pp. 3253–3256 (2012).
- 19** - Schneider M., Stracke F., Hansen S. and Schaefer U.F., Nanoparticles and their interactions with the dermal barrier, *Dermato-Endocrinology* 1:4, 197-206 (2009).
- 20** - Borm P.J.A., Robbins D., Haubold S., Kuhlbusch T., Fissan H., Donaldson K., Schins R., Stone V., Kreyling W., Lademann J., Krutmann J., Warheit D. and

Oberdorster E., The potential risks of nanomaterials: a review carried out for ECETOC, *Particle and Fibre Toxicology*, 3:11 (2006).

**21** - Ferrari M., Cancer nanotechnology: opportunities and challenges, *Nat. Rev. Cancer* 5, 161–171 (2005).

**22** - Vasir J.K., Reddy M.K., Labhasetwar V.D., Nanosystems in drug targeting: opportunities and challenges, *Curr. Nanosci.*1, 47–64 (2005).

**23** - Lewinski N., Colvin V., Drezek R., Cytotoxicity of nanoparticles, *Small* 4, 26–49 (2008).

**24** - Arora S., Rajwade J.M., Paknikar K.M., Nanotoxicology and *in vitro* studies: The need of the hour, *Toxicology and Applied Pharmacology* 258, 151–165 (2012).

**25** - Gurr J.R., Wang A.S.S., Chen C.H., and Jan K.Y., Ultrafine titanium dioxide particles in the absence of photoactivation can induce oxidative damage to human bronchial epithelial cells, *Toxicology* 213, nos. 1–2: 66–73 (2005).

**26** - Takenaka S., Karg E., Roth C., Schulz H., Ziesenis A., Heinzmann U., Schramel P. and Heyder J., Pulmonary and systemic distribution of inhaled ultrafine silver particles in rats, *Environmental Health Perspectives* 109, Suppl. no. 4: 547–51 (2001).

**27** - Donaldson K. and Stone V., Current hypotheses on the mechanisms of toxicity of ultrafine particles, *Annali dell'Istituto Superiore di Sanita'* 39, no. 3: 405–10 (2003).

**28** - Risom L., Møller P. and Loft S., Oxidative stress-induced DNA damage by particulate air pollution, *Mutation Research* 592, nos. 1–2: 119–37 (2005).

**29** - Treuel L., Jiang X., Nienhaus G.U., New views on cellular uptake and trafficking of manufactured nanoparticles, *J R Soc Interface* 10: 20120939 (2015).

- 30** – Kettler K., Veltman K., Van de Meent D., Van Wezel A., Hendricks A.J., Cellular Uptake of nanoparticles as determined by particle properties, experimental conditions, and cell type, *Environmental Toxicology and Chemistry*, Vol. 33, No. 3, pp. 481–492 (2014).
- 31** - Moghadam B.Y., Hou W-C., Corredor C., Westerhoff P., Posner J.D., Role of nanoparticle surface functionality in the disruption of model cell membranes, *Langmuir* 28:16318–16326 (2012).
- 32** - Mercer J., Helenius A., Virus entry by macropinocytosis, *Nat Cell Biol* 11:510–520 (2009).
- 33** - Kannan S., Kolhe P., Raukova V., Glibatec M., Kannan R., Lieh-Lai M., Bassett D., Dynamics of cellular entry and drug delivery by dendritic polymers into human lung epithelial carcinoma cells, *J Biomater Sci* 15:311–330 (2004).
- 34** - Chithrani B.D., Chan W.C.W., Elucidating the mechanism of cellular uptake and removal of protein coated gold nanoparticles of different sizes and shapes, *Nano Lett* 7:1542–1550 (2007).
- 35** - Yuan H., Zhanga S., Effects of particle size and ligand density on the kinetics of receptor-mediated endocytosis of nanoparticles, *Appl Phys Lett* 96:033704 (2010).
- 36** - Gao H., Shi W., Freund L.B., Mechanics of receptor-mediated endocytosis, *Proc Natl Acad Sci USA* 102:9469–9474 (2005).
- 37** – Murphy M., How mitochondria produce reactive oxygen species, *Biochem. J.* 417, 1–13 (2009).
- 38** - Alberts B., Johnson A., Lewis J., *Molecular Biology of the Cell*, 4th edition, New York: Garland Science (2002).
- 39** - SP Cullen S.P., Martin S.J., Caspase activation pathways: some recent progress, *Cell Death and Differentiation* 16, 935–938 (2009).
- 40** - Lademann J., Richter H., Teichmann A., Otberg N., Blume-Peytavi U., Luengo J., Nanoparticles - An efficient carrier for drug delivery into the hair

follicles, *European Journal of Pharmaceutics and Biopharmaceutics* 66:159-64 (2007).

**41** - Sattler K.D., *Handbook of Nanophysics*, CRC Press (2010).

**42** - Moghimi H.R., Barry B.W., Williams A.C., Stratum corneum and barrier performance: A model lamellar structural approach. In: Bronaugh RL, Maibach HI, eds. *Drugs—Cosmetics—Mechanisms—Methodology*. New York, Basel, Hong Kong: Marcel Dekker 515-53 (1999).

**43**- Curtis J., Greenberg M., Kester J., Phillips S., Krieger G., *Nanotechnology and nanotoxicology: a primer for clinicians*, *Toxicol. Sci.* 25, 245–260 (2006).

**44** - Hagens W.I., Oomen A.G., de Jong W.H., Cassee F.R., Sips A.J., What do we (need to) know about the kinetic properties of nanoparticles in the body?, *Regul. Toxicol. Pharmacol.* 49, 217–219 (2007).

**45** - Oberdorster G., Oberdorster E., Oberdorster J., *Nanotoxicology: an emerging discipline evolving from studies of ultrafine particles*, *Environ. Health Perspect.* 113, 823–839 (2005).

**46** - Oberdorster G., Maynard A., Donaldson K., Castranova V., Fitzpatrick J., Ausman K., Carter J., Karn B., Kreyling W., Lai D., Olin S., Monteiro-Riviere N., Warheit D., Yang H., *Principles for characterizing the potential human health effects from exposure to nanomaterials: elements of a screening strategy*, *Part. Fibre Toxicol* 2, 8–43 (2005).

**47** – Tyshenko M.G., *Risk Management and Surveillance of Nanomaterials For Public Health*, Chapter 2.5 of *Nanoengineering: Global Approaches to Health and Safety Issues*, pag. 285-299, Elsevier (2015).

**48** – Gellert R., Mantovani E., De Hert P., *The EU Regulation of Nanomaterials: Smoother or Harder? Precautionary Tool Chest as the Basis for Better Regulating Nanomaterials*, Chapter 2.7 of *Nanoengineering: Global Approaches to Health and Safety Issues*, pag. 339-374, Elsevier (2015).

**49** - [http://www.reachready.co.uk/reach\\_faq\\_free.php#nano](http://www.reachready.co.uk/reach_faq_free.php#nano)

- 50** - <http://www.fda.gov/ScienceResearch/SpecialTopics/Nanotechnology/default.htm>
- 51** - <http://www.fda.gov/RegulatoryInformation/Guidances/ucm257698.htm>
- 52** - <http://www.fda.gov/Cosmetics/GuidanceRegulation/GuidanceDocuments/ucm300886.htm#III.B>
- 53** - Tinkle S., McNeil S.E., Muehlebach S., Raj Bawa R., Borchard G., Barenholz Y., Tamarkin L., Desai N., Nanomedicines: addressing the scientific and regulatory gap, *Ann. N.Y. Acad. Sci.* ISSN 0077-8923 (2014).
- 54** – Ventola C.L., The Nanomedicine Revolution Part 2: Current and Future Clinical Applications, *Pharmacy and Therapeutics* 37(10): 582–591 (2012).
- 55** – Pillai G., Nanomedicines for Cancer Therapy: An Update of FDA Approved and Those under Various Stages of Development, *SOJ Pharmacy & Pharmaceutical Sciences* (2014).
- 56** - Napierska D., Thomassen L.C.J., Lison D., Martens J.A., Hoet P.H., The nanosilica hazard: another variable entity, *Particle and Fibre Toxicology*, 7:39 (2010).
- 57** – Liberman A., Mendez N., Trogler W.C., Kummel A.C., Synthesis and surface functionalization of silica nanoparticles for nanomedicine, *Surface Science Reports*69, 132–158 (2014).
- 58** - Wang X.D., Shen Z.X., Sang T., Cheng X.B., Li M.F., Chen L:Y., Wang Z.S., Preparation of spherical silica particles by Stöber process with high concentration of tetra-ethyl-orthosilicate, *Journal of Colloid and Interface Science* 341, 23–29 (2010).
- 59** - Stöber W., Fink A., Bohn E., Controlled growth of monodisperse silica spheres in the micron size range, *J. Colloid. Interface Sci.*, 26, 62–69 (1968).
- 60** - Nozawa K., Gailhanou H., Raison L., Panizza P., Ushiki H., Sellier E., Delville J.P., Delville M.H., Smart Control of Monodisperse Stöber Silica Particles: Effect of Reactant Addition Rate on Growth Process, *Langmuir* 21, 1516–1523 (2005).

**61** - Shimura N., Ogawa M., Porous silica spheres in macroporous structures and on nanofibres, *J.Mater.Sci.*42, 5299–5306 (2007).

**62** - Zhang H., Dunphy D.R., Jiang X., Meng H., Sun B., Tarn D., Xue M., Wang X., Lin S., Ji Z., Li R., Garcia F.L.,‡ Jing Yang, Kirk M.L., Xia T., Zink J.I., Nel A. and Brinker C.J., Processing Pathway Dependence of Amorphous Silica Nanoparticle Toxicity: Colloidal vs Pyrolytic, *J. Am. Chem. Soc.* 134, 15790–158046 (2012).

**63** – Perkins T.N., Shukla A., Peeters P.M., Steinbacher J.L., Landry C.C., Lathrop S.A., Steele C., Reynaert N.L., Wouters E.F.M., Mossman B.T., Differences in gene expression and cytokine production by crystalline vs. amorphous silica in human lung epithelial cells, *Particle and Fibre Toxicology*, 9:6 (2012).

**64** - Rancan F., Gao Q., Graf C., Troppens S., Hadam S., Hackbarth S., Kembuan C., Blume-Peytavi U., Ruehl E., Lademann J., Vogt A., Skin Penetration and Cellular Uptake of Amorphous Silica Nanoparticles with Variable Size, Surface Functionalization, and Colloidal Stability, *ACS Nano* Vol. 6, Number 8, 6829–6842 (2012).

**65** – Kato K.S., Hidaka M., Un K., Kawanishi T., Okuda H., Physicochemical properties and *in vitro* intestinal permeability properties and intestinal cell toxicity of silica particles, performed in simulated gastrointestinal fluids, *Biochimica et Biophysica Acta* 1840, 1171–1180 (2014).

**66** - Park Y.H., Bae H.C., Jang Y., Jeong S.H., Lee H.N., Ryu W.I., Yoo M.G., Kim Y.R., Kim M.K., Lee J.K., Jeong J., Son S.W., Effect of the size and surface charge of silica nanoparticles on cutaneous toxicity, *Molecular & Cellular Toxicology* Volume 9, Issue 1, pp 67-74 (2013).

**67** - Kim I.Y., Joachim E., Choi H., Kim K., Toxicity of silica nanoparticles depends on size, dose, and cell type, *Nanomedicine: Nanotechnology, Biology, and Medicine* 11, 1407–1416 (2015).



**68** - Yoshida T., Yoshioka Y., Morishita Y., Aoyama M., Tochigi S., Hirai T., Tanaka K., Nagano K., Kamada H., Tsunoda S., Nabeshi H., Yoshikawa T., Higashisaka K., Tsutsumi Y., Protein corona changes mediated by surface modification of amorphous silica nanoparticles suppress acute toxicity and activation of intrinsic coagulation cascade in mice, *Nanotechnology* 26, 245101 (2015).

**69** - Kim Y.R., Lee S.Y., Lee E.J., Park S.H., Seong N.W., Seo H.S., Shin S.S., Kim S.J., Meang E.H., Park M.K., Kim M.S., Kim C.S., Kim S.K., Son S.W., Seo W.R., Kang B.H., Han B.S., Soo A An S., Lee B.J., Kim M.K., Toxicity of colloidal silica nanoparticles administered orally for 90 days in rats, *Int J Nanomedicine* 9 (Suppl 2): 67–78 (2014).

**70** - Brohem C. , da Silva Cardeal L.B., Tiago M. , Soengas M.S. , de Moraes Barros S.B. and Maria-Engler S.S. , Artificial skin in perspective: concepts and applications, *Pigment Cell Melanoma Res.* 24; 35–50 (2010).

**71** - Rolin G., Placet V., Jacquet E., Tauzin H., Robin S., Pazart L. , Viennet C. , Saas P., Muret P., Binda D. and Humbert P., Development and characterization of a human dermal equivalent with physiological mechanical properties, *Skin Research and Technology* 2012; 18: 251–258 (2011).

**72** - Boyce S.T., and Warden G.D., Principles and practices for treatment of cutaneous wounds with cultured skin substitutes, *Am. J. Surg.* 183, 445–456 (2002).

**73** - Feliciani C., Gupta A.K., and Sauder D.N., Keratinocytes and cytokine / growth factors, *Crit. Rev. Oral Biol. Med.* 7, 300–318 (1996).

**74** - Phillips T.J., New skin for old: developments in biological skin substitutes, *Arch. Dermatol.* 134, 344–349 (1998).

**75** - Regnier M., Duval C., and Schmidt R., Potential cosmetic applications of reconstructed epidermis, *Int. J. Cosmet. Sci.* 21, 51–58 (1999).

**76** - Iozzo R.V., Basement membrane proteoglycans: from cellar to ceiling, *Nat. Rev. Mol. Cell Biol.* 6, 646–656 (2005).

- 77** - Del Rosso J.Q., Levin J., The Clinical Relevance of Maintaining the Functional Integrity of the Stratum Corneum in both Healthy and Disease-affected Skin, *Clinical Aesthetic Dermatology*, Volume 4, Number 9 (2011).
- 78** - Lee S.H., Jeong S.K., and Ahn S.K., An Update of the Defensive Barrier Function of Skin, *Yonsei Medical Journal* Vol. 47, No. 3, pp. 293 – 306 (2006).
- 79** - Zhang Z. and Michniak-Kohn B.B., Tissue Engineered Human Skin Equivalents, *Pharmaceutics* 4, 26-41 (2012).
- 80** - Wertz P.W., Van den Bergh B., The physical, chemical and functional properties of lipids in the skin and other biological barriers, *Chemistry and Physics of Lipids* 91, 85–96 (1998).
- 81** – Breslin S. And O’Driscoll L., Three-dimensional cell culture: the missing link in drug discovery, *Drug Discovery Today*, Volume 18, Numbers 5/6 (2013).
- 82** - Pappinen S., Pryazhnikov E., Khiroug L., Ericson M.B., Yliperttula M., Urtti A., Organotypic cell cultures and two-photon imaging: Tools for *in vitro* and *in vivo* assessment of percutaneous drug delivery and skin toxicity, *Journal of Controlled Release* 161, 656–667 (2012).
- 83** - Ataç B., Wagner I., Horland R., Lauster R., Marx U., Tonevitsky A.G., Azarc R.P, Lindner G., Skin and hair on-a-chip: *in vitro* skin models versus *ex vivo* tissue maintenance with dynamic perfusion, *Lab Chip* 13, 3555–3561 (2013).
- 84** - Murray A.R., Kisin E., Inman A., Young S.H., Muhammed M., Burks T., Uheida A., Tkach A., Waltz M., Castranova V., Fadeel B., Kagan V.E., Riviere J.E., Monteiro-Riviere N., Shvedova A.A., Oxidative Stress and Dermal Toxicity of Iron Oxide Nanoparticles *In Vitro*, *Cell Biochem Biophys*, 67:461–476 (2013).
- 85** - Cohen D., Soroka Y., Ma’or Z., Oron M., Portugal-Cohen M., Brégégère F.M., Berhanu D., Valsami-Jones E., Hai N., Milner Y., Evaluation of topically applied copper(II) oxide nanoparticle cytotoxicity in human skin organ culture, *Toxicology in Vitro* 27, 292–298 (2013).

- 86** - Choi J., Kim H., Choi J., Min Oh S., Park J., Park K., Skin corrosion and irritation test of sunscreen nanoparticles using reconstructed 3D human skin model, Korean Society of Environmental Health and Toxicology, Volume 29, <http://dx.doi.org/10.5620/eht.2014.29.e2014004> (2014).
- 87** – Korani M., Rezayat S.M., Bidgoli S.A., Sub-chronic Dermal Toxicity of Silver Nanoparticles in Guinea Pig: Special Emphasis to Heart, Bone and Kidney Toxicities, Iranian Journal of Pharmaceutical Research, 12 (3): 511-519 (2013).
- 88** – Sander K., Wilhelm Roux and his programme for developmental biology, Landmarks in Developmental Biology 1883–1924, pp 1-3 (1997).
- 89** – Freshney R.I., Introction to basic principles (Chapter 1), Animal Cell Culture Third Edition, Oxford University Press, ISBN 0-19-963796-2 (2005).
- 90** – Hay R.J., Durkin S., Cell line preservation and authentication (Chapter 3), Animal Cell Culture Third Edition, Oxford University Press, ISBN 0-19-963796-2 (2005).
- 91** – Gstraunthaler G., Alternatives to the use of Fetal Bovine Serum: Serum-Free Cell Culture, Altex 20, 4/03 (2003).
- 92** – Gunawan C., Lim M., Marquis C.P., Amal R., Nanoparticle–protein corona complexes govern the biological fates and functions of nanoparticles, J. Mater. Chem. B, 2, 2060 (2014).
- 93** – Mortensen N.P., Hurst G.B., Wang W., Foster C.M., Nallathamby P.D., Retterer S.T., Dynamic development of the protein corona on silica nanoparticles: composition and role in toxicity, Nanoscale, 5, 6372 (2013).
- 94** – Izak-Nau E., Voetz M., Eiden S., Duschl A., Puentes V.F., Altered characteristics of silica nanoparticles in bovine and human serum: the importance of nanomaterial characterization prior to its toxicological evaluation, Particle and Fibre Toxicology, 10:56 (2013).

- 95** – Aggarwal P., Hall J.B., McLeland C.B., Dobrovolskaia M.A., McNeil S.E., Nanoparticle interaction with plasma proteins as it relates to particle biodistribution, biocompatibility and therapeutic efficacy, *Advanced Drug Delivery Reviews* 61, 428–437 (2009).
- 96** - Lesniak A., Fenaroli F., Monopoli M.P., Åberg C., Dawson K.A., Salvati A., Effects of the presence or absence of a protein corona on silica nanoparticle uptake and impact on cells, *ACS Nano*, Jul 24;6(7):5845-57 (2012).
- 97** – NTA: Principles and Methodology, Malvern 2015.
- 98** – Zetasizer User Manual, Malvern 2015.
- 99** - Electron microscopy. By: Cannon, Byron D., Salem Press Encyclopedia of Science, January, 2015.
- 100** - <http://www.fei.com/introduction-to-electron-microscopy>
- 101** - Amelinckx S., van Dyck D., van Landuyt J. and van Tendeloo G., *Electron Microscopy*, DOI: 10.1002/9783527614561.fmatter.
- 102** - Egerton R., *Physical Principles of Electron Microscopy: An Introduction to TEM, SEM, and AEM*, ISBN-10: 0-387-25800-0.
- 103** – Freshney R.I., *Introduction to basic principles (Chapter 1), Animal Cell Culture Third Edition*, Oxford University Press, ISBN 0-19-963796-2 (2005).
- 104** - Boukamp P., Petrussevska R.T., Breitkreutz D., Hornung J., Markham A., Fusenig N.E., Normal keratinization in a spontaneously immortalized aneuploid human keratinocyte cell line, *Journal of Cell Biology*, Volume 106, 761-771 (1988).
- 105** - BJ (ATCC® CRL2522™) Product Sheet.
- 106** – Sitte N., Merker K., Von Zglinicki t., Grune T., Davis K.J.A., Protein oxidation and degradation during cellular senescence of human BJ fibroblasts: part I—effects of proliferative senescence, *The FASEB Journal*, Vol. 14 (2000).

**107** - Human Dermal Fibroblasts, adult (HDFa) Cat. no. C-013-5C, Specification Sheet, Gibco.

**108** - Storey A., Pim D., Murray A., Osborn K., Banks L. and Crawford L., Comparison of the *in vitro* transforming activities of human papillomavirus types, The EMBO Journal, vol.7 no.6 1815 – 1820 (1988).

**109** - Berridge M.V., Herst P.M., Tan A.S., Tetrazolium dyes as tools in cell biology: New insights into their cellular reduction, Biotechnology Annual Review, DOI: 10.1016/S1387-2656(05)11004-7 (2005).

**110** – Ishiyama M., Shiga M., Sasamoto K., Mizoguchi M., He P., A new sulfonated tetrazolium salt that produces a high water-soluble formazan dye, Chem. Pharm. Bull. 41(6), 1118-1122 (1993).

**111** – Cree I.A., Cancer Cell Culture –Methods and protocols (Chapter 20), Humana Press, DOI 10.1007/978-1-61779-080-5.

**112** – LDH Technical Bulletin, Sigma Aldrich.

**113** - <http://www.leica-microsystems.com/science-lab/phase-contrast/>

**114** - <http://www.microscopyu.com/articles/phasecontrast/phasemicroscopy.html>

**115** - <http://www.nobelprize.org/educational/physics/microscopes/phase/>

**116** - Introduction to Flow Cytometry: A Learning Guide, BD Biosciences.

**117** - Krysko D.V., Vanden Berghe T., D’Herde K., Vandenabeele P., Apoptosis and necrosis: Detection, discrimination and phagocytosis, Methods 44 205–221 (2008).

**118** - Lee S.H., Meng X.W., Flatten K.S., Loegering D.A., Kaufmann S.H., Phosphatidylserine exposure during apoptosis reflects bidirectional trafficking between plasma membrane and cytoplasm, Cell Death and Differentiation 20, 64–76 (2013).

**119** - Vranic S., Boggetto N., Contremoulins V., Mornet S., Reinhardt N., Marano F., Baeza-Squiban A., Boland S., Deciphering the mechanisms of

cellular uptake of engineered nanoparticles by accurate evaluation of internalization using imaging flow cytometry, *Particle and Fibre Toxicology* 10:2 (2013).

**120** - Hondow N., Brydson R., Brown A., The use of transmission electron microscopy in the quantification of nanoparticle dose, *Journal of Physics: Conference Series* 522:012055 (2014).

**121** - Brown A.P., Brydson R.M.D., Hondow N.S., Measuring *in vitro* cellular uptake of nanoparticles by transmission electron microscopy, *Journal of Physics: Conference Series* 522: 012058 (2014).

**122** - <http://www.olympusfluoview.com/theory/confocalintro.html>.

**123** – Pawley J., *Handbook of Biological Confocal Microscopy*, Springer, ISBN 13: 987-0-387-25921-5 (2010).

**124** – Guan J.L., *Cell Migration-Developmental Methods and Protocols*, Humana Press, ISBN 1-58829-382-3.

**125** - Chereddy K.K. , Her C.H. , Comune M. , Moia C., Lopes A., Porporato P.E. , Vanacker J., Lame C.M., Steintraesser L., Sonveaux P., Huijun Zhu H., Ferreira L., Vandermeulen G., Pr at V., PLGA nanoparticles loaded with host defense peptide LL37 promote wound healing, *Journal of Controlled Release* 194, 138–147 (2014).

**126** – Velnar T., Bailey T., Smrkolj V., The Wound Healing Process: an Overview of the Cellular and Molecular Mechanisms, *The Journal of International Medical Research* 37: 1528 – 1542 (2009).

**127** – Liang C.C., Park A.I., Guan J.L., In vitro scratch assay: a convenient and inexpensive method for analysis of cell migration *in vitro*, *Nature Protocol*, Vol. 2 No.2 (2007).

**128** – Mahmood T., Yang P.C., *Western Blot: Technique, Theory, and Trouble Shooting*, *North American Journal of Medical Sciences*, Volume 4 Issue 9 (2012).

- 129** – Hogson E., A textbook of modern toxicology, Wiley-Interscience (2004).
- 130** - Logan J., Edwards K., Saunders N., Real-Time PCR: Current Technology and Applications, Caister Academic Press, ISBN 978-1-904455-39-4 (2009).
- 131** - Mo Y., Wan R., Zhang Q., Application of Reverse Transcription-PCR and Real-Time PCR in Nanotoxicity Research, from Nanotoxicity: Methods and Protocols, Methods in Molecular Biology (Chapter 7).
- 132** - [http://premierbiosoft.com/tech\\_notes/TaqMan.html](http://premierbiosoft.com/tech_notes/TaqMan.html)
- 133** - <http://www.sabiosciences.com/newsletter/validating.pdf>
- 134** - Peirson S.N., Butler J.N., RNA Extraction From Mammalian Tissues, from Circadian Rhythms: Methods and Protocols, Humana Press.
- 135** – QIAGEN RNeasy kit for total RNA extraction manual.
- 136** - Slee A., Harte M.T., Kluck R.M., Wolf B.B., Casiano C.A., Newmeyer D.D., Wang H.G., Reed J.C., Nicholson D.W., Alnemri E.S., Green D.R., Martin S.J., Ordering the Cytochrome c-initiated Caspase Cascade: Hierarchical Activation of Caspases-2, -3, -6, -7, -8, and -10 in a Caspase-9-dependent Manner, The Rockefeller University Press 144 (2): 281 (1999).
- 137** - <http://www.ncbi.nlm.nih.gov/gene/534>
- 138** - Belmokhtar C.A., Josette Hillion J., Ségal-Bendirdjian E., Staurosporine induces apoptosis through both caspase-dependent and caspase-independent mechanisms, Oncogene 20, 3354 ± 3362 (2001).
- 139** - Orts-Gil G., Natte K., Drescher D., Bresch H., Manton A., Kneipp J., Österle W., Characterisation of silica nanoparticles prior to *in vitro* studies: from primary particles to agglomerates, Journal of Nanoparticle Research 13:9910 (2010).
- 140** – Nichols G., Byard S., Bloxham M.J., Botterill J., Dawson N.J., Dennis A., Diart V., North N.C., Sherwood J.D., A Review of the Terms Agglomerate and Aggregate with a Recommendation for Nomenclature Used in Powder and

Particle Characterization, Journal Of Pharmaceutical Sciences, Vol. 91 N°10 (2002).

**141** - Allouni Z.E., Cimpan M.R., Hølb P.J., Skodvin T., Gjerdet N.R., Agglomeration and sedimentation of TiO<sub>2</sub> nanoparticles in cell culture medium, Colloids and Surfaces B: Biointerfaces 68, 83–87 (2009).

**142** - Delgado A.V., Gonzalez-Caballero F., Hunter R.J., Koopal L.K., Lyklema J., Measurement and interpretation of electrokinetic phenomena (IUPAC Technical Report), Pure Appl Chem 77:1753–1850 (2005).

**143** - Powers K.W., Carpinone P.L., Siebein K.N., Characterization of Nanomaterials for Toxicological Studies, Chapter 2 of Nanotoxicity:Methods and Protocols, Humana Press, DOI 10.1007/978-1-62703-002-1 (2012).

**144** - Maiorano G., Sabella S., Sorce B., Brunetti V., Malvindi M.A., Cingolani R., Pompa P.P., Effects of Cell Culture Media on the Dynamic Formation of Protein-Nanoparticle Complexes and Influence on the Cellular Response, ACS Nano Vol. 4, n° 12, 7481–7491 (2010).

**145** - Irfan A., Cauchi M., Edmands W., Gooderham N.J., Njuguna J., Zhu H., Assessment of Temporal Dose-Toxicity Relationship of Fumed Silica Nanoparticle in Human Lung A549 Cells by Conventional Cytotoxicity and <sup>1</sup>H-NMR-Based Extracellular Metabonomic Assays, Toxicological Sciences 138(2), 354–364 (2014).

**146** - Sun B., Pokhrel S., Dunphy D.R., Zhang H., Ji Z., Wang X., Wang M., Liao Y., Chang C.H., Dong J., Li R., Mädler L., Brinker C.J., Nel A.E., Xia T., Reduction of Acute Inflammatory Effects of Fumed Silica Nanoparticles in the Lung by Adjusting Silanol Display through Calcination and Metal Doping, ACS Nano 10.1021/acsnano.5b03443 (2015).

**147** - Lynch I., Cedervall T., Lundqvist M., Cabaleiro-Lago C., Linse S., Dawson K.A., The nanoparticle–protein complex as a biological entity; a complex fluids and surface science challenge for the 21st century, Adv. Colloid Interface Sci. 134–135, 167–174 (2007).



- 148** - Lynch I., Dawson K.A., Protein-nanoparticle interactions, *Nano Today* 3, 40–47 (2008).
- 149** - Casals E., Pfaller T., Duschl A., Oostingh G.J., Puntès V., Time evolution of the nanoparticle protein corona, *ACS Nano* 7, 3623–3632 (2010).
- 150** - Gebauer J.S., Malissek M., Simon S., Knauer S.K., Maskos M., Stauber R.H., Peukert W., Treuel L., Impact of the nanoparticle–protein corona on colloidal stability and protein structure *Langmuir* 28, 9673–9679 (2012).
- 151** - Ji Z., Jin X., George S., Xia T., Meng H., Wang X., Suarez E., Zhang H., Hoek E.M.V., Godwin H., Nel A.E., Zink J. I., Dispersion and Stability Optimization of TiO<sub>2</sub> Nanoparticles in Cell Culture Media, *Environ. Sci. Technol.* 44, 7309–7314 (2010).
- 152** - Roach P., Farrar D., Perry C.C., Surface Tailoring for Controlled Protein Adsorption: Effect of Topography at the Nanometer Scale and Chemistry, *J. Am. Chem. Soc.* 128, 3939–3945 (2006).
- 153** - Orts-Gil G., Natte K., Thiermann R., Girod M., Rades S., Kalbe H., Thünemann A.F., Maskos M., Österle W., On the role of surface composition and curvature on biointerface formation and colloidal stability of nanoparticles in a protein-rich model system, *Colloids and Surfaces B: Biointerfaces* 108, 110–119 (2013).
- 154** – Puddu V., Perry C.C., Interactions at the Silica–Peptide Interface: The Influence of Particle Size and Surface Functionality, *Langmuir* 30, 227–233 (2014).
- 155** – Mukherjee B., Weaver J.W., Aggregation and Charge Behavior of Metallic and Nonmetallic Nanoparticles in the Presence of Competing Similarly-Charged Inorganic Ions, *Environ. Sci. Technol.* 44, 3332–3338 (2010).
- 156** - Lesniak A., Campbell A., Monopoli M.P., Lynch I., Salvati A., Dawson K. A., Serum Heat Inactivation Affects Protein Corona Composition and Nanoparticle Uptake, *Biomaterials* 31, 9511–9518 (2010).

**157** - Petersdorf R. G., Chills and Fever, Harrison's Principles of Internal Medicine, McGraw-Hill: New York, 1974.

**158** – Mahmoudi M., Abdelmonem A.M., Behzadi S., Clement J.H., Dutz S., Ejtehadi M.R., Hartmann R., Kantner K., Linne U., Maffre P., Metzler S., Moghadam M.K., Pfeiffer C., Rezaei M., Ruiz-Lozano P., Serpooshan V., Shokrgozar M.A., Nienhaus G.U., Parak W.J., Temperature: The "Ignored" Factor at the NanoBio Interface, ACS Nano Vol. 7 , n° 8, 6555–6562 (2013).

**159** - Mu Q., Hondow N.S., Krzemiński L., Brown A.P., Jeuken L.J.C., Routledge M.N., Mechanism of cellular uptake of genotoxic silica nanoparticles, Particle and Fibre Toxicology 9:29 (2012).

**160** - Al-Rawi M., Diabaté S., Weiss C., Uptake and intracellular localization of submicron and nano-sized SiO<sub>2</sub> particles in HeLa cells, Arch Toxicol 85:813–826 (2011).

**161** - <http://www.reade.com/home/10039>

**162** - Yameen B., Choi W.I., Vilos C., Swami A., Shi J., Farokhzad O.C., Insight into nanoparticle cellular uptake and intracellular targeting, Journal of Controlled Release 190, 485–499 (2014).

**163** - Rajendran L., Knölker H.J., Simons K., Subcellular targeting strategies for drug design and delivery, Nat. Rev. Drug Discov. 9, 29–42 (2010).

**164** - Doherty G.J., McMahon H.T., Mechanisms of endocytosis, Annu. Rev. Biochem. 78, 857–902 (2009).

**165** - Salvati A., Pitek A.S., Monopoli M.P., Prapainop K., Bombelli F.B., Hristov D.R., Kelly P.M., Åberg C., Mahon E., Dawson K.A., Transferrin-functionalized nanoparticles lose their targeting capabilities when a biomolecule corona adsorbs on the surface, Nature Nanotechnology 8:137-143 (2013).

**166** – Nowak J.S., Mehn D., Nativo P., Garcia C.P., Gioria S., Ojea-Jimenez I., Gilliland D., Rossi F., Silica nanoparticle uptake induces survival mechanism in

A549 cells by the activation of autophagy but not apoptosis, *Toxicology Letters* 224, 84–92 (2014).

**167** - Ye D., Raghnaill M.N., Bramini M., Mahon E., Åberg C., Salvati A., Dawson K.A., Nanoparticle accumulation and transcytosis in brain endothelial cell layers, *Nanoscale* 5, 11153 (2013).

**168** - Herd H.L., Malugin A., Ghandehari H., Silica nanoconstruct cellular toleration threshold *in vitro*, *Journal of Controlled Release* 153, 40–48 (2011).

**169** - Huang X., Teng X., Chen D., Tang D., He J., The effect of the shape of mesoporous silica nanoparticles on cellular uptake and cell function, *Biomaterials* 31, 438–448 (2010).

**170** - Chu Z., Huang Y., Taob Q., Li Q., Cellular uptake, evolution, and excretion of silica nanoparticles in human cells, *Nanoscale* 3, 3291 (2011).

**171** - Rivera-Gil P., Clift M.J.D., Rothen Rutishauser B., Parak W.J., Methods for Understanding the Interaction Between Nanoparticles and Cells, Chapter 3 of *Nanotoxicity Methods and Protocols* by Joshua Reneke, Humana Press, DOI 10.1007/978-1-62703-002-1 (2012).

**172** - Greish K., Thiagarajan G., Ghandehari H., *In Vivo* Methods of Nanotoxicology, Chapter 17 of *Nanotoxicity Methods and Protocols* by Joshua Reneke, Humana Press, DOI 10.1007/978-1-62703-002-1 (2012).

**173** - Zhu J., Liao L., Zhu L., Zhang P., Guo K., Kong J., Ji C., Liu B., Size-dependent cellular uptake efficiency, mechanism, and cytotoxicity of silica nanoparticles toward HeLa cells, *Talanta* 107, 408–415 (2013).

**174** - Li Y., Sun L., Jin M., Du Z., Liu X., Guo C., Li Y., Huang P., Sun Z., Size-dependent cytotoxicity of amorphous silica nanoparticles in human hepatoma HepG2 cells, *Toxicology in Vitro* 25, 1343–1352 (2011).

**175** - Lu X., Qian J., Zhou H., Gan Q., Tang W., Lu J., Yuan Y., Liu C., *In vitro* cytotoxicity and induction of apoptosis by silica nanoparticles in human HepG2 hepatoma cells, *International Journal of Nanomedicine* 6, 1889–1901 (2011).

- 176** - Ahmad J., Ahamed M., Akhtar M.J., Alrokayan S.A., Siddiqui M.A., Musarrat J., Al-Khedhairy A.A., Apoptosis induction by silica nanoparticles mediated through reactive oxygen species in human liver cell line HepG2, *Toxicology and Applied Pharmacology* 259, 160–168 (2012).
- 177** - Nemmar A., Albarwani S., Beegam S., Yuvaraju P., Yasin J., Attoub S., Ali B.H., Amorphous silica nanoparticles impair vascular homeostasis and induce systemic inflammation, *International Journal of Nanomedicine* 9:2279-2789 (2014).
- 178** - Brown D.M., Kanase N., Gaiser B., Johnston H., Stone V., Inflammation and gene expression in the rat lung after instillation of silica nanoparticles: Effect of size, dispersion medium and particle surface charge, *Toxicol Lett*, 224:147-156 (2014).
- 179** - Hassankhani R., Esmaeillou M., Tehrani A.A., Nasirzadeh K., Khadir F., Maadi H., *In vivo* toxicity of orally administrated silicon dioxide nanoparticles in healthy adult mice. *Environmental Science and Pollution Research* (2014).
- 180** - Lee S., Kim M., Lee D., Kwon T.K., Khang D., Yun H., Kim S., The comparative immunotoxicity of mesoporous silica nanoparticles and colloidal silica nanoparticles in mice, *International Journal of Nanomedicine* 8:147-158 (2013).
- 181** – Green D.R., *Means to an End: Apoptosis and Other Cell Death Mechanisms*, Cold Spring Harbor Laboratory Press (2011).
- 182** - Dolez, P.I., *Nanoengineering: Global Approaches to Health and Safety Issues*, Elsevier (2015).
- 183** - Torres F., Fadeel B., *Programmed Cell Death: Molecular Mechanisms and Implications for Safety Assessment of Nanomaterials*, *Accounts of Chemical research* Vol. 46, n° 3, 733–742 (2013).
- 184** - Chen X., Chen C.B., Udalagama C.N.B., Ren M., Fong K.E., Yung L.Y.L., Pastorin G., Bettiol A.A., Watt F., High-Resolution 3D Imaging and

Quantification of Gold Nanoparticles in a Whole Cell Using Scanning Transmission Ion Microscopy, *Biophysical Journal*. 104 (7):1419-1425 (2013).

**185** - Sizova E., Miroshnikov S., Yausheva E., Polyakova V., Assessment of Morphological and Functional Changes in Organs of Rats after Intramuscular Introduction of Iron Nanoparticles and Their Agglomerates, *BioMed Research Internationa*, <http://dx.doi.org/10.1155/2015/243173> (2015).

**186** - Lee Y.H., Cheng F.Y., Chiu H.W., Tsai J.C., Fang C.Y., Chen C.W., Wang Y.J., Cytotoxicity, oxidative stress, apoptosis and the autophagic effects of silver nanoparticles in mouse embryonic fibroblasts, *Biomaterials* 35, 4706-4715 (2014).

**187** - Alarifi S., Ali D., Alkahtani S., Verma A., Ahamed M., Ahmed M., Alhadlaq H.A., Induction of oxidative stress, DNA damage, and apoptosis in a malignant human skin melanoma cell line after exposure to zinc oxide nanoparticles, *International Journal of Nanomedicine* 8, 983–993 (2013).

**188** - Poon I.K.H., Hulett M.D., Parish C.R., Molecular mechanisms of late apoptotic/necrotic cell clearance, *Cell Death and Differentiation* 17, 381–397 (2010).

**189** - Jia L., Shen J., Li Z., Zhang D., Zhang Q., Liu G., Zheng D., Tian X., *In vitro* and *in vivo* evaluation of paclitaxel-loaded mesoporous silica nanoparticles with three pore sizes, *International Journal of Pharmaceutics* 445, 12– 19 (2013).

**190** - Laha D., Pramanik A., Maity J., Mukherjee A., Pramanik P., Laskar A., Karmakar P., Interplay between autophagy and apoptosis mediated by copper oxide nanoparticles in human breast cancer cells MCF7, *Biochimica et Biophysica Acta* 1840, 1–9 (2014).

**191** – Elmore S., Apoptosis: A Review of Programmed Cell Death, *Toxicologic Pathology*, 35:495–516 (2007).

**192** – Zeiss C. J., The apoptosis-necrosis continuum: insights from genetically altered mice, *Vet Pathol* 40, 481–95 (2003).

**193** - Denecker G., Vercammen D., Declercq W., Vandenaabeele P., Apoptotic and necrotic cell death induced by death domain receptors, *Cell Mol Life Sci* 58, 356–70 (2001).

**194** - Igney F. H., Krammer P. H., Death and anti-death: tumour resistance to apoptosis. *Nat Rev Cancer* 2, 277–88 (2002).

**195** - Costantini L.M., Gilberti R.M., Knecht D.A., The Phagocytosis and Toxicity of Amorphous Silica, *PLoS ONE* 6(2): e14647. doi:10.1371/journal.pone.0014647 (2011).

**196** - Sun L., Li Y., Liu X., Jin M., Zhang L., Du Z., Guo C., Huang P., Sun Z., Cytotoxicity and mitochondrial damage caused by silica nanoparticles, *Toxicology in Vitro* 25, 1619–1629 (2011).

**197** - Kobayashi S., Choose Delicately and Reuse Adequately: The Newly Revealed Process of Autophagy, *Biological & pharmaceutical bulletin* 38 (8): 1098–103 (2015).

**198** - Hussain S., Al-Nsour F., B. Rice A.B., Marshburn J., Yingling B., Ji Z., Zink J.I., Walker N.J., Garantzotis S., Cerium Dioxide Nanoparticles Induce Apoptosis and Autophagy in Human Peripheral Blood Monocytes, *ACS Nano* Vol. 6, N°7, 5820-5829 (2012).

**199** – Ahamed M., Silica nanoparticles-induced cytotoxicity, oxidative stress and apoptosis in cultured A431 and A549 cells, *Human and Experimental Toxicology* 32(2) 186–195 (2013).

**200** - Okoturo-Evans O., Dybowska A., Valsami-Jones E., Cupitt J., Gierula M., Boobis A.R., Edwards R.J., Elucidation of Toxicity Pathways in Lung Epithelial Cells Induced by Silicon Dioxide Nanoparticles, *PLoS ONE* 8(9): e72363. doi:10.1371/journal.pone.0072363 (2013).

**201** - Fede C., Millino C., Pacchioni B., Celegato B., Compagnin C., Martini P., Selvestrel F., Mancin F., Celotti L., Lanfranchi G., Mognato M., Cagnin S., Altered Gene Transcription in Human Cells Treated with Ludox® Silica Nanoparticles, *Int. J. Environ. Res. Public Health* 11, 8867-8890 (2014).

**202** –Chigurupati S., Mughal M.R., Okun E., Das S., Kumar A., McCaffery M., Seal S., Mattson M.P., Effects of cerium oxide nanoparticles on the growth of keratinocytes, fibroblasts and vascular endothelial cells in cutaneous wound healing, *Biomaterials* 34, 2194-2201 (2013).

**203** – Liang C., Park A.Y., Guan J., *In vitro* scratch assay: a convenient and inexpensive method for analysis of cell migration *in vitro*, *Nature Protocols* Vol. 2 N° 2 (2007).

**204** - Nickoloff B.J., Hendrix M.J.C., Pollock P.M., Trent J.M., Miele L., Qin J., Notch and NOXA-Related Pathways in Melanoma Cells, *J Investig Dermatol Symp Proc* 10:95 –104 (2005).

**205** - Karlsson M., Carlsson U., Protein adsorption orientation in the light of fluorescent probes: Mapping of the interaction between site-directly labeled human carbonic anhydrase II and silica nanoparticles, *Biophys J* 88:3536-3544 (2005).

**206** - Feng J., Yan W., Gou Z., Weng W., Yang D., Stimulating effect of silica-containing nanospheres on proliferation of osteoblast-like cells, *J Mater Sci Mater Med* 18:2167-2172 (2007).

**207** - Meddahi-Pellé A., Legrand A., Marcellan A., Louedec L., Letourneur D., Leibler L., Organ repair, hemostasis, and *in vivo* bonding of medical devices by aqueous solutions of nanoparticles, *Angewandte Chemie - International Edition* 53:6369-6373 (2014).

**208** - Sohaebuddin S.K., Thevenot P.T., Baker D., Eaton J.W., Tang L., Nanomaterial cytotoxicity is composition, size, and cell type dependent, *Particle and Fibre Toxicology* 7:22 (2010).

**209** - Schrand A.M., Dai L., Schlager J.J., Hussain S.M., Osawa E., Differential biocompatibility of carbon nanotubes and nanodiamonds, *Diamond and Related Materials* 16:2118-2123 (2007).

**210** - Rothen-Rutishauser B., Muhlfeld C., Blank F., Musso C., Gehr P., Translocation of particles and inflammatory responses after exposure to fine

particles and nanoparticles in an epithelial airway model, *Particle and Fibre Toxicology* 4:9 (2007).

**211** - Olschläger V., Schrader A., Hockertz S., Comparison of primary human fibroblasts and keratinocytes with immortalized cell lines regarding their sensitivity to sodium dodecyl sulfate in a neutral red uptake cytotoxicity assay, *Arzneimittelforschung* 59(3):146-52 (2009).

**212** - Schoop V.M., Mirancea N., Fusenig N.E., Epidermal Organization and Differentiation of HaCaT Keratinocytes in Organotypic Coculture with Human Dermal Fibroblasts, *Journal of Investigative Dermatology* 112, 343–353 (1999).

**213** - Kolbe M., Xiang Z., Dohle E., Tonak M., Kirkpatrick C.J., Fuchs S., Paracrine effects influenced by cell culture medium and consequences on microvessel-like structures in cocultures of mesenchymal stem cells and outgrowth endothelial cells, *Tissue Eng Part A*. 17-18:2199-212 (2011). D

**214** - Hsiao S.T., Asgari A., Lokmic Z., Sinclair R., Dusting G.J., Lim S.Y., Dilley R.J., Comparative analysis of paracrine factor expression in human adult mesenchymal stem cells derived from bone marrow, adipose, and dermal tissue, *Stem Cells Dev.* 21(12):2189-203 (2012).

**215** – Gilbert S.F., *Developmental Biology*. 6<sup>th</sup> edition, Sunderland (MA): Sinauer Associates; 2000.

**216** - Cornelia Wiegand C., Hipler U., Methods for the measurement of cell and tissue compatibility including tissue regeneration processes, *GMS Krankenhaushygiene Interdisziplinär Vol. 3(1)*, ISSN 1863-5245 (2008).

**217** - Singh D., Singh D., Choi S.M., Zo S., Painuli R.M., Kwon S.W., Han S.S., Effect of Extracts of *Terminalia chebula* on Proliferation of Keratinocytes and Fibroblasts Cells: An Alternative Approach for Wound Healing, *Evidence-Based Complementary and Alternative Medicine*, Volume 2014, Article ID 701656 (2014).

**218** - Bertonecelj V., Pelipenko J., Kristl J., Jeras M., Cukjati M., Kocbek P., Development and bioevaluation of nanofibers with blood-derived growth factors



for dermal wound healing, *European Journal of Pharmaceutics and Biopharmaceutics* 88, 64–74 (2014).

**219** - Blechinger J., Bauer A.T., Torrano A.A., Gorzelanny C., Bräuchle C., Schneider S.W., Uptake Kinetics and Nanotoxicity of Silica Nanoparticles Are Cell Type Dependent, *Small* 9, No. 23, 3970–3980 (2013).

**220** - Wu Y., Tang W., Wang P., Liu C., Yuan Y., Qian J., Cytotoxicity and Cellular Uptake of Amorphous Silica Nanoparticles in Human Cancer Cells, *Part. Part. Syst. Charact.* 32, 779–787 (2015).

**221** - Bauer A.T., Strozyk E.A., Gorzelanny C., Westerhausen C., Desch A., Schneider M.F., Schneider S. W., Cytotoxicity of silica nanoparticles through exocytosis of von Willebrand factor and necrotic cell death in primary human endothelial cells, *Biomaterials* 32, 8385 (2011).

**222** - S.B. Lim, et al., Improvement of drug safety by the use of lipid-based nanocarriers, *J. Control. Release*, doi:10.1016/j.jconrel.2012.06.002 (2012).

**223** - Bhaskar K., Anbu J., Ravichandiran V., Venkateswarlu V. and Madhusudan Rao Y., Lipid nanoparticles for transdermal delivery of flurbiprofen: formulation, *in vitro*, *ex vivo* and *in vivo* studies, *Lipids in Health and Disease* 8:6 (2009).

**224** - Üner M., Yener G., Importance of solid lipid nanoparticles (SLN) in various administration routes and future perspectives, *International Journal of Nanomedicine* 2(3) 289–300 (2007).

**225** - Pathak P. and Nagarsenker M., Formulation and Evaluation of Lidocaine Lipid Nanosystems for Dermal Delivery, *PharmSciTech* Vol. 10, No. 3 (2009).

**226** - Khokhlov A.Y.G.a.A.R., *Giant Molecules: Here, There, and Everywhere*, 2 ed., World Scientific Publishing Co. Pte. Ltd, Singapore (1997).

**227** - Devadasu V.R., Bhardwaj V., Kumar M., Can Controversial Nanotechnology Promise Drug Delivery?, *Chemical Reviews* 113, 1686---1735 (2013).

**228** - Ramos J., Forcada J., Hidalgo---Alvarez R., Cationic Polymer Nanoparticles and Nanogels: From Synthesis to Biotechnological Applications, *Chemical Reviews* 114, 367---428 (2014).

**229** - E. Soussan, S. Cassel, M. Blanzat, I. Rico---Lattes, Drug Delivery by Soft Matter: Matrix and Vesicular Carriers, *Angewandte Chemie International Edition* 48, 274---288 (2009).

**230** - Z. An, Q. Qiu, G. Liu, Synthesis of architecturally well-defined nanogels *via*RAFT polymerization for potential bioapplications, *Chem. Commun.*, 47, 12424---12440 (2011).

**231** - G. Deepa, A.K.T. Thulasidasan, R.J. Anto, J.J. Pillai, G.S.V. Kumar, *International journal of nanomedicine*, 2012, 7, 4077---4088.

**232** – Kuruppuarachchi M., Savoie H., Lowry A., Alonso C., Boyle R., Polyacrylamide Nanoparticles as a Delivery System in Photodynamic Therapy, *Mol. Pharmaceutics* 2011, 8, 920–931 (2011).

## APPENDICES

### Appendix A Collaboration Work

#### A.1 Preliminary analysis of lipid nanoparticles for drug delivery of Dacarbazine

Lipid-based nanocarriers are generally composed of lipid components such as phospholipids, cholesterol and triglycerides. These materials are mostly from natural sources and have good *in vivo* biocompatibility, as well as being biodegradable. Many of these lipid excipients have been used in FDA approved pharmaceutical products and have well-established safety profiles and toxicological data [222].

The first lipid-nanocarriers to be produced and studied were liposomes, which were composed of a closed bilayer of phospholipids offering a hydrophobic compartment (lipid layer) as well as a hydrophilic compartment (inner volume of the liposome) for drug encapsulation. However, phospholipids are expensive, thus hindering the possibility of meaningful scale-up processes. In the early Nineties Solid Lipid Nanoparticles (SLNs) were introduced as drug carriers in the pharmaceutical field. In general SLNs can be defined as a colloidal carrier system for controlled drug delivery composed of high melting point lipids (glycerides and waxes) solid at room temperature [223, 224]. They are characterized by a better physical stability, and synthesis doesn't require the use of phospholipids and organic solvents, making scale-up processes much easier to perform. However, they present some disadvantages, especially in terms of drug-loading capability. For this reason, a new generation of lipid NPs, called Nanostructured Lipid Carriers (NLCs) was designed in order to overcome such limitations related to old generation SLNs. NLCs are composed of a solid lipid matrix with a certain content of liquid lipid. Because of this modification, the drug is located in the liquid lipid, which in turn is surrounded by the solid lipid. This provides some degree of mobility to the drug, which contributes to the overall carrier stability [225]. The incorporation of a liquid lipid into solid lipid matrix leads to great imperfections in the crystal lattice of the nanocarriers, thus

leading to improved drug loading capacity and reduced drug expulsion during storage. Because of these improved characteristics, as well as for the ease of scaling up, NLCs have been investigated for drug delivery through different routes, including oral, ocular and dermal. This preliminary study has been conducted in order to characterize a first batch of NLCs synthesized by our group, as well as to give a preliminary analysis of the potential toxicological effects these particles have *in vitro* on HaCaT keratinocytes. The data acquired through this analysis have proven useful to correct particle formulation, providing the basis for further work on drug encapsulation, drug loading capacity studies and *in vitro* drug release.

In order to assess size, solubility, structure and behaviour in culture medium, anionic NLC (NLC-) and cationic NLC (NLC+) at 25-100 µg/ml were analysed by Dynamic Light Scattering (DLS) at 0 and 24 hours. Medium with 0% FBS (CM) (**Table A.1**) was used as background control. Compared with the negative control, DLS of NLC- and NLC+ in CM (**Table A.2**) showed different behaviour. Whereas NLC- showed average around 200 nm and PDI levels 0.3-0.4 at all tested concentrations and time points, NLC+ showed high average, above 2 µm, and varying PDI levels, between 0.4 and 1.0, suggesting that either synthesis was not efficient or positive particles were highly unstable and aggregating in CM.

**Table A.1** DLS assay of CM as background control.

Neg. Contr.	0 h		24 h	
	Average	PDI	Average	PDI
CM	4.4	0.3	9.3	0.5

**Table A.2** DLS assay of NLC+ and NLC- in CM at 0 and 24 h after incubation at 4°C (storage conditions).

NPs	25 µg/ml				50 µg/ml				100 µg/ml			
	0H		24H		0H		24H		0H		24H	
	Ave.	PDI	Ave.	PDI	Ave.	PDI	Ave.	PDI	Ave.	PDI	Ave.	PDI
NLC-	187	0.4	185	0.4	184	0.5	187	0.4	194.2	0.5	261	0.5
NLC+	4373	0.5	3281	0.6	2977	1.0	2831	0.6	2177	0.6	2944	0.4

Considering characterization data, cytotoxicity potential was assessed by assay of cell viability in HaCaT cells using MTT test. Two new sets of particles, neutral NLC (NLC) and anionic NLC conjugated with Ludox Silica (NLC/Ludox) were added for further reference. Particles were tested at concentrations 25-100 µg/ml at 4 and 24 hours in CM (**Figure A.1**). At 4 hours a particle-dependent increase in cell viability was detected, with NLC/Ludox composites giving the most prominent effect; at 24 hours, on the other hand, no toxicity was detected in any of the samples, suggesting that the whole set of samples had little to no toxicity.

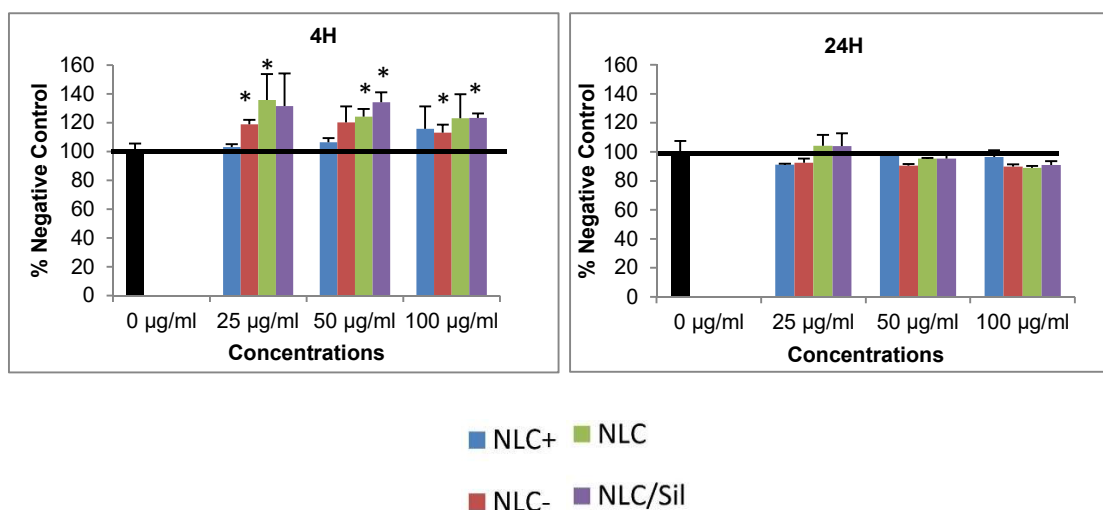


**Figure A.1** MTT assay for NLCs particles. HaCaT cells were treated 24 h with NLCs 25-100 µg/ml, then analysed for mitochondrial activity.

One of the concentrations chosen for MTT (50  $\mu\text{g/ml}$ ) was also used to assess morphology changes in HaCaT cells by phase contrast microscopy imaging. Cells were assessed after treatment with CM at 24 hours (**Figure A.2**). While NLC+ and NLC- treated cells showed shape loss and reduced viability, NLC and NLC/Ludox treated cells showed little to no effect, suggesting a role of surface charge on the toxicity of these particles.

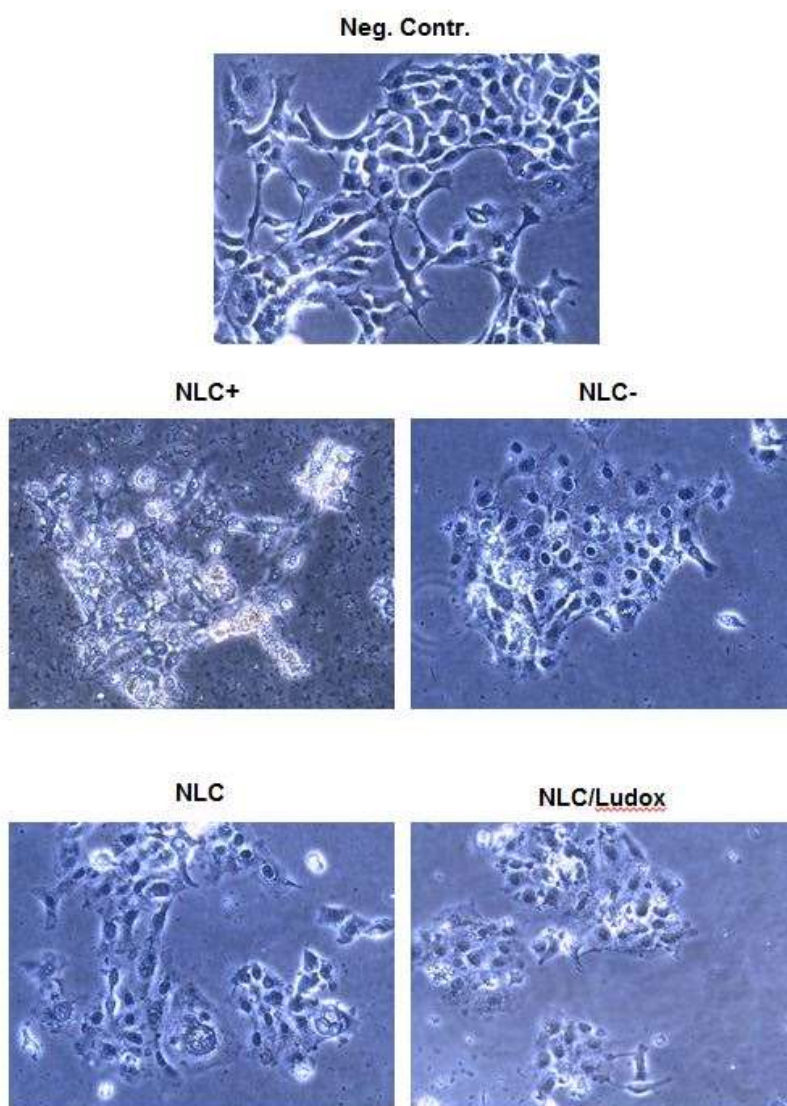


**Figure A.2** Phase contrast imaging of HaCaT cells following treatment with NLCs. Cells were treated with NLC, NLC+, NLC- and NLC/Ludox at 50  $\mu\text{g/ml}$  for 24 hours at 37°C.

The results here reported have been used for further development of NLCs synthesis; as NLC+, based on the data acquired, were deemed too unstable to get suitable carriers, further work has been done on optimizing synthesis for the other three types, as well as encapsulation of Dacarbazine in the final product. For further reference, see Appendix C.

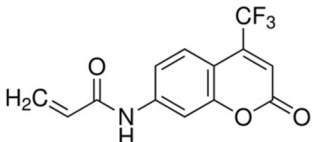
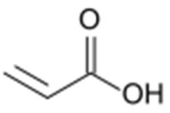
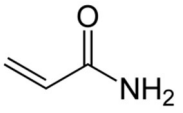
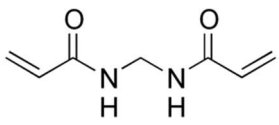
## **A.2 Collaboration with Queen Mary University of London (QMUL) for toxicological assessment of polyacrylamide nanoparticles**

As introduced before, in the last 20 years nanomaterials and their potential applications as drug delivery systems have attracted significant interest, with micelles, lysosomes and solid-lipid nanoparticles being among the most interesting because of their unique physico-chemical properties. These types of nanomaterials are self-assembled systems, and present several advantages, such as increasing bioavailability of drugs, increasing drug deposition in diseased tissues and reducing side effects associated with the drug. However, a number of issues, including instability in certain solvent systems and ability to deliver a drug mainly through diffusion remained unsolved, therefore limiting their applications as drug delivery vehicles [226, 227]. Polymeric nanomaterials, in contrast, are normally characterized by high stability, as a direct result of the presence of a strong network of covalent bonds. Among these, nanogels stand out as interesting nanomaterials for biomedical applications, given their ability to support stable colloidal solutions [228]. Nanogels are polymeric cross-linked particles forming a 3-dimensional network; their ability to cross-link gives them a significant advantage over simple block co-polymers, as a) they don't need to rely on self-assembly; b) their stability is higher and c) they have increased polymer density [229, 230]. The selection of components used for nanogel preparation is responsible for its characteristics: the use of monomers with a high degree of hydrophilicity, such as acrylic acid, will result in the production of a nanogel with a high affinity for water. This type of particle will provide an ideal vehicle for drug delivery, as the high hydrophilicity of the carrier will facilitate the

administration of otherwise insoluble drugs [231]. Another important requirement for the preparation of the nanogels is the cross-linker, which must have a similar chemical structure compared to the monomer in order to achieve successful polymerization. Among different type of polymeric nanogels, polyacrylamide nanogels have demonstrated an interesting potential as a delivery system [232]. Acrylamide is a compound capable of forming polymers with good solubility in water. It's also characterized by amide bonds, which have a relatively good affinity to water thanks to hydrogen bonding and which are also abundant in the human body as the result of peptide bonds. As part of the same NANODRUG Network, assessment of two polyacrylamide nanogels, JR-P2-34 and JR-P2-35 (**Table A.3 and A.4**), for behaviour in culture medium, as well as cytotoxic potential and uptake in HaCaT cells has been performed in collaboration with Prof. Marina Resmini group at Queen Mary University of London (QMUL).

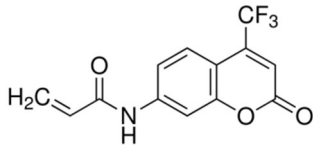
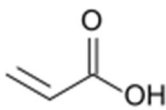
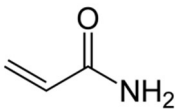
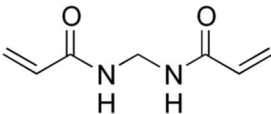
### **JR-P2-34**

**Table A.3** Composition of JR-P2-34.

Component	Structure	Percentage In Formulation
7-trifluoromethyl coumarin acrylamide		2.5%
Acrylic Acid		10%
Acrylamide		67.5%
Methylene bisacrylamide		20%



**JR-P2-35****Table A.4** Composition of JR-P2-35.

Component	Structure	Percentage	In
7-trifluoromethyl coumarin acrylamide		5%	
Acrylic Acid		10%	
Acrylamide		65%	
Methylene bisacrylamide		20%	

In order to gain information about particle behavior in culture medium, both JR-P2-34 and Jr-P2-35 were dispersed in CM-10% at 10-200  $\mu\text{g/ml}$  and assessed by DLS analysis. Particle-free medium was employed as background control. The data obtained is reported in **Table A.6**. Particles size was 14.9/20.8 nm, much smaller compared to the size previously measured by QMUL in water (**Table A.5**), suggesting particle sedimentation in culture medium.

**Table A.5** JR-P2-34 and JR-P2-35 specifications.

	JR-P2-34	Jr-P2-35
<b>Particle size in water</b>	171 nm	123 nm
<b>Solubility (mg/ml)</b>	1 mg/ml	1 mg/ml

**Table A.6** DLS assay of JR-P2-34 and JR-P2-35.

	10 µg/ml				200 µg/ml			
	0H		24H		0H		24H	
	Ave.	PDI	Ave.	PDI	Ave.	PDI	Ave.	PDI
<b>JR-P2-34</b>	14.9	0.4	17.4	0.4	15.6	0.4	18.5	0.4
<b>JR-P2-35</b>	14.8	0.4	18.3	0.4	20.8	0.6	20.2	0.4

Unfortunately, due to the limited amount of available sample, no confirmation of size, solubility and shape could be obtained by SEM or TEM. Instead, assessment on cytotoxic potential was performed by MTT assay in HaCaT cells for concentrations 10- 200 µg/ml at 24 h in CM-10% and CM (**Figure A.3**). In CM-10% a notable increase in cell viability could be detected for both particles at 25 and 50 µg/ml, while a decrease could be detected at 10 µg/ml. In CM, on the other hand, no reduction of cell viability could be detected; on the other hand, a 10-20% increase in cell viability could be detected for both particles at all concentrations tested.

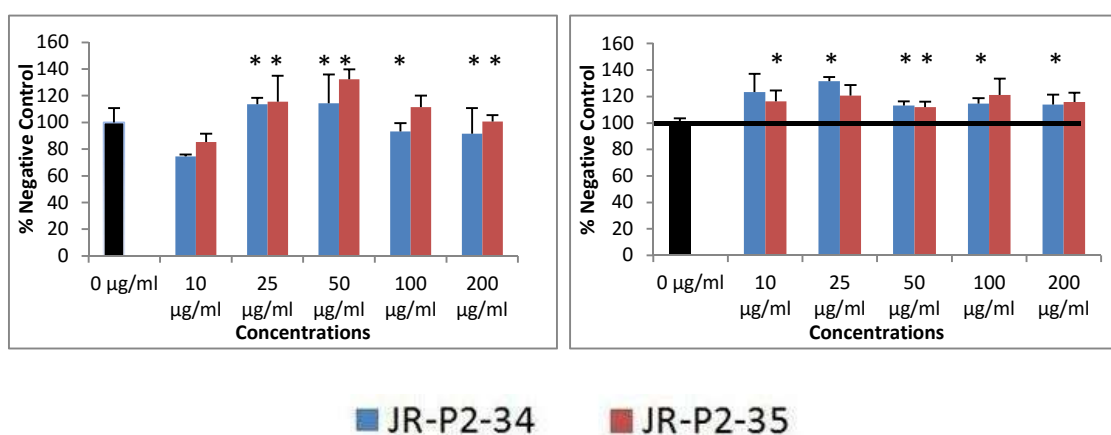


**Figure A.3** Cytotoxicity assessment in HaCaT cells. JR-P2-34 and JR-P2-35 at 10-200 µg/ml were used to treat cells for 24 h at 37°C.

To verify uptake inside HaCaT cells, flow cytometry analysis in CM-10% at 24 hours using the same concentrations as MTT assay; unfortunately, the results were inconclusive, as the wavelength of the particle fluorophore could not properly be detected by the instrument (data not shown). In conclusion, even though the characterization and viability data proved quite interesting, no further analysis could be performed due to lack of sample availability as well as time constraints and technical issues. Further work has been done by Prof. Resmini's group to test the particles toxicity *in vivo*, using Casper zebrafish embryos as model.

### **A.3 Collaboration with Universite' Catholique de Louvain (UCL) on PLGA nanoparticles**

Wound treatment and its medical complications remain one of the most prevalent and economically challenging healthcare issues in the world. One of the simplest and pragmatic solutions to faster wound healing process is the application of exogenous lactate, which accelerates angiogenesis, activation of procollagen factors and recruitment of endothelial progenitor cells in wounds. Utilization of poly (lactic-co-glycolic acid) (PLGA) is one of the strategies to supply lactate sustainably; using it as a drug delivery system would perform the dual role of wound healing agent itself as well as system to release loaded drugs to the wound. As part of the NANODRUG Network, in collaboration with Prof. Veronique Pr eat at Universit  Catholique de Louvain (UCL, Belgium), *in vitro* toxicological assessment of PLGA nanoparticles loaded with human host defense peptide LL37 was performed in HaCaT keratinocytes and BJ fibroblasts; further details regarding this study can be found in Appendix C.

# Appendix B Particles Specification Sheets

## SiNP7 (S5130) – SiNP14 (S5505)



3050 Spruce Street  
Saint Louis, Missouri 63103 USA  
Telephone 801-525-5800 • (314) 771-0700  
Fax (314) 286-7828  
email: techserv@sigma.com  
sigma-aldrich.com

### Product Information

#### FUMED SILICA

Product Number S 5130

Replacement for Product Code 38,126-8

CAS NUMBER: 112045-52-5

SYNONYMS: fumed silicon dioxide, Aerosil™, Cab-O-Sil™

#### PHYSICAL DESCRIPTION:

Fumed silica is composed of submicron-sized spheres, which are 40-60% fused into short chains, very highly branched, 0.1-0.2 microns long. The spheres are quite uniform in size for a given product, but the chain lengths are quite variable, 10 to 30 units in length. The surface area, which varies with the particle size, gives a good approximation of the sphere diameter. The smaller the particles, the larger the estimated surface area.<sup>2</sup>

Sigma product	Particle size (µm)	Surface area (m <sup>2</sup> /gram)	Density (lb/cu. ft)
S5130	0.007	390 ∇ 40	2.3
S5255	0.008	325 ∇ 25	2.3
S5380	0.011	255 ∇ 15	4.5 ∇ 0.5
S2128	0.012	200 ∇ 25	2.3
S5505	0.014	200 ∇ 25	2.3

#### METHOD OF PREPARATION:<sup>2</sup>

Silicon tetrachloride is burned in a flame of hydrogen and oxygen (at approximately 1800EC) to produce molten spheres of silicon dioxide (and hydrogen chloride). Depending on process parameters, the size of these silica spheres can be varied and, within a given batch, show excellent uniformity (by electron micrograph). The molten spheres collide and fuse with one another to form branched, three-dimensional chain-like aggregates.

# SiNP20 (Ludox Silica)

**SIGMA-ALDRICH®**

[sigma-aldrich.com](http://sigma-aldrich.com)

3050 Spruce Street, Saint Louis, MO 63103, USA

Website: [www.sigmaaldrich.com](http://www.sigmaaldrich.com)

Email USA: [techserv@sial.com](mailto:techserv@sial.com)

Outside USA: [eurtechserv@sial.com](mailto:eurtechserv@sial.com)

## Product Specification

Product Name:

Product Number: **420875** SiO<sub>2</sub>  
MDL: MFCD00011232  
Formula: O<sub>2</sub>Si  
Formula Weight: 60.08 g/mol

TEST	Specification
Appearance (Color)	Colorless
Appearance (Form)	Liquid
ICP Major Analysis	Confirmed
Confirms Silicon Component	
pH	8.6 - 9.3
Specific Gravity	1.199 - 1.216
Viscosity	≤ 25.0 cps
Silica	29.0 - 31.0 %
Miscellaneous Assay	≥ 62.0 %
Transmission	
Miscellaneous Assay	198 - 258
Surface Area (m <sup>2</sup> /g)	
Miscellaneous Assay	0.17 - 0.21 %
Al <sub>2</sub> O <sub>3</sub>	
Registered Trademark	Confirmed
LUDOX is a registered trademark of W.R. Grace & Co.-Conn.	

Specification: PRD.0.ZQ5.1000035229

Sigma-Aldrich warrants, that at the time of the quality release or subsequent retest date this product conformed to the information contained in this publication. The current Specification sheet may be available at Sigma-Aldrich.com. For further inquiries, please contact Technical Service. Purchaser must determine the suitability of the product for its particular use. See reverse side of invoice or packing slip for additional terms and conditions of sale.

1 of 1

### SiNP70, SMP200, SMP500

	Z-PS-SIL-GFP-0,07	Z-PS-SIL-GFP-0,2	Z-PS-SIL-GFP-0,5
<b>Surface</b>	Plain	Plain	Plain
<b>Diameter</b>	70 nm	200 nm	500 nm
<b>Concentration</b>	25 mg/ml	50 mg/ml	50 mg/ml
<b>Quantity</b>	10 ml	10 ml	10 ml
<b>Polydispersity Index</b>	< 0.2	< 0.2	< 0.2
<b>Shape</b>	Spherical	Spherical	Spherical
<b>Density</b>	2.0 g/ccm	2.0 g/ccm	2.0 g/ccm
<b>Porosity</b>	Non Porous	Non Porous	Non Porous
<b>Stable in</b>	Acqueous Solutions and Organic Solvents	Acqueous Solutions and Organic Solvents	Acqueous Solutions and Organic Solvents
<b>Unstable in</b>	Acid and Strong Bases	Acid and Strong Bases	Acid and Strong Bases
<b>Product Form</b>	Acqueous Suspension	Acqueous Suspension	Acqueous Suspension
<b>Particle per ml</b>	$7.0 \times 10^{13}$	$6.0 \times 10^{12}$	$3.8 \times 10^{11}$
<b>Particle pro mg</b>	$2.8 \times 10^{12}$	$1.2 \times 10^{11}$	$7.6 \times 10^{10}$
<b>Optical Characteristics</b>	Green Fluorescence	Green Fluorescence	Green Fluorescence
<b>Colour</b>	Yellow	Yellow	Yellow
<b>Excitation</b>	485 nm	485 nm	485 nm
<b>Emission</b>	510 nm	510 nm	510 nm
<b>Other Comments</b>	Store at room temperature, do not freeze	Store at room temperature, do not freeze	Store at room temperature, do not freeze

# Appendix C Awards and Publications

## C.1 Awards

Best Poster Presentation British Toxicology Society (BTS) Spring Meeting 2014  
 – Title: Internalization and Toxicity of Amorphous Silica Nanoparticles And Submicroparticles In Human Skin HaCaT Cells.

### Internalization and Toxicity of Amorphous Silica Nanoparticles and Submicroparticles in Human Skin HaCaT cells

C. Moia<sup>1</sup>, D. Dinsdale<sup>2</sup>, M. MacFarlane<sup>2</sup>, H. Zhu<sup>1\*</sup>

<sup>1</sup> School of Applied Sciences, Cranfield University, Cranfield, Bedfordshire, MK43 0AL  
<sup>2</sup> MRC Toxicology Unit, University of Leicester, Leicester, Leicestershire, LE1 9HN

\*corresponding author, Email: h.zhu@cranfield.ac.uk

#### Introduction

Amorphous silica nanoparticles (A-SiNP) and submicroparticles (A-SMP) have been increasingly applied in a variety of fields such as pharmaceuticals, food and cosmetics. Although generally considered safe, concerns have been raised over their toxicological behaviour, especially in terms of size-related effects. For these reasons, this study aimed to assess the internalization and toxicity of A-SiNP and A-SMP in relation to their size in human skin HaCaT cells.

#### Materials & Methods

Cells were treated with green fluorescein isothiocyanate (FITC)-labelled A-SiNP (70 nm) and A-SMP (200 nm and 500 nm) at 10, 25, 50, 100, 200 µg/ml in culture medium with and without Fetal Bovine Serum (FBS). Multiparameter assays were performed at different time points, using untreated HaCaT cells as negative control. Flow cytometry and transmission electron microscopy (TEM) were used to determine the internalization of particles into the cells, whereas light microscopy combined with Annexin V-FITC/Propidium Iodide staining flow cytometry was applied to assess cytotoxicity.

#### Results

**Uptake** in the presence of FBS was evident for A-SiNP 70 nm and A-SMP 200 nm at 50 µg/ml, and at 10 µg/ml for A-SMP 500. In the absence of FBS it was more pronounced, starting as low as 10 µg/ml (Figure 1).

**TEM** assay showed that the internalized particles were largely confined to large endosomes, with few found in the early tubular-vesicular network and free in the cytoplasm (Figure 2).

Figure 1. Uptake of A-SiNP 70 nm, A-SMP 200 and 500 nm in HaCaT cells.

Figure 3. Microscopy imaging of HaCaT cells treated with A-SiNP 70 nm, A-SMP 200 and 500 nm at 50 µg/ml.

Figure 2. TEM imaging of A-SiNP 70 nm internalization.

Figure 4. Induction of necrosis and apoptosis in HaCaT cells by A-SiNP 70 nm, A-SMP 200 and 500 nm.

Light microscopy showed that in the presence of FBS untreated cells shared some morphology features with cells treated with A-SiNP 70 nm and A-SMP 200 nm, indicative of cell growth; whereas cells treated with A-SMP 500 nm didn't display the same morphology (Figure 3). In the absence of FBS, silica particles induced a dose- and size-dependent reduction of cell density, which were consistent with the occurrence of both necrotic and apoptotic cell death, as indicated with an increase in cells with high in FITC and PI staining (Figure 4).

#### Conclusion

This study indicated that internalization of A-SiNP and A-SMP into HaCaT cells was not size selective, whilst the toxicity was size-dependent and was reduced by FBS. This in vitro study provides evidence supporting further assessment of A-SiNP and A-SMP toxicity in relation to their size in different in vitro and in vivo models.

This study is part of NANODRUG Project funded by the EU (Grant No. 289454)

[www.cranfield.ac.uk/sas](http://www.cranfield.ac.uk/sas)

Supervisor: Dr. Huijun Zhu  
Cranfield University, Cranfield, Bedfordshire, MK43 0AL

## C.2 Publications

Cherreddy K.K. , Her C.H. , Comune M. , **Moia C.**, Lopes A., Porporato P.E. , Vanacker J., Lame C.M., Steinstraesser L., Sonveaux P., Huijun Zhu H., Ferreira L., Vandermeulen G., Pr at V., PLGA nanoparticles loaded with host defense peptide LL37 promote wound healing, *Journal of Controlled Release* 194, 138–147 (2014).

**Moia C.**, Huijun Zhu H., Almousallam M., Cell type- and size-dependent *in vitro* toxicity of silica particles in human skin cells, *ScientificTracks Abstracts: J Clin Toxicol*, DOI: 10.4172/2161-0495.S1.012 (2014).

Zhu H., **Moia C.**, Vilela P., *Nanomaterials for skin regeneration*, Chapter 8 of *Biomaterials: The Design, Synthetic Strategies and Biocompatibility of Polymer Scaffolds for Biomedical Application*, Bentham E-Books, ISBN: 978-1-60805-877-8 (2014).

Cherreddy K.K., Lopes A., Koussoroplis S., Payen V., **Moia C.**, Zhu H., Sonveaux P., Carmeliet P., des Rieux A., Vandermeulen G., Pr at V., Combined effects of PLGA and vascular endothelial growth factor 2 promote the healing of non-diabetic and diabetic wounds, *Nanomedicine: Nanotechnology, Biology and Medicine*, doi:10.1016/j.nano.2015.07.006 (2015).

Almousallam M., **Moia C.**, Zhu H., Development of nanostructured lipid carrier for dacarbazine delivery, *International Nano Letters* pp1-8, DOI: 10.1007/s40089-015-0161-8 (2015).

**Submitted: Moia C.**, Dinsdale D., Comune M., Almousallam M., Ferreira L., MacFarlane M., Zhu H., The size of colloidal silica particles dictates their stability in culture medium, cytotoxicity and wound healing effects in human skin keratinocyte HaCaT cells, *Advanced Healthcare Materials*.